SECOND-ORDER DIRECT ANALYSIS FOR DESIGN OF MODERN STEEL STRUCTURES WITH NONSYMMETRIC CROSS-SECTIONS

CHEN LIANG

PhD

The Hong Kong Polytechnic University

2023

THE HONG KONG POLYTECHNIC UNIVERSITY

DEPARTMENT OF CIVIL AND ENVIRONMENTAL ENGINEERING

Second-order Direct Analysis for Design of Modern Steel Structures with Nonsymmetric Cross-sections

Chen Liang

A thesis submitted in partial fulfilment of the requirements for the degree of Doctor of Philosophy

September 2022

CERTIFICATE OF ORIGINALITY

I hereby declare that this thesis is my own work and that, to the best of my knowledge and belief, it reproduces no material previously published or written, nor material that has been accepted for the award of any other degree or diploma, except where due acknowledgement has been made in the text.

____ (Signed)

CHEN Liang

____ (Name of student)

To my Family

ABSTRACT

Steel members with nonsymmetric cross-sections are widely used in modern steel structures because of their fast construction and structural efficiency. The disadvantage in fabricating nonsymmetric cross-sections is no longer as significant because most steel members can be formed and/or robotically welded, thereby enabling arbitrary shapes to be made easily and economically. Innovative structural forms and section shapes are gradually proposed and employed in modern steel structures.

The direct adoption of traditional design methods may be inappropriate because their design formulae are basically derived for regular sections with symmetrical shapes. Therefore, lacking a suitable design method could cause certain obstacles when developing an innovative structural system using nonsymmetric cross-sections with higher structural efficiency in modern steel structures. In view of such a need, this research develops an innovative structural design method, namely the second-order direct analysis, to tackle the problem of designing steel frames using nonsymmetric cross-sections.

This thesis proposed a new numerical analysis framework for modern steel frames with nonsymmetric cross-sections using the Line Finite-Element Method (LEM), which is the most practical and widely used method in practice. A refined line element and an improved Gaussian line element for members with nonsymmetric thin-walled sections are introduced. The element formulations are derived based on the nonsymmetrical section assumption, where the Wagner effects and the

noncoincidence of the shear center and centroid of the nonsymmetric sections are directly considered, and therefore, the lateral-torsional and flexural-torsional of nonsymmetric section members can be captured robustly. Further, a novel line element for members with nonsymmetric thick-walled sections is proposed, where the non-negligible shear deformation in thick-walled members is considered by incorporating the shear deformation in the element stiffness matrices.

More parameters inherent to nonsymmetric sections are required for the analysis, where the Warping and Wagener effects are more critical and need to be reflected through additional coefficients. Therefore, five additional section properties are required, including the coordinates of the shear center and the Wagner coefficients. Two cross-section analysis methods, namely the Coordinate Method and the 2D Finite-Element method, are introduced for the calculation of the section properties of nonsymmetric thin- and thick-walled sections.

The successful structural design of steel structures requires a realistic assessment of a structural system's ultimate strength capacity under extreme loading conditions, such as super-typhoon and seismic attacks, to ensure structural safety without collapse. As such, this research proposes a second-order inelastic analysis method for the nonsymmetric members. The concentrated plasticity (CP) model is integrated into the LFEM, and the modified tangent modulus (MTM) approach originally proposed by Ziemian and McGuire (2002) is adopted to represent partial material yielding. Moreover, this research proposes a numerical analysis method for the nonsymmetric members under fire conditions. A novel line element formulation based on the co-rotational (CR) method is developed. The proposed CR line element formulation can conveniently consider the material degradation and the thermal expansion. A refined

Newton-Raphson-typed numerical procedure for the analysis at elevated temperatures is proposed and elaborated.

A series of verification examples are given to verify the accuracy of the proposed cross-section analysis methods, the line element formulations, and the inelastic analysis method. Results from literatures, experiments, and sophisticated Finite Element Analysis have been used as the benchmark answers.

The distinct feature of this research is the development of a second-order direct analysis framework for the steel frames with nonsymmetric cross-sections, integrating the techniques such as robust cross-section analysis methods, LFEM with several line element formulations included, and inelastic analysis method. The research work in the thesis is expected to lead to a significant improvement in the design of more economical and safer structures, enhancement of construction efficiency, and reduction of manpower demands.

Keywords: Second-order direct analysis; Steel frames; Nonsymmetric cross-sections; Warping; Wagner effects; Inelastic analysis; Fire.

PUBLICATION & AWARD

Journal Paper:

[1] **Liang Chen**, Wen-Long Gao, Si-Wei Liu, Ronald D. Ziemian and Siu-Lai Chan, Geometric and Material Nonlinear Analysis of Steel Members with Nonsymmetric Sections - Modified Tangent Modulus Approach, Journal of Constructional Steel Research, 2022, 198: 107537. ***(Published)***

[2] **Liang Chen**, Si-Wei Liu, Jing-Zhou Zhang, Michael C.H. Yam. Efficient Algorithm for Buckling Strength of Corroded I-Section Steel Members with Monte Carlo Simulation, Thin-Walled Structures, 2022, 175:109216. ***(Published)***

[3] **Liang Chen**, A.H.A. Abdelrahman, Si-Wei Liu, Ronald D. Ziemian and Siu-Lai Chan. Gaussian-Beam-Column Element Formulation for Large-Deflection Analysis of Steel Members with Open-sections Subjected to Torsion, Journal of Structural Engineering, ASCE, 2021, 147(12): 04021206. ***(Published)***

[4] **Liang Chen**, Si-Wei Liu, Chi-Kin Lau and Siu-Lai Chan. Nonlinear Finite-element-analysis and Design of Steel-concrete Composite Ring (SCCR) joints. Journal of Constructional Steel Research, 161 (2019) 400-415 ***(Published)*** *– Awarded for HKIE Structural Excellence Award 2020 - Research and Development Award – Grand Award*

[5] **Liang Chen**, Si-Wei Liu, Rui Bai and Siu-Lai Chan, Co-Rotational Formulations for Geometrically Nonlinear Analysis of Beam-Columns

Including Warping and Wagener Effects. International Journal of Structural Stability and Dynamics, 2022: 2350052. ***(Published)***

[6] **Liang Chen**, Si-Wei Liu, and Siu-Lai Chan, Large Deflection Analysis of Steel Structures with Nonsymmetric Sections under Elevated Temperatures by Novel Co-rotational Formulation, Engineering Structures. ***(Under Review)***

[7] **Liang Chen**, Jing-Zhou Zhang, Si-Wei Liu, and Zhi-Wei Yu. Bifurcation Buckling Load of Steel Angle with Random Corrosion Damage. Thin-Walled Structures. ***(Under Review)***

[8] **Liang Chen**, Hao-Yi Zhang, Si-Wei Liu and Ronald D. Ziemian. Efficient Finite-element framework for Second-order Analysis of Steel Members with Nonsymmetric Thick-walled Sections, Journal of Structural Engineering, ASCE. ***(Under Review)***

[9] **Liang Chen**, Hao-Yi Zhang, Si-Wei Liu and Siu-Lai Chan, Second-order Analysis of Beam-columns by Machine Learning-based Structural Analysis through Physics-Informed Neural Networks, Engineering Structures. ***(Under Review)***

[10] A.H.A. Abdelrahman, **Liang Chen**, Si-Wei Liu and Ronald D. Ziemian. Timoshenko Line-element for Stability Analysis of Tapered-I-section Steel Members Considering Warping Effects, Thin-Walled Structures, 2022, 175:109198. ***(Published)***

[11] Jing-Zhou Zhang, **Liang Chen**, Si-Wei Liu, Michael C.H. Yam. Efficient Elastic Buckling Assessment Algorithm for Steel Members with Random Non-uniform Corrosion. Engineering Structures, 2022, 266: 114550. ***(Published)***

[12] Weihang Ouyang, Guanhua Li, **Liang Chen**, Si-Wei Liu and Siu-Lai Chan, Machine Learning-based Soil-Structure Interaction Analysis of Laterally-loaded Piles through Physics-Informed Neural Networks, Computers and Geotechnics. ***(Under Review)***

Conference Paper:

[1] **Liang Chen**, A.H.A. Abdelrahman, Si-Wei Liu, Ronald D. Ziemian and Siu-Lai Chan. Large Deflection Analysis of Beam-Columns with General Sections Using Gaussian Line-element Method. Proceedings of the Cold-Formed Steel Research Consortium Colloquium. 20-22 October 2020

[2] **Liang Chen**, Si-Wei Liu and Siu-Lai Chan. An efficient numerical implementation for stability analysis of steel members using nonsymmetric sections at the elevated temperatures, Tenth International Conference on Advances in Steel Structures, Chengdu, China, August 21-23, 2022.

[3] **Liang Chen**, Weihang Ouyang, Si-Wei Liu and Ronald D. Ziemian. Numerical Implementation of GMNIA for Steel Frame with Nonsymmetric Sections, CFSRC Colloquium 2022, 17-19 October 2022. – *Awarded for Best Student Paper Award – Modelling Insights by The Cold-formed Steel Research Consortium in CFSRC Colloquium 2022*

[4] Wen-Long Gao, **Liang Chen** and Si-Wei Liu. Analysis of transient structural responses of steel frames with nonsymmetric sections under earthquake motion, Tenth International Conference on Advances in Steel Structures, Chengdu, China, August 21-23, 2022.

[5] Hao-Yi Zhang, **Liang Chen**, Guan-Hua Li and Si-Wei Liu. Second-order analysis of steel members using nonsymmetric sections with moderately thick-walled steel plates, Tenth International Conference on Advances in Steel Structures, Chengdu, China, August 21-23, 2022.

[6] Weihang Ouyang, **Liang Chen** and Si-Wei Liu. Second-order direct analysis for steel H-piles accounting for post-driving residual stresses, Tenth International Conference on Advances in Steel Structures, Chengdu, China, August 21-23, 2022.

Award:

- Structural Excellence Award 2020 - Research and Development Award – Grand Award. *by The Hong Kong Institution of Engineers - the Structural Division*
- Best Student Paper Award – Modeling Insights – *by The Cold-formed Steel Research Consortium in CFSRC Colloquium 2022*

ACKNOWLEDGEMENTS

I would like to express my sincere gratitude to my supervisor, Professor S.L. Chan, for his enlightening guidance, support, and encouragement throughout the course of my Ph.D. study. His rigorous attitude to academic research, keen engineering insight, and enduring enthusiasm for life encourage and influence me a lot and inspire me to strive for excellence in the future.

I would also like to express my profound appreciation to Dr. S.W. Liu for his enlightening guidance and enthusiastic support, and special appreciation to Dr. Y.P. Liu for his valuable discussions and continuous encouragement.

I would like to thank the Department of Civil and Environment Engineering, The Hong Kong Polytechnic University, for providing me with financial support and research facilities.

I wish to express my gratitude and appreciation to all the NIDA team members for their companionship and help over these years.

I would like to extend my thanks to Professor R. D. Ziemian. I truly appreciate the opportunity to work with him and the informative guidance he gave me.

Finally, I would like to express my deepest gratitude to my wife, Ya-Jun Tang, and my parents, Zhou-Qiang Chen and Xin-Shu Li, for their unconditional love, support, and encouragement.

CONTENTS

ABSTRACT I
PUBLICATION & AWARD IV
ACKNOWLEDGEMENTS IX
CONTENTS X
LIST OF FIGURES XIV
LIST OF TABLES XVIII
LIST OF SYMBOLS XX

CHAPTER 1. INTRODUCTION 1
1.1 Background 2
1.2 Objectives 8
1.3 Outline of the Thesis 11

CHAPTER 2. LITERATURE REVIEW 13
2.1 Introduction 13
2.2 Line Finite-Element Method 13
2.3 Members with Nonsymmetric Cross-sections 16
2.3.1 Cross-section analysis 17
2.3.2 Nonsymmetric thin-walled members 18
2.3.3 Nonsymmetric thick-walled members 20
2.3.4 Inelastic analysis of nonsymmetric members 22
2.3.5 Nonsymmetric members under fire 25

CHAPTER 3. CROSS-SECTION ANALYSIS METHODS 29
3.1 Introduction 29
3.2 Coordinate Method (CM) for Thin-walled Sections 29
3.2.1 Section modelling 30
3.2.2 Warping ordinate 32
3.2.3 Wagner coefficients 34

3.2.4 Verification examples 35
3.3 2D FE Method for Thick-walled Sections 40
3.3.1 Section modelling 40
3.3.2 Shape functions and Jacobian matrix of the CST element 43
3.3.3 Basic geometric properties 43
3.3.4 Torsion and warping properties 44
3.3.5 Shear coefficients 50
3.3.6 Verification examples 56

CHAPTER 4. ELASTIC ANALYSIS OF STEEL MEMBERS WITH THIN-WALLED SECTIONS...69
4.1 Introduction 69
4.2 Refined Line Element for Wanger Effect Based on Euler-Bernoulli Beam Theory 71
4.2.1 Element reference axes 71
4.2.2 Shape functions 73
4.2.3 Strain and stress descriptions 74
4.2.4 Total potential energy 78
4.2.5 Linear and geometric stiffness matrices 82
4.2.6 Element tangent stiffness matrix 85
4.3 Improved Gaussian Line Element for Members under Large Torsion 86
4.3.1 Element reference axes 89
4.3.2 Total potential energy function 91
4.3.3 Gaussian-Quadrature method 92
4.3.4 Section properties for each Gauss point 94
4.3.5 Tangent stiffness matrix 96
4.4 Modified Updated Lagrangian Approach 102
4.5 Verification Examples 106
4.5.1 Verification of the refined line element 106
4.5.2 Verification of the improved GLE element 115

CHAPTER 5. ELASTIC ANALYSIS OF STEEL MEMBERS WITH THICK-WALLED SECTIONS...132
5.1 Introduction 132
5.2 Line Element Based on Timoshenko Beam Theory...132

5.2.1 Element reference axes 132
5.2.2 Shape interpolation functions and shear deformations 133
5.2.3 Strain descriptions and total potential energy function 134
5.2.4 Tangent stiffness matrix 137
5.3 Verification Examples 139

CHAPTER 6. INELASTIC ANALYSIS 149
6.1 Introduction 149
6.2 Assumptions 150
6.3 Line Element Formulation 151
6.4 Modified Tangent Modulus (MTM) Method 152
6.4.1 Concentrated plasticity (CP) model 152
6.4.2 Implementation 153
6.5 Full-yield Criterion Using a Yield Surface 157
6.5.1 Full-yield criterion 157
6.5.2 Cross-section modelling 159
6.5.3 Yield surface generation 160
6.6 Post Yielding Behavior 164
6.6.1 Correction of force point outside the yield surface 165
6.6.2 The plastic reduction matrix 165
6.6.3 Gradients to the yield surface 168
6.7 Numerical Procedure 169
6.7.1 Global stiffness matrix and element resistant forces 169
6.7.2 Analysis procedure 170
6.8 Verification Examples 172
6.8.1 Verification of the yield surfaces generation 172
6.8.2 Nonlinear analysis of steel members 189
6.8.3 Nonlinear analysis of planar frames 199
6.8.4 Nonlinear analysis of spatial frames 207

CHAPTER 7. SECOND-ORDER ELASTIC ANALYSIS UNDER FIRE 211
7.1 Introduction 211
7.2 Assumptions 215
7.3 Co-rotational (CR) Formulation 215

7.3.1 Element local reference axes and shape functions 215
7.3.2 Strain definitions...218
7.3.3 Total potential energy...219
7.3.4 Secant relations...222
7.3.5 Tangent stiffness and transformation matrices..228
7.4 Numerical Procedure..232
7.5 Verification Examples...234

CHAPTER 8. CONCLUSIONS AND RECOMMENDATIONS.......................248
8.1 Conclusions..248
8.2 Recommendations for Future Work...249

REFERENCES...252

LIST OF FIGURES

Figure 1.1 Nonsymmetric members in modern steel constructions. 3

Figure 1.2 Typical symmetric and nonsymmetric sections 4

Figure 1.3 Research roadmap 9

Figure 2.1 Examples of nonsymmetric thin-walled sections 18

Figure 2.2 Structural behaviors of thin- and thick-walled members 21

Figure 2.3 The yield surface of a symmetric section (Chen et al. 2021) 24

Figure 2.4 The yield surface of a nonsymmetric section (Chen et al. 2021) 25

Figure 2.5 Schematic behaviors of cantilever beams in fire 27

Figure 3.1 Modeling an open section via points and segments 31

Figure 3.2 The coordinates and the warping ordinate at a point 33

Figure 3.3 Dimensions of the mono-symmetric-I section 36

Figure 3.4 Four sections for the verification of CM method 37

Figure 3.5 Example of section modeling 41

Figure 3.6 Constant strain triangle (CST) element 42

Figure 3.7 Verification examples of geometric and torsional properties 57

Figure 3.8 Comparation results 63

Figure 3.9 Verification examples of shear deformation coefficients 66

Figure 4.1 Examples of non-symmetric thin-walled sections 70

Figure 4.2 Deformations and forces in the element local axes 72

Figure 4.3 Local coordinate systems 76

Figure 4.4 Illustrations of the simulations using different elements 88

Figure 4.5 Illustrations of the deformations and forces in the element local axes 89

Figure 4.6 Gauss points along the element length 90

Figure 4.7 An illustration of the section rotation at a general Gauss point 94

Figure 4.8 The traditional UL and the proposed modified approaches 105

Figure 4.9 Simply-supported beams with mono-symmetric-I sections 108

Figure 4.10 The mono-symmetric-I-beam under a concentrated load 110

Figure 4.11 Comparison results of the mon-symmetric I-beam (Downward) 111

Figure 4.12 Comparison results of the non-symmetric I-beam (Upward) 112

Figure 4.13 The cantilever column with channel section 113

Figure 4.14 Load-deflections of the cantilevered channel column 114

Figure 4.15 Load-displacement curves for member with symmetric I section 118

Figure 4.16 Load-displacement curves for the member with channel section 122

Figure 4.17 Load-displacement curves for the member with mono-I section 123

Figure 4.18 Load-displacement curves for member with nonsymmetric section 128

Figure 4.19 Load-displacement curves for a member with nonsymmetric section ... 130

Figure 4.20 Load-displacement curves of the L-shaped frame 131

Figure 5.1 The deflection along the beams 140

Figure 5.2 Load versus displacement curves for the member under compression 141

Figure 5.3 Load-displacement curve for the cantilever beam with I section 145

Figure 5.4 Load-displacement curve for the cantilever beam with channel section .. 146

Figure 5.5 Load-displacement curve for the beam with lipped channel section 147

Figure 5.6 Load-displacement curve for the beam with nonsymmetric box section . 148

Figure 6.1 Concentrated plasticity (CP) model..152

Figure 6.2 Plots of the τ factor. 154

Figure 6.3 A spatial yield surface 158

Figure 6.4 Cross-section modelling 159

Figure 6.5 Strain and stress over the cross-section 161

Figure 6.6 A flowchart to generate the complete yield surface 163

Figure 6.7 Correction of force point outside the yield surface 164

Figure 6.8 Plastic deformation...167

Figure 6.9 Yield surface and the gradient on it...169

Figure 6.10 Flowchart of numerical analysis procedure...........................171

Figure 6.11 Doubly symmetric sections (Unit: mm) 173

Figure 6.12 Comparison results for the doubly symmetric sections.........175

Figure 6.13 Nonsymmetric sections (Unit: mm) 176

Figure 6.14 Comparison results for section A 179

Figure 6.15 Comparison results for section B 182

Figure 6.16 Comparison results for section C 185

Figure 6.17 Comparison results for section D 188

Figure 6.18 Post-buckling behavior of the beam. 191

Figure 6.19 Load-deflection curve of fixed-ended beam..........................193

Figure 6.20 Post-buckling behavior of the channel member. 194

Figure 6.21 Post-buckling behavior of the nonsymmetric member..........195

Figure 6.22 Load-deflections of the columns 198

Figure 6.23 Load-deflection curve of portal frame...................................201

Figure 6.24 Sophisticated Finite element model.......................................203

Figure 6.25 Load-deflection curve of nonsymmetric portal frame. 204

Figure 6.26 Response curves for Ziemian frame. 205

Figure 6.27 Load deflection behavior of six-story frame 206

Figure 6.28 Load deflection behavior of two-story space frame 208

Figure 6.29 Twenty-story space frame 209

Figure 7.1 Element local DOF and temperature distribution in the cross-section 216

Figure 7.2 The reduction factors for the Young's modulus 235

Figure 7.3 Section dimensions and member boundary conditions 237

Figure 7.4 Temperature-displacement cures for the middle points of the columns ... 238

Figure 7.5 Section dimensions and boundary conditions 239

Figure 7.6 Temperature-displacement cures for the middle points of the beams 241

Figure 7.7 Temperature-displacement cures for the cantilever beam 243

Figure 7.8 Model for the nonlinear analysis of the nonsymmetric steel beams 244

Figure 7.9 Temperature-displacement cures of the nonsymmetric steel beams 245

Figure 7.10 Temperature-displacement at the middle span of the star frame 246

LIST OF TABLES

Table 3.1 Section properties of the mono-symmetric-I section....................................38

Table 3.2 Section properties of the WT, L, and C sections 39

Table 3.3 Geometric and torsional properties – Section A (Unit: mm).......................58

Table 3.4 Geometric and torsional properties – Section B (Unit: mm).......................59

Table 3.5 Geometric and torsional properties – Section C (Unit: mm).......................60

Table 3.6 Geometric and torsional properties – Section D (Unit: mm).......................61

Table 3.7 Shear coefficients of Section a...67

Table 3.8 Shear coefficients of Section b 67

Table 3.9 Shear coefficients of Section c...68

Table 3.10 Shear coefficients of Section d 68

Table 4.1 Coefficients in modification matrix $\boldsymbol{\xi L}$..98

Table 4.2 Coefficients in modification matrix $\boldsymbol{\xi U}$ 99

Table 4.3 Buckling strengths under positive bending moment.................................108

Table 4.4 Buckling strengths under negative bending moment................................109

Table 4.5 Section properties of the channel section 115

Table 4.6 Results summary for the member with symmetric I section 119

Table 4.7 Results summary for the member with channel section 125

Table 4.8 Results summary for the member with nonsymmetric section..................129

Table 5.1 Section properties and shear coefficients of the sections 144

Table 6.1 Comparison of the predicted ultimate load factor of the beam................192

Table 6.2 Section properties of the solid rectangle...199

Table 6.3 Comparison of ultimate load factor of portal frame. 201

Table 6.4 Section properties of the lipped channel section 202

Table 6.5 Ultimate load of two-story space frame...208

Table 7.1 Critical buckling temperatures of the columns with L section 237

Table 7.2 Critical buckling temperatures of the beams (under negative temperature gradient) 240

Table 7.3 Critical buckling Temperatures of the beams (under positive temperature gradient) 240

LIST OF SYMBOLS

A	The section area
$\boldsymbol{B}$	Shape function matrix
$\boldsymbol{d\Delta}$	Incremental displacement
$\boldsymbol{D}$	The constitutive matrix
E	Young's modulus
$\boldsymbol{f}$	Shape functions of line element
$\boldsymbol{F}$	The vector of the element forces
$\boldsymbol{F_a}$	The applied load vector
F_x	Force along the x axis
F_y	Force along the y axis
F_z	Force along the z axis
G	The shear modulus
$\boldsymbol{G}$	The gradient of the yield surface
I_y	Moment of Inertia about the y axis
I_{yz}	Product of Inertia
I_z	Moment of Inertia about the z axis
I_ω	Warping constant
J	Torsional Constant
$\boldsymbol{J}$	Jacobian matrix
k_y	Shear coefficients along the y axis
k_z	Shear coefficients along the z axis

$\boldsymbol{K}$	The total stiffness matrix for warping function
$\boldsymbol{K_E}$	The element global stiffness matrix
$\boldsymbol{K_g}$	The total global stiffness matrix
$\boldsymbol{k_E}$	Element local stiffness matrix
$\boldsymbol{k_G}$	Linear stiffness matrix
$\boldsymbol{k_L}$	Geometric stiffness matrix
$\boldsymbol{k_m}$	The element plastic reduction matrix
$\boldsymbol{k_T}$	Thermal-related geometric stiffness
$\boldsymbol{k_U}$	Additional geometric stiffness matrix for nonsymmetric sections
L	The length of segment or member.
L_r	Loading ratio
M_b	Bi-moment
M_{cr}	Critical buckling moment
M_y	Bending moment about the x axis
M_y	Bending moment about the y axis
M_z	Bending moment about the z axis
$\boldsymbol{n}$	Unit normal vector
$\boldsymbol{N}$	Shape functions of 2D element
P	The axial force
P_{cr}	Critical buckling force
P_T	The axial force caused by the thermal expansion
$\boldsymbol{P}_w$	The load vector for warping function
$\boldsymbol{R}$, $\boldsymbol{R}_G$	Reaction force
t	The thick of segment

$\boldsymbol{T}$	Transformation matrix
T_0	The room temperature
u	Displacement along the x axis
$\boldsymbol{u}$	The vector of the DOFs
$\boldsymbol{u}_T$	The total element deformation
U	The strain energy stored by the element
v	Displacement along the y axis
V	The work done by the external forces
V_y	Shear force along the y axis
V_z	Shear force along the z axis
w	Displacement along the z axis
W_i	The weight of each Gauss points
y	y coordinate
y_s	y coordinate of the shear center
Y_o	Y coordinate of the section centroid
z	z coordinate
z_s	z coordinate of the shear center
Z_o	Z coordinate of the section centroid
α	The thermal expansion coefficient
$\boldsymbol{\alpha}$	Transformation matrix
α_y, α_z	Empirical factors
$\beta_y, \beta_z, \beta_\omega$	Wagner coefficients
$\boldsymbol{\Gamma}$	Transformation matrix
δW	Virtual work

$\Delta\boldsymbol{f}$	The vector of the incremental nodal forces
$\Delta\boldsymbol{F_g}$	The unbalanced force vector
$\Delta\boldsymbol{R}_G$	The element incremental force
$\Delta\boldsymbol{u}$	The vector of the incremental nodal displacements
$\Delta\boldsymbol{U_g}$	The global incremental displacement vector
$\boldsymbol{\varepsilon}$	Strain tensor
ε_{xx}	The normal strain
ε_{xy}	The strains in x-y plane
ε_{xz}	The strains in x-z plane
$\boldsymbol{\varepsilon}_T$	The thermal-related strain
$\boldsymbol{\varepsilon_\sigma}$	The force-related strain
η	Element local axis
θ_b	Warping deformation
θ_x	Rotation about x axis
θ_y	Rotation about y axis
θ_z	Rotation about z axis
τ	Reduction factor in MTM method
τ_{xy}, τ_{xz}	Shear stress
ν	Poisson’s ratios
ξ	Element local axis
$\boldsymbol{\xi_L}$	The modification matrices for $\boldsymbol{k_L}$
$\boldsymbol{\xi_U}$	The modification matrices for $\boldsymbol{k_U}$
Π	The total potential energy

$\boldsymbol{\rho_{et}}$	Reduction matrix
σ_x	Axial stress
$\mathit{\Phi}$	The yield surface
$\mathbf{\Phi}$	Shear function
ω	Warping ordinate
ϵ	Element lateral displacement

CHAPTER 1.

INTRODUCTION

Robotic welding machines and building information modelling (BIM) are extensively utilized in modern steel constructions, eliminating the constraints of fabricating nonsymmetrical sections. Innovative structural forms and section shapes are gradually proposed and employed in modern structures. One of the dominant features among such structures is their section shapes are nonsymmetrical, usually for improving material-usage efficiency.

The traditional design methods are inappropriate for the design of nonsymmetric members because their design formulae are basically derived based on the double-symmetrical section assumption, which causes the ignorance of noncoincidence between the centroid and shear center as well as the Wagner's effects. Hence, there is an urgent need to develop a numerical analysis method that meets the analysis requirements for the design of modern steel structures made of nonsymmetric sections.

In view of such a need, this research develops a second-order direct analysis framework for the steel frames with nonsymmetric cross-sections, where robust cross-section analysis methods, a Line Finite-Element Method (LFEM) with several line element formulations included, and an inelastic analysis method is given.

This chapter gives the review of the research background, the research objectives, and the outlines of the thesis.

1.1 Background

Steel members with nonsymmetric cross-sections are more commonly employed in modern structures because they can significantly ease erection difficulties and costs, improving construction efficiency. Automatic welding machines and BIM techniques are extensively used in modern steel constructions, eliminating the constraints and reducing the cost of fabricating nonsymmetric sections. Innovative structural forms and nonsymmetric sections, such as those shown in Figure 1.1 and Figure 1.2 (b), are proposed and employed in modern structures, particularly in modular integrated construction (MiC). One of the dominant features among these structures is that their sectional shapes are usually nonsymmetric to improve material usage as members are commonly under different load intensities in various directions.

In recent years, new prefabricated steel structural systems, such as modular integrated construction (MiC) with light steel frames, have become popular worldwide and locally for constructing modern structures in congested cities, such as Shanghai and Shenzhen. Due to their many advantages, including high quality, fast construction, less on-site labor and reduced construction waste, these systems are promoted locally as an essential implementation of “Construction 2.0” and as substitutions for traditional RC structures. Most of the system is fabricated in factory before delivery to the construction site, where automatic welding machines or robots are extensively used to quickly fabricate complex sectional shapes for members. Steel members with nonsymmetric cross-sections are commonly employed in these light structural systems because they can significantly ease erection difficulties and improve construction efficiency (Figure 1.1).

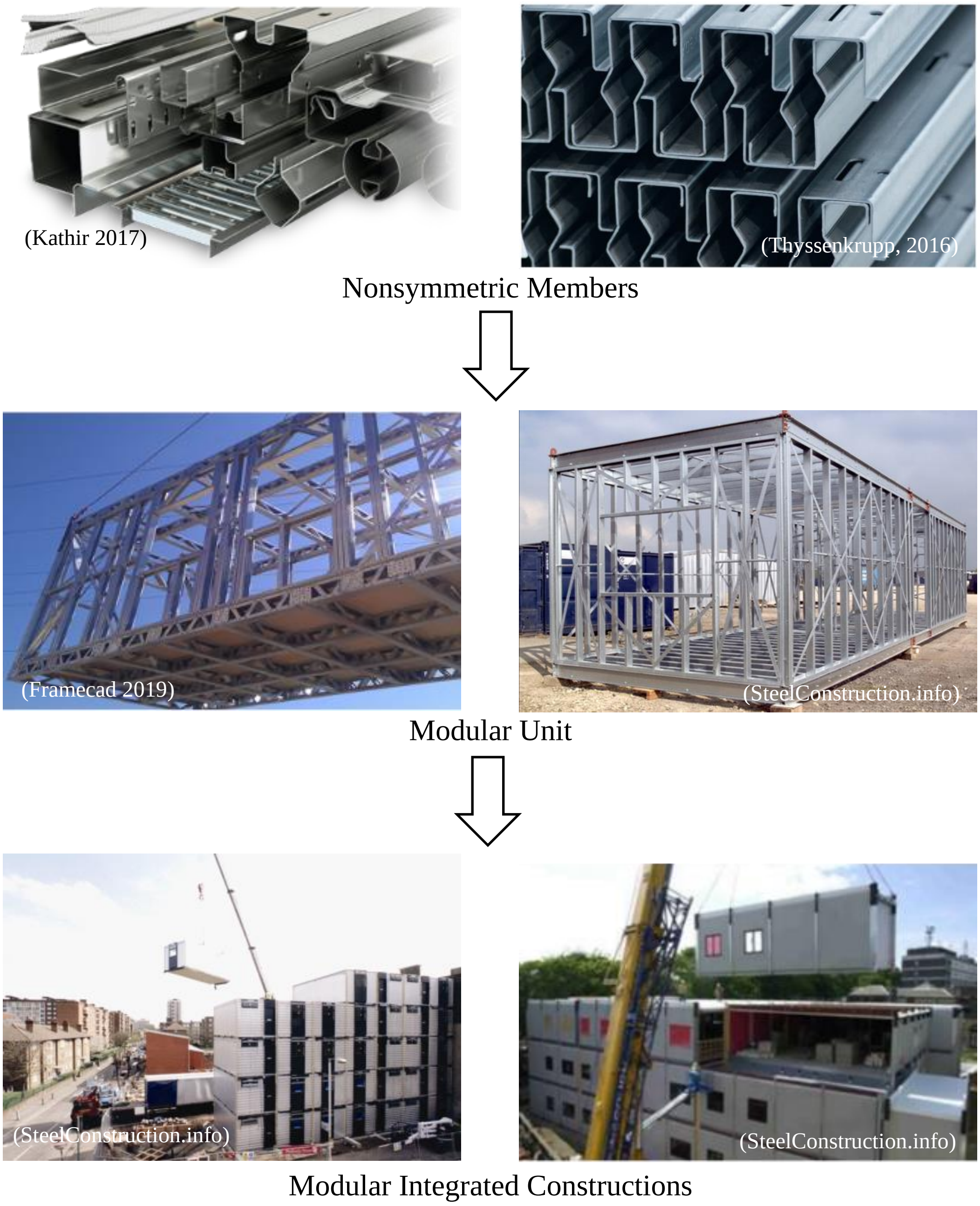

Figure 1.1 Nonsymmetric members in modern steel constructions.

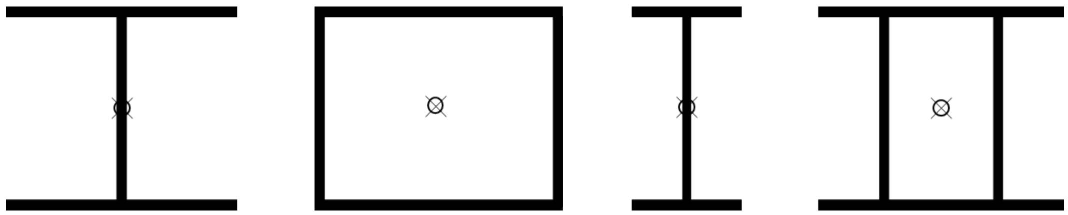

(a) Symmetric sections

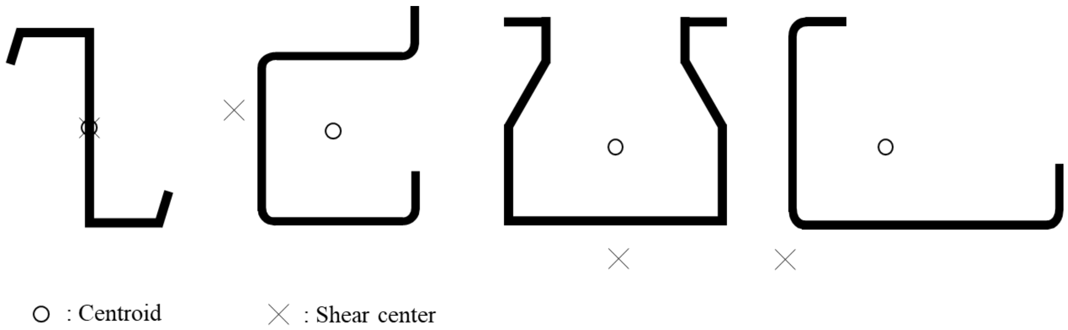

(b) Nonsymmetric sections

Figure 1.2 Typical symmetric and nonsymmetric sections

However, the direct adoption of traditional design methods is inappropriate for nonsymmetric members because their design formulae are basically derived for regular sections with symmetrical shapes. Generally, when the cross-section is nonsymmetric, the effect of misalignment for the centroid and the shear center must be considered (Figure 1.2). In current engineering practice, for simplicity, the design practice mainly focuses on traditional steel columns with regular section shapes and commonly adopts a doubly symmetrical section assumption when deriving the element formulations. This causes ignorance regarding the non-coincidence between the centroid and the shear center and the Wagner effects. Hence, there is an urgent need to develop a numerical analysis method that meets the analysis requirements for the design of modern steel structures made of nonsymmetric sections.

Nowadays, engineers commonly use the traditional design method based on the first-order linear analysis associated with the empirical assumption for designing steel members on the basis of experimental tests. However, this method is not suitable for designing members with nonsymmetric cross-sections because it lacks sufficient test results to generate the empirical design equations. Nevertheless, sticking to this method is unnecessary due to modern design methods using the second-order direct analysis available in AISC (2016), Eurocode-3 (2005) and Hong Kong steel codes (2011), which relies less on tests and more on refined numerical analysis. The structural design executed by second-order direct analysis simulates the members buckling and the material yielding under design loads to examine structural safety by direct computer simulation. This design method is applicable to the new structural forms with nonsymmetric sections once the members’ behaviors are modelled via numerical algorithms.

In general, structural design relies on the robustness of the analysis method to assess the ultimate strength behavior of structural systems. The second-order analysis method is a modern stability design approach for steel structures that commonly use Line Finite-Element Method (LFEM). The second-order analysis should be nonlinear to consider initial imperfections in the global frame and at the local member levels and to detect the system's buckling and members' instability. It also requires the analysis method to accurately simulate structural behaviors, where the robustness of the line elements is essential.

This thesis proposed a new numerical analysis framework for modern steel frames with nonsymmetric cross-sections using the LFEM, which is the most practical and widely used method in practice. The second-order direct analysis method is a modern stability design approach for steel structures that commonly use LFEM. The second-order direct analysis belongs to one of the nonlinear analysis methods with consideration of initial imperfections in the global frame and at the local member levels to detect the system's buckling and members' instability. It also requires the analysis method to simulate structural behaviors accurately; therefore, the line elements' robustness is essential. The novelty of this research project lies in the development of new mathematical models for steel members with nonsymmetric sections, which has not been conducted previously.

In this thesis, a refined line element for members with nonsymmetric thin-walled sections and cross-section analysis methods for determining pertinent section properties are proposed. The element formulations are derived based on the nonsymmetrical section assumption, where the Wagner effects and the noncoincidence of the shear center and centroid of the nonsymmetric sections are directly considered, and therefore, the lateral-torsional and flexural-torsional of nonsymmetric section members can be captured robustly. Furthermore, a novel line element for members with nonsymmetric thick-walled sections is proposed, where the non-negligible shear deformation in thick-walled members is considered by incorporating the shear deformation in the element stiffness matrices.

More parameters inherent to nonsymmetric sections are required for the analysis, where the Warping and Wagener effects are more critical and need to be reflected through additional coefficients. Therefore, five additional section properties are required, including the coordinates of the shear center and the Wagner coefficients. For sections of relatively simple shapes, such as mono-symmetric-I, T-, and L-shapes, the mathematical expressions of the Wagner coefficients can be generated, but such expressions are complicated and perhaps impossible to be generated for nonsymmetric sections with more complex shapes. The Wagner coefficients are rarely used due to the complexity of calculating their values, which could thereby lead to inaccurate results and cannot capture the real structural behavior. This project proposes robust cross-section analysis algorithms, where a Coordinate Method (CM) is introduced for the thin-walled sections, and a 2D Finite Element (FE) method is given for the thick-walled sections. The additional section properties for the nonsymmetric sections and the shear coefficients of nonsymmetric thick-walled sections can be calculated accordingly.

The successful structural design of steel structures requires a realistic assessment of a structural system's ultimate strength capacity under extreme loading conditions, such as super-typhoon and seismic attacks, to ensure structural safety without collapse. As such, this research proposes a second-order inelastic analysis method for the nonsymmetric members. The concentrated plasticity (CP) model is integrated into the LFEM, and the modified tangent modulus (MTM) approach originally proposed by Ziemian and McGuire (2002) is adopted to represent partial material yielding. Besides, a yield surface describing the full yield capacity of a nonsymmetric section is given to evaluate the full-yield condition, and the gradients to the yield surfaces are calculated and used to control the plastic flow.

Nonsymmetrical section members are usually fabricated from thin steel sheets, which makes them sensitive to fires. The high temperature will rapidly deteriorate the strength and stiffness of structural steel. The passive fire protection (PFP) method, using heat resisting (HR) coatings, is commonly adopted, but it is very expensive. When adopting the simulation-based design method to investigate the actual structural behavior under fires for identifying the critical regions and avoiding spraying HR coatings in unimportant regions, the cost for PFP can be dramatically reduced. Therefore, this research proposes a numerical analysis method for the nonsymmetric members under fire conditions. A novel line element formulation based on the co-rotational (CR) method is developed. The proposed CR line element formulation can conveniently consider the material degradation and the thermal expansion. A refined Newton-Raphson-typed numerical procedure for the analysis at elevated temperatures is proposed and elaborated.

This thesis proposed a second-order analysis framework for modern steel frames with nonsymmetric cross-sections. Two cross-section analysis methods are firstly introduced to calculate the section properties of the nonsymmetric thin-walled and thick-walled sections. A refined line element and an improved Gaussian line element for members with nonsymmetric thin-walled sections are given. Then, a novel line element for members with nonsymmetric thick-walled sections is proposed. At last, the analysis methods of the modern steel frames with nonsymmetric cross-sections under some extreme scenarios, such as fire and plasticity, are introduced.

1.2 Objectives

The main objective of this thesis is to propose a second-order analysis framework for the modern steel frames with nonsymmetric cross-sections. Since the robustness of the line elements is essential for the simulation of structural behaviors, several refined line elements for nonsymmetric members in different analysis cases are given. The element formulations are derived based on the nonsymmetrical section assumption, where the Wagner effects and the noncoincidence of the shear center and centroid of the nonsymmetric sections are directly considered. Besides, robust cross-section analysis methods are introduced to calculate the section properties of the nonsymmetric sections.

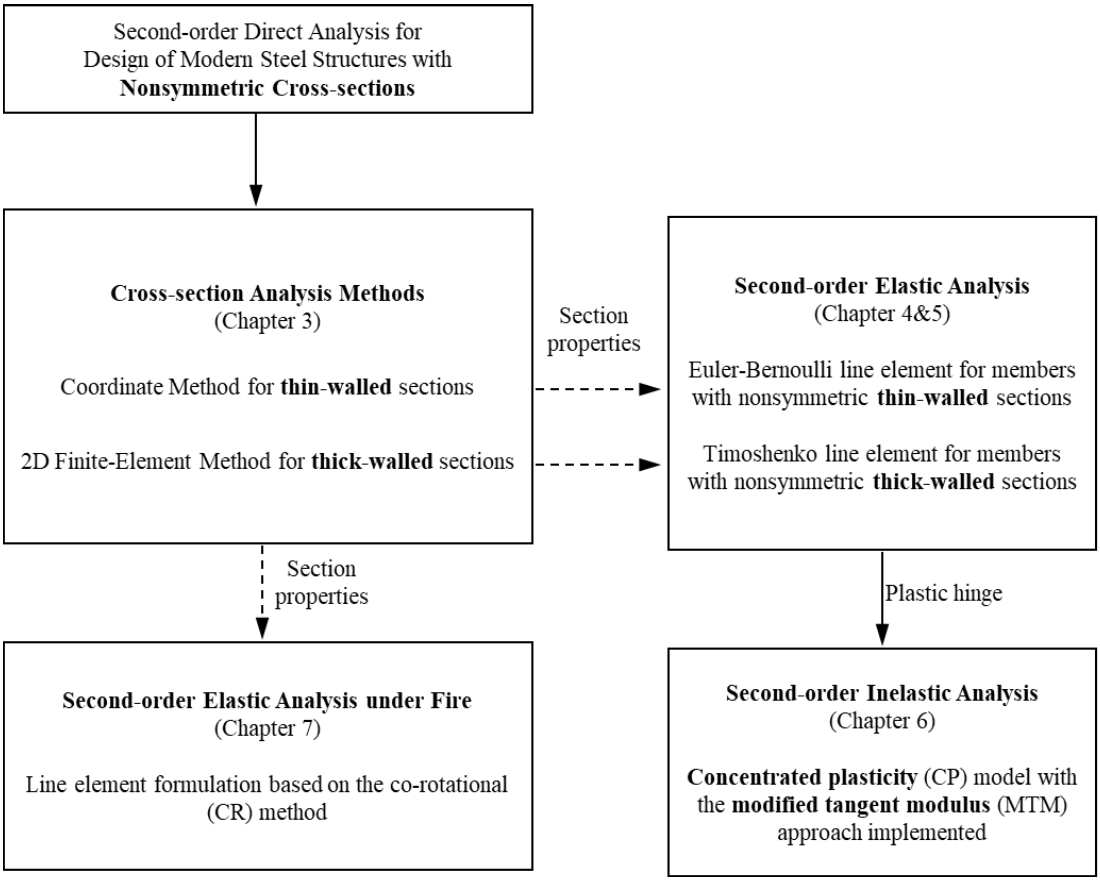

Figure 1.3 Research roadmap

The research roadmap of this thesis is given in Figure 1.3 and the research objectives are summarized below.

• To propose a second-order analysis framework for the steel frames with nonsymmetric cross-sections. The framework consists of several line elements for the analysis of nonsymmetric members in different cases and robust cross-section analysis methods.

- To develop line elements for the most common nonsymmetric sections, the thin-walled nonsymmetric sections. The element formulations will be derived based on the nonsymmetrical section assumption, where the Wagner effects and the noncoincidence of the shear center and centroid of the nonsymmetric sections are directly considered.

- To develop an improved Timoshenko line element for the second-order analysis of nonsymmetric thick-walled members. As the shear deformation will be non-negligible in nonsymmetric thick-walled members, the line element considering such effect should be given.

- To propose cross-section analysis methods for the nonsymmetric sections. Five additional section properties are needed to consider the effects of nonsymmetric sections, including the coordinates of the shear center (z_s and y_s) and the Wagner coefficients (β_y, β_z and β_ω). Besides, the shear coefficients of the nonsymmetric sections are required for the second-order analysis of nonsymmetric thick-walled members.

- To integrate the concentrated plasticity (CP) model into the line element formulation for the inelastic analysis of nonsymmetric members. A yield surface, describing the full yield capacity of a section resisting axial force and major-axis bending and/or minor-axis bending, is also given. Such yield surfaces will be used to evaluate the full-yield condition, and the gradients to the yield surfaces will be calculated and used to control the plastic flow.

- To propose analysis methods for the nonsymmetric members under some extreme scenarios like fire, where the material degradation and the thermal expansion will be considered.

1.3 Outline of the Thesis

This thesis consists of eight chapters, and the layout is presented as follows.

Chapter 1 gives the background of this research, where an urgent need to develop a numerical analysis method that meets the analysis requirements for the design of modern steel frames with nonsymmetric cross-sections is revealed. The research objectives and the outline of the thesis are also given in this chapter.

Chapter 2 gives a detailed review of previous research on the second-order analysis of nonsymmetric members. Firstly, the development of the LFEM, the most practical and widely used method in practice, is introduced. Then, a detailed review of studies about nonsymmetric members is given,

Chapter 3 proposes the cross-section analysis methods, where a Coordinate Method (CM) is introduced for the thin-walled sections, and a 2D Finite Element (FE) method is given for the thick-walled sections. Five additional section properties for the nonsymmetric sections, including the coordinates of the shear center (z_s and y_s) and the Wagner coefficients (β_y, β_z, and β_ω), and the shear coefficients of nonsymmetric thick-walled sections can be generated accordingly.

Chapter 4 presents a refined line element for members with nonsymmetric thin-walled sections and an improved Gaussian line element for the large-deflection analysis of steel members with nonsymmetric sections subjected to torsion. The element formulations are derived based on the nonsymmetrical section assumption, where the Wagner effects and the noncoincidence of the shear center and centroid of the nonsymmetric sections are directly considered, and therefore, the lateral-torsional and flexural-torsional of nonsymmetric section members can be captured robustly.

Chapter 5 proposes an improved Timoshenko line element for the second-order analysis of nonsymmetric thick-walled members. The non-negligible shear deformation in nonsymmetric thick-walled members is considered by incorporating the shear deformation in the element stiffness matrices.

Chapter 6 gives a second-order inelastic analysis method for the nonsymmetric members. The concentrated plasticity (CP) model is integrated into the line element formulation given in Chapter 4, and the modified tangent modulus (MTM) approach is adopted to represent partial material yielding. A yield surface, describing the full yield capacity of a nonsymmetric section, is given to evaluate the full-yield condition, and the gradients to the yield surfaces are calculated and used to control the plastic flow.

Chapter 7 proposes an analysis method for the nonsymmetric members under fire conditions. A novel line element formulation based on the co-rotational (CR) method is given. The proposed CR line element formulation can conveniently consider the material degradation and the thermal expansion. A Newton-Raphson-typed numerical procedure for the analysis at elevated temperatures is proposed and elaborated.

Chapter 8 presents the summary and conclusion of this thesis. The significance of this research is given along with the recommendations for future works.

CHAPTER 2.

LITERATURE REVIEW

2.1 Introduction

This chapter gives a review of the studies of steel frames with nonsymmetric cross-sections. The development of one of the most efficient and effective second-order analysis methods, the Line Finite-Element Method, is introduced along with a comprehensive review of the studies of nonsymmetric members, including the cross-section analysis of nonsymmetric sections, investigations of nonsymmetric thin-walled and thick-walled members, and inelastic and fire resistance analysis of nonsymmetric members.

2.2 Line Finite-Element Method

Modern structural design methods (e.g. the direct analysis method in AISC 2016 and the second-order design approach in Eurocode 3) require performing the nonlinear analysis of explicitly simulating the members' buckling behaviors. Against such a requirement, the following numerical solutions are proposed for analyzing nonsymmetric members: they are the Sophisticated Finite-Element Method (Schafer and Peköz 1998; Yu and Schafer 2007; Tang, Liu, and Chan 2018), the Finite-Strip method (Schafer 2002; Ádány and Schafer 2014; Bian et al. 2016), the Generalized Beam Theory (Shakourzadeh et al. 1995; Gonçalves et al. 2010; Martins et al. 2018) and the Line Finite-Element Method(Chan and Cho 2008; Du et al. 2017).

The Sophisticated Finite Element method (SFEM) adopts a large number of shell or solid elements for constructing an analysis model, and it is considered the most accurate solution; however, it requires enormous computational expense, making this method mainly used in research work for individual members or simple structures. Finite-Strip method (FSM) solves spatial problems through planar analysis by using line finite strips, which is efficient in studying the distortional and local buckling modes of individual members; however, it is unable to investigate global frame structural behaviors. Generalized Beam Theory (GBT) introduces SFEM to consider complex buckling modes and derives curve-fitting equations to compute effective stiffness for use in the Line Finite-Element Method (LFEM). This aims for practical applications in large-scale structures but is sometimes inapplicable when the SFEM results for the specific section shape are unavailable. LFEM employs line elements to simulate members' global behaviors in nonlinear analysis, and it is the most popular and efficient approach for engineering applications. However, the elements used in LFEM are mostly derived from the doubly symmetrical section assumption that will cause errors when used for member with nonsymmetric cross-section. In current engineering practice, LFEM is extensively used and is considered one of the most efficient and effective solutions in terms of computational efficiency and programming convenience (Park, Kim, and Kim 2019). The accuracy of LFEM relies on the robustness of the basic line element that is capable of simulating members' behaviors under design loads (Ding and Zhang 2019).

LFEM is the most practical and widely used method in practice. The second-order analysis method is a modern stability design approach for steel structures that commonly use LFEM. The second-order analysis should be nonlinear to consider initial imperfections in the global frame and at the local member levels and to detect the system's buckling and members' instability (El Masri and Lui 2019). It also requires the analysis method to accurately simulate structural behaviors, where the robustness of the line elements is essential. For this requirement, several line-elements are derived, including the Hermite cubic element, the stability function element, the flexibility-based element, the mixed field element, the high-order shape function element, and the warping line element and so on.

Features of these elements can be summarized as follows. First derived by Connor et al. (1968) and then improved by Bathe and Bolourchi (1979) and Chan and Kitipornchai (1987), the Hermite cubic element is the simplest line element, in which the third-order displacement shape function is assumed. However, So and Chan (1991) noticed a significant error when the axial force is large, the P-δ effect cannot be modelled in the cubic element with one element is used to model a member. White and Hajjar (1991) reported that at least three Hermite cubic elements are required to model a structural member, particularly when the member is subjected to high axial force. To tackle these drawbacks, researchers including Chen and Lui (1987), Liew et al. (1999), Chan and Gu (2000) and Feng and Wu (2020) used the stability functions to account for the effect of axial forces on member stiffness. The stiffness matrix is directly derived from the exact integration of the total potential energy equation making these elements show unique superiority for geometric nonlinear analysis in terms of computational efficiency and accuracy. Likewise, Izzuddin and Lloyd Smith (1996) and Neuenhofer and Filippou (1997) proposed the flexibility-based (also known as forced-based) element, which was refined recently by Zhang and Tien (2020). This element usually adopts a numerical integration to form a flexibility matrix, which leads to more complicated numerical procedures, and hence, more computational effort. For a more accurate analysis, the element condensation method is used to form the compound or mixed-field element derived by Zienkiewicz et al. (2005) and Bathe (2007), where several Hermite beam-column elements are combined into a compound element. However, the behavior of the inner critical section cannot be reflected in an inelastic analysis. Thus, Liu et al. (2014b) and Bai et al. (2020) established a higher-order element adopting the fourth- or fifth-order polynomial displacement functions. This can make the practical design more convenient since the capability to model per member with one element is highly improved. Therefore, the warping line element, provided by Shakourzadeh et al. (1995), Kim et al. (1996) and Liu et al. (2018), which permits nonuniform torsion along the member length, is essential for analysing steel members with nonsymmetric cross-sections.

2.3 Members with Nonsymmetric Cross-sections

The behaviors of the members with nonsymmetric cross-sections are complex. Some of them are weak in resisting torsion and minor axis bending. As a result, they might be susceptible to buckling in a lateral-torsional mode under bending, in a flexural-torsional mode under compression, or in a coupled mode under eccentric axial load. Experimental studies have shown that the buckling modes of members with nonsymmetric cross-sections are more complicated than those of typical section members. Furthermore, the prominent geometrical feature of nonsymmetric cross-section is that the shear center and the centroid do not coincide, which can lead to the Wagner effects that further causes additional twisting when a member is subjected to a positive cross-sectional force. This weakness can result in torsional deformation when the member is under loading, thus significantly reducing load capacity.

Generally, when the cross-section is nonsymmetric, the effect of misalignment for the centroid and the shear center must be considered. In current engineering practice, for simplicity, the design practice mainly focuses on traditional steel columns with regular section shapes and commonly adopts a doubly symmetrical section assumption when deriving the element formulations. This causes ignorance regarding the non-coincidence between the centroid and the shear center and the Wagner effects. Hence, there is an urgent need to develop a numerical analysis method that meets the analysis requirements for the design of modern steel structures made of nonsymmetric sections.

2.3.1 Cross-section analysis

An accurate calculation of the cross-section properties, especially for the key parameters related to nonsymmetric sections, such as the location of the shear center (z_s and y_s) and the Wagner coefficients (β_y, β_z and β_ω) (Chen and Atsuta 2007), is essential for the LFEM. For the simple shapes of thin-walled sections, such as mono-symmetric-I, T-, and L-shapes, the analytical expressions of the Wagner coefficients can be easily derived and are given by Ziemian (2010). These expressions, however, tend to be very complicated and are usually difficult to apply in practical design methods. Although cold-formed sections with irregular, nonsymmetric and complex shapes are commonly adopted in light load-bearing structural systems, such as light gauge façade framing and non-load bearing roof systems, their Wagner coefficients are in most circumstances nearly impossible to represent with closed-form mathematical expressions.

In the past decades, a 2D FE method has been proposed for the cross-section analysis of arbitrary sections. For instance, investigations on utilizing FE simulation in solving the Sanit-Venant torsion problem have been presented by early researchers such as Herrmann (1965), Krahula and Lauterbach (1969). Calculation of shear deformation coefficients using 2D elements has been investigated by Mason et al. (1968), Schramm et al. (1994), and Gruttmann and Wagner (2001). Those works show that the 2D FE method is a reliable approach for the cross-sectional analysis.

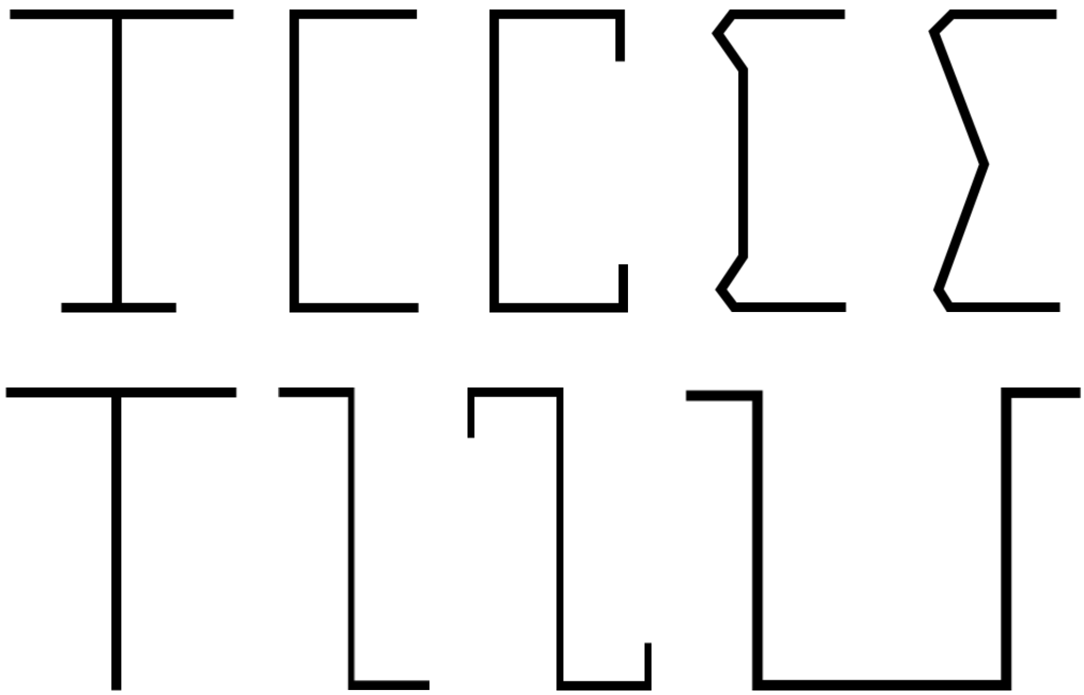

Figure 2.1 Examples of nonsymmetric thin-walled sections

2.3.2 Nonsymmetric thin-walled members

Thin-walled sections, such as those shown in Figure 2.1, are extensively used in metal structures because of their material efficiency and ease in manufacturing, with the latter often promoting the utilization of nonsymmetric sections. Members with these sections are usually weak in resisting torsion and minor-axis bending. As a result, they are susceptible to buckling in a lateral-torsional mode under bending, in a flexural-torsional mode under compression, or in a coupled mode under eccentric axial load.

Theoretical solutions for calculating the buckling strengths of the slender thin-walled members with the idealized boundary conditions were studied extensively by the 1950s and1960s (Bleich 1952; Salvadori 1956; Timoshenko and Gere 1961; Vlasov 1962). Based on these analytical methods, some design codes and guidelines, such as BS 5950-5 (1998), adopted empirical equations for determining the buckling strength of cold-formed members with open-sections. However, in more modern codes, such as AISC (2016), Hong Kong steel codes (2011), and Eurocode 3 (2005), the simulation-based design approach is adopted whereby the structural responses of members can be directly simulated for confirming the buckling strength under design loads. Therefore, a reliable numerical method, which accurately reflects member behavior within the analysis, is essential for a successful design.

Research on the stability of thin-walled beam members was initiated when the linear theory of non-uniform torsion for elastic beams was proposed by Vlasov in 1962. This topic has received continuous attention over the past 56 years and has been studied by several researchers who have been employing beam-column element theories. Such investigators include Bradford and his associates (Bradford and Ronagh 1997; Bradford 1986; Bradford and Cuk 1988; Bradford and Hancock 1984), Kitipornchai and Trahair (1972; 1975), Yang and his associates (Yang and McGuire 1986; Yang 1987), Rasmussen and his research team (Zhang et al. 2015; Rasmussen et al. 2016), and several others (Saleeb et al. 1992; Teh and Clarke 1998; Kim and Kim 2000; McGuire et al. 2000). These researchers have assumed the section to be doubly symmetric, and the effects caused by the shear center and the centroid not being coincidental are not included their element formulations. As reported by Mohri *et al.* (2003), the buckling strength of a slender beam with a mono-symmetric I-shape section can be dramatically over-estimated (by as much as a factor of two) when conventional symmetric warping elements are used.

More recently, some researchers, such as Chan and Kitipornchai (1987), Shakourzadeh et al. (1995), Kim et al. (1996), Hsiao and Lin (2000), Pi and Bradford (2001), Saade et al. (2004) and Machado (2008), have formulated beam-column elements with a warping degree of freedom (DOF) for the members with general thin-walled sections. These elements, however, were developed assuming the load is only applied at the shear center, which are inconsistent with the conventional elements that adopt the centroid as the origin for the element's local axes.

2.3.3 Nonsymmetric thick-walled members

Steel members with nonsymmetric cross-sections are more commonly employed in innovative modern structures. However, current frame analysis approaches for the members with nonsymmetric cross-sections are mainly based on thin-walled assumptions (Yang and McGuire 1986; Chan and Kitipornchai 1987; Prokić 1993; Hsiao and Lin 2000; Saadé et al. 2004), where the transverse shear deformations are neglected, leading to over-estimate the member stiffness of the thick-walled members. Existing approaches for the simulation of the nonsymmetric thick-walled members generally involve shell or solid elements, which are limited to single members due to high computational costs.

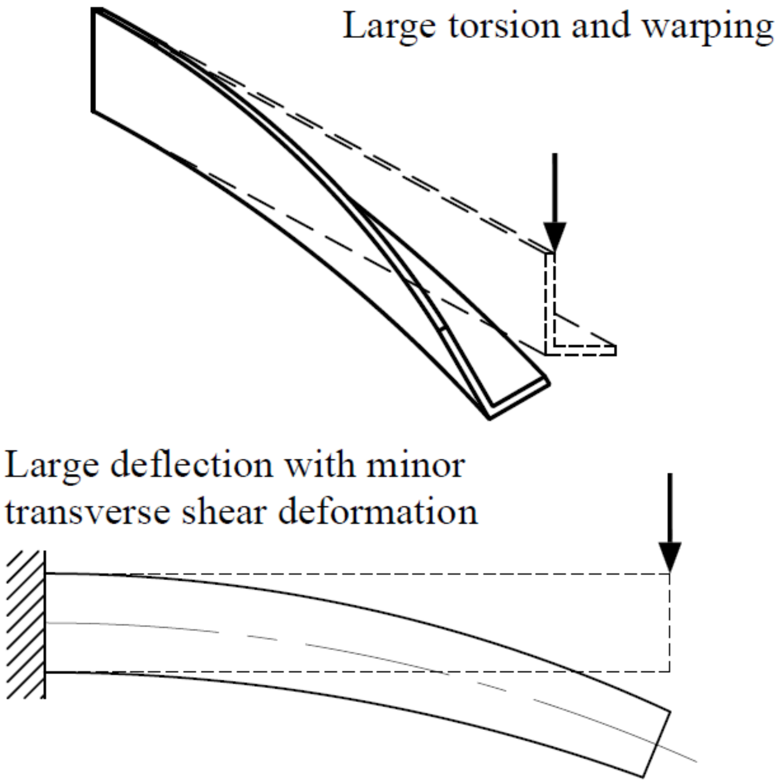

(a) Members with thin-walled section

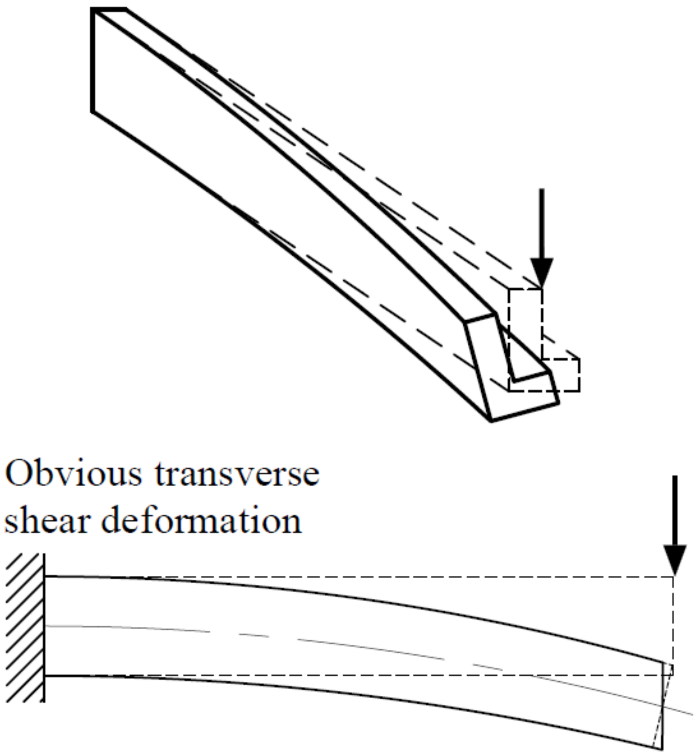

(b) Members with thick-walled section

Figure 2.2 Structural behaviors of thin- and thick-walled members

Structural behaviors of steel members with different section wall thicknesses are quite different. Generally, thin-walled members are more susceptible to local buckling, torsion, and warping effects (Figure 2.2 (a)). The transverse shear deformation is often neglected since it is usually relatively small. Comparatively, thick-walled members may have more obvious shear deformation, especially when subjected to transverse loads (Figure 2.2 (b)), and this shear deformation shall be considered in the analysis.

One of the most common ways to capture the shear deformation is by implementing the Timoshenko beam theory into the element formulation (Davis et al. 1972; Kim and Kim 2005; Arboleda-Monsalve et al. 2008; Murín et al. 2014). Friedman and Kosmatka (1993) developed a two-node Timoshenko beam element for the transverse displacements and rotational problems using cubic and quadratic Lagrangian polynomials for interpolation. Caillerie et al. (2015) developed a Timoshenko straight beam element with internal degrees of freedom for solving nonlinear material problems. Edem (2006) derived a beam-column element in which bending and shear rotation shape functions are interdependent by considering nonsymmetric flexural modes. Recently, Abdelrahman et al. (2022) proposed a Timoshenko beam-column element for steel members with the tapered I section, where warping effects are considered. Those research works have validated the reliability of the Timoshenko beam theory. But those elements are mainly based on a symmetric-section assumption where the nonsymmetric section effects will be ignored.

2.3.4 Inelastic analysis of nonsymmetric members

The successful structural design for steel structures requires a realistic assessment of the ultimate strength capacity of a structure under extreme loading conditions, such as super-typhoon and seismic events, to ensure structural safety. As such, nonlinear analysis method, which include geometric (second-order) and material (inelastic) nonlinear effects, is crucial and has been extensively studied over the past 65 years (Driscoll 1965; Porter and Powell 1971; King et al. 1992; Ziemian et al. 1992; Chen and Chan 1995; Liew et al. 2000; Thai and Kim 2011; Liu et al. 2014b). The research presented herein mostly adopts the concentrated plasticity (plastic hinge) analysis method for inelastic simulation, aiming for practical application via efficient computational procedures. The modified tangent modulus (MTM) approach, proposed by Ziemian and McGuire (2002), is an implementation of plastic hinge analysis methods that have been used widely for nearly two decades, thereby establishing its robustness and effectiveness. This method has been used in designing systems of steel members with symmetric section shapes.

In concentrated plasticity analysis method, a yield surface, describing the full yield capacity of a section resisting axial force and major-axis bending and/or minor-axis bending, is required. For steel sections with symmetric shapes, a governing equation proposed by McGuire et al. (2000) is commonly used (Figure 2.3) but has long been recognized as unsuitable for nonsymmetric sections (Figure 2.4). This research proposed a rigorous cross-section analysis method to generate the yield surfaces of the nonsymmetric sections, the detailed derivation of which is given in Chapter 6.

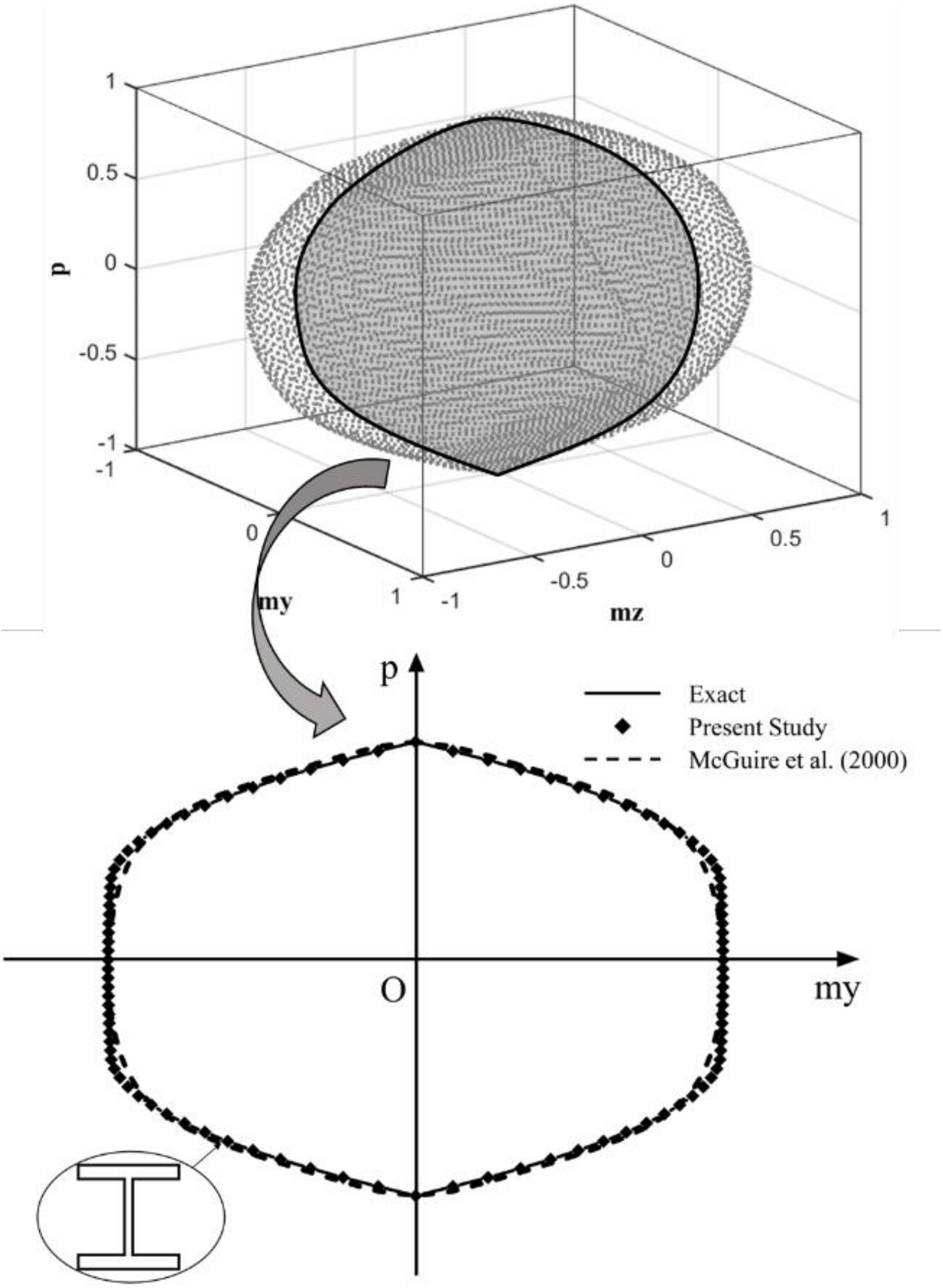

Figure 2.3 The yield surface of a symmetric section (Chen et al. 2021)

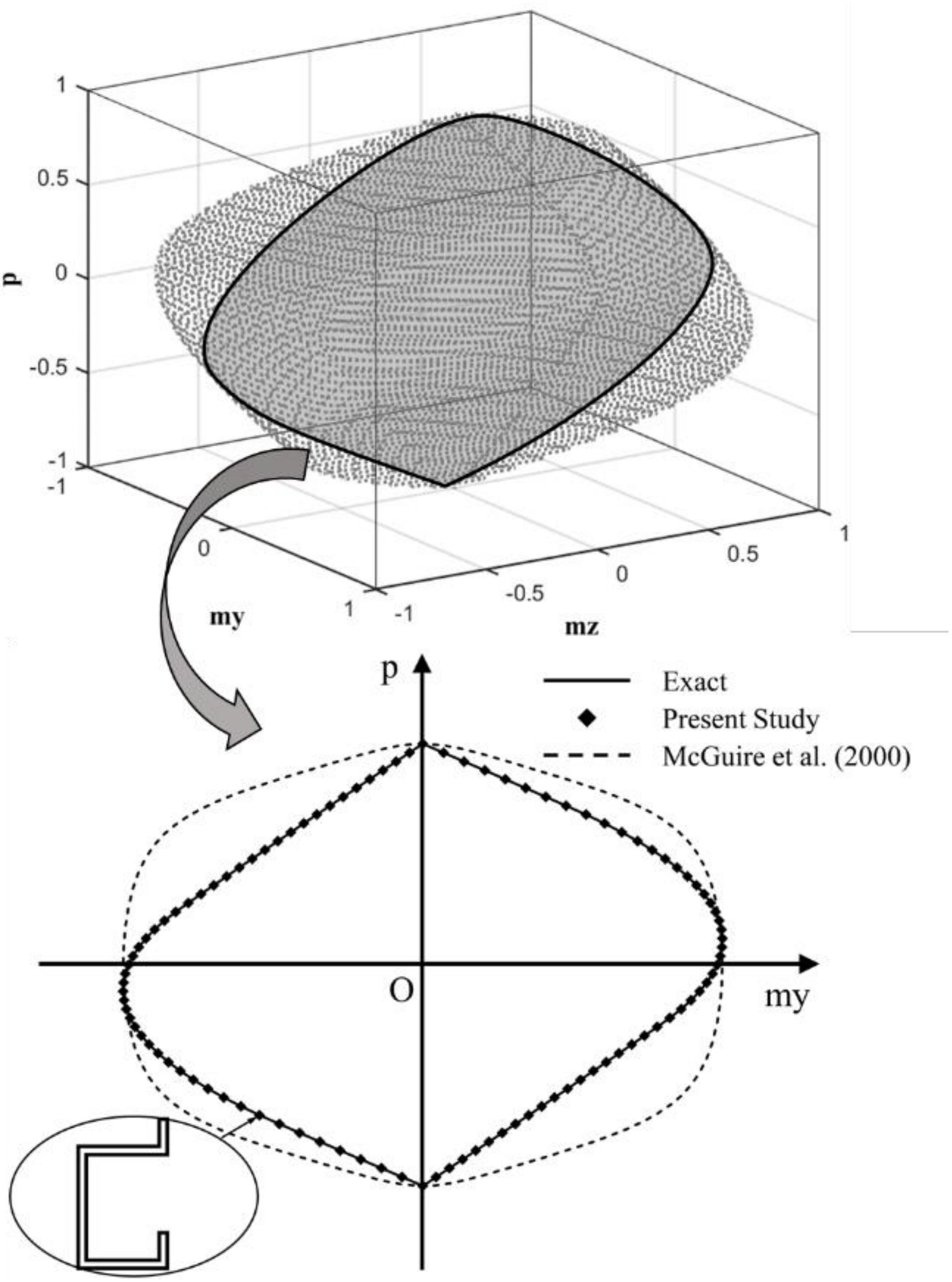

Figure 2.4 The yield surface of a nonsymmetric section (Chen et al. 2021)

2.3.5 Nonsymmetric members under fire

Steel structures are sensitive to fires and elevated temperatures because the thermal effects will rapidly deteriorate the strength and stiffness of steel material (Wang and Moore 1995; C. K. and Chan 2004; Wang et al. 2013). Fire safety engineering is required to examine the behaviors of steel members under fire conditions. The related design approaches can be categorized into two types, such as the prescriptive (De et al. 2014; Qureshi et al. 2020) and the performance-based approaches (Liew et al. 2002; Parkinson et al. 2009; Dwaikat and Kodur 2011), where the former is an element-based approach using experimental results from standard fire tests. At the same time, the latter is a system-based approach that relies on sophisticated analysis of checking global and local stabilities of structures. Adopting the performance-based design method is attractive because it could reduce or eliminate the usage of expensive fire-resistant coating materials. However, the practicability of this design method relies on the robustness of the analysis method, which should be able to predict the nonlinear behaviors of steel structures at elevated temperatures and under fire conditions.

The members with nonsymmetric cross-sections are susceptible to lateral-torsional or flexural-torsional buckling due to the offset between the shear center and the centroid in the cross-section (Liu, Gao, and Ziemian 2019a; Chen et al. 2021). Regarding fire conditions, the steel members may exhibit a temperature gradient. Under this circumstance, the twisting may be induced if its cross-section is nonsymmetric (see Figure 2.5), which may lead to lateral-torsional buckling. The buckling behaviors of these steel members are usually complex, making their buckling design difficult, especially at elevated temperatures.

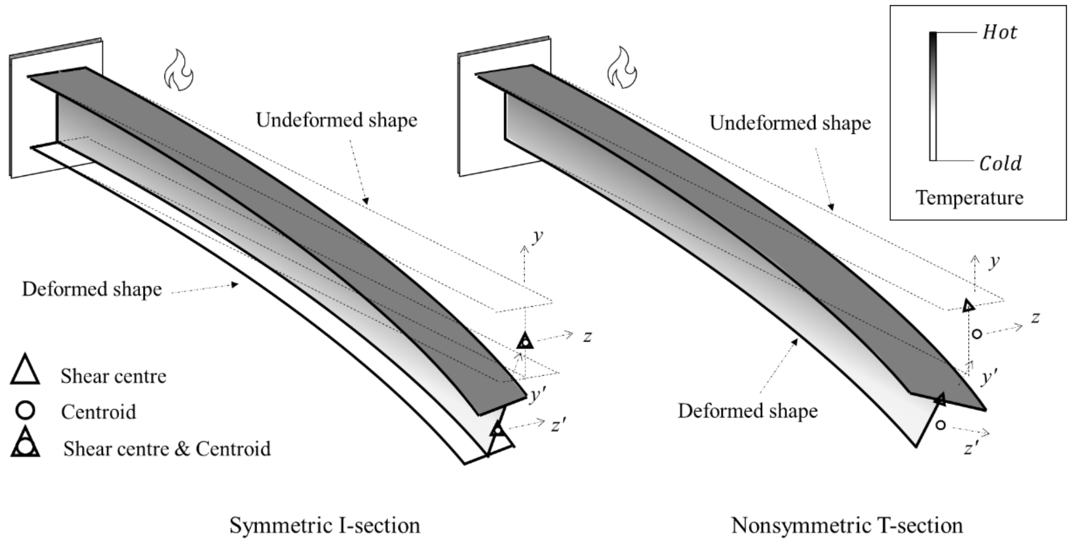

Figure 2.5 Schematic behaviors of cantilever beams in fire

To investigate the structural behaviors of the steel member with nonsymmetric cross-sections in fire, several experimental investigations and numerical simulations using Finite Elements (FE) were conducted. For example, Wang and his colleagues (2002; 2003; 2003a; 2003b) studied the structural behaviors of cold-formed thin-walled steel channels under non-uniform temperatures, where more than 50 short channel columns were tested and studied to develop the design methods. Kim et al. (2015) investigated the buckling behavior of cold-formed steel channel-section beams at elevated temperatures using a two-dimensional FE heat transfer analysis and found that the buckling modes of the beam with temperature variation in its section are quite different from that of the beam with a uniform temperature in its section. Recently, Laím *et al.* (2013; 2014; 2015; 2016) conducted experiments and numerical analysis of cold-formed steel members in the fire, where the beams with lipped C, compound C, Sigma, and compound Sigma sections were studied and noticed that the lateral-torsional buckling is the primary failure mode. These investigations provided some basic understanding of the buckling behaviors of steel members with nonsymmetric sections at elevated temperatures. However, they are too complicated and time-consuming to conduct physical tests and numerical FE simulations. A more convenient analysis method, namely the Line Fine-Element method, is preferred and suitable for extensive studies and practical designs.

Several line elements have been proposed in the literature for the nonlinear analysis of steel members at elevated temperatures. For example, Li and Jiang (Li and Jiang 1999) derived a line element considering the temperature variation across the cross-section. Iu and Chan (2005) developed a beam-column element formulation to simulate the large deflection and inelastic behavior of steel members in fire. Huang and Tan (2007) proposed an element formulation with the warping degree of freedom (DOF) to study the responses of a steel frame at elevated temperatures. However, these element formulations are mostly proposed for the conventional steel members with symmetric sections, which are inapplicable for the use of nonsymmetric sections.

CHAPTER 3.

CROSS-SECTION ANALYSIS METHODS

3.1 Introduction

This chapter introduces the cross-section analysis methods for nonsymmetric sections, where a Coordinate Method (CM) is introduced for the thin-walled sections and a 2D Finite Element (FE) method is given for the thick-walled sections. Five additional section properties for the nonsymmetric sections, including the coordinates of the shear center (z_s and y_s) and the Wagner coefficients (β_y, β_z and β_ω), and the shear coefficients of nonsymmetric thick-walled sections can be generated accordingly.

3.2 Coordinate Method (CM) for Thin-walled Sections

In a conventional beam-column element that includes warping, there are five cross-section properties that are required for a three-dimensional analysis, including the cross-sectional area A, second moments of area I_y and I_z about the y- and z- axes, torsional constant J, and warping constant I_ω. For most common sections, these properties can be easily calculated using closed-form equations that are readily available. To consider the effects of non-symmetric sections, five additional section properties are needed, including the coordinates of the shear center (z_s and y_s) and the Wagner coefficients (β_y, β_z and β_ω) (Chen and Atsuta 2007). For thin-walled sections of relatively simple shapes, such as mono-symmetric-I, T-, and L-shapes, the mathematical expressions of the Wagner coefficients can be generated (Ziemian 2010), but such expressions are complicated and perhaps difficult to use in routine practice.

For the more complex shapes, the use of Wagner coefficients is often avoided due to the complexity of calculating their values, which could thereby result in significant errors when computing structural behavior. To resolve such difficulties, a generalized computational approach for providing these properties for arbitrary thin-walled sections was developed.

3.2.1 Section modelling

An open-section can be modelled via a series of points and segments as indicated in Figure 3.1, which will be classified as either Chain-Type or Tree-Type. Each segment is a line element constructed by two points with the plate thickness *t*. A global coordinate system, namely the Z-O-Y axis, is initially established for describing the positions of points; and a local axis with the origin as the centroid (i.e., z-o-y axis) is determined for computing the related section parameters. The coordinates of the centroid of the section can then be computed by,

$$Z_o = \frac{\sum_{i=1}^{n_S} L_i t_i (Z_{Li} + Z_{Ri})/2}{A} \tag{3.1}$$

$$Y_o = \frac{\sum_{i=1}^{n_S} L_i t_i (Y_{Li} + Y_{Ri})/2}{A} \tag{3.2}$$

where n_S is the total number of segments; the subscripts $_L$ and $_R$ denote the start and end points of the i^{th} segment, respectively; L_i is the length of the i^{th} segment; and A is the total cross-section area, which is given by,

$$A = \sum_{i=1}^{n_S} L_i t_i \tag{3.3}$$

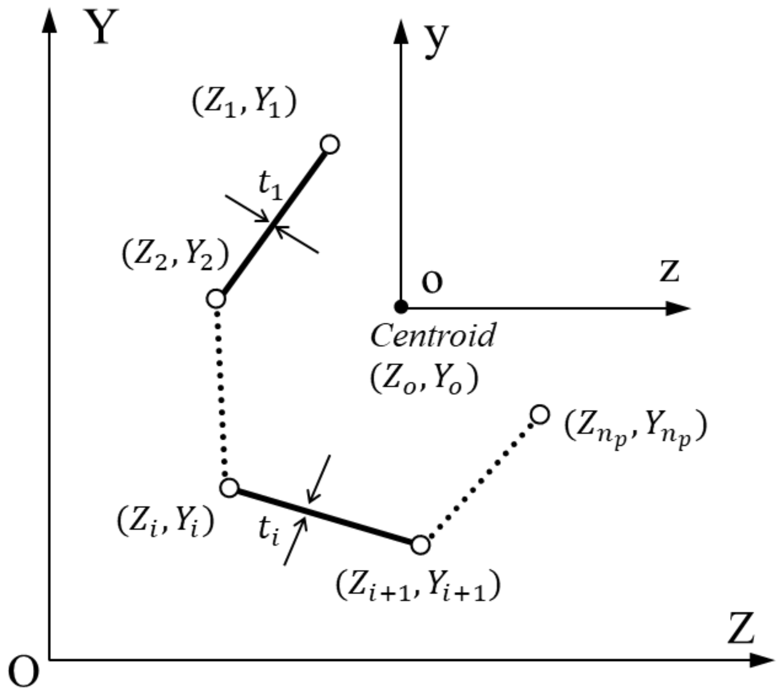

(a) Chain-Type

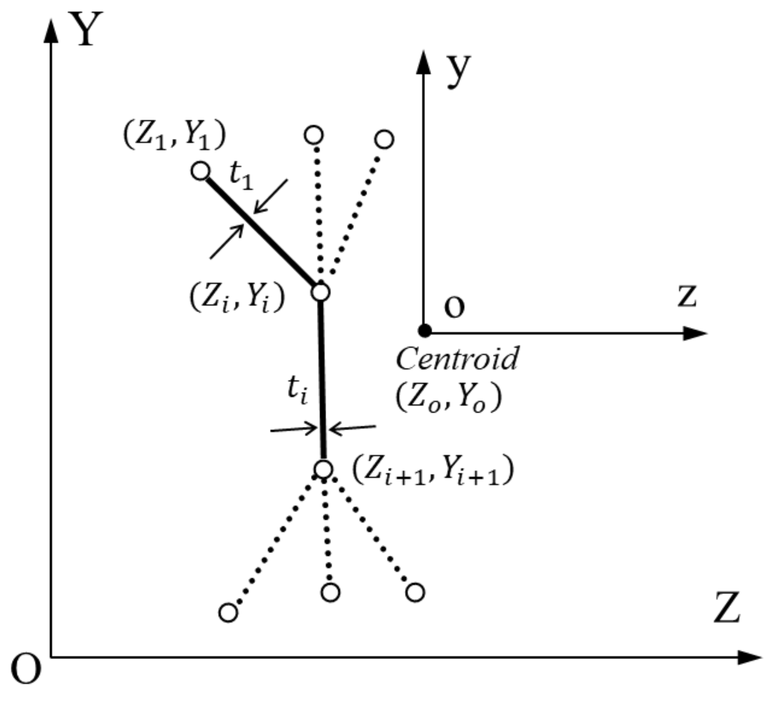

(b) Tree-Type

Figure 3.1 Modeling an open section via points and segments

The coordinates (z_i, y_i,) of the i^{th} point in the z-o-y axis are given by,

$$z_i = Z_i - Z_o \tag{3.4}$$

$$y_i = Y_i - Y_o \tag{3.5}$$

3.2.2 Warping ordinate

The warping ordinate ω_{oi} and ω_{si} of the i^{th} point can be calculated by referring to the centroid and the shear center, respectively, and are thereby given as,

$$\omega_{oi} = \omega_{oj} + \left[y_j(z_i - z_j) - z_j(y_i - y_j)\right] \tag{3.6}$$

$$\omega_{si} = \omega_{sj} + \left[(z_s - z_j)(y_i - y_j) - (y_s - y_j)(z_i - z_j)\right] \tag{3.7}$$

where the subscript j represents the previous point in the Chain-Type section and also represents the upper level point in a Tree-Type section; and z_s and y_s are the coordinates of the shear center and can be calculated by,

$$y_s = \left(I_z I_{\omega z} - I_{yz} I_{\omega y}\right) / \left(I_y I_z - {I_{yz}}^2\right) \tag{3.8}$$

$$z_s = \left(I_y I_{\omega y} - I_{yz} I_{\omega z}\right) / \left(I_y I_z - {I_{yz}}^2\right) \tag{3.9}$$

where,

$$I_z = \int_A y^2 dA = \sum_{i=1}^{n_S} \left(\frac{y_{Li} + y_{Ri}}{2}\right)^2 A_i + \frac{1}{12}(y_{Li} - y_{Ri})^2 A_i \tag{3.10}$$

$$I_y = \int_A z^2 dA = \sum_{i=1}^{n_S} \left(\frac{z_{Li} + z_{Ri}}{2}\right)^2 A_i + \frac{1}{12}(z_{Li} - z_{Ri})^2 A_i \tag{3.11}$$

$$I_{yz} = \int_A yz dA = \sum_{i=1}^{n_S} \left(\frac{z_{Li} + z_{Ri}}{2}\right)\left(\frac{y_{Li} + y_{Ri}}{2}\right) A_i$$

$$+ \sum_{i=1}^{n_S} \left(\frac{z_{Li} + z_{Ri}}{2}\right)\left(\frac{y_{Li} + y_{Ri}}{2}\right) A_i \tag{3.12}$$

$$I_{\omega z} = \int_A z\omega_o dA = \sum_{i=1}^{n_S} \frac{A_i}{6}\left[\omega_{oLi}(2z_{Li} + z_{Ri}) + \omega_{oRi}(z_{Li} + 2z_{Ri})\right] \tag{3.13}$$

$$I_{\omega y} = \int_A y\omega_o dA = \sum_{i=1}^{n_S} \frac{A_i}{6}\left[\omega_{oLi}(2y_{Li} + y_{Ri}) + \omega_{oRi}(y_{Li} + 2y_{Ri})\right] \tag{3.14}$$

in which ω_o is the warping ordinate that is illustrated in Figure 3.2; and y, z are point coordinates with reference to the centroid.

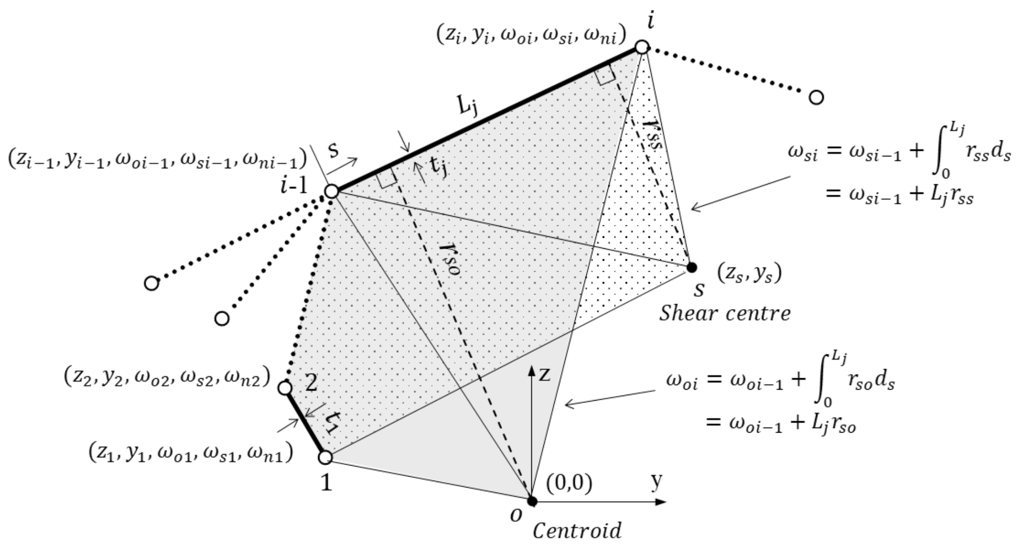

Figure 3.2 The coordinates and the warping ordinate at a point

The normalized warping ordinate ω_n is determined as following,

$$\omega_n = \frac{1}{A}\int \omega_s dA - \omega_s = \frac{1}{2A}\sum_{i=1}^{n_S}(\omega_{Lsi} + \omega_{Rsi})\,A_i - \omega_s \tag{3.15}$$

With these equations, the coordinate and the warping ordinate of an arbitrary point on the cross section are obtained (as illustrated in Figure 3.2) and will now be used for calculating the Wagner coefficients.

3.2.3 Wagner coefficients

With the availability of the coordinates and warping ordinate for the segment end points, the three Wagner coefficients can be calculated from the following equations.

$$\beta_y = \frac{1}{I_y}\int_A (z^3 + zy^2)dA - 2z_s$$

$$= \frac{1}{12I_y}\sum_{i=1}^{n_S} A_i[2y_{Li}y_{Ri}(z_{Li} + z_{Ri}) + {y_{Li}}^2(3z_{Li} + z_{Ri})] \tag{3.16}$$

$$+\frac{1}{12I_y}\sum_{i=1}^{n_S} A_i[{y_{Ri}}^2(z_{Li} + 3z_{Ri}) + 3(z_{Li} + z_{Ri})({z_{Li}}^2 + {z_{Ri}}^2)] - 2z_s$$

$$\beta_z = \frac{1}{I_z}\int_A (y^3 + yz^2)dA - 2y_s$$

$$= \frac{1}{12I_z}\sum_{i=1}^{n_S} A_i[2z_{Li}z_{Ri}(y_{Li} + y_{Ri}) + {z_{Li}}^2(3y_{Li} + y_{Ri})] \tag{3.17}$$

$$\frac{1}{12I_z}\sum_{i=1}^{n_S} A_i[{z_{Ri}}^2(y_{Li} + 3y_{Ri}) + 3(y_{Li} + y_{Ri})({y_{Li}}^2 + {y_{Ri}}^2)] - 2y_s$$

$$\beta_\omega = \frac{1}{I_\omega}\int_A \omega_n(y^2+z^2)dA$$

$$= \frac{1}{12I_\omega}\sum_{i=1}^{n_S} A_i[\omega_{Li}(3{y_{Li}}^2+2y_{Li}y_{Ri}+{y_{Ri}}^2+3{z_{Li}}^2+2z_{Li}z_{Ri}+{z_{Ri}}^2)] \quad (3.18)$$

$$+\frac{1}{12I_\omega}\sum_{i=1}^{n_S} A_i[\omega_{Ri}({y_{Li}}^2+2y_{Li}y_{Ri}+3{y_{Ri}}^2+{z_{Li}}^2+2z_{Li}z_{Ri}+3{z_{Ri}}^2)]$$

Finally, the warping constant I_ω can be computed from,

$$I_\omega = \int_A {\omega_n}^2 dA = \sum_{i=1}^{n_S} A_i\left[\omega_{Lni}\omega_{Rni} + \frac{(\omega_{Rni}-\omega_{Lni})^2}{3}\right] \quad (3.19)$$

3.2.4 Verification examples

Knowing that the location of the shear center (y_s and z_s) and the Wagner coefficients (β_y, β_z, and β_ω) are essential for an accurate analysis of a system that contains non-symmetric sections, four such sections are studied, with their dimensions given in Figure 3.4. Given that the mono-symmetric-I section is symmetric about the y-axis (Figure 3.3), the Wagner coefficients β_y and β_ω are zero. The closed-form equation for calculating the Wagner coefficient β_z is derived by Ziemian (2010) and given below.

$$\beta_z = -(\chi_1 - \chi_2 + \chi_3)/I_z - 2y_s \quad (3.20)$$

where,

$$\chi_1 = \frac{{b_{fc}}^3}{12}(d_o')t_{fc} + \frac{{b_{fc}}^3}{24}{t_{fc}}^2 + b_{fc}(d_o')^3 t_{fc} + \frac{3}{2}b_{fc}(d_o')^2{t_{fc}}^2 \quad (3.21)$$

$$+b_{fc}(d_o{}')t_{fc}{}^3+\frac{b_{fc}}{4}t_{fc}{}^4$$

$$\chi_2=\frac{b_{ft}{}^3}{12}d_ot_{ft}+\frac{b_{ft}{}^3}{24}t_{ft}{}^2+b_{ft}t_{ft}d_o{}^3+1.5b_{ft}t_{ft}{}^2d_o{}^2+b_{ft}t_{ft}{}^3d_o$$

(3.22)

$$+\frac{1}{4}b_{ft}t_{ft}{}^4$$

$$\chi_3=\frac{(d_o{}')^4}{4}t_w+\frac{(d_o{}')^2}{24}t_w{}^3-\frac{d_o{}^4}{4}t_w-\frac{d_o{}^2}{24}t_w{}^3 \qquad (3.23)$$

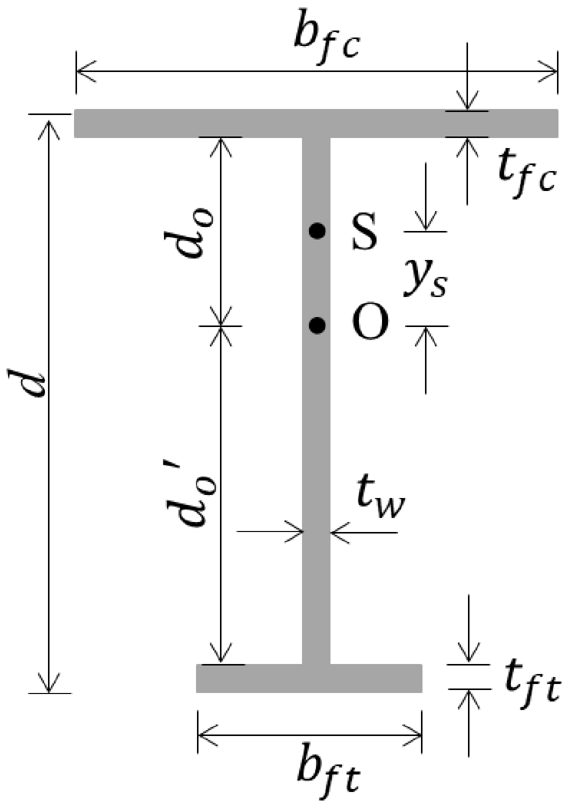

Figure 3.3 Dimensions of the mono-symmetric-I section

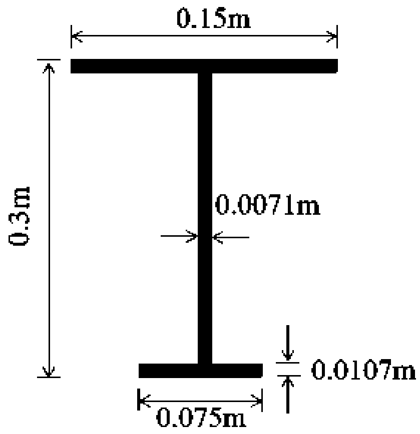

(a) Mono-Symmetric-I

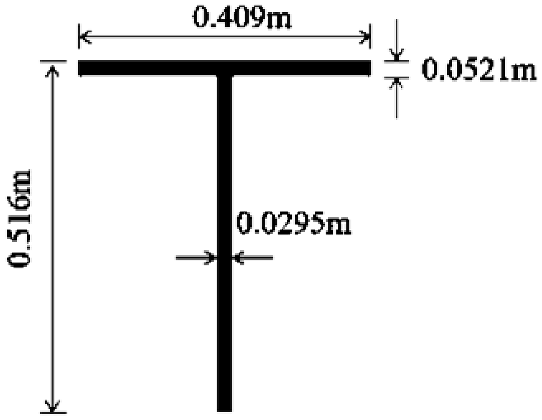

(b) WT500x277

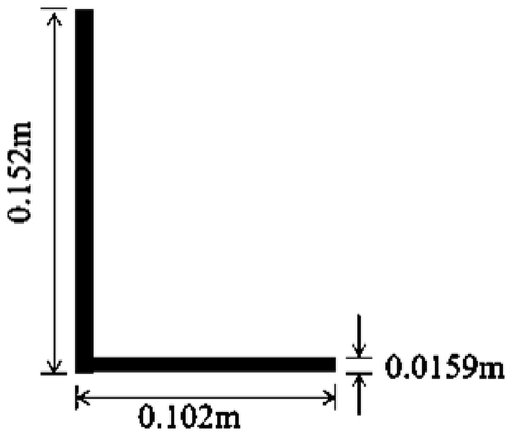

(c) L152x102x15.9

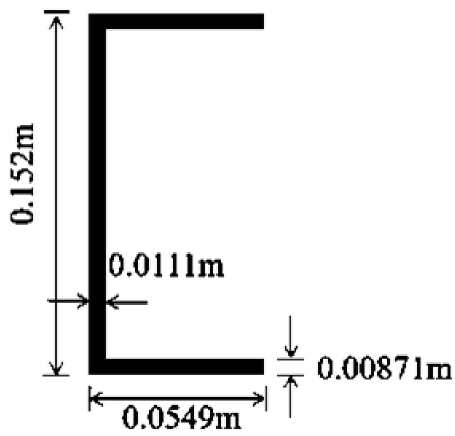

(d) C150x19.3

Figure 3.4 Four sections for the verification of CM method

The properties for the other sections are obtained from version 15.0 of the AISC 2016 database. Using these properties as a basis, the values computed by the section definition module based on the proposed algorithm presented earlier, are then verified. Sections were constructed via a series of points and segments working from the mid-points of the through-thicknesses.

Although limited to one mono-symmetric-I section, the comparison presented in Table 3.1 tends to confirm the accuracy of the proposed computational algorithm in defining properties for an open-section. In practice, the properties of common shapes such as T-, L-, and C-sections are usually obtained from the section tables in design codes, such as AISC (2016), but the Wagner coefficients are often not provided. Herein, three sections selected from the AISC shapes database, including WT500x277, L152x102x15.9, and C150x19.3, are studied, where the common section properties apart from the Wagner coefficients are compared in Table 3.2 with the values calculated by the proposed computational algorithm. Any small differences are assumed to be attributed to the AISC database accounting for fillets and/or rounded edges. Of course, the generalized computational algorithm presented in this chapter can be used for generating the Wagner coefficients for non-symmetric sections, which may be further incorporated into current section tables with codes.

Table 3.1 Section properties of the mono-symmetric-I section

Parameter	***Closed-form Solution***	***Present Study***	***Differences***
$\boldsymbol{A}$	$4.462x10^{-3}\ m^2$	$4.462x10^{-3}\ m^2$	*0*
$\boldsymbol{I_y}$	$3.394x10^{-6}\ m^4$	$3.394x10^{-6}\ m^4$	*0*
$\boldsymbol{I_z}$	$6.171x10^{-5}\ m^4$	$6.170x10^{-5}\ m^4$	*0*
$\boldsymbol{J}$	$1.264x10^{-7}\ m^4$	$1.264x10^{-7}\ m^4$	*0*
$\boldsymbol{I_w}$	$2.799x10^{-8}\ m^6$	$2.799x10^{-8}\ m^6$	*0*
$\boldsymbol{y_c}$	$8.745x10^{-2}\ m$	$8.627x10^{-2}\ m$	*-1.3%*
$\boldsymbol{z_c}$	*0*	*0*	*0*
$\boldsymbol{\beta_y}$	--	*0*	--
$\boldsymbol{\beta_z}$	$-2.052\ x10^{-1}\ m$	$-2.077\ x10^{-1}\ m$	*1.2%*
$\boldsymbol{\beta_w}$	--	*0*	--

Table 3.2 Section properties of the WT, L, and C sections

Section B - WT500x277			
Parameter	**Section Table**	**Present Study**	**Differences**
A	$3.53 \times 10^{-2}\ m^2$	$3.57 \times 10^{-2}\ m^2$	*1.0%*
I_y	$8.03 \times 10^{-4}\ m^4$	$8.11 \times 10^{-4}\ m^4$	*1.0%*
I_z	$2.95 \times 10^{-4}\ m^4$	$2.98 \times 10^{-4}\ m^4$	*1.1%*
J	$2.40 \times 10^{-5}\ m^4$	$2.35 \times 10^{-5}\ m^4$	*-2.2%*
I_w	$1.50 \times 10^{-7}\ m^6$	$1.51 \times 10^{-7}\ m^6$	*0.7%*
y_c	$9.99 \times 10^{-2}\ m$	$9.87 \times 10^{-2}\ m$	*-1.3%*
z_c	*0*	*0*	*0*
β_y	--	*0*	--
β_z	--	$-3.47 \times 10^{-1} m$	--
β_w	--	*0*	--
Section C - L152x102x15.9			
Parameter	**Section Table**	**Present Study**	**Differences**
A	$3.780 \times 10^{-3}\ m^2$	$3.786 \times 10^{-3}\ m^2$	*0.2%*
I_y	$3.11 \times 10^{-6}\ m^4$	$3.15 \times 10^{-6}\ m^4$	*1.3%*
I_z	$8.74 \times 10^{-6}\ m^4$	$8.69 \times 10^{-6}\ m^4$	*-0.6%*
J	$3.23 \times 10^{-7}\ m^4$	$3.19 \times 10^{-7}\ m^4$	*-1.2%*
I_w	$4.27 \times 10^{-10}\ m^6$	$4.27 \times 10^{-10}\ m^6$	*-0.1%*
y_c	$1.825 \times 10^{-2}\ m$	$1.883 \times 10^{-2}\ m$	*3.2%*
z_c	$4.365 \times 10^{-2}\ m$	$4.266 \times 10^{-2}\ m$	*-2.3%*
β_y	--	$1.071 \times 10^{-1}\ m$	--
β_z	--	$6.515 \times 10^{-2}\ m$	--
β_w	--	*0*	--
Section D - C150x19.3			
Parameter	**Section Table**	**Present Study**	**Differences**
A	$2.46 \times 10^{-3}\ \mathrm{m}^2$	$2.45 \times 10^{-3}\ \mathrm{m}^2$	-0.4%
I_y	$7.20 \times 10^{-6}\ \mathrm{m}^4$	$7.14 \times 10^{-6}\ \mathrm{m}^4$	-0.8%

$\boldsymbol{I_z}$	4.37x10^{-7} m^4	4.39x10^{-7} m^4	0.5%
$\boldsymbol{J}$	9.86x10^{-8} m^4	9.75x10^{-8} m^4	-1.1%
$\boldsymbol{I_w}$	1.93x10^{-9} m^6	1.92x10^{-9} m^6	-0.5%
$\boldsymbol{y_c}$	0	0	
$\boldsymbol{z_c}$	-2.275x10^{-2} m	-2.284x10^{-2} m	0.4%
$\boldsymbol{\beta_y}$	--	-1.799x10^{-1} m	--
$\boldsymbol{\beta_z}$	--	0	--
$\boldsymbol{\beta_w}$	--	0	--

3.3 2D FE Method for Thick-walled Sections

3.3.1 Section modelling

An 2D FE-based cross-section analysis algorithm is employed to calculate section properties for nonsymmetric thick-walled sections. Instead of modelling the cross-section with the centerline as in the CM method, this research adopted a new cross-section modelling method using the outline. This method not only is applicable to arbitrary sections but also can take the wall thickness into considerations. A modelling example of a complex section is provided in Figure 3.5 (a), where the vertices of the cross-section P_i are firstly described with coordinates and then connected by outlines L_i.

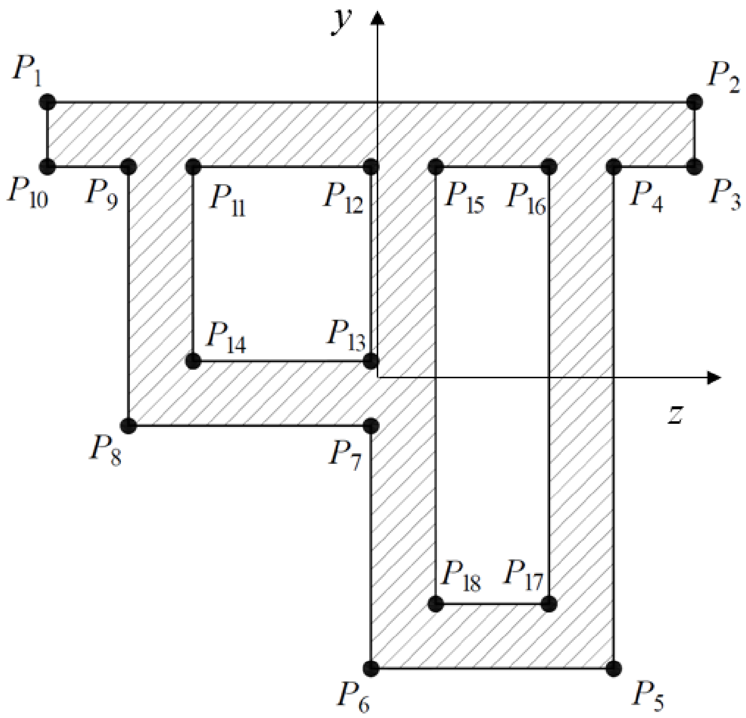

(a) Section modelling

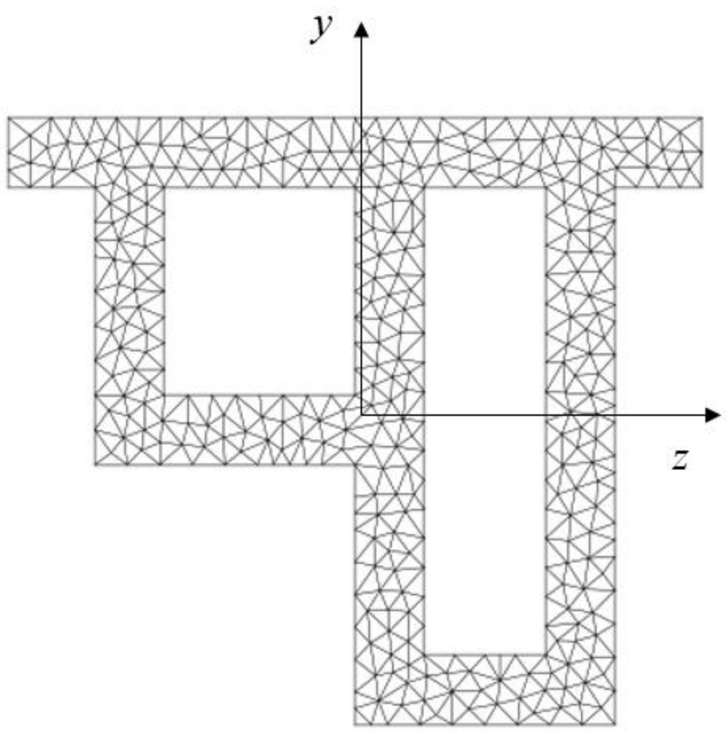

(b) Generated FE mesh

Figure 3.5 Example of section modeling

As shown in Figure 3.5 (a), the outlines are defined as:

$$L_1 = P_1 \to P_2 \to P_3 \to P_4 \dots P_8 \to P_9 \to P_{10} \to P_1$$

$$L_2 = P_{11} \to P_{12} \to P_{13} \to P_{14} \to P_{11}$$

$$L_3 = P_{15} \to P_{16} \to P_{17} \to P_{18} \to P_{15}$$

Note that the outlines can be classified as the ones for solids and holes. In this example, L_1 describes a continuous solid outline where FE mesh will be generated within the enclosed region; L_2 and L_3 describe continuous hole outlines where FE mesh will be deleted within the enclosed region, as shown in Figure 3.5 (b).

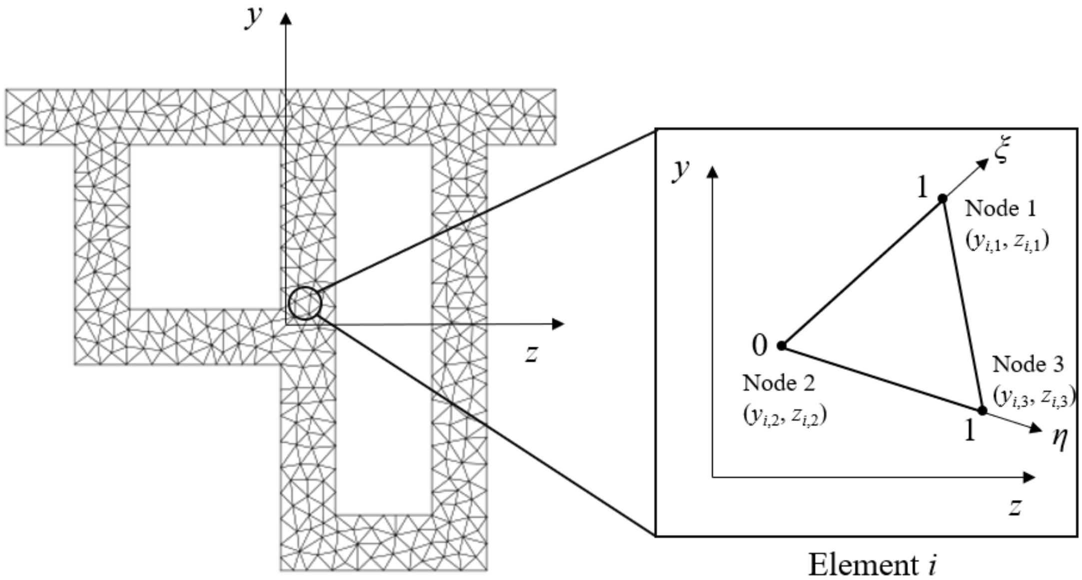

Figure 3.6 Constant strain triangle (CST) element

An iso-parametric constant strain triangle (CST) element is employed to generate 2D-meshes of cross-sections. The CST element is a simple and efficient triangular finite element for the cross-section analysis. Besides, the element has a high adaptability to mesh sections with arbitrary shapes. As shown in Figure 3.6, besides the global coordinate system y-o-z, a local coordinate system η-o-ξ will established to derive the element formulations. Note that the nodes for each element will be listed following anticlockwise sequences.

3.3.2 Shape functions and Jacobian matrix of the CST element

The CST element is a simple first-order element. The shape function $\boldsymbol{N}$ and Jacobian matrix $\boldsymbol{J}$ of this element are defined as:

$$\boldsymbol{N}(\eta,\xi) = [\eta \quad \xi \quad 1-\eta-\xi] \tag{3.24}$$

$$\boldsymbol{J} = \begin{bmatrix} \dfrac{\partial z}{\partial \eta} & \dfrac{\partial y}{\partial \eta} \\ \dfrac{\partial z}{\partial \xi} & \dfrac{\partial y}{\partial \xi} \end{bmatrix} = \begin{bmatrix} \dfrac{\partial \boldsymbol{N}}{\partial \eta} \\ \dfrac{\partial \boldsymbol{N}}{\partial \xi} \end{bmatrix} [\boldsymbol{z}^e \quad \boldsymbol{y}^e] = \begin{bmatrix} z_1 - z_3 & y_1 - y_3 \\ z_2 - z_3 & y_2 - y_3 \end{bmatrix} \tag{3.25}$$

where the superscript e denotes column vectors containing element nodal global coordinates, for example, $\boldsymbol{y}^e = (y_1, y_2, y_3)$.

3.3.3 Basic geometric properties

The calculation of area A, global coordinate of centroid y_c and z_c, and moment of inertia I_y, I_z and I_{yz} in this study is based on geometric approaches. Since the cross-section will be meshed into a series of CST elements, those basic geometric properties can by calculated by,

$$A = \sum A^e = \frac{1}{2}\sum_{i=1}^{NE}\sum_{j=1}^{n}\left(y_{i,j+1}z_{i,j} - y_{i,j}z_{i,j+1}\right) \tag{3.26}$$

$$y_c = \frac{\sum A^e y_c^e}{A} = \frac{1}{6A}\sum_{i=1}^{NE}\sum_{j=1}^{n}\left(y_{i,j} + y_{i,j+1}\right)\left(y_{i,j+1}z_{i,j} - y_{i,j}z_{i,j+1}\right) \tag{3.27}$$

$$z_c = \frac{\sum A^e z_c^e}{A} = \frac{1}{6A}\sum_{i=1}^{NE}\sum_{j=1}^{n}\left(z_{i,j} + z_{i,j+1}\right)\left(y_{i,j+1}z_{i,j} - y_{i,j}z_{i,j+1}\right) \tag{3.28}$$

$$I_y = \sum I_y^e = \frac{1}{12}\sum_{i=1}^{NE}\sum_{j=1}^{n}\left(y_{i,j+1}z_{i,j} - y_{i,j}z_{i,j+1}\right)\left(z_{i,j}^2 + z_{i,j}z_{i,j+1} + z_{i,j+1}^2\right) \tag{3.29}$$

$$I_z = \sum I_z^e = \frac{1}{12}\sum_{i=1}^{NE}\sum_{j=1}^{n}\left(y_{i,j+1}z_{i,j} - y_{i,j}z_{i,j+1}\right)\left(y_{i,j}^2 + y_{i,j}y_{i,j+1} + y_{i,j+1}^2\right) \tag{3.30}$$

$$\begin{aligned} I_{yz} = \sum I_{yz}^e = \frac{1}{24}\sum_{i=1}^{NE}\sum_{j=1}^{n}&\left(y_{i,j+1}z_{i,j} - y_{i,j}z_{i,j+1}\right) \\ &\times\left[y_{i,j+1}z_{i,j} + y_{i,j}z_{i,j+1} + 2\left(y_{i,j}z_{i,j} + y_{i,j+1}z_{i,j+1}\right)\right] \end{aligned} \tag{3.31}$$

where $n = 3$ is the number of nodes in each element. Note that in the triangular element, $y_{n+1} = y_1$ and $z_{n+1} = z_1$.

3.3.4 Torsion and warping properties

To get the torsion and warping properties of a cross-section, a classic Saint-Venant torsion problem should be considered, in which the principle of virtual work gives:

$$\delta W = \delta W_{int} - \delta W_{ext} = \int_V \boldsymbol{\sigma}\delta\boldsymbol{\varepsilon}dV - \int_L m_x\delta\theta dx = 0 \tag{3.32}$$

where m_x is the torque per length uniformly distributed along the entire member length L, θ is the twist angle of the member. This can be expressed in a strain from as:

$$\int_V G\left[\left[\left(\frac{\partial\boldsymbol{\omega}}{\partial z}-y\right)\frac{\partial}{\partial x}\delta\theta+\frac{\partial\theta}{\partial x}\frac{\partial}{\partial z}\delta\boldsymbol{\omega}\right]\frac{\partial\theta}{\partial x}\left(\frac{\partial\boldsymbol{\omega}}{\partial z}-y\right)\right]$$

$$+\left[\left(\frac{\partial\boldsymbol{\omega}}{\partial y}-z\right)\frac{\partial}{\partial x}\delta\theta+\frac{\partial\theta}{\partial x}\frac{\partial}{\partial y}\delta\boldsymbol{\omega}\right]\frac{\partial\theta}{\partial x}\left(\frac{\partial\boldsymbol{\omega}}{\partial y}+z\right)\Big]\,dV-\int_L m_x\delta\theta dx=0 \tag{3.33}$$

where $\boldsymbol{\omega}$ is the warping ordinate function and the $\delta\theta$ term can be separated as:

$$\int_L G\frac{\partial}{\partial x}\delta\theta\frac{\partial\theta}{\partial x}dx\int_A\left[\left[\left(\frac{\partial\boldsymbol{\omega}}{\partial y}\right)^2+\left(\frac{\partial\boldsymbol{\omega}}{\partial z}\right)^2+z\frac{\partial\boldsymbol{\omega}}{\partial y}-y\frac{\partial\boldsymbol{\omega}}{\partial z}\right]\right.$$

$$\left.+\left(z\frac{\partial\boldsymbol{\omega}}{\partial y}-y\frac{\partial\boldsymbol{\omega}}{\partial z}+y^2+z^2\right)\right]dA-\int_L m_x\delta\theta dx \tag{3.34}$$

in which, the first part of the $\delta\theta$ term can be simplified with the Green's theorem and harmonic function:

$$\int_A\left[\left(\frac{\partial\boldsymbol{\omega}}{\partial y}\right)^2+\left(\frac{\partial\boldsymbol{\omega}}{\partial z}\right)^2+z\frac{\partial\boldsymbol{\omega}}{\partial y}-y\frac{\partial\boldsymbol{\omega}}{\partial z}\right]dA$$

$$=\oint\boldsymbol{\omega}\left[\left(\frac{\partial\boldsymbol{\omega}}{\partial y}+z\right)n_y+\left(\frac{\partial\boldsymbol{\omega}}{\partial z}-y\right)n_z\right]ds \tag{35}$$

Where n_y an n_z are the module of vector components along y and z-axis. The vector is outward normal to the outline s of the cross section. Based on the surface condition, this part equals to zero. The following part of $\delta\theta$ term can be simplified to J, it leads to:

$$\int_L G\frac{\partial}{\partial x}\delta\theta\frac{\partial\theta}{\partial x}dx\int_A\left[\left(z\frac{\partial\boldsymbol{\omega}}{\partial y}-y\frac{\partial\boldsymbol{\omega}}{\partial z}+y^2+z^2\right)\right]dA-\int_L m_x\delta\theta dx \tag{3.36}$$

$$= \int_L \frac{d}{dx}\delta\theta GJ\frac{d\theta}{dx}dx - \int_L m_x \delta\theta dx = \int_L \delta\theta\left(\frac{d}{dx}GJ\frac{d\theta}{dx} - m_x\right)dx$$

This part also equals to zero based on the governing equation for torsional motion along the longitudinal *x*-axis. Hence the rest $\delta\boldsymbol{\omega}$ term would be:

$$\int_V G\left(\frac{\partial\theta}{\partial x}\right)^2\left(\frac{\partial}{\partial y}\delta\boldsymbol{\omega}\frac{\partial\boldsymbol{\omega}}{\partial y} + \frac{\partial}{\partial z}\delta\boldsymbol{\omega}\frac{\partial\boldsymbol{\omega}}{\partial z} + \frac{\partial}{\partial y}\delta\boldsymbol{\omega}z - \frac{\partial}{\partial z}\delta\boldsymbol{\omega}y\right)dV$$

$$= G\int_L \left(\frac{\partial\theta}{\partial x}\right)^2 dx \int_A \left[\left(\frac{\partial}{\partial y}\delta\boldsymbol{\omega}\frac{\partial\boldsymbol{\omega}}{\partial y} + \frac{\partial}{\partial z}\delta\boldsymbol{\omega}\frac{\partial\boldsymbol{\omega}}{\partial z}\right) - \left(\frac{\partial}{\partial z}\delta\boldsymbol{\omega}y - \frac{\partial}{\partial y}\delta\boldsymbol{\omega}z\right)\right]dA = 0$$

(3.37)

This gives that:

$$\int_A \left[\left(\frac{\partial}{\partial y}\delta\boldsymbol{\omega}\frac{\partial\boldsymbol{\omega}}{\partial y} + \frac{\partial}{\partial z}\delta\boldsymbol{\omega}\frac{\partial\boldsymbol{\omega}}{\partial z}\right) - \left(\frac{\partial}{\partial z}\delta\boldsymbol{\omega}y - \frac{\partial}{\partial y}\delta\boldsymbol{\omega}z\right)\right]dA = 0 \quad (3.38)$$

By solving this equation, the warping ordinate function $\boldsymbol{\omega}$ (*y*, *z*) can be solved. The above equation can be written in the FE formulation. For each CST element it can be approximated written as:

$$\int_0^1\int_0^{1-\xi} \delta\boldsymbol{\omega}^{eT}\left[\left(\frac{\partial\boldsymbol{N}^T}{\partial y}\frac{\partial\boldsymbol{N}}{\partial y} + \frac{\partial\boldsymbol{N}^T}{\partial z}\frac{\partial\boldsymbol{N}}{\partial z}\right)\boldsymbol{\omega}^e - \left(\boldsymbol{N}\boldsymbol{y}^e\frac{\partial\boldsymbol{N}^T}{\partial z} - \boldsymbol{N}\boldsymbol{z}^e\frac{\partial\boldsymbol{N}^T}{\partial y}\right)\right]\frac{1}{2}\det|\boldsymbol{J}|d\eta\, d\xi = 0 \quad (3.39)$$

It gives that:

$$\int_0^1\int_0^{1-\xi} \left[\left(\frac{\partial\boldsymbol{N}^T}{\partial y}\frac{\partial\boldsymbol{N}}{\partial y} + \frac{\partial\boldsymbol{N}^T}{\partial z}\frac{\partial\boldsymbol{N}}{\partial z}\right)\boldsymbol{\omega}^e - \left(\boldsymbol{N}\boldsymbol{y}^e\frac{\partial\boldsymbol{N}^T}{\partial z} - \boldsymbol{N}\boldsymbol{z}^e\frac{\partial\boldsymbol{N}^T}{\partial y}\right)\right]\frac{1}{2}\det|\boldsymbol{J}|d\eta\, d\xi = 0 \quad (3.40)$$

The element stiffness matrix $\boldsymbol{K}^e$ and load vector $\boldsymbol{P}_w^e$ are formulated as:

$$\boldsymbol{K}^e = \int_0^1 \int_0^{1-\xi} \left(\frac{\partial \boldsymbol{N}^T}{\partial y} \frac{\partial \boldsymbol{N}}{\partial y} + \frac{\partial \boldsymbol{N}^T}{\partial z} \frac{\partial \boldsymbol{N}}{\partial z} \right) \frac{1}{2} \det|\boldsymbol{J}| d\eta \, d\xi \tag{3.41}$$

$$\boldsymbol{P}_w^e = \int_0^1 \int_0^{1-\xi} \left(\boldsymbol{N} \boldsymbol{y}^e \frac{\partial \boldsymbol{N}^T}{\partial z} - \boldsymbol{N} \boldsymbol{z}^e \frac{\partial \boldsymbol{N}^T}{\partial y} \right) \frac{1}{2} \det|\boldsymbol{J}| d\eta \, d\xi \tag{3.42}$$

The Gaussian quadrature method is adopted to solve the numerical integrations above and improve computational efficiency. Seven Gauss points are introduced on the CST element as per introduced by Bathe (Bathe 2006), and the above equations can be written as:

$$\boldsymbol{K}^e = \frac{1}{2} \sum_{i=1}^{n} \left[\frac{\partial \boldsymbol{N}(\eta_i, \xi_i)^T}{\partial y} \frac{\partial \boldsymbol{N}(\eta_i, \xi_i)}{\partial y} + \frac{\partial \boldsymbol{N}(\eta_i, \xi_i)^T}{\partial z} \frac{\partial \boldsymbol{N}(\eta_i, \xi_i)}{\partial z} \right] \det|\boldsymbol{J}| \tag{3.43}$$

$$\boldsymbol{P}_w^e = \frac{1}{2} \sum_{i=1}^{n} \left[\boldsymbol{N}(\eta_i, \xi_i) \boldsymbol{y}^e \frac{\partial \boldsymbol{N}(\eta_i, \xi_i)^T}{\partial z} - \boldsymbol{N}(\eta_i, \xi_i) \boldsymbol{z}^e \frac{\partial \boldsymbol{N}(\eta_i, \xi_i)^T}{\partial y} \right] \det|\boldsymbol{J}| \tag{3.44}$$

Where $n = 7$ is the number of Gauss points and W_i is the weight of each Gauss points.

The total stiffness matrix $\boldsymbol{K}$ and load vector $\boldsymbol{P}_w$ for warping ordinate function can therefore be formed with elemental matrices:

$$\boldsymbol{K} = \sum^{NE} \boldsymbol{K}^e \tag{3.45}$$

$$\boldsymbol{P}_w = \sum^{NE} \boldsymbol{P}_w^e \tag{3.46}$$

$$\boldsymbol{K\omega} = \boldsymbol{P}_w \tag{3.47}$$

where NE is the number of CST elements. Nodal values of warping ordinate function as a column vector can be obtained by solving this equation. Note that a boundary condition shall be applied first by fixing the warping DOF of an arbitrary node. The location of shear center, y_s and z_s, is then calculated:

$$y_s = \frac{1}{I_y}\int_A z\omega dA = \frac{1}{I_y}\sum^{NE}\int_0^1\int_0^{1-\xi} \boldsymbol{N}\boldsymbol{z}^{\boldsymbol{e}}\boldsymbol{N}\boldsymbol{\omega}^e \frac{1}{2}\det|\boldsymbol{J}|d\eta\, d\xi$$
$$= \frac{1}{2I_y}\sum^{NE}\sum_{i=1}^{n} W_i\boldsymbol{N}(\eta_i,\xi_i)\boldsymbol{z}^{\boldsymbol{e}}\boldsymbol{N}(\eta_i,\xi_i)\boldsymbol{\omega}^e\det|\boldsymbol{J}| \tag{3.48}$$

$$z_s = \frac{1}{I_z}\int_A y\omega dA = \frac{1}{I_z}\sum^{NE}\int_0^1\int_0^{1-\xi} \boldsymbol{N}\boldsymbol{y}^{\boldsymbol{e}}\boldsymbol{N}\boldsymbol{\omega}^e \frac{1}{2}\det|\boldsymbol{J}|d\eta\, d\xi$$
$$= \frac{1}{2I_z}\sum^{NE}\sum_{i=1}^{n} W_i\boldsymbol{N}(\eta_i,\xi_i)\boldsymbol{y}^{\boldsymbol{e}}\boldsymbol{N}(\eta_i,\xi_i)\boldsymbol{\omega}^e\det|\boldsymbol{J}| \tag{3.49}$$

where I_y and I_z are moments of inertia. The warping ordinate function $\boldsymbol{\omega}$ can be standardized to $\boldsymbol{\omega}_s$:

$$\boldsymbol{\omega}_s = \boldsymbol{\omega} - \frac{1}{A}\int_A \boldsymbol{\omega} dA + z_s\boldsymbol{y} - y_s\boldsymbol{z}$$
$$= \boldsymbol{\omega} - \frac{1}{A}\sum^{NE}\int_0^1\int_0^{1-\xi} \boldsymbol{N}\boldsymbol{\omega}^e \frac{1}{2}\det|\boldsymbol{J}|d\eta\, d\xi + z_s\boldsymbol{y} - y_s\boldsymbol{z} \tag{3.50}$$
$$= \boldsymbol{\omega} - \frac{1}{2A}\sum^{NE}\sum_{i=1}^{n} W_i\boldsymbol{N}(\eta_i,\xi_i)\boldsymbol{\omega}^e\det|\boldsymbol{J}| + z_s\boldsymbol{y} - y_s\boldsymbol{z}$$

The calculation of torsional constant J, warping constant I_w and Wagner coefficients β_y, β_z, β_ω are given as:

$$J = \int_A \left[\frac{\partial \boldsymbol{\omega}_s}{\partial y}(z - z_s) + (z - z_s)^2\right] - \left[\frac{\partial \boldsymbol{\omega}_s}{\partial z}(y - y_s) - (y - y_s)^2\right] dA$$

$$= \sum^{NE} \int_0^1 \int_0^{1-\xi} \left[\left[\frac{\partial \boldsymbol{N}}{\partial y} \boldsymbol{\omega}_s^e(\boldsymbol{N}\boldsymbol{z}^e - z_s) + (\boldsymbol{N}\boldsymbol{z}^e - z_s)^2\right]\right.$$

$$\left. - \left[\frac{\partial \boldsymbol{N}}{\partial z} \boldsymbol{\omega}_s^e(\boldsymbol{N}\boldsymbol{y}^e - y_s) - (\boldsymbol{N}\boldsymbol{y}^e - y_s)^2\right]\right] \frac{1}{2} \det|\boldsymbol{J}| d\eta d\xi \tag{3.51}$$

$$= \frac{1}{2} \sum^{NE} \sum_{i=1}^{n} W_i \left[\left[\frac{\partial \boldsymbol{N}(\eta_i, \xi_i)}{\partial y} \boldsymbol{\omega}_s^e[\boldsymbol{N}(\eta_i, \xi_i)\boldsymbol{z}^e - z_s] + [\boldsymbol{N}(\eta_i, \xi_i)\boldsymbol{z}^e - z_s]^2\right]\right.$$

$$\left. - \left[\frac{\partial \boldsymbol{N}(\eta_i, \xi_i)}{\partial z} \boldsymbol{\omega}_s^e[\boldsymbol{N}(\eta_i, \xi_i)\boldsymbol{y}^e - y_s] + [\boldsymbol{N}(\eta_i, \xi_i)\boldsymbol{y}^e - y_s]^2\right]\right] \det|\boldsymbol{J}|$$

$$I_\omega = \int_A \boldsymbol{\omega}_s^2 dA = \sum^{NE} \int_0^1 \int_0^{1-\xi} (\boldsymbol{N}\boldsymbol{\omega}^e)^2 \frac{1}{2} \det|\boldsymbol{J}| d\eta\, d\xi$$

$$= \frac{1}{2} \sum^{NE} \sum_{i=1}^{n} W_i [\boldsymbol{N}(\eta_i, \xi_i)\boldsymbol{\omega}^e]^2 \det|\boldsymbol{J}| \tag{3.52}$$

$$\beta_y = \frac{1}{I_y} \int_A \bar{z}^3 + \bar{z}\bar{y}^2 dA - 2z_s$$

$$= \frac{1}{I_y} \sum^{NE} \int_0^1 \int_0^{1-\xi} [(\boldsymbol{N}\bar{\boldsymbol{z}}^e)^3 + \boldsymbol{N}\bar{\boldsymbol{z}}^e(\boldsymbol{N}\bar{\boldsymbol{y}}^e)^2] \frac{1}{2} \det|\boldsymbol{J}| d\eta\, d\xi - 2z_s \tag{3.53}$$

$$= \frac{1}{2I_y} \sum^{NE} \sum_{i=1}^{n} W_i [[\boldsymbol{N}(\eta_i, \xi_i)\bar{\boldsymbol{z}}^e]^3 + \boldsymbol{N}(\eta_i, \xi_i)\bar{\boldsymbol{z}}^e [N(\eta_i, \xi_i)\bar{\boldsymbol{y}}^e]^2] \det|\boldsymbol{J}| - 2z_s$$

$$\beta_z = \frac{1}{I_z} \int_A \bar{y}^3 + \bar{y}\bar{z}^2 dA - 2y_s \tag{3.54}$$

$$= \frac{1}{I_z}\sum^{NE}\int_0^1\int_0^{1-\xi}[(\boldsymbol{N}\bar{\boldsymbol{y}}^e)^3 + \boldsymbol{N}\bar{\boldsymbol{y}}^e(\boldsymbol{N}\bar{\boldsymbol{z}}^e)^2]\frac{1}{2}\det|\boldsymbol{J}|d\eta\, d\xi - 2y_s$$

$$= \frac{1}{2I_z}\sum^{NE}\sum_{i=1}^{n}W_i[[\boldsymbol{N}(\eta_i,\xi_i)\bar{\boldsymbol{y}}^e]^3 + \boldsymbol{N}(\eta_i,\xi_i)\bar{\boldsymbol{y}}^e[\boldsymbol{N}(\eta_i,\xi_i)\bar{\boldsymbol{z}}^e]^2]\det|\boldsymbol{J}| - 2y_s$$

$$\beta_\omega = \frac{1}{I_\omega}\int_A \omega(\bar{y}^2 + \bar{z}^2)dA$$

$$= \frac{1}{I_\omega}\sum^{NE}\int_0^1\int_0^{1-\xi}\boldsymbol{N}\boldsymbol{\omega}^e[(\boldsymbol{N}\bar{\boldsymbol{y}}^e)^2 + (\boldsymbol{N}\bar{\boldsymbol{z}}^e)^2]\frac{1}{2}\det|\boldsymbol{J}|d\eta\, d\xi \tag{3.55}$$

$$= \frac{1}{2I_\omega}\sum^{NE}\sum_{i=1}^{n}W_i\boldsymbol{N}(\eta_i,\xi_i)\boldsymbol{\omega}^e[[\boldsymbol{N}(\eta_i,\xi_i)\bar{\boldsymbol{y}}^e]^2 + [\boldsymbol{N}(\eta_i,\xi_i)\bar{\boldsymbol{z}}^e]^2]\det|\boldsymbol{J}|$$

3.3.5 Shear coefficients

Assuming a beam subjected to a non-uniform bending moment M_z and a shear force V_y. The longitudinal normal stress can be calculated by:

$$\sigma_x = \frac{I_y M_z y - I_{yz} M_z z}{I_y I_z - I_{yz}^2} \tag{3.56}$$

With zero body force, the equation of equilibrium gives:

$$\frac{\partial\sigma_x}{\partial x} + \frac{\partial\tau_{xy}}{\partial y} + \frac{\partial\tau_{xz}}{\partial z} = 0 \tag{3.57}$$

Submitting equation(3.57) into equation (3.56) leads to:

$$\frac{\partial\tau_{xy}}{\partial y} + \frac{\partial\tau_{xz}}{\partial z} = \frac{V_y\left(I_{yz}z - I_y y\right)}{I_y I_z - I_{yz}^2} \tag{3.58}$$

For uniform isotropic materials, the kinetical strain-displacement equations can be expressed in Hooke's stress-strain relationship as:

$$\frac{\partial^2 \sigma_x}{\partial x \partial y} = \frac{1+\nu}{\nu}\frac{\partial}{\partial z}\left(\frac{\partial \tau_{xy}}{\partial z} - \frac{\partial \tau_{xz}}{\partial y} - \frac{\partial \tau_{yz}}{\partial x}\right) \tag{3.59}$$

$$\frac{\partial^2 \sigma_x}{\partial x \partial z} = \frac{1+\nu}{\nu}\frac{\partial}{\partial y}\left(\frac{\partial \tau_{xz}}{\partial y} - \frac{\partial \tau_{xy}}{\partial z} - \frac{\partial \tau_{yz}}{\partial x}\right) \tag{3.60}$$

Assuming no torsion, τ_{yz} equals zero. Submitting equation (3.56) into equations(3.59) and (3.60) leads to:

$$\frac{\partial}{\partial y}\left(\frac{\partial \tau_{xy}}{\partial z} - \frac{\partial \tau_{xz}}{\partial y}\right) = \frac{\nu V_y I_{yz}}{(1+\nu)\left(I_y I_z - I_{yz}^2\right)} \tag{3.61}$$

$$\frac{\partial}{\partial z}\left(\frac{\partial \tau_{xz}}{\partial y} - \frac{\partial \tau_{xy}}{\partial z}\right) = \frac{\nu V_y I_y}{(1+\nu)\left(I_y I_z - I_{yz}^2\right)} \tag{3.62}$$

The shear function **Φ** (y, z) can be employed to describe τ_{xy} and τ_{xz}:

$$\tau_{xy} = \frac{I_y I_z - I_{yz}^2}{2V_y(1+\nu)}\left[\frac{\partial \mathbf{\Phi}}{\partial y} + \nu\left(I_{yz} yz + I_y \frac{z^2 - y^2}{2}\right)\right] \tag{3.63}$$

$$\tau_{xz} = \frac{I_y I_z - I_{yz}^2}{2V_y(1+\nu)}\left[\frac{\partial \mathbf{\Phi}}{\partial z} + \nu\left(I_{yz} \frac{z^2 - y^2}{2} - I_y yz\right)\right] \tag{3.64}$$

Submitting equations (3.63) and (3.64) into equation (3.58), the partial derivative gives the governing equation:

$$\frac{\partial^2 \mathbf{\Phi}}{\partial y^2} + \frac{\partial^2 \mathbf{\Phi}}{\partial z^2} = 2\left(I_{yz} z - I_y y\right) \tag{3.65}$$

Since the beam is free of surface forces, the stress normal to the boundary curve shall be zero:

$$\tau_{xy}n_y + \tau_{xz}n_z = 0 \tag{3.66}$$

Where n_y and n_z are components of outward unit vector normal to the surface along y and z directions. Submitting equations (3.63) and (3.64) into equation (3.66) leads to:

$$\left[\frac{\partial \boldsymbol{\Phi}}{\partial y} + \nu\left(I_{yz}yz + I_y\frac{z^2 - y^2}{2}\right)\right]n_y + \left[\frac{\partial \boldsymbol{\Phi}}{\partial z} + \nu\left(I_{yz}\frac{z^2 - y^2}{2} - I_y yz\right)\right]n_z = 0 \tag{3.67}$$

Utilizing the Galerkin's method, with an appropriate trial function f, a weak form can be established as:

$$\begin{aligned}
&\int_A f\left[\frac{\partial^2 \boldsymbol{\Phi}}{\partial y^2} + \frac{\partial^2 \boldsymbol{\Phi}}{\partial z^2} - 2(I_{yz}z - I_y y)\right]dA \\
&+ \int_s f\left[\nu\left(I_y yz - I_{yz}\frac{z^2 - y^2}{2}\right)n_z - \nu\left(I_{yz}yz + I_y\frac{z^2 - y^2}{2}\right)n_y\right. \\
&\qquad\qquad \left. - \left(\frac{\partial \boldsymbol{\Phi}}{\partial y}n_y + \frac{\partial \boldsymbol{\Phi}}{\partial z}n_z\right)\right]ds = 0
\end{aligned} \tag{3.68}$$

Using the Green's first identity for the first integral part and the divergence theorem for the second integral part, the equation can be transformed into:

$$\begin{aligned}
&\int_A \left(\frac{\partial f}{\partial y} + \frac{\partial f}{\partial z}\right)\left(\frac{\partial \boldsymbol{\Phi}}{\partial y} + \frac{\partial \boldsymbol{\Phi}}{\partial z}\right) + 2f(1+\nu)\big(I_{yz}z - I_y y\big) \\
&-\nu\left[\frac{\partial f}{\partial y}\left(I_y yz - I_{yz}\frac{z^2 - y^2}{2}\right) + \frac{\partial f}{\partial z}\left(I_{yz}yz + I_y\frac{z^2 - y^2}{2}\right)\right]dA = 0
\end{aligned} \tag{3.69}$$

The above equation can be written in the elemental formulation:

$$\int_0^1 \int_0^{1-\xi} f^{eT}\left[\left(\frac{\partial \boldsymbol{N}^T}{\partial y}\frac{\partial \boldsymbol{N}}{\partial y} + \frac{\partial \boldsymbol{N}^T}{\partial z}\frac{\partial \boldsymbol{N}}{\partial z}\right)\boldsymbol{\Phi}^e \right. \tag{3.70}$$

$$-\left[\frac{\nu}{2}\begin{bmatrix}\frac{\partial \boldsymbol{N}}{\partial y} & \frac{\partial \boldsymbol{N}}{\partial z}\end{bmatrix}\begin{bmatrix} I_y[(\boldsymbol{Nz}^e)^2-(\boldsymbol{Ny}^e)^2]+2\boldsymbol{Ny}^e N\boldsymbol{z}^e I_{yz} \\ -I_{yz}[(\boldsymbol{Nz}^e)^2-(\boldsymbol{Ny}^e)^2]+2\boldsymbol{Ny}^e N\boldsymbol{z}^e I_y\end{bmatrix}\right.$$

$$\left.+2(1+\nu)\boldsymbol{N}^T\left(I_y\boldsymbol{Ny}^e-I_{yz}\boldsymbol{Nz}^e\right)\right]\Bigg]\frac{1}{2}\det|\boldsymbol{J}|d\eta d\xi=0$$

It gives that:

$$\int_0^1\int_0^{1-\xi}\left[\left(\frac{\partial \boldsymbol{N}^T}{\partial y}\frac{\partial \boldsymbol{N}}{\partial y}+\frac{\partial \boldsymbol{N}^T}{\partial z}\frac{\partial \boldsymbol{N}}{\partial z}\right)\boldsymbol{\Phi}^e\right.$$
$$-\left[\frac{\nu}{2}\begin{bmatrix}\frac{\partial \boldsymbol{N}}{\partial y} & \frac{\partial \boldsymbol{N}}{\partial z}\end{bmatrix}\begin{bmatrix} I_y[(\boldsymbol{Nz}^e)^2-(\boldsymbol{Ny}^e)^2]+2\boldsymbol{Ny}^e N\boldsymbol{z}^e I_{yz} \\ -I_{yz}[(\boldsymbol{Nz}^e)^2-(\boldsymbol{Ny}^e)^2]+2\boldsymbol{Ny}^e N\boldsymbol{z}^e I_y\end{bmatrix}\right. \tag{3.71}$$
$$\left.+2(1+\nu)\boldsymbol{N}^T\left(I_y\boldsymbol{Ny}^e-I_{yz}\boldsymbol{Nz}^e\right)\right]\Bigg]\frac{1}{2}\det|\boldsymbol{J}|d\eta d\xi=0$$

From above, the element stiffness matrix $\boldsymbol{K}^e$ and load vector $\boldsymbol{P}_y^e$ are formulated as:

$$K^e=\int_0^1\int_0^{1-\xi}\left(\frac{\partial \boldsymbol{N}^T}{\partial y}\frac{\partial \boldsymbol{N}}{\partial y}+\frac{\partial \boldsymbol{N}^T}{\partial z}\frac{\partial \boldsymbol{N}}{\partial z}\right)\frac{1}{2}\det|\boldsymbol{J}|d\eta\, d\xi$$
$$=\frac{1}{2}\sum_{i=1}^{n}\left[\frac{\partial \boldsymbol{N}(\eta_i,\xi_i)^T}{\partial y}\frac{\partial \boldsymbol{N}(\eta_i,\xi_i)}{\partial y}+\frac{\partial \boldsymbol{N}(\eta_i,\xi_i)^T}{\partial z}\frac{\partial \boldsymbol{N}(\eta_i,\xi_i)}{\partial z}\right]\det|\boldsymbol{J}| \tag{3.72}$$

$$\boldsymbol{P}_y^e=\int_0^1\int_0^{1-\xi}\left[\frac{\nu}{2}\begin{bmatrix}\frac{\partial \boldsymbol{N}}{\partial y} & \frac{\partial \boldsymbol{N}}{\partial z}\end{bmatrix}\begin{bmatrix} I_y[(\boldsymbol{Nz}^e)^2-(\boldsymbol{Ny}^e)^2]+2\boldsymbol{Ny}^e N\boldsymbol{z}^e I_{yz} \\ -I_{yz}[(\boldsymbol{Nz}^e)^2-(\boldsymbol{Ny}^e)^2]+2\boldsymbol{Ny}^e N\boldsymbol{z}^e I_y\end{bmatrix}\right.$$
$$\left.+2(1+\nu)\boldsymbol{N}^T\left(I_y\boldsymbol{Ny}^e-I_{yz}\boldsymbol{Nz}^e\right)\right]\frac{1}{2}\det|\boldsymbol{J}|d\eta d\xi$$
$$=\frac{1}{2}\sum_{i=1}^{n}\left[\frac{\nu}{2}\begin{bmatrix}\frac{\partial \boldsymbol{N}(\eta_i,\xi_i)}{\partial y} & \frac{\partial \boldsymbol{N}(\eta_i,\xi_i)}{\partial z}\end{bmatrix}\right. \tag{3.73}$$
$$\begin{bmatrix} I_y[[\boldsymbol{N}(\eta_i,\xi_i)\boldsymbol{z}^e]^2-[\boldsymbol{N}(\eta_i,\xi_i)\boldsymbol{y}^e]^2]+2\boldsymbol{N}(\eta_i,\xi_i)\boldsymbol{y}^e N(\eta_i,\xi_i)\boldsymbol{z}^e I_{yz} \\ -I_{yz}[[\boldsymbol{N}(\eta_i,\xi_i)\boldsymbol{z}^e]^2-[\boldsymbol{N}(\eta_i,\xi_i)\boldsymbol{y}^e]^2]+2\boldsymbol{N}(\eta_i,\xi_i)\boldsymbol{y}^e N(\eta_i,\xi_i)\boldsymbol{z}^e I_y\end{bmatrix}$$

$$+2(1+\nu)\boldsymbol{N}^T\left[I_y\boldsymbol{N}(\eta_i,\xi_i)\boldsymbol{y}^e - I_{yz}\boldsymbol{N}(\eta_i,\xi_i)\boldsymbol{z}^e\right]\Big]\det|\boldsymbol{J}|$$

Therefore, the calculation of shear coefficients k_y can be obtained by solving the equation between the total stiffness matrix $\boldsymbol{K}$ and total load vector $\boldsymbol{P}_y$ and gives as,

$$k_y = \frac{\Delta^2}{A\kappa_y} \tag{3.74}$$

where,

$$\Delta = 2(1+\nu)\left(I_{\bar{y}}I_{\bar{z}} - I_{\bar{y}\bar{z}}^2\right) \tag{3.75}$$

$$\kappa_y = \int_A \left(\begin{bmatrix} \dfrac{\partial \boldsymbol{\Phi}}{\partial y} \\ \dfrac{\partial \boldsymbol{\Phi}}{\partial z} \end{bmatrix}^T - \frac{\nu}{2}\boldsymbol{h}^T \right) \left(\begin{bmatrix} \dfrac{\partial \boldsymbol{\Phi}}{\partial y} \\ \dfrac{\partial \boldsymbol{\Phi}}{\partial z} \end{bmatrix} - \frac{\nu}{2}\boldsymbol{h} \right) dA$$

$$= \sum^{NE} \int_0^1 \int_0^{1-\xi} \left(\begin{bmatrix} \dfrac{\partial \boldsymbol{N}}{\partial y}\boldsymbol{\Phi}^e \\ \dfrac{\partial \boldsymbol{N}}{\partial z}\boldsymbol{\Phi}^e \end{bmatrix}^T - \frac{\nu}{2}\boldsymbol{h}^T \right) \left(\begin{bmatrix} \dfrac{\partial \boldsymbol{N}}{\partial y}\boldsymbol{\Phi}^e \\ \dfrac{\partial \boldsymbol{N}}{\partial z}\boldsymbol{\Phi}^e \end{bmatrix} - \frac{\nu}{2}\boldsymbol{h} \right) \frac{1}{2}\det|\boldsymbol{J}|d\eta\, d\xi$$

$$\tag{3.76}$$

$$= \frac{1}{2}\sum^{NE}\sum_{i=1}^{n} W_i \left(\begin{bmatrix} \dfrac{\partial \boldsymbol{N}(\eta_i,\xi_i)}{\partial y}\boldsymbol{\Phi}^e \\ \dfrac{\partial \boldsymbol{N}(\eta_i,\xi_i)}{\partial z}\boldsymbol{\Phi}^e \end{bmatrix}^T - \frac{\nu}{2}\boldsymbol{h}(\eta_i,\xi_i)^T \right)$$

$$\left(\begin{bmatrix} \dfrac{\partial \boldsymbol{N}(\eta_i,\xi_i)}{\partial y}\boldsymbol{\Phi}^e \\ \dfrac{\partial \boldsymbol{N}(\eta_i,\xi_i)}{\partial z}\boldsymbol{\Phi}^e \end{bmatrix} - \frac{\nu}{2}\boldsymbol{h}(\eta_i,\xi_i) \right) \det|\boldsymbol{J}|$$

$$\boldsymbol{h}(\eta_i,\xi_i) = \begin{bmatrix} -I_{\bar{y}}(\bar{z}^2 - \bar{y}^2) - 2I_{\bar{y}\bar{z}}\bar{y}\bar{z} \\ -I_{\bar{y}\bar{z}}(\bar{z}^2 - \bar{y}^2) + 2I_{\bar{y}}\bar{y}\bar{z} \end{bmatrix} \tag{3.77}$$

$$= \begin{bmatrix} -I_{\bar{y}}[[\boldsymbol{N}(\eta_i,\xi_i)\bar{\boldsymbol{z}}^e]^2 - [\boldsymbol{N}(\eta_i,\xi_i)\bar{\boldsymbol{y}}^e]^2] - 2I_{\bar{y}\bar{z}}\boldsymbol{N}(\eta_i,\xi_i)\bar{\boldsymbol{y}}^e\boldsymbol{N}(\eta_i,\xi_i)\bar{\boldsymbol{z}}^e \\ -I_{\bar{y}\bar{z}}[[\boldsymbol{N}(\eta_i,\xi_i)\bar{\boldsymbol{z}}^e]^2 - [\boldsymbol{N}(\eta_i,\xi_i)\bar{\boldsymbol{y}}^e]^2] + 2I_{\bar{y}}\boldsymbol{N}(\eta_i,\xi_i)\bar{\boldsymbol{y}}^e\boldsymbol{N}(\eta_i,\xi_i)\bar{\boldsymbol{z}}^e \end{bmatrix}$$

Similarly, shear coefficients k_z can be generated by,

$$k_z = \frac{\Delta^2}{A\kappa_z} \tag{3.78}$$

$$\kappa_z = \int_A \left(\begin{bmatrix} \frac{\partial \boldsymbol{\Psi}}{\partial y} \\ \frac{\partial \boldsymbol{\Psi}}{\partial z} \end{bmatrix}^T - \frac{\nu}{2}\boldsymbol{d}^T \right) \left(\begin{bmatrix} \frac{\partial \boldsymbol{\Psi}}{\partial y} \\ \frac{\partial \boldsymbol{\Psi}}{\partial z} \end{bmatrix} - \frac{\nu}{2}\boldsymbol{d} \right) dA$$

$$= \sum^{NE} \int_0^1 \int_0^{1-\xi} \left(\begin{bmatrix} \frac{\partial \boldsymbol{N}}{\partial y}\boldsymbol{\Psi}^e \\ \frac{\partial \boldsymbol{N}}{\partial z}\boldsymbol{\Psi}^e \end{bmatrix}^T - \frac{\nu}{2}\boldsymbol{d}^T \right) \left(\begin{bmatrix} \frac{\partial \boldsymbol{N}}{\partial y}\boldsymbol{\Psi}^e \\ \frac{\partial \boldsymbol{N}}{\partial z}\boldsymbol{\Psi}^e \end{bmatrix} - \frac{\nu}{2}\boldsymbol{d} \right) \frac{1}{2}\det|\boldsymbol{J}| d\eta\, d\xi \tag{3.79}$$

$$= \frac{1}{2}\sum^{NE}\sum_{i=1}^{n} W_i \left(\begin{bmatrix} \frac{\partial \boldsymbol{N}(\eta_i,\xi_i)}{\partial y}\boldsymbol{\Psi}^e \\ \frac{\partial \boldsymbol{N}(\eta_i,\xi_i)}{\partial z}\boldsymbol{\Psi}^e \end{bmatrix}^T - \frac{\nu}{2}\boldsymbol{d}(\eta_i,\xi_i)^T \right)$$

$$\left(\begin{bmatrix} \frac{\partial \boldsymbol{N}(\eta_i,\xi_i)}{\partial y}\boldsymbol{\Psi}^e \\ \frac{\partial \boldsymbol{N}(\eta_i,\xi_i)}{\partial z}\boldsymbol{\Psi}^e \end{bmatrix} - \frac{\nu}{2}\boldsymbol{d}(\eta_i,\xi_i) \right) \det|\boldsymbol{J}|$$

$$\boldsymbol{d}(\eta_i,\xi_i) = \begin{bmatrix} I_{\bar{y}\bar{z}}(\bar{z}^2 - \bar{y}^2) + 2I_{\bar{z}}\bar{y}\bar{z} \\ I_{\bar{z}}(\bar{z}^2 - \bar{y}^2) - 2I_{\bar{y}\bar{z}}\bar{y}\bar{z} \end{bmatrix} \tag{3.80}$$

$$= \begin{bmatrix} I_{\bar{y}\bar{z}}[[\boldsymbol{N}(\eta_i,\xi_i)\bar{\boldsymbol{z}}^e]^2 - [\boldsymbol{N}(\eta_i,\xi_i)\bar{\boldsymbol{y}}^e]^2] + 2I_{\bar{z}}\boldsymbol{N}(\eta_i,\xi_i)\bar{\boldsymbol{y}}^e\boldsymbol{N}(\eta_i,\xi_i)\bar{\boldsymbol{z}}^e \\ I_{\bar{z}}[[\boldsymbol{N}(\eta_i,\xi_i)\bar{\boldsymbol{z}}^e]^2 - [\boldsymbol{N}(\eta_i,\xi_i)\bar{\boldsymbol{y}}^e]^2] - 2I_{\bar{y}\bar{z}}\boldsymbol{N}(\eta_i,\xi_i)\bar{\boldsymbol{y}}^e\boldsymbol{N}(\eta_i,\xi_i)\bar{\boldsymbol{z}}^e \end{bmatrix}$$

where $\boldsymbol{\Psi}$ is the corresponding shear function.

3.3.6 Verification examples

To validate the accuracy of the proposed cross-section analysis method, two examples are presented in this section, where the section properties from the proposed method are compared with those from other algorithms. Parameters involved in the verification consist of geometric properties (cross-section area A, the moment of inertia I_y and I_z), torsional properties (torsional constant J, warping constant I_ω, shear center coordinate y_c and z_c, Wagner coefficients β_v, β_w and β_ω), and shear properties (shear coefficient along y- and z-axis k_y, k_z).

Example 1: Geometric and torsional properties

The geometric and torsional properties of four typical sections are calculated. The section width and depth of each section are given in Figure 3.7. Three different wall thicknesses, 10mm, 15mm, and 20mm, are adopted. Results generated by the proposed CST element are compared with the benchmark results obtained from SkyCiv Section Builder (2017), a commercial software for the cross-section analyses based on the 2D Finite Element method, and the differences are plotted in Figure 3.8. Besides, the section properties from the CM method given in Section 3.2 are also given for comparison. Detailed section properties are given in **Table 1-Table 4** and the differences between the calculation results and the benchmark results are given in Figure 3.8.

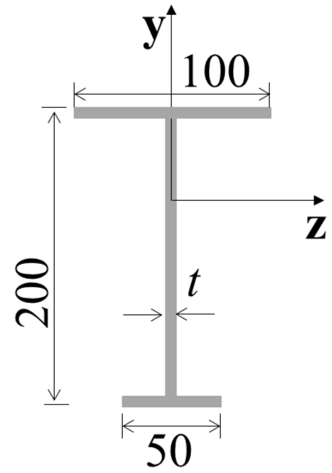

Section A: Monosymmetric I

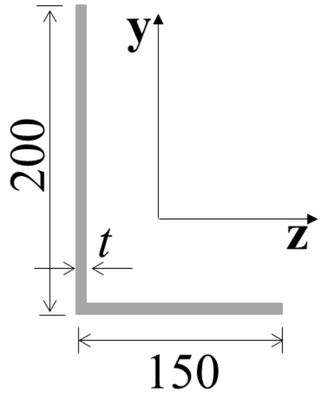

Section B: L section

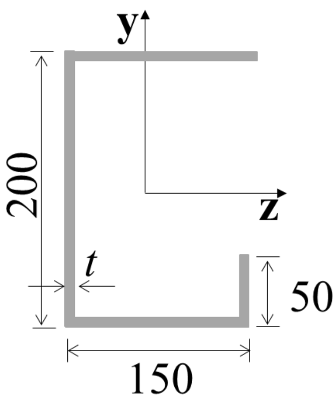

Section C: Lipped C section

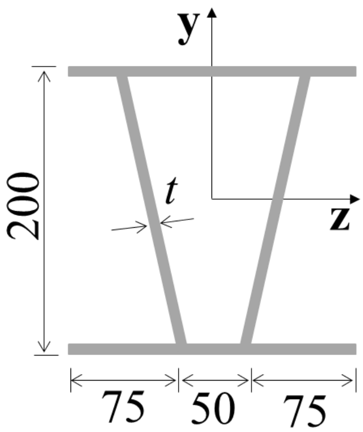

Section D: Box girder

t=10, 15, 20 (Unit: mm)

Figure 3.7 Verification examples of geometric and torsional properties

Table 3.3 Geometric and torsional properties – Section A (Unit: mm)

	Section A - Monosymmetric I Section								
	SkyCiv			**CM Method**			**Present Study**		
	***t* = 10**	***t* = 15**	***t* = 20**	***t* = 10**	***t* = 15**	***t* = 20**	***t* = 10**	***t* = 15**	***t* = 20**
$\boldsymbol{A}$	3.30×10^{3}	4.80×10^{3}	6.20×10^{3}	3.30×10^{3}	4.80×10^{3}	6.20×10^{3}	3.30×10^{3}	4.80×10^{3}	6.20×10^{3}
$\boldsymbol{I_y}$	9.53×10^{5}	1.45×10^{6}	1.98×10^{6}	9.53×10^{5}	1.45×10^{6}	1.98×10^{6}	9.53×10^{5}	1.45×10^{6}	1.98×10^{6}
$\boldsymbol{I_z}$	1.77×10^{7}	2.44×10^{7}	2.99×10^{7}	1.77×10^{7}	2.44×10^{7}	2.99×10^{7}	1.77×10^{7}	2.44×10^{7}	2.99×10^{7}
$\boldsymbol{J}$	1.11×10^{5}	3.65×10^{5}	8.44×10^{5}	1.13×10^{5}	3.60×10^{5}	8.27×10^{5}	1.13×10^{5}	3.71×10^{5}	8.54×10^{5}
$\boldsymbol{I_w}$	3.43×10^{9}	5.00×10^{9}	6.47×10^{9}	3.34×10^{9}	4.76×10^{9}	6.02×10^{9}	3.43×10^{9}	5.00×10^{9}	6.48×10^{9}
$\boldsymbol{y_c}$	5.81×10^{1}	5.45×10^{1}	5.07×10^{1}	5.86×10^{1}	5.56×10^{1}	5.25×10^{1}	5.81×10^{1}	5.46×10^{1}	5.08×10^{1}
$\boldsymbol{z_c}$	0	0	0	0	0	0	0	0	0
$\boldsymbol{\beta_v}$	0	0	0	0	0	0	0	0	0
$\boldsymbol{\beta_w}$	-1.34×10^{2}	-1.25×10^{2}	-1.18×10^{2}	-1.35×10^{2}	-1.28×10^{2}	-1.21×10^{2}	-1.33×10^{2}	-1.25×10^{2}	-1.18×10^{2}
$\boldsymbol{\beta_\omega}$	-	-	-	0	0	0	0	0	0

Table 3.4 Geometric and torsional properties – Section B (Unit: mm)

	Section B - L Section								
	SkyCiv			**CM Method**			**Present Study**		
	t **= 10**	t **= 15**	t **= 20**	t **= 10**	t **= 15**	t **= 20**	t **= 10**	t **= 15**	t **= 20**
A	3.40×10^{3}	5.02×10^{3}	6.60×10^{3}	3.40×10^{3}	5.03×10^{3}	6.60×10^{3}	3.40×10^{3}	5.03×10^{3}	6.60×10^{3}
I_y	6.94×10^{6}	9.93×10^{6}	1.27×10^{7}	6.93×10^{6}	9.93×10^{6}	1.26×10^{7}	6.94×10^{6}	9.93×10^{6}	1.27×10^{7}
I_z	1.41×10^{7}	2.04×10^{7}	2.62×10^{7}	1.41×10^{7}	2.04×10^{7}	2.61×10^{7}	1.41×10^{7}	2.04×10^{7}	2.65×10^{7}
J	1.14×10^{5}	3.69×10^{5}	8.56×10^{5}	1.13×10^{5}	3.77×10^{5}	8.80×10^{5}	1.13×10^{5}	3.72×10^{5}	8.61×10^{5}
I_w	2.89×10^{8}	9.27×10^{8}	2.07×10^{9}	2.91×10^{8}	9.40×10^{8}	2.13×10^{9}	2.89×10^{8}	9.26×10^{8}	2.07×10^{9}
y_c	-5.55×10^{1}	-5.43×10^{1}	-5.29×10^{1}	-5.58×10^{1}	-5.49×10^{1}	-5.40×10^{1}	-5.55×10^{1}	-5.43×10^{1}	-5.29×10^{1}
z_c	-3.09×10^{1}	-3.02×10^{1}	-2.95×10^{1}	-3.10×10^{1}	-3.04×10^{1}	-2.99×10^{1}	-3.09×10^{1}	-3.02×10^{1}	-2.95×10^{1}
β_v	2.30×10^{2}	2.23×10^{2}	2.16×10^{2}	2.31×10^{2}	2.26×10^{2}	2.22×10^{2}	2.30×10^{2}	2.23×10^{2}	2.16×10^{2}
β_w	8.20×10^{1}	8.10×10^{1}	7.95×10^{1}	8.24×10^{1}	8.17×10^{1}	8.09×10^{1}	8.20×10^{1}	8.10×10^{1}	7.95×10^{1}
β_ω	-	-	-	-2.17×10^{-1}	-2.18×10^{-1}	-2.19×10^{-1}	-2.73×10^{-1}	-2.73×10^{-1}	-2.69×10^{-1}

Table 3.5 Geometric and torsional properties – Section C (Unit: mm)

	Section C - Lipped C Section								
	SkyCiv			**CM Method**			**Present Study**		
	***t* = 10**	***t* = 15**	***t* = 20**	***t* = 10**	***t* = 15**	***t* = 20**	***t* = 10**	***t* = 15**	***t* = 20**
A	5.20×10^{3}	7.58×10^{3}	9.80×10^{3}	5.20×10^{3}	7.58×10^{3}	9.80×10^{3}	5.20×10^{3}	7.58×10^{3}	9.80×10^{3}
I_y	1.46×10^{7}	2.00×10^{7}	2.45×10^{7}	1.45×10^{7}	1.99×10^{7}	2.42×10^{7}	1.46×10^{7}	2.00×10^{7}	2.45×10^{7}
I_z	3.38×10^{7}	4.70×10^{7}	5.81×10^{7}	3.38×10^{7}	4.68×10^{7}	5.75×10^{7}	3.38×10^{7}	4.70×10^{7}	5.81×10^{7}
J	1.73×10^{5}	5.66×10^{5}	1.30×10^{6}	1.73×10^{5}	5.68×10^{5}	1.31×10^{6}	1.75×10^{5}	5.72×10^{5}	1.31×10^{6}
I_w	1.17×10^{11}	1.52×10^{11}	1.76×10^{11}	1.16×10^{11}	1.50×10^{11}	1.72×10^{11}	1.17×10^{11}	1.52×10^{11}	1.76×10^{11}
y_c	-2.42×10^{1}	-2.10×10^{1}	-1.77×10^{1}	-2.44×10^{1}	-2.14×10^{1}	-1.83×10^{1}	-2.42×10^{1}	-2.10×10^{1}	-1.77×10^{1}
z_c	-1.17×10^{2}	-1.13×10^{2}	-1.09×10^{2}	-1.18×10^{2}	-1.15×10^{2}	-1.11×10^{2}	-1.17×10^{2}	-1.14×10^{2}	-1.09×10^{2}
β_v	2.96×10^{2}	2.86×10^{2}	2.75×10^{2}	2.97×10^{2}	2.89×10^{2}	2.80×10^{2}	2.96×10^{2}	2.86×10^{2}	2.75×10^{2}
β_w	2.29×10^{1}	2.09×10^{1}	1.86×10^{1}	2.34×10^{1}	2.22×10^{1}	2.10×10^{1}	2.29×10^{1}	2.09×10^{1}	1.86×10^{1}
β_ω	-	-	-	7.33×10^{-2}	7.83×10^{-2}	8.37×10^{-2}	7.04×10^{-2}	7.13×10^{-2}	7.03×10^{-2}

Table 3.6 Geometric and torsional properties – Section D (Unit: mm)

	Section D – Box Girder								
	SkyCiv			**CM Method**			**Present Study**		
	***t* = 10**	***t* = 15**	***t* = 20**	***t* = 10**	***t* = 15**	***t* = 20**	***t* = 10**	***t* = 15**	***t* = 20**
A	7.74×10^{3}	1.13×10^{4}	1.47×10^{4}	7.96×10^{3}	1.18×10^{4}	1.56×10^{4}	7.74×10^{3}	1.13×10^{4}	1.47×10^{4}
I_y	2.17×10^{7}	3.07×10^{7}	3.88×10^{7}	2.21×10^{7}	3.17×10^{7}	4.05×10^{7}	2.17×10^{7}	3.07×10^{7}	3.88×10^{7}
I_z	4.62×10^{7}	6.43×10^{7}	7.94×10^{7}	4.81×10^{7}	6.81×10^{7}	8.57×10^{7}	4.62×10^{7}	6.43×10^{7}	7.94×10^{7}
J	2.11×10^{7}	2.85×10^{7}	3.44×10^{7}	2.00×10^{7}	2.62×10^{7}	3.04×10^{7}	2.12×10^{7}	2.87×10^{7}	3.45×10^{7}
I_w	9.84×10^{11}	6.55×10^{11}	5.02×10^{11}	6.24×10^{10}	9.96×10^{10}	1.39×10^{11}	5.91×10^{10}	8.94×10^{10}	1.20×10^{11}
y_c	-7.54×10^{-1}	-1.13×10^{0}	-1.54×10^{0}	-8.31×10^{-1}	-1.21×10^{0}	-1.54×10^{0}	-7.56×10^{-1}	-1.15×10^{0}	-1.57×10^{0}
z_c	0	0	0	0	0	0	0	0	0
β_v	0	0	0	0	0	0	0	0	0
β_w	6.97×10^{0}	7.19×10^{0}	7.54×10^{0}	8.08×10^{0}	8.83×10^{0}	9.95×10^{0}	6.95×10^{0}	7.24×10^{0}	7.59×10^{0}
β_ω	-	-	-	0	0	0	0	0	0

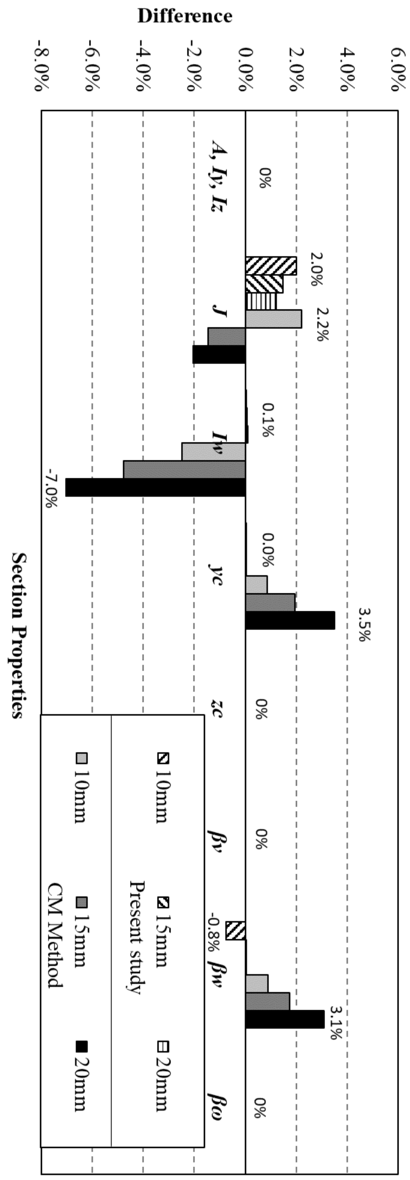

Section A: Monosymmetric I

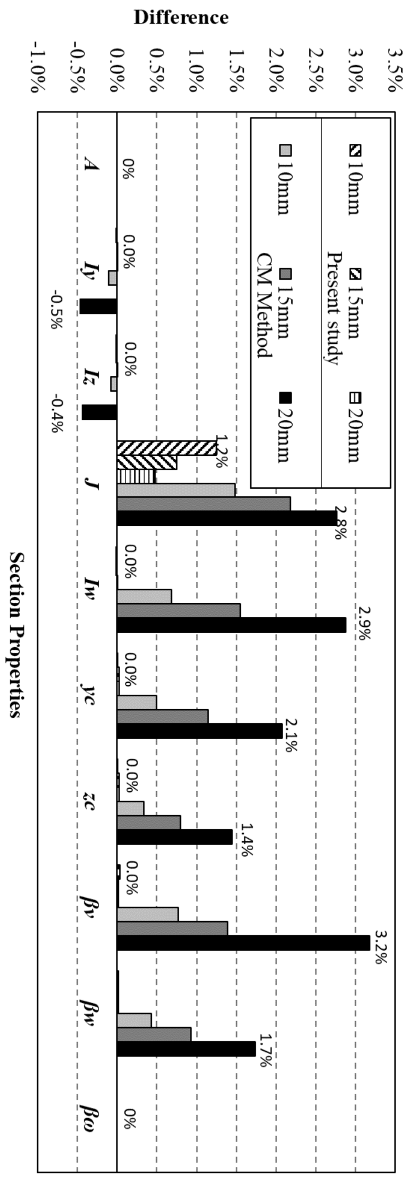

Section B: L section

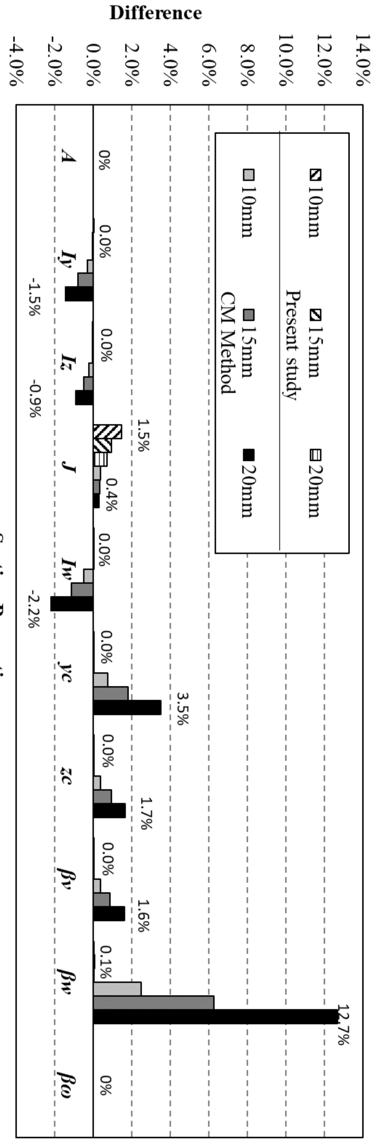

Section C: Lipped C section

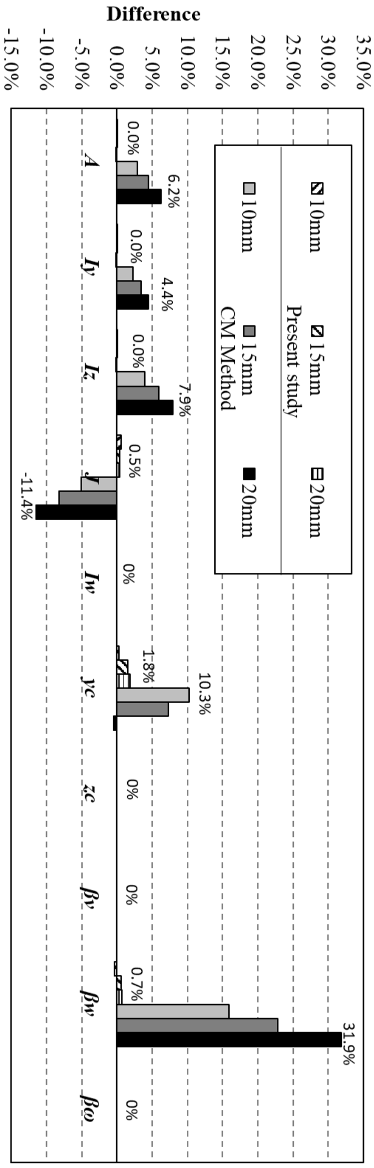

Section D: Box girder

Figure 3.8 Comparation results

From Figure 3.8, it can be observed that with the increment of the wall thickness, the differences between the results from the CM method and the benchmark results are increasing with the maximum differences equals to 31.9%. This is because the CM method is based on the thin-walled assumption, which is not suitable for calculating the section properties of thick-walled sections. The differences between the results from the proposed CST elements and the benchmark results are relatively small (no more than 2%) for all the wall thicknesses. It can be concluded that the proposed cross-section analysis algorism can calculate the section geometric and torsional properties accurately.

Example 2: Shear coefficients

This example is intended to validate the accuracy of the shear coefficients calculation. As shown in Figure 3.9, four types of cross-sections, rectangular sections with different height-to-width ratios, a T section, a Crane rail section and a bridge cross-section, reported by Gruttmann and Wanger (2001), are studied. Shear coefficients with different Poisson’s ratios are calculated using the proposed CST element and compared with those given by Gruttmann and Wanger (2001).

Table 3.7 - Table 3.10shows that the Poisson’s ratios have little influence on the shear coefficients of sections with large height-to-width ratios. It is also clear that all the results agree well with the benchmark, where differences do not exceed 0.1%, showing that the proposed cross-section analysis algorism can get the shear coefficients accurately.

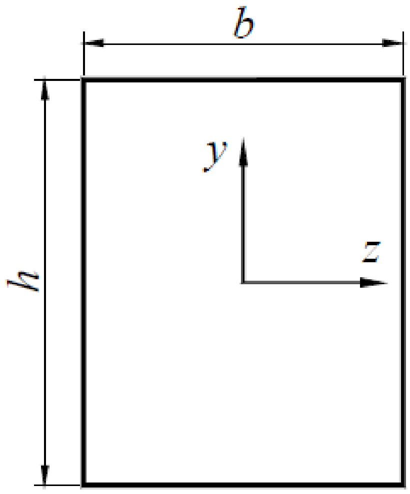

(a) Rectangular cross-section

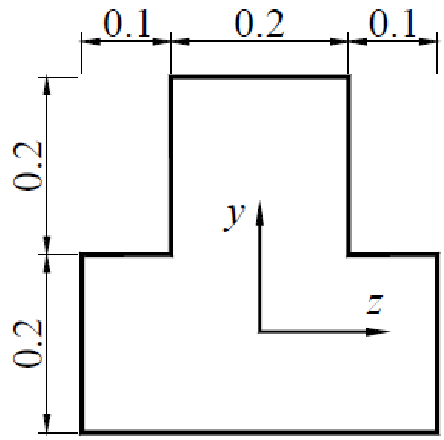

(b) T section (Unit: m)

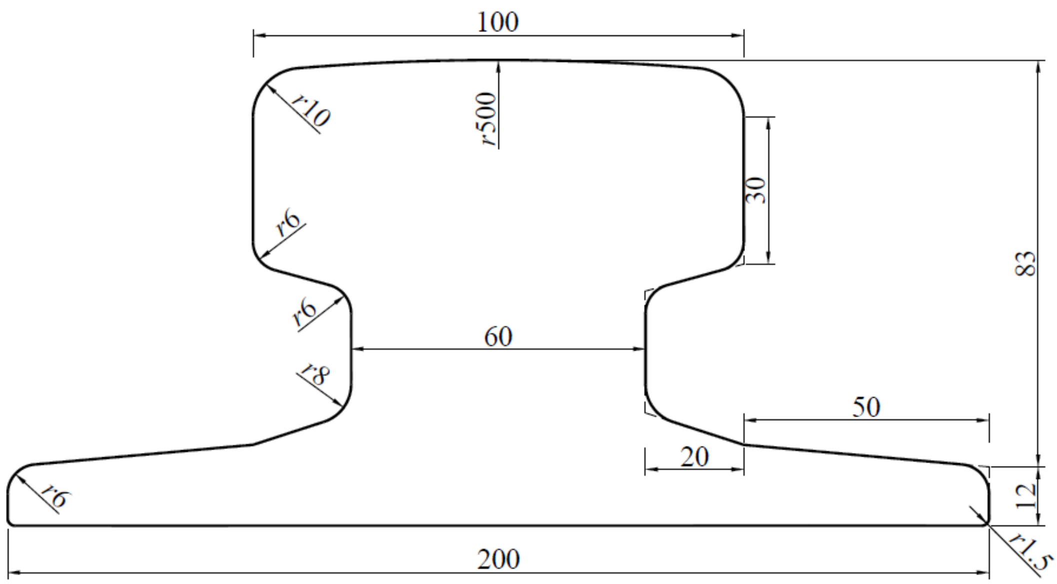

(c) Crane rail A100 (Unit: mm)

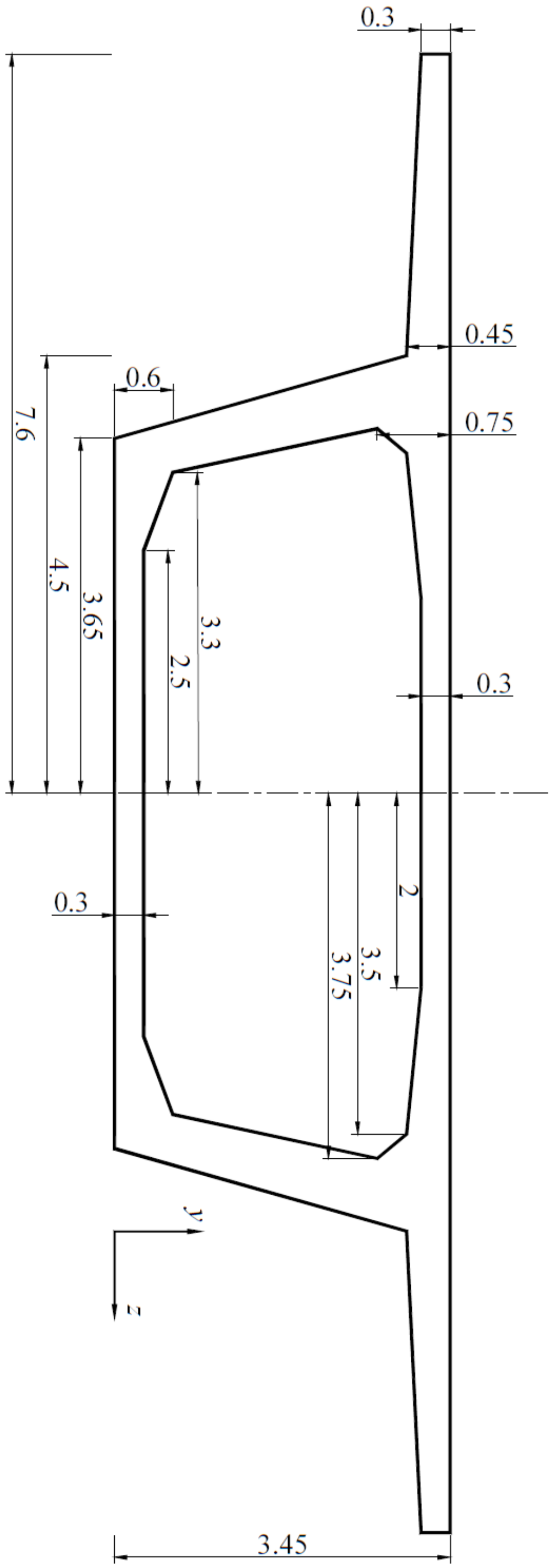

(d) Bridge cross-section (Unit: m)

Figure 3.9 Verification examples of shear deformation coefficients

Table 3.7 Shear coefficients of Section a

Section A - Rectangular Section				
Parameter		k_y		
Poisson's ratios		**Gruttmann and Wagner (2001)**	**Present Study**	**Differences**
$\nu = 0$	$h/b = 2$	0.8333	0.8336	0.04%
	$h/b = 1$	0.8333	0.8336	0.04%
	$h/b = 0.5$	0.8333	0.8334	0.01%
	$h/b = 0.25$	0.8333	0.8334	0.01%
$\nu = 0.25$	$h/b = 2$	0.8331	0.8331	0.00%
	$h/b = 1$	0.8295	0.8295	0.00%
	$h/b = 0.5$	0.7961	0.7961	0.00%
	$h/b = 0.25$	0.6308	0.6308	0.00%
$\nu = 0.5$	$h/b = 2$	0.8325	0.8325	0.00%
	$h/b = 1$	0.8228	0.8227	0.01%
	$h/b = 0.5$	0.7375	0.7375	0.00%
	$h/b = 0.25$	0.4404	0.4404	0.00%

Table 3.8 Shear coefficients of Section b

	Poisson's ratios	*Gruttmann and Wagner (2001)*	*Present Study*	*Differences*
k_y	$\nu = 0$	0.6767	0.6773	0.09%
	$\nu = 0.25$	0.6753	0.6758	0.07%
	$\nu = 0.5$	0.6727	0.6733	0.09%
k_z	$\nu = 0$	0.7395	0.7399	0.05%
	$\nu = 0.25$	0.7355	0.7362	0.10%
	$\nu = 0.5$	0.7294	0.7297	0.04%

Table 3.9 Shear coefficients of Section c

	Poisson's ratios	***Gruttmann and Wagner (2001)***	***Present Study***	***Differences***
k_y	$\nu = 0$	0.4474	0.4488	0.31%
	$\nu = 0.3$	0.4468	0.4481	0.29%
k_z	$\nu = 0$	0.6845	0.687	0.37%
	$\nu = 0.3$	0.6836	0.686	0.35%

Table 3.10 Shear coefficients of Section d

	Poisson's ratios	***Gruttmann and Wagner (2001)***	***Present Study***	***Differences***
k_y	$\nu = 0$	0.2312	0.2314	0.09%
	$\nu = 0.2$	0.2311	0.2313	0.09%
k_z	$\nu = 0$	0.5993	0.5994	0.02%
	$\nu = 0.2$	0.5993	0.5994	0.02%

CHAPTER 4.

ELASTIC ANALYSIS OF STEEL MEMBERS WITH THIN-WALLED SECTIONS

4.1 Introduction

This chapter presents the LFEM for the steel frames with nonsymmetric thin-walled sections. A refined line element for members with nonsymmetric thin-walled sections and an improved Gaussian line element for the large-deflection analysis of steel members with nonsymmetric sections subjected to torsion is given.

Thin-walled sections, such as those shown in Figure 4.1, are extensively used in metal structures because of their material efficiency and ease in manufacturing, with the latter often promoting the utilization of non-symmetric sections. Members with these sections are usually weak in resisting torsion and minor axis bending. As a result, they are susceptible to buckling in a lateral-torsional mode under bending, in a flexural-torsional mode under compression, or in a coupled mode under eccentric axial load. The behavior of these non-symmetric sections is more complex because its shear center does not coincide with its centroid. As a preferred design method for handling such sections, simulation-based design approaches come to the forefront – approaches in which more factors known to influence system stability are modelled directly within the analysis, and thereby require that a smaller number of prescriptive equations be employed in the design process. The key to such approaches, however, is a robust, efficient, and reliable computational analysis method that accurately models member and system behavior. To this end, a refined warping element for the bifurcation and large-deflection analysis of beam-columns with arbitrary thin-walled open-sections is presented in this section.

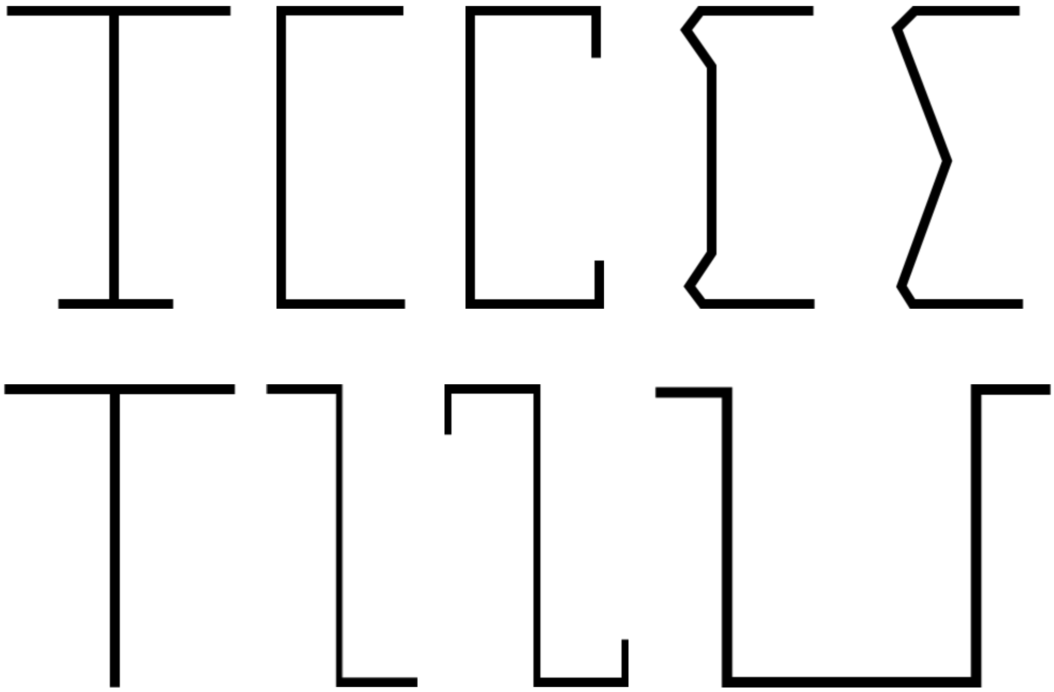

Figure 4.1 Examples of non-symmetric thin-walled sections

In summary, this chapter provides a detailed derivation of the element stiffness formulations for thin-walled members with nonsymmetric cross-sections. The kinematic motion is based on the UL formulation and is discussed, and several examples are given that demonstrate the accuracy of the results.

4.2 Refined Line Element for Wanger Effect Based on Euler-Bernoulli Beam Theory

4.2.1 Element reference axes

An additional warping degree of freedom (DOF) is included in the proposed three-dimensional line-element formulation. As a result, there are seven DOFs at each node of an element end, and therefore, the total number of DOFs for the element is fourteen (see Figure 4.2(a)). There are two reference local axes per element, one located at the centroid and the other at the shear center. In order to simplify the formulations, the rotations, translations, and warping deformations due to moments, shears, and bi-moments are defined relative to the shear center axis, while the nodal displacements in the direction of the element length are specified with reference to the centroid axis. This assumption is also used by other researchers, such as Chan and Kitipornchai (1987).

Therefore, the vector of the DOFs for an element (see Figure 4.2 (a)) are given as,

$$\boldsymbol{u} = [u_1 \quad v_1 \quad w_1 \quad \theta_{x1} \quad \theta_{y1} \quad \theta_{z1} \quad \theta_{b1} \quad u_2 \quad v_2 \quad w_2 \quad \theta_{x2} \quad \theta_{y2} \quad \theta_{z2} \quad \theta_{b2}] \tag{4.1}$$

where u, v, and w are the displacements along the x-, y-, and z-axes, respectively; θ_x, θ_y, and θ_z are the rotations about the x-, y-, and z-axes; and θ_b is the warping deformation.

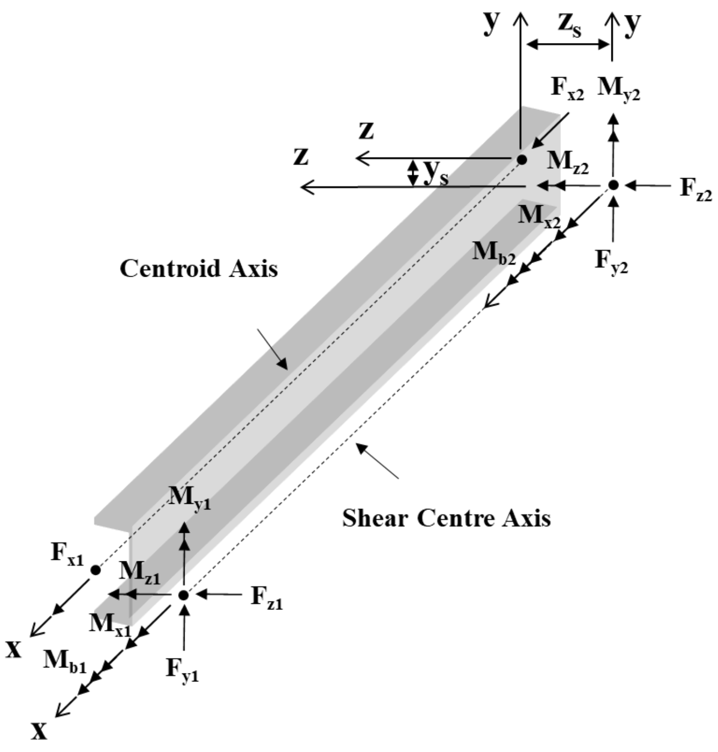

(a) Local element forces

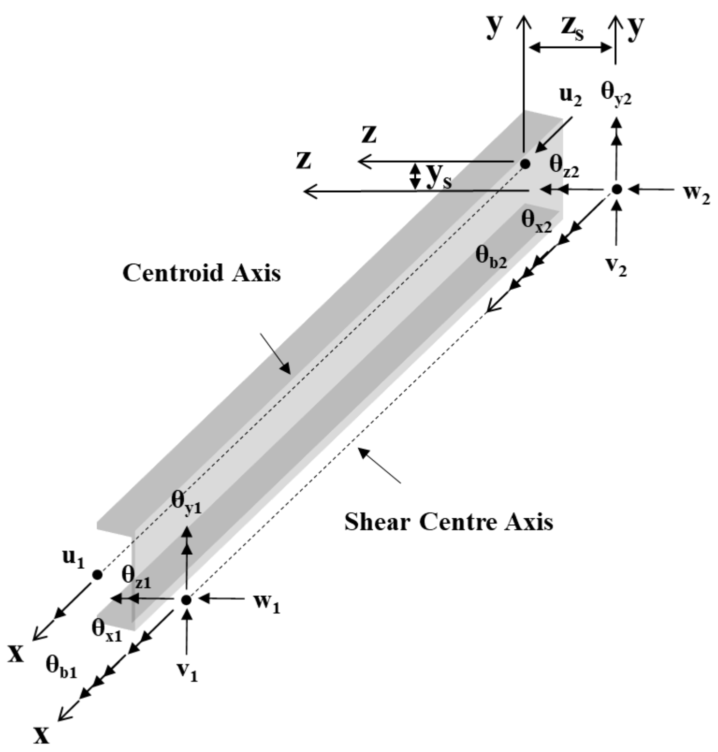

(b) Local DOFs

Figure 4.2 Deformations and forces in the element local axes

The forces and moments corresponding to these DOFs are given as,

$$\boldsymbol{F} = [F_{x1} \quad F_{y1} \quad F_{z1} \quad M_{x1} \quad M_{y1} \quad M_{z1} \quad M_{b1} \quad F_{x2} \quad F_{y2} \quad F_{z2} \quad M_{x2} \quad M_{y2} \quad M_{z2} \quad M_{b2}] \tag{4.2}$$

in which F_x, F_y, and F_z are the forces along the x-, y-, and z-axes, respectively; M_x, M_y, and M_z are the moments about the x-, y-, and z-axes; and M_b is the bi-moment.

4.2.2 Shape functions

The following interpolating polynomials, as defined in terms of the adopted shape functions, are used to describe the deformations along the element length,

$$u_0(x) = \left(1 - \frac{x}{L}\right) u_1 + \frac{x}{L} u_2 \tag{4.3}$$

$$\begin{aligned} v_0(x) = v_2 \left(\frac{3x^2}{L^2} - \frac{2x^3}{L^3}\right) + v_1 \left(1 - \frac{3x^2}{L^2} + \frac{2x^3}{L^3}\right) \\ + \theta_{1z} \left(x - \frac{2x^2}{L} + \frac{x^3}{L^2}\right) - \theta_{2z} \left(\frac{x^2}{L} - \frac{x^3}{L^2}\right) \end{aligned} \tag{4.4}$$

$$\begin{aligned} w_0(x) = w_2 \left(\frac{3x^2}{L^2} - \frac{2x^3}{L^3}\right) + w_1 \left(1 - \frac{3x^2}{L^2} + \frac{2x^3}{L^3}\right) \\ - \theta_{1y} \left(x - \frac{2x^2}{L} + \frac{x^3}{L^2}\right) + \theta_{2y} \left(\frac{x^2}{L} - \frac{x^3}{L^2}\right) \end{aligned} \tag{4.5}$$

$$\begin{aligned} \theta(x) = \left(x - \frac{2x^2}{L} + \frac{x^3}{L^2}\right) \theta_{b1} + \left(-\frac{x^2}{L} + \frac{x^3}{L^2}\right) \theta_{b2} \\ + \left(1 - \frac{3x^2}{L^2} + \frac{2x^3}{L^3}\right) \theta_{x1} + \left(\frac{3x^2}{L^2} - \frac{2x^3}{L^3}\right) \theta_{x2} \end{aligned} \tag{4.6}$$

in which θ(x) is the torsional rotation or twist along the element length showing the influence of member warping on member rotation; this shape function to describe the torsional rotation is a well-established equation that has been used by researchers like Seaburg and Carter (1996), and McGuire et al. (2000). $u(x)$ is the axial displacement along the x-axis; $v(x)$ and $w(x)$ are the lateral displacements along y- and z-axes, respectively; and.

4.2.3 Strain and stress descriptions

As shown in Figure 4.3 (a), the primary reference local-axis system is established with the origin at the centroid. The shear center is then defined at the coordinates (z_s, y_s), as illustrated in Figure 4.3(b). Displacements u, v, w at an arbitrary point on the section can be written as

$$u(x,y,z) = u_0(x) - y\frac{\partial v_0(x)}{\partial x} - z\frac{\partial w_0(x)}{\partial x} - \omega_n\frac{\partial \theta(x)}{\partial x} \tag{4.7}$$

$$v(x,y,z) = v_0(x) - (z - z_s)\theta(x) \tag{4.8}$$

$$w(x,y,z) = w_0(x) + (y - y_s)\theta(x) \tag{4.9}$$

where ω_n is the normalized unit warping constant.

The pertinent portion of the Green-Lagrange strain tensor is,

$$\varepsilon_{xx} = \varepsilon_{xx}^L + \varepsilon_{xx}^N = (\frac{\partial u_i}{\partial x}) + \frac{1}{2}\left[(\frac{\partial u_i}{\partial x})^2 + (\frac{\partial v_i}{\partial x})^2 + (\frac{\partial w_i}{\partial x})^2\right] \tag{4.10}$$

$$\varepsilon_{xy} = \varepsilon_{xy}^L + \varepsilon_{xy}^N = \frac{1}{2}\left[\frac{\partial u_i}{\partial y} + \frac{\partial v_i}{\partial x}\right] + \frac{1}{2}\left[\frac{\partial u_i}{\partial x}\frac{\partial u_i}{\partial y} + \frac{\partial v_i}{\partial x}\frac{\partial v_i}{\partial y} + \frac{\partial w_i}{\partial x}\frac{\partial w_i}{\partial y}\right] \tag{4.11}$$

$$\varepsilon_{xz} = \varepsilon_{xz}^{L} + \varepsilon_{xz}^{N} = \frac{1}{2}\left[\frac{\partial u_i}{\partial z} + \frac{\partial w_i}{\partial x}\right] + \frac{1}{2}\left[\frac{\partial u_i}{\partial x}\frac{\partial u_i}{\partial z} + \frac{\partial v_i}{\partial x}\frac{\partial v_i}{\partial z} + \frac{\partial w_i}{\partial x}\frac{\partial w_i}{\partial z}\right] \tag{4.12}$$

in which ε_{xx} is the normal strain; ε_{xy} and ε_{xz} are the strains in x-y and x-z planes, respectively; and the superscripts ^{L} and ^{N} denote the linear and nonlinear parts.

By substituting equations (4.7) -(4.9) into equations (4.10) to (4.12), the Green-Lagrange strain tensor is given as,

$$\varepsilon_{xx}^{L} = \frac{\partial u_0(x)}{\partial x} - y\frac{\partial^2 v_0(x)}{\partial x^2} - z\frac{\partial^2 w_0(x)}{\partial x^2} - \omega_n \frac{\partial^2 \theta(x)}{\partial x^2} \tag{4.13}$$

$$\begin{aligned}\varepsilon_{xx}^{N} \approx &\frac{1}{2}\left[\left(\frac{\partial v_0(x)}{\partial x}\right)^2 + \left(\frac{\partial w_0(x)}{\partial x}\right)^2\right] + \frac{1}{2}\left[\left(y-y_s\right)^2 + \left(z-z_s\right)^2\right]\left(\frac{\partial \theta(x)}{\partial x}\right)^2 \\ &+\left(y-y_s\right)\frac{\partial \theta(x)}{\partial x}\frac{\partial w_0(x)}{\partial x} - \left(z-z_s\right)\frac{\partial \theta(x)}{\partial x}\frac{\partial v_0(x)}{\partial x}\end{aligned} \tag{4.14}$$

$$\varepsilon_{xy}^{L} = \frac{1}{2}\left[-\left(z-z_s\right) - \frac{\partial \omega_n}{\partial y}\right]\frac{\partial \theta(x)}{\partial x} \tag{4.15}$$

$$\varepsilon_{xy}^{N} \approx -\frac{1}{2}\frac{\partial u_0(x)}{\partial x}\frac{\partial v_0(x)}{\partial x} + \frac{1}{2}\left[\frac{\partial w_0(x)}{\partial x} + (y-y_s)\frac{\partial \theta(x)}{\partial x}\right]\theta(x) \tag{4.16}$$

$$\varepsilon_{xz}^{L} = \frac{1}{2}\left[\left(y-y_s\right) - \frac{\partial \omega_n}{\partial z}\right]\frac{\partial \theta(x)}{\partial x} \tag{4.17}$$

$$\varepsilon_{xz}^{N} \approx -\frac{1}{2}\frac{\partial u_0(x)}{\partial x}\frac{\partial w_0(x)}{\partial x} - \frac{1}{2}\left[\frac{\partial v_0(x)}{\partial x} - (z-z_s)\frac{\partial \theta(x)}{\partial x}\right]\theta(x) \tag{4.18}$$

And, the shear strains are given as,

$$\gamma_{xy} = 2\varepsilon_{xy} = \left[-(z-z_s) - \frac{\partial \omega_n}{\partial y}\right]\frac{\partial \theta(x)}{\partial x} \tag{4.19}$$

$$\gamma_{xz} = 2\varepsilon_{xz} = \left[(y-y_s) - \frac{\partial \omega_n}{\partial z}\right]\frac{\partial \theta(x)}{\partial x} \tag{4.20}$$

where, γ_{xy} and γ_{xz} are the shear strains in x-y and x-z planes, respectively.

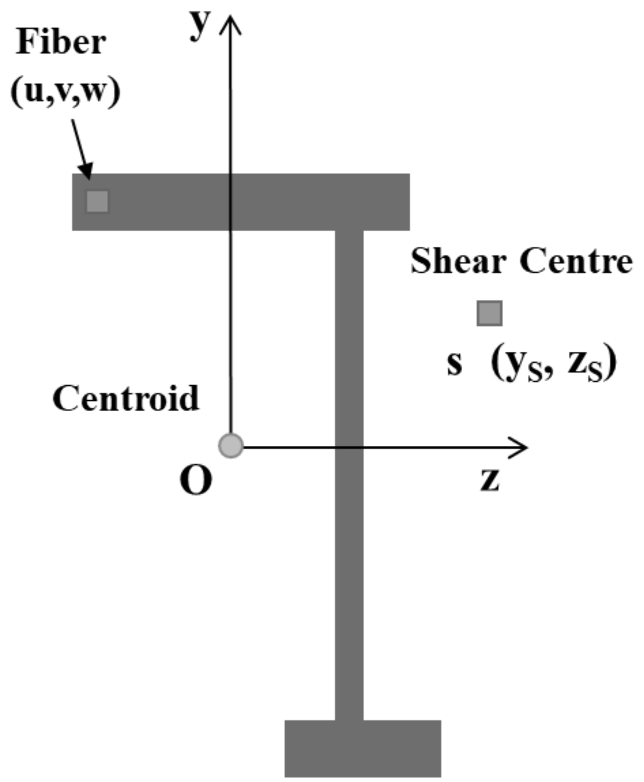

(a) Section coordinate axis

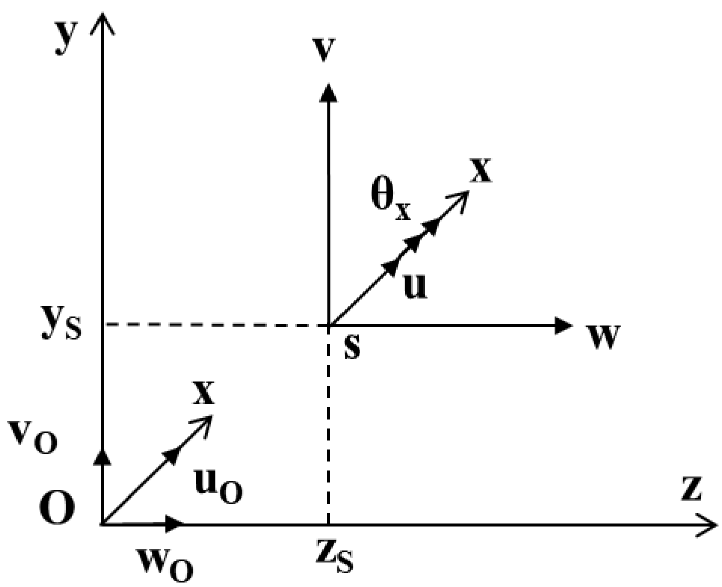

(b) Relations between the axes

Figure 4.3 Local coordinate systems

Noting that the Poisson effect (contraction in the directions transverse to the direction of normal strain) is purposely neglected for simplicity, which is done for almost all line-element formulations, the constitutive relationship is expressed by Hooke's law and given by,

$$\sigma_{xx} = E\varepsilon_{xx} \tag{4.21}$$

$$\tau_{xy} = G\gamma_{xy} \tag{4.22}$$

$$\tau_{xz} = G\gamma_{xz} \tag{4.23}$$

in which *E* is Young's modulus; and, *G* is the shear modulus.

The stresses on the section along the element length can be represented in terms of the nodal forces and moments, and are given as,

$$\sigma_{xx} = \frac{P}{A} + \left[M_{y1}\left(1-\frac{x}{L}\right) - M_{y2}\frac{x}{L}\right]\frac{z}{I_y} + \left[M_{z1}\left(1-\frac{x}{L}\right) - M_{z2}\frac{x}{L}\right]\frac{y}{I_z} + M_b\frac{\omega_n}{I_\omega} \tag{4.24}$$

$$\tau_{xy} = V_y/A = -(M_{z1} + M_{z2})/AL \tag{4.25}$$

$$\tau_{xz} = V_z/A = \left(M_{y1} + M_{y2}\right)/AL \tag{4.26}$$

where *P* is the axial force along the x-axis; M_{y1} and M_{y2} are the bending moments about the y-axis at the element ends; M_{z1} and M_{z2} are the corresponding bending moments about the z-axis; V_y and V_z are the shear forces along the y- and z-axes, respectively; and M_b is the bi-moment.

4.2.4 Total potential energy

The element stiffness matrix can be derived from the second variation of the total potential energy, which is given as,

$$\Pi = U - V \tag{4.27}$$

in which U is the strain energy stored by the element; and V is the work done by the external forces.

The strain energy U is expressed as,

$$U = \frac{1}{2}\int_V (\boldsymbol{\sigma}^T \boldsymbol{\varepsilon})\, dv = \frac{1}{2}\int_V (\boldsymbol{\varepsilon}^T \boldsymbol{D}\boldsymbol{\varepsilon})\, dv \tag{4.28}$$

where $\boldsymbol{D}$ is the constitutive matrix with relates the stresses and the strains in equations (21) to (23), and is written as,

$$\boldsymbol{D} = \begin{bmatrix} E & 0 & 0 \\ 0 & G & 0 \\ 0 & 0 & G \end{bmatrix} \tag{4.29}$$

As indicated earlier, the Green-Lagrange strain tensor is represented in linear and nonlinear parts, and given as,

$$\boldsymbol{\varepsilon} = \boldsymbol{\varepsilon_L} + \boldsymbol{\varepsilon_N} \tag{4.30}$$

After substituting equation (4.30) into equation (4.28) and neglecting high-order terms, the strain energy U can be expressed as,

$$U = \frac{1}{2}\int_V (\boldsymbol{\varepsilon_L}^T \boldsymbol{D}\boldsymbol{\varepsilon_L} + 2\boldsymbol{\sigma}^T \boldsymbol{\varepsilon_N})\, dv \tag{4.31}$$

By substituting equations (4.13) to (4.26) into equation (4.31), the total strain energy becomes,

$$U = \frac{1}{2}\int_0^L \left[EA\left(\frac{\partial u_0(x)}{\partial x}\right)^2 + EI_z\left(\frac{\partial^2 v_0(x)}{\partial x^2}\right)^2 + EI_y\left(\frac{\partial^2 w_0(x)}{\partial x^2}\right)^2\right]dx$$

$$+\frac{1}{2}\int_0^L \left[+EI_\omega\left(\frac{\partial^2 \theta(x)}{\partial x^2}\right)^2 + GJ\left(\frac{\partial \theta(x)}{\partial x}\right)^2\right]dx$$

$$+\frac{1}{2}\int_0^L P\left[\left(\frac{\partial v_0(x)}{\partial x}\right)^2 + \left(\frac{\partial w_0(x)}{\partial x}\right)^2\right]dx$$

$$+\frac{1}{2}\int_0^L P\int_A \frac{1}{A}[(y-y_s)^2 + (z-z_s)^2]dA\left(\frac{\partial \theta(x)}{\partial x}\right)^2 dx$$

$$+\int_0^L P\left[\frac{\partial w_0(x)}{\partial x}\int_A \frac{1}{A}(y-y_s)dA - \frac{\partial v_0(x)}{\partial x}\int_A \frac{1}{A}(z-z_s)dA\right]\frac{\partial \theta(x)}{\partial x}dx$$

$$+\frac{M_{y1}}{I_y}\int_0^L \left(1-\frac{x}{L}\right)\int_A \frac{1}{2}zdA\left[\left(\frac{\partial v_0(x)}{\partial x}\right)^2 + \left(\frac{\partial w_0(x)}{\partial x}\right)^2\right]dx$$

$$+\frac{M_{y1}}{I_y}\int_0^L \left(1-\frac{x}{L}\right)\int_A \frac{1}{2}[z(y-y_s)^2 + z(z-z_s)^2]dA\left(\frac{\partial \theta(x)}{\partial x}\right)^2 dx$$

$$+\frac{M_{y1}}{I_y}\int_0^L \left(1-\frac{x}{L}\right)\int_A z(y-y_s)dA\frac{\partial \theta(x)}{\partial x}\frac{\partial w_0(x)}{\partial x}dx$$

$$-\frac{M_{y1}}{I_y}\int_0^L \left(1-\frac{x}{L}\right)\int_A z(z-z_s)dA\frac{\partial \theta(x)}{\partial x}\frac{\partial v_0(x)}{\partial x}dx$$

$$-\frac{M_{y2}}{I_y}\int_0^L \frac{x}{L}\int_A \frac{1}{2}zdA\left[\left(\frac{\partial v_0(x)}{\partial x}\right)^2 + \left(\frac{\partial w_0(x)}{\partial x}\right)^2\right]dx$$

$$-\frac{M_{y2}}{I_y}\int_0^L \frac{x}{L}\int_A \frac{1}{2}[z(y-y_s)^2 + z(z-z_s)^2]dA\left(\frac{\partial \theta(x)}{\partial x}\right)^2 dx$$

$$-\frac{M_{y2}}{I_y}\int_0^L \frac{x}{L}\int_A z(y-y_s)dA\frac{\partial \theta(x)}{\partial x}\frac{\partial w_0(x)}{\partial x}dx$$

$$+\frac{M_{z1}}{I_z}\int_0^L\left(1-\frac{x}{L}\right)\int_A\frac{1}{2}ydA\left[\left(\frac{\partial v_0(x)}{\partial x}\right)^2+\left(\frac{\partial w_0(x)}{\partial x}\right)^2\right]dx$$

$$+\frac{M_{z1}}{I_z}\int_0^L\left(1-\frac{x}{L}\right)\int_A\frac{1}{2}[y(y-y_s)^2+y(z-z_s)^2]dA\left(\frac{\partial\theta(x)}{\partial x}\right)^2dx$$

$$+\frac{M_{z1}}{I_z}\int_0^L\left(1-\frac{x}{L}\right)\int_A y(y-y_s)dA\frac{\partial\theta(x)}{\partial x}\frac{\partial w_0(x)}{\partial x}dx$$

$$-\frac{M_{z1}}{I_z}\int_0^L\left(1-\frac{x}{L}\right)\int_A y(z-z_s)dA\frac{\partial\theta(x)}{\partial x}\frac{\partial v_0(x)}{\partial x}dx$$

$$-\frac{M_{z2}}{I_z}\int_0^L\frac{x}{L}\int_A\frac{1}{2}ydA\left[\left(\frac{\partial v_0(x)}{\partial x}\right)^2+\left(\frac{\partial w_0(x)}{\partial x}\right)^2\right]dx$$

$$-\frac{M_{z2}}{I_z}\int_0^L\frac{x}{L}\int_A\frac{1}{2}[y(y-y_s)^2+y(z-z_s)^2]dA\left(\frac{\partial\theta(x)}{\partial x}\right)^2dx$$

$$-\frac{M_{z2}}{I_z}\int_0^L\frac{x}{L}\int_A y(y-y_s)dA\frac{\partial\theta(x)}{\partial x}\frac{\partial w_0(x)}{\partial x}dx$$

$$+\frac{M_{z2}}{I_z}\int_0^L\frac{x}{L}\int_A y(z-z_s)dA\frac{\partial\theta(x)}{\partial x}\frac{\partial v_0(x)}{\partial x}dx$$

$$+\int_V\left[\frac{V_y}{A}\left[-\frac{\partial u_0(x)}{\partial x}\frac{\partial v_0(x)}{\partial x}+\left[\frac{\partial w_0(x)}{\partial x}+(y-y_s)\frac{\partial\theta(x)}{\partial x}\right]\theta(x)\right]\right]dv$$

$$+\int_V\left[\frac{V_z}{A}\left[-\frac{\partial u_0(x)}{\partial x}\frac{\partial w(x)}{\partial x}-\left[\frac{\partial v(x)}{\partial x}-(z-z_s)\frac{\partial\theta(x)}{\partial x}\right]\theta(x)\right]\right]dv$$

$$+\frac{M_b}{I_\omega}\int_0^L\int_A\frac{1}{2}\omega dA\left[\left(\frac{\partial v_0(x)}{\partial x}\right)^2+\left(\frac{\partial w_0(x)}{\partial x}\right)^2\right]dx$$

$$+\frac{M_b}{I_\omega}\int_0^L\int_A\frac{1}{2}[\omega(y-y_s)^2+\omega(z-z_s)^2]dA\left(\frac{\partial\theta(x)}{\partial x}\right)^2dx$$

$$+\frac{M_b}{I_\omega}\int_0^L\int_A\omega(y-y_s)dA\frac{\partial\theta(x)}{\partial x}\frac{\partial w_0(x)}{\partial x}dx$$

$$-\frac{M_b}{I_\omega}\int_0^L\int_A\omega(z-z_s)dA\frac{\partial\theta(x)}{\partial x}\frac{\partial v_0(x)}{\partial x}dx$$

(4.32)

By noting that several terms in equation (4.32), such as $\int_A ydA$ $\int_A zdA$ $\int_A \omega dA$ $\int_A yzdA$ $\int_A y\omega dA$ and $\int_A z\omega dA$, are zero, and by further neglecting additional high-order terms, the potential strain equation U can be simplified to,

$$U = \frac{1}{2}\int_0^L \left[EA\left(\frac{\partial u_0(x)}{\partial x}\right)^2 + EI_z\left(\frac{\partial^2 v_0(x)}{\partial x^2}\right)^2 + EI_y\left(\frac{\partial^2 w_0(x)}{\partial x^2}\right)^2\right]dx$$

$$+\frac{1}{2}\int_0^L \left[EI_\omega\left(\frac{\partial^2 \theta(x)}{\partial x^2}\right)^2 + GJ\left(\frac{\partial \theta(x)}{\partial x}\right)^2\right]dx$$

$$+\frac{1}{2}\int_0^L P\left[\left(\frac{\partial v_0(x)}{\partial x}\right)^2 + \left(\frac{\partial w_0(x)}{\partial x}\right)^2\right]dx + \frac{1}{2}\int_0^L Pr^2\left(\frac{\partial \theta(x)}{\partial x}\right)^2 dx$$

$$+\frac{1}{2}\int_0^L P\left[2y_s\frac{\partial w_0(x)}{\partial x} - 2z_s\frac{\partial v_0(x)}{\partial x}\right]\frac{\partial \theta(x)}{\partial x}dx$$

$$+\int_0^L M_{y1}\frac{L-x}{L}\frac{\partial \theta(x)}{\partial x}\left[\frac{\partial v_0(x)}{\partial x} + \frac{1}{2}\beta_y\frac{\partial \theta(x)}{\partial x}\right]dx$$

$$-\int_0^L M_{y2}\frac{x}{L}\frac{\partial \theta(x)}{\partial x}\left[\frac{\partial v_0(x)}{\partial x} + \frac{1}{2}\beta_y\frac{\partial \theta(x)}{\partial x}\right]dx$$

$$+\int_0^L M_{z1}\frac{L-x}{L}\frac{\partial \theta(x)}{\partial x}\left[\frac{\partial w_0(x)}{\partial x} + \frac{1}{2}\beta_z\frac{\partial \theta(x)}{\partial x}\right]dx$$

$$-\int_0^L M_{z2}\frac{x}{L}\frac{\partial \theta(x)}{\partial x}\left[\frac{\partial w_0(x)}{\partial x} + \frac{1}{2}\beta_z\frac{\partial \theta(x)}{\partial x}\right]dx$$

$$+\int_0^L \left[V_y\left(\theta(x)\frac{\partial w_0(x)}{\partial x} - \frac{\partial u_0(x)}{\partial x}\frac{\partial v_0(x)}{\partial x}\right)\right]dx$$

$$\int_0^L \left[-V_z\left(\theta(x)\frac{\partial v_0(x)}{\partial x} + \frac{\partial u_0(x)}{\partial x}\frac{\partial w_0(x)}{\partial x}\right)\right]dx$$

$$+\frac{1}{2}\int_0^L M_b\beta_\omega\left(\frac{\partial \theta(x)}{\partial x}\right)^2 dx$$

(4.33)

where A is the cross-section area; I_y and I_z are the second moment of areas about the y- and z-axes; $I_\omega = \int_A \omega_n{}^2 dA$ is the warping section constant; J is the torsional rigidity; β_y, β_z, and β_ω are the Wagner coefficients, and $r^2 = \left(I_y + I_z\right)/A$.

4.2.5 Linear and geometric stiffness matrices

The linear and nonlinear stiffness matrices are obtained from the second variation of the total potential energy Π given in equation (27), which results in

$$\delta^2 \Pi = \frac{\delta^2 \Pi}{\delta u_i \delta u_j} \delta u_i \delta u_j = (\boldsymbol{k_L} + \boldsymbol{k_G} + \boldsymbol{k_U})\Delta \boldsymbol{u} - \Delta \boldsymbol{f} = 0 \tag{4.34}$$

$(i, j =$1-14)

where $\Delta\boldsymbol{u}$ is the vector of the incremental nodal displacements; $\Delta\boldsymbol{f}$ is the vector of the incremental nodal forces; $\boldsymbol{k_L}$ and $\boldsymbol{k_G}$ are well established linear and geometric stiffness matrices given by McGuire et al.(2000) for an element with a doubly-symmetric cross section; and, $\boldsymbol{k_U}$ is an additional geometric stiffness matrix (given in below) that accounts for the effects caused by the section being non-symmetric. For a doubly symmetrical shape, the additional geometric stiffness term $\boldsymbol{k_U}$ would reduce to a null matrix.

$$[k_U]=\begin{bmatrix} 0 & 0 & 0 & 0 & 0 & 0 & 0 & 0 & 0 & 0 & 0 & 0 & 0 & 0 \\ & 0 & 0 & k^u_{2,4} & 0 & 0 & k^u_{2,7} & 0 & 0 & 0 & k^u_{2,11} & 0 & 0 & k^u_{2,14} \\ & & 0 & k^u_{3,4} & 0 & 0 & k^u_{3,7} & 0 & 0 & 0 & k^u_{3,11} & 0 & 0 & k^u_{3,14} \\ & & & k^u_{4,4} & k^u_{4,5} & k^u_{4,6} & k^u_{4,7} & 0 & k^u_{4,9} & k^u_{4,10} & k^u_{4,11} & k^u_{4,12} & k^u_{4,13} & k^u_{4,14} \\ & & & & 0 & 0 & k^u_{5,7} & 0 & 0 & 0 & k^u_{5,11} & 0 & 0 & k^u_{5,14} \\ & & & & & 0 & k^u_{6,7} & 0 & 0 & 0 & k^u_{6,11} & 0 & 0 & k^u_{6,14} \\ & S. & & & & & k^u_{7,7} & 0 & k^u_{7,9} & k^u_{7,10} & k^u_{7,11} & k^u_{7,12} & k^u_{7,13} & k^u_{7,14} \\ & & & & & & & 0 & 0 & 0 & 0 & 0 & 0 & 0 \\ & & & Y. & & & & & 0 & 0 & k^u_{9,11} & 0 & 0 & k^u_{9,14} \\ & & & & & & & & & 0 & k^u_{10,11} & 0 & 0 & k^u_{10,14} \\ & & & & & M. & & & & & k^u_{11,11} & k^u_{11,12} & k^u_{11,13} & k^u_{11,14} \\ & & & & & & & & & & & 0 & 0 & k^u_{12,14} \\ & & & & & & & & & & & & 0 & k^u_{13,14} \\ & & & & & & & & & & & & & k^u_{14,14} \end{bmatrix} \tag{4.35}$$

in which,

$$k^u_{4,4}=\frac{M_{y1}(10z_s-6\beta_y)}{10L}+\frac{M_{y2}(10z_s+6\beta_y)}{10L}+\frac{M_{z1}(-10y_s+6\beta_z)}{10L}$$

$$+\frac{M_{z2}(-10y_s-6\beta_z)}{10L}+\frac{6M_b\beta_\omega}{5L}$$

$$k^u_{7,7}=-\frac{M_{y1}L\beta_y}{10}+\frac{M_{y2}L\beta_y}{30}+\frac{M_{z1}L\beta_z}{10}-\frac{M_{z2}L\beta_z}{30}+\frac{2M_bL\beta_\omega}{15}$$

$$k^u_{11,11}=\frac{M_{y1}(-10z_s-6\beta_y)}{10L}+\frac{M_{y2}(-10z_s+6\beta_y)}{10L}+\frac{M_{z1}(10y_s+6\beta_z)}{10L}$$

$$+\frac{M_{z2}(10y_s-6\beta_z)}{10L}+\frac{6M_b\beta_\omega}{5L}$$

$$k^u_{14,14}=-\frac{M_{y1}L\beta_y}{30}+\frac{M_{y2}L\beta_y}{10}+\frac{M_{z1}L\beta_z}{30}-\frac{M_{z2}L\beta_z}{10}+\frac{2M_bL\beta_\omega}{15}$$

$$k^u_{4,11}=\frac{3M_{y1}\beta_y}{5L}-\frac{3M_{y2}\beta_y}{5L}-\frac{3M_{z1}\beta_z}{5L}+\frac{3M_{z2}\beta_z}{5L}-\frac{6M_b\beta_\omega}{5L}$$

$$k_{7,14}^{u} = \frac{LM_{y1}\beta_y}{60} - \frac{LM_{y2}\beta_y}{60} - \frac{LM_{z1}\beta_z}{60} + \frac{LM_{z2}\beta_z}{60} - \frac{LM_b\beta_\omega}{30}$$

$$k_{4,5}^{u} = k_{4,12}^{u} = k_{7,10}^{u} = k_{10,14}^{u} = -\frac{Py_s}{10}$$

$$k_{4,7}^{u} = \frac{M_{y2}\beta_y}{10} - \frac{M_{z2}\beta_z}{10} + \frac{M_b\beta_\omega}{10}$$

$$k_{3,7}^{u} = k_{3,14}^{u} = k_{5,11}^{u} = k_{11,12}^{u} = \frac{Py_s}{10}$$

$$k_{4,14}^{u} = -\frac{M_{y1}\beta_y}{10} + \frac{M_{z1}\beta_z}{10} + \frac{M_b\beta_\omega}{10}$$

$$k_{6,11}^{u} = k_{7,9}^{u} = k_{9,14}^{u} = k_{11,13}^{u} = \frac{Pz_s}{10}$$

$$k_{7,11}^{u} = -\frac{M_{y2}\beta_y}{10} + \frac{M_{z2}\beta_z}{10} - \frac{M_b\beta_\omega}{10}$$

$$k_{11,14}^{u} = \frac{M_{y1}\beta_y}{10} - \frac{M_{z1}\beta_z}{10} - \frac{M_b\beta_\omega}{10}$$

$$k_{2,4}^{u} = k_{9,11}^{u} = -\frac{6Pz_s}{5L}$$

$$k_{2,7}^{u} = k_{2,14}^{u} = -\frac{Pz_s}{10}$$

$$k_{3,4}^{u} = k_{10,11}^{u} = \frac{6Py_s}{5L}$$

$$k_{4,6}^{u} = k_{4,13}^{u} = -\frac{Pz_s}{10}$$

$$k_{2,11}^{u} = \frac{6Pz_s}{5L}$$

$$k_{5,14}^{u} = k_{7,12}^{u} = \frac{LPy_s}{30}$$

$$k_{5,7}^{u} = k_{12,14}^{u} = -\frac{2}{15}LPy_s$$

$$k_{6,7}^{u} = k_{13,14}^{u} = -\frac{2}{15}LPz_s$$

$$k_{3,11}^{u} = k_{4,10}^{u} = -\frac{6Py_s}{5L}$$

$$k_{6,14}^{u} = k_{7,13}^{u} = \frac{LPz_s}{30}$$

$$k_{4,9}^{u} = \frac{6Pz_s}{5L}$$

4.2.6 Element tangent stiffness matrix

With the exception of the axial displacement, all DOFs in the element formulation are defined with reference to the shear center axis, and hence, will need to be transformed to reference the centroidal axis. To achieve this, the element tangent stiffness can be computed as,

$$\boldsymbol{k_E} = \boldsymbol{T}(\boldsymbol{k_L} + \boldsymbol{k_G} + \boldsymbol{k_U})\boldsymbol{T}^T \tag{4.36}$$

where the transformation matrix $\boldsymbol{T}$ is introduced per McGuire et al. (2000) and written as,

$$
\boldsymbol{T} = \begin{bmatrix}
1 & 0 & 0 & 0 & 0 & 0 & 0 & 0 & 0 & 0 & 0 & 0 & 0 & 0 \\
0 & 1 & 0 & 0 & 0 & 0 & 0 & 0 & 0 & 0 & 0 & 0 & 0 & 0 \\
0 & 0 & 1 & 0 & 0 & 0 & 0 & 0 & 0 & 0 & 0 & 0 & 0 & 0 \\
0 & -z_s & y_s & 1 & 0 & 0 & 0 & 0 & 0 & 0 & 0 & 0 & 0 & 0 \\
0 & 0 & 0 & 0 & 1 & 0 & 0 & 0 & 0 & 0 & 0 & 0 & 0 & 0 \\
0 & 0 & 0 & 0 & 0 & 1 & 0 & 0 & 0 & 0 & 0 & 0 & 0 & 0 \\
0 & 0 & 0 & 0 & 0 & 0 & 1 & 0 & 0 & 0 & 0 & 0 & 0 & 0 \\
0 & 0 & 0 & 0 & 0 & 0 & 0 & 1 & 0 & 0 & 0 & 0 & 0 & 0 \\
0 & 0 & 0 & 0 & 0 & 0 & 0 & 0 & 1 & 0 & 0 & 0 & 0 & 0 \\
0 & 0 & 0 & 0 & 0 & 0 & 0 & 0 & 0 & 1 & 0 & 0 & 0 & 0 \\
0 & 0 & 0 & 0 & 0 & 0 & 0 & 0 & -z_s & y_s & 1 & 0 & 0 & 0 \\
0 & 0 & 0 & 0 & 0 & 0 & 0 & 0 & 0 & 0 & 0 & 1 & 0 & 0 \\
0 & 0 & 0 & 0 & 0 & 0 & 0 & 0 & 0 & 0 & 0 & 0 & 1 & 0 \\
0 & 0 & 0 & 0 & 0 & 0 & 0 & 0 & 0 & 0 & 0 & 0 & 0 & 1
\end{bmatrix} \tag{4.37}
$$

in which z_s and y_s are the coordinates of the shear center, as shown in Figure 4.3 (a).

4.3 Improved Gaussian Line Element for Members under Large Torsion

Above section proposed an element formulation derived based on the nonsymmetrical section assumption, where the Wagner effects and the noncoincidence of the shear center and centroid of the nonsymmetric sections are directly considered. An improved Gaussian line element will be given in this section for the large-deflection analysis of steel members with nonsymmetric sections subjected to torsion.

In recent years, a few researchers consider the Wagner effects, resulting from the offset between the shear center and the centroid, in the beam-column element formulation based on the nonsymmetric section assumption. For example, Mohri and his associates (Bourihane et al. 2016; Elkaimbillah et al. 2021) have conducted the nonlinear and stability analyses of open-section beams under different loading conditions by a refined beam-column element. Alsafadie et al. (2010) propose a corotational mixed finite element formulation for the beams with generic cross-section. Rasmussen and his colleagues (Hancock and Rasmussen 2016, 2020) develop an advanced beam-column element with seven degrees of freedoms (DOFs) at each element node, allowing a misalignment of the shear center and the centroid.

Though recent research has made a significant contribution to simulate such complex behaviors of members with nonsymmetric sections, these beam-column elements still have some problems when the member is loaded under large torsion. When the member is under torsion, the inclined angle between the cross-section axes and the element local axes is varied along the element length due to the twisting, causing difficulty in summating the cross-section stiffness to form the element stiffness matrix. The conventional warping line (CWL) element assumes the inclined angle between the cross-section and the element local axes is constant along the element length, as seen in Figure 4.4, and that requires a certain number of CWL elements to simulate one structural member under torsion.

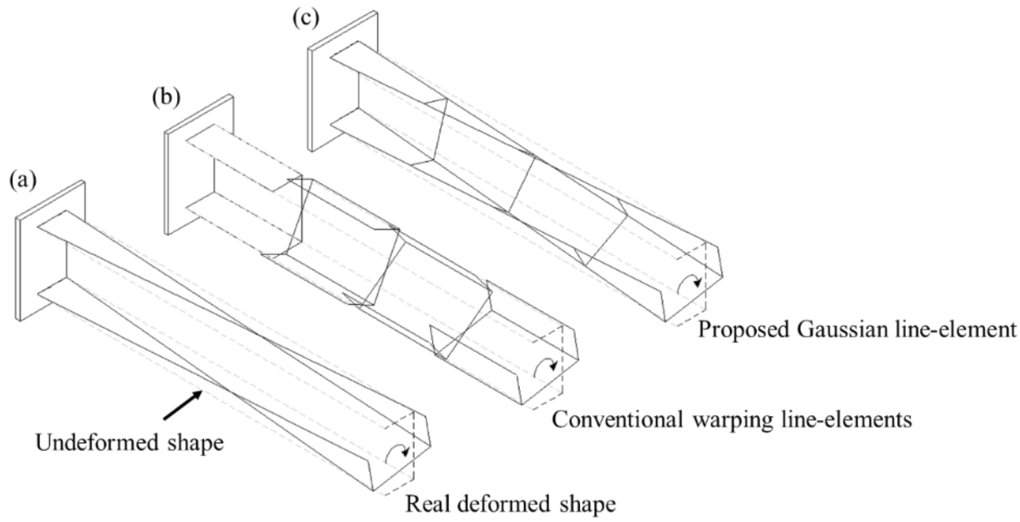

Figure 4.4 Illustrations of the simulations using different elements

For improving the numerical efficiency by using less element for a member, this section proposes a new element, namely Gaussian line element (GLE), which includes a twisting angle (θ) along the member length in the element formulation. The Gaussian-Quadrature method is introduced to summate the varied cross-section properties caused by twisting to form the element stiffness matrix. The proposed GLE element can describe the element deformations with large twisting along the member length more accurately, as shown in Figure 4.4.

In this section, the element formulation with derivations for the GLE element are given with details. The Gaussian-Quadrature method is elaborated, and the numerical implementation is illustrated. Finally, a series of benchmark examples are provided for demonstrating the accuracy and efficiency of the proposed method.

4.3.1 Element reference axes

Similarly, two additional warping degrees of freedom (one at each end), will be included in the proposed beam-column formulation to consider the warping behaviors of nonsymmetric members. Accordingly, a 14-DOF beam-column element is proposed, and the deformations and forces in the element local axis are shown in Figure 4.5.

It should be noted that, since the proposed element is twisted along the element length, the actual centroid axis will be a spiral line. A cross-centroid axis, which is a straight line connecting the section centroids at element ends, is defined for the element local axis. To simplify the formulations, only the nodal displacements along the element length are specified with reference to the cross-centroid axis, while other DOFs are defined relative to the shear center axis (Figure 4.5).

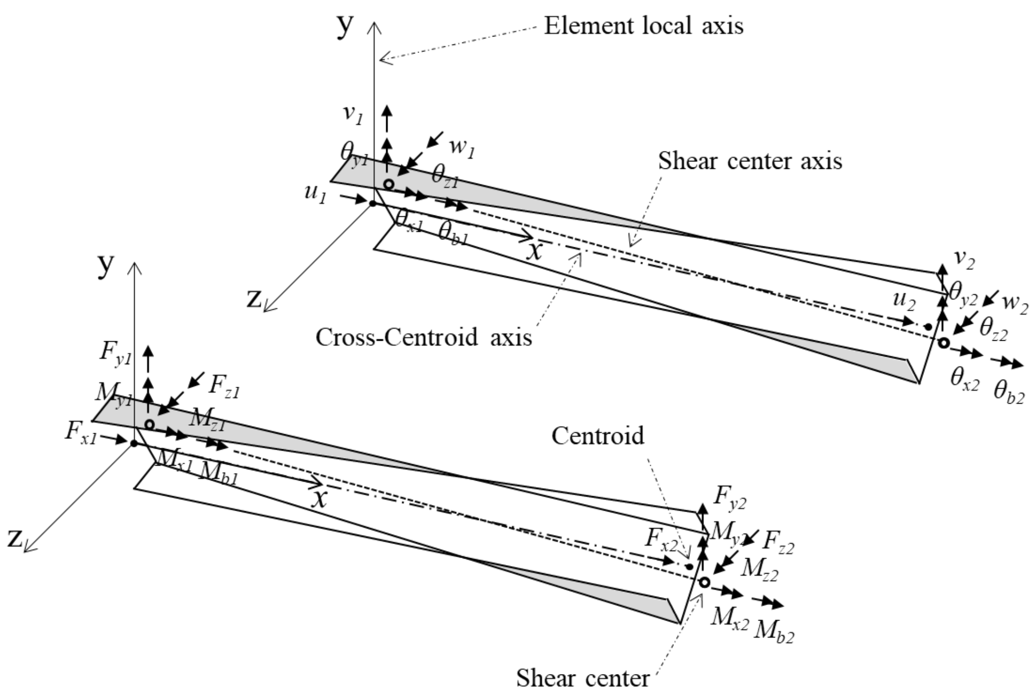

Figure 4.5 Illustrations of the deformations and forces in the element local axes

Deformations along the element can be described by utilizing detailed shape functions for the displacements and twist rotation, which are available in the literature (e.g. McGuire, et al. 2000). Since the twisting deformations along the element length (*x*) are supposed to be calculated at each internal gauss point along the element, the third-order polynomial displacement function is adopted and given for easy reference as follows,

$$\theta(x) = \left(x - \frac{2x^2}{L} + \frac{x^3}{L^2}\right)\theta_{b1} + \left(-\frac{x^2}{L} + \frac{x^3}{L^2}\right)\theta_{b2} \\ + \left(1 - \frac{3x^2}{L^2} + \frac{2x^3}{L^3}\right)\theta_{x1} + \left(\frac{3x^2}{L^2} - \frac{2x^3}{L^3}\right)\theta_{x2} \tag{4.38}$$

in which $\theta(x)$ is the element twisting angle along the element length x, θ_{b1}.and θ_{b2} are the warping at the element starting and ending points, and θ_{x1} and θ_{x2} are the corresponding twisting angle.

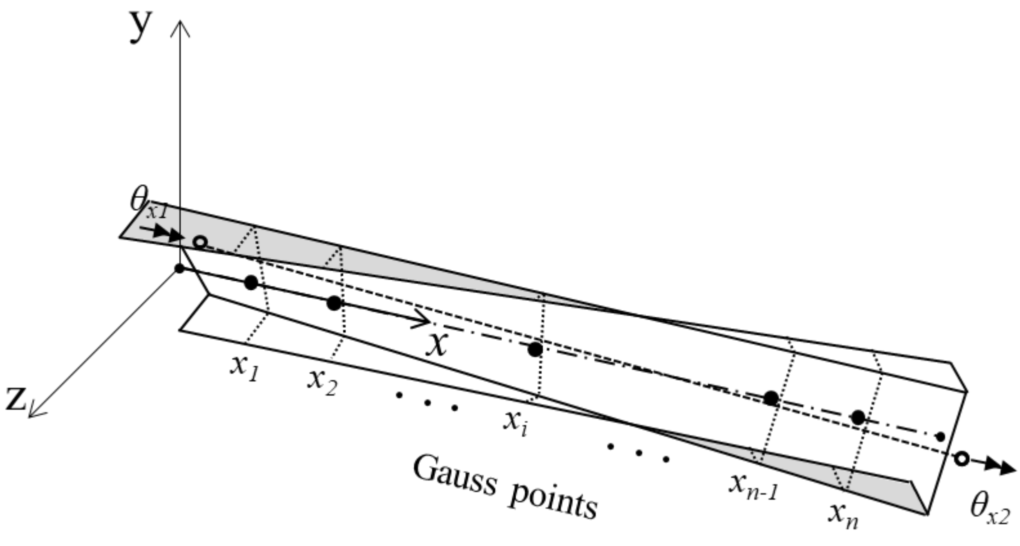

Figure 4.6 Gauss points along the element length

4.3.2 Total potential energy function

The total potential energy function of a beam-column element can be written as,

$$\Pi = U - V \tag{4.39}$$

where, Π is the total potential energy, V is the work done by the external forces, and U is the strain energy stored by the element, which was previously formulated above and is given as follows,

$$U \approx \frac{1}{2}\int_0^L \left[EA\left(\frac{\partial u_0(x)}{\partial x}\right)^2 + EI_\omega\left(\frac{\partial^2\theta(x)}{\partial x^2}\right)^2 + GJ\left(\frac{\partial\theta(x)}{\partial x}\right)^2\right]dx$$

$$+\frac{1}{2}\int_0^L P\left[\left(\frac{\partial v_0(x)}{\partial x}\right)^2 + \left(\frac{\partial w_0(x)}{\partial x}\right)^2\right]dx$$

$$+M_{y1}\int_0^L \frac{L-x}{L}\frac{\partial\theta(x)}{\partial x}\frac{\partial v_0(x)}{\partial x}dx - M_{y2}\int_0^L \frac{x}{L}\frac{\partial\theta(x)}{\partial x}\frac{\partial v_0(x)}{\partial x}dx$$

$$+M_{z1}\int_0^L \frac{L-x}{L}\frac{\partial\theta(x)}{\partial x}\frac{\partial w_0(x)}{\partial x}dx - M_{z2}\int_0^L \frac{x}{L}\frac{\partial\theta(x)}{\partial x}\frac{\partial w_0(x)}{\partial x}dx$$

$$-\frac{M_{z1}+M_{z2}}{L}\int_0^L \left[\left(\theta(x)\frac{\partial w_0(x)}{\partial x} - \frac{\partial u_0(x)}{\partial x}\frac{\partial v_0(x)}{\partial x}\right)\right]dx$$

$$-\frac{M_{y1}+M_{y2}}{L}\int_0^L \left[\left(\theta(x)\frac{\partial v_0(x)}{\partial x} + \frac{\partial u_0(x)}{\partial x}\frac{\partial w_0(x)}{\partial x}\right)\right]dx$$

$$+\frac{1}{2}\int_0^L \left[EI_{z\theta}\left(\frac{\partial^2 v_0(x)}{\partial x^2}\right)^2 + EI_{y\theta}\left(\frac{\partial^2 w_0(x)}{\partial x^2}\right)^2\right]dx$$

$$+\frac{1}{2}\int_0^L M_b\beta_{\omega\theta}\left(\frac{\partial\theta(x)}{\partial x}\right)^2 dx + \frac{1}{2}\int_0^L Pr^2\left(\frac{\partial\theta(x)}{\partial x}\right)^2 dx$$

$$+\frac{1}{2}\int_0^L P\left[2y_{s\theta}\frac{\partial w_0(x)}{\partial x} - 2z_{s\theta}\frac{\partial v_0(x)}{\partial x}\right]\frac{\partial\theta(x)}{\partial x}dx$$

$$+M_{y1}\int_0^L \frac{L-x}{L}\frac{\partial\theta(x)}{\partial x}\left[\frac{1}{2}\beta_{y\theta}\frac{\partial\theta(x)}{\partial x}\right]dx - M_{y2}\int_0^L \frac{x}{L}\frac{\partial\theta(x)}{\partial x}\left[\frac{1}{2}\beta_{y\theta}\frac{\partial\theta(x)}{\partial x}\right]dx$$

$$+M_{z1}\int_0^L \frac{L-x}{L}\frac{\partial\theta(x)}{\partial x}\left[\frac{1}{2}\beta_{z\theta}\frac{\partial\theta(x)}{\partial x}\right]dx - M_{z2}\int_0^L \frac{x}{L}\frac{\partial\theta(x)}{\partial x}\left[\frac{1}{2}\beta_{z\theta}\frac{\partial\theta(x)}{\partial x}\right]dx$$

(4.40)

where, $u_0(x)$, $v_0(x)$, and $w_0(x)$, describe the axial displacement along the longitudinal x-axis and the lateral deflections with respect to the element's local y- and z-axes, respectively; E is Young's modulus and G is the shear modulus; I_ω and J are, respectively, the warping constant and torsion rigidity; P, M_y, and M_z denote the generalized nodal axial force and bending moments about the element's local y- and z-axes, respectively; and M_b represents the bi-moment. While, $y_{s\theta}$, $z_{s\theta}$, $I_{y\theta}$, $I_{z\theta}$, $\beta_{y\theta}$, $\beta_{z\theta}$, and $\beta_{\omega\theta}$ are section properties along the element after the twisting, which are supposed to be calculated at different Gauss points along the element length (Figure 4.6), and r^2 can be calculated by, $r^2 = \frac{I_{y\theta}+I_{z\theta}}{A} + y_{s\theta}^2 + z_{s\theta}^2$.

4.3.3 Gaussian-Quadrature method

When the element twists, section properties such as the coordinates of the shear center with respect to the centroid ($y_{s\theta}$ and $z_{s\theta}$) might be not constant along the element length, thereby making the explicit expression of Equation (4.40) very complicated. Thus, Gaussian quadrature method is adopted to summate the varied cross-section properties. Several internal Gauss points, as shown in Figure 4.6, are introduced, where n is the number of Gauss points. The section properties at each point will be calculated to integrate the energy function. The location of each point is determined by the Gaussian quadrature method, and the section twisting angle of each point can be generated according to the shape interpolation functions (equation (4.38)). Accordingly, the strain energy stored by the element can be simplified as given below.

$$U \approx \frac{1}{2}\int_0^L \left[EA\left(\frac{\partial u_0(x)}{\partial x}\right)^2 + EI_\omega\left(\frac{\partial^2\theta(x)}{\partial x^2}\right)^2 + GJ\left(\frac{\partial\theta(x)}{\partial x}\right)^2\right]dx$$
$$+\frac{1}{2}\int_0^L P\left[\left(\frac{\partial v_0(x)}{\partial x}\right)^2 + \left(\frac{\partial w_0(x)}{\partial x}\right)^2\right]dx$$
$$+\int_0^L M_{y1}\frac{L-x}{L}\frac{\partial\theta(x)}{\partial x}\frac{\partial v_0(x)}{\partial x}dx - \int_0^L M_{y2}\frac{x}{L}\frac{\partial\theta(x)}{\partial x}\frac{\partial v_0(x)}{\partial x}dx$$
$$+\int_0^L M_{z1}\frac{L-x}{L}\frac{\partial\theta(x)}{\partial x}\frac{\partial w_0(x)}{\partial x}dx - \int_0^L M_{z2}\frac{x}{L}\frac{\partial\theta(x)}{\partial x}\frac{\partial w_0(x)}{\partial x}dx$$
$$-\frac{M_{z1}+M_{z2}}{L}\int_0^L \left[\left(\theta(x)\frac{\partial w_0(x)}{\partial x} - \frac{\partial u_0(x)}{\partial x}\frac{\partial v_0(x)}{\partial x}\right)\right]dx$$
$$-\frac{M_{y1}+M_{y2}}{L}\int_0^L \left[\left(\theta(x)\frac{\partial v_0(x)}{\partial x} + \frac{\partial u_0(x)}{\partial x}\frac{\partial w_0(x)}{\partial x}\right)\right]dx$$
$$+\frac{L}{2}\sum_{i=1}^{n} H_i\left[EI_{z\theta i}\left(\frac{\partial^2 v_0(x_i)}{\partial x^2}\right)^2 + EI_{y\theta i}\left(\frac{\partial^2 w_0(x_i)}{\partial x^2}\right)^2\right]$$
$$+\frac{L}{2}\sum_{i=1}^{n} H_i M_b \beta_{\omega\theta i}\left(\frac{\partial\theta(x)}{\partial x}\right)^2 + \frac{1}{2}\int_0^L Pr^2\left(\frac{\partial\theta(x)}{\partial x}\right)^2 dx$$
$$+\frac{L}{4}\sum_{i=1}^{n} H_i P\left[2y_{s\theta i}\frac{\partial w_0(x_i)}{\partial x} - 2z_{s\theta i}\frac{\partial v_0(x_i)}{\partial x}\right]\frac{\partial\theta(x_i)}{\partial x}$$
$$+\frac{L}{2}\sum_{i=1}^{n} H_i M_{y1}\frac{L-x_i}{L}\frac{\partial\theta(x_i)}{\partial x}\left[\frac{1}{2}\beta_{y\theta i}\frac{\partial\theta(x_i)}{\partial x}\right]$$
$$-\frac{L}{2}\sum_{i=1}^{n} H_i M_{y2}\frac{x_i}{L}\frac{\partial\theta(x_i)}{\partial x}\left[\frac{1}{2}\beta_{y\theta i}\frac{\partial\theta(x_i)}{\partial x}\right]$$
$$+\frac{L}{2}\sum_{i=1}^{n} H_i M_{z1}\frac{L-x_i}{L}\frac{\partial\theta(x_i)}{\partial x}\left[\frac{1}{2}\beta_{z\theta i}\frac{\partial\theta(x_i)}{\partial x}\right]$$

$$-\frac{L}{2}\sum_{i=1}^{n} H_i M_{z2} \frac{x_i}{L} \frac{\partial\theta(x_i)}{\partial x} \left[\frac{1}{2}\beta_{z\theta i} \frac{\partial\theta(x_i)}{\partial x}\right]$$

(4.41)

where, H_i is the weight factor of the i^{th} Gauss point determined by the Gaussian quadrature method; x_i is the coordinate of the i^{th} Gauss point as shown in Figure 4.6; and n is the number of Gauss points.

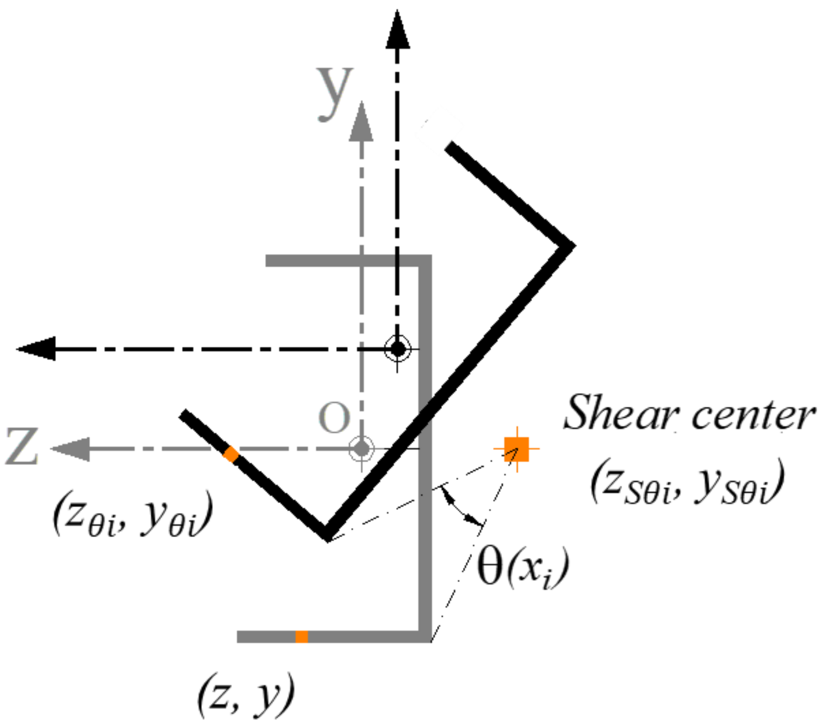

Figure 4.7 An illustration of the section rotation at a general Gauss point

4.3.4 Section properties for each Gauss point

To consider the non-coincidence between the centroid and the shear center for the nonsymmetric section as well as the Wagner effects more accurately, the section properties including the coordinates of the shear center and Wagner coefficients at each Gauss point should be calculated. As given in the shape interpolation functions in Equation (4.38), the element twisting angle is a function of the location x along the element length. For a general Gauss point located at the element length of x_i, the section rotation is shown in Figure 4.7, and the updated coordinates ($z_{s\theta}$, $y_{s\theta}$) of any point (z, y) of the section can be calculated by,

$$y_{\theta i} = y\cos[\theta(x_i)] + z\sin[\theta(x_i)] \tag{4.42}$$

$$z_{\theta i} = z\cos[\theta(x_i)] - y\sin[\theta(x_i)] \tag{4.43}$$

and the section properties at the i^{th} Gauss point can be generated by

$$y_{s\theta i} = y_s\cos[\theta(x_i)] + z_s\sin[\theta(x_i)] \tag{4.44}$$

$$z_{s\theta i} = z_s\cos[\theta(x_i)] - y_s\sin[\theta(x_i)] \tag{4.45}$$

$$I_{y\theta i} = \int_A z_{\theta i}^2\, dA \tag{4.46}$$

$$I_{z\theta i} = \int_A y_{\theta i}^2\, dA \tag{4.47}$$

$$\beta_{y\theta i} = \frac{1}{I_{y\theta i}}\int_A \left(z_{\theta i}^3 + z_{\theta i}y_{\theta i}^2\right)dA - 2z_{s\theta i} \tag{4.48}$$

$$\beta_{z\theta i} = \frac{1}{I_{z\theta i}}\int_A \left(y_{\theta i}^3 + y_{\theta i}z_{\theta i}^2\right)dA - 2y_{s\theta i} \tag{4.49}$$

$$\beta_{\omega\theta i} = \frac{1}{I_\omega}\int_A \omega_n\left(y_{\theta i}^2 + z_{\theta i}^2\right)dA \tag{4.50}$$

By substituting equations (4.42) and (4.43) to (4.44) -(4.50), it gives.

$$I_{y\theta i} = \frac{I_y + I_z}{2} + \frac{I_y - I_z}{2}\cos[2\theta(x_i)] + I_{yz}\sin[2\theta(x_i)] \tag{4.51}$$

$$I_{z\theta i} = \frac{I_y + I_z}{2} - \frac{I_y - I_z}{2}\cos[2\theta(x_i)] - I_{yz}\sin\big(2\theta(x_i)\big) \tag{4.52}$$

$$\beta_{y\theta i} = \frac{\alpha_y \cos[2\theta(x_i)] - \alpha_z \sin[2\theta(x_i)]}{I_{y\theta i}} - 2z_{s\theta i} \tag{4.53}$$

$$\beta_{z\theta i} = \frac{\alpha_z \cos[2\theta(x_i)] + \alpha_y \sin[2\theta(x_i)]}{I_{z\theta i}} - 2z_{y\theta i} \tag{4.54}$$

$$\beta_{\omega\theta i} = \beta_\omega \tag{4.55}$$

where, $\alpha_y = \big(\beta_y + 2z_s\big)I_y$, and $\alpha_z = (\beta_z + 2y_s)I_z$.

4.3.5 Tangent stiffness matrix

According to the minimal total potential energy principle, the linear and geometric stiffness matrices can be formulated by the second variation of Equation(4.39),

$$\delta^2\Pi = \frac{\delta^2\Pi}{\delta u_i \delta u_j}\delta u_i \delta u_j = (\boldsymbol{k_L} \odot \boldsymbol{\xi_L} + \boldsymbol{k_G} + \boldsymbol{k_U} \odot \boldsymbol{\xi_U})\Delta\boldsymbol{u} - \Delta\boldsymbol{f} = 0 \tag{4.56}$$

$(i, j =$1-14)

where $\odot$ indicates the Hadamard product, $\boldsymbol{k_U}$ is the additional geometric stiffness matrix which accounts for the effects caused by the section being non-symmetric given above; $\boldsymbol{\xi_L}$ and $\boldsymbol{\xi_U}$ are the modification matrices for $\boldsymbol{k_L}$ and $\boldsymbol{k_U}$, respectively. They are generated by employing 5 Gauss points and given below.

$$[\xi_L] = \begin{bmatrix}
1 & 1 & 1 & 1 & 1 & 1 & 1 & 1 & 1 & 1 & 1 & 1 & 1 & 1 \\
. & \omega_{z1} & 1 & 1 & 1 & \omega_{z2} & 1 & 1 & -\omega_{z1} & 1 & 1 & 1 & \omega_{z3} & 1 \\
. & & \omega_{y1} & 1 & -\omega_{y2} & 1 & 1 & 1 & 1 & -\omega_{y1} & 1 & -\omega_{y3} & 1 & 1 \\
. & & & 1 & 1 & 1 & 1 & 1 & 1 & 1 & 1 & 1 & 1 & 1 \\
. & & & & \omega_{y4} & 1 & 1 & 1 & 1 & \omega_{y2} & 1 & \omega_{y5} & 1 & 1 \\
. & & & & & \omega_{z4} & 1 & 1 & -\omega_{z2} & 1 & 1 & 1 & \omega_{z5} & 1 \\
. & S. & & & & & 1 & 1 & 1 & 1 & 1 & 1 & 1 & 1 \\
. & & & & & & & 1 & 1 & 1 & 1 & 1 & 1 & 1 \\
. & & & Y. & & & & & \omega_{z1} & 1 & 1 & 1 & -\omega_{z3} & 1 \\
. & & & & & & & & & \omega_{y1} & 1 & \omega_{y3} & 1 & 1 \\
. & & & & & M. & & & & & 1 & 1 & 1 & 1 \\
. & & & & & & & & & & & \omega_{y6} & 1 & 1 \\
. & & & & & & & & & & & & \omega_{z6} & 1 \\
 & & & & & & & & & & & & & 1
\end{bmatrix}$$

where, $\omega_{aj} = \frac{\sum_{i=1}^{5} \alpha_{ji}\, I_{ai}}{I_a}$; for example, $\omega_{z1} = \frac{\sum_{i=1}^{5} \alpha_{1i}\, I_{zi}}{I_z}$**;** and α_{ki} are the coefficients for the modification matrix $\boldsymbol{\xi_L}$ given in Table 4.1**.**

Table 4.1 Coefficients in modification matrix $\boldsymbol{\xi}_{\boldsymbol{L}}$

Gauss point ID *i*	**1**	**2**	**3**	**4**	**5**
x_i	0.046910*L*	0.230765*L*	0.5*L*	0.769235*L*	0.953090*L*
H_i	0.23692689	0.47862867	0.56888889	0.47862867	0.23692689
α_{1i}	0.29183333	0.2081673	0	0.2081673	0.2918333
α_{2i}	0.18448419	0.0793034	0	0.3370307	0.3991825
α_{3i}	0.39918247	0.3370307	0	0.0793034	0.1844842
α_{4i}	0.08746668	0.0226586	0.0711109	0.4092486	0.4095143
α_{5i}	0.37851663	0.1925929	-0.1422217	0.1925929	0.3785166
α_{6i}	0.40951369	0.4092484	0.0711108	0.0226587	0.0874669

Note: *L* is the length of the element.

Table 4.2 Coefficients in modification matrix $\boldsymbol{\xi_U}$

Gauss point ID *i*	**1**	**2**	**3**	**4**	**5**
x_i	0.046910L	0.230765L	0.5L	0.769235L	0.953090L
H_i	0.23692689	0.47862867	0.56888889	0.47862867	0.23692689
χ_{1i}	0.00710404	0.2262292	0.5333333	0.2262292	0.007104
χ_{2i}	0.02771685	0.769185	1.066665	-0.60331	-0.260255
χ_{3i}	-0.260255	-0.60331	1.066665	0.769185	0.0277169
χ_{4i}	0.0067587	0.163452	0.1333335	0.1005574	0.5958975
χ_{5i}	0.2538495	0.512817	-0.533334	0.512817	0.2538495
χ_{6i}	0.5958975	0.1005574	0.1333335	0.163452	0.0067587
χ_{7i}	0.0006665	0.1044117	0.5333333	0.3480467	0.0135416
χ_{8i}	0.01354158	0.3480467	0.5333333	0.1044117	0.0006665
χ_{9i}	0.0013002	0.1775005	0.533335	-0.464088	-0.2480465
χ_{10i}	0.02641665	0.59168	0.533335	-0.1392235	-0.0122086
χ_{11i}	-0.0122086	-0.1392235	0.533335	0.59168	0.0264167
χ_{12i}	0.2480465	0.464088	-0.53334	-0.1775	-0.0013
χ_{13i}	0.00042273	0.050292	0.088889	0.1031365	0.75726
χ_{14i}	0.02576653	0.5029316	0.2666668	0.0928205	0.1118146
χ_{15i}	0.11181456	0.0928205	0.2666668	0.5029316	0.0257665
χ_{16i}	0.75726	0.1031365	0.088889	0.050292	0.0004227

Note: L is the length of the element.

$$
[\xi_U] = \begin{bmatrix}
1 & 1 & 1 & 1 & 1 & 1 & 1 & 1 & 1 & 1 & 1 & 1 & 1 & 1 \\
 & 1 & 1 & \xi^U_{2,4} & 1 & 1 & \xi^U_{2,7} & 1 & 1 & 1 & \xi^U_{2,11} & 1 & 1 & \xi^U_{2,14} \\
 & & 1 & \xi^U_{3,4} & 1 & 1 & \xi^U_{3,7} & 1 & 1 & 1 & \xi^U_{3,11} & 1 & 1 & \xi^U_{3,4} \\
 & & & \xi^U_{4,4} & \xi^U_{4,5} & \xi^U_{4,6} & \xi^U_{4,7} & 1 & \xi^U_{4,9} & \xi^U_{4,10} & \xi^U_{4,11} & \xi^U_{4,12} & \xi^U_{4,13} & \xi^U_{4,14} \\
 & & & & 1 & 1 & \xi^U_{5,7} & 1 & 1 & 1 & \xi^U_{5,11} & 1 & 1 & \xi^U_{5,14} \\
 & & & & & 1 & \xi^U_{6,7} & 1 & 1 & 1 & \xi^U_{6,11} & 1 & 1 & \xi^U_{6,14} \\
 & S. & & & & & \xi^U_{7,7} & 1 & \xi^U_{7,9} & \xi^U_{7,10} & \xi^U_{7,11} & \xi^U_{7,12} & \xi^U_{7,13} & \xi^U_{7,14} \\
 & & & & & & & 1 & 1 & 1 & 1 & 1 & 1 & 1 \\
 & & & Y. & & & & & 1 & 1 & \xi^U_{9,11} & 1 & 1 & \xi^U_{9,14} \\
 & & & & & & & & & 1 & \xi^U_{10,11} & 1 & 1 & \xi^U_{10,14} \\
 & & & & & M. & & & & & \xi^U_{11,11} & \xi^U_{11,12} & \xi^U_{11,13} & \xi^U_{11,14} \\
 & & & & & & & & & & & 1 & 1 & \xi^U_{12,14} \\
 & & & & & & & & & & & & 1 & \xi^U_{13,14} \\
 & & & & & & & & & & & & & \xi^U_{14,14}
\end{bmatrix}
$$

in which,

$$\xi^U_{2,4} = -\xi^U_{2,11} = -\xi^U_{4,9} = \xi^U_{9,11} = \frac{\sum_{i=1}^{5} -\chi_{1i} z_{si}}{z_s}$$

$$\xi^U_{2,7} = \xi^U_{4,6} = -\xi^U_{6,11} = -\xi^U_{7,9} = \frac{\sum_{i=1}^{5} -\chi_{2i} z_{si}}{z_s}$$

$$\xi^U_{2,14} = \xi^U_{4,13} = -\xi^U_{9,14} = -\xi^U_{11,13} = \frac{\sum_{i=1}^{5} \chi_{3i} z_{si}}{z_s}$$

$$\xi^U_{3,4} = -\xi^U_{3,11} = -\xi^U_{4,10} = \xi^U_{10,11} = \frac{\sum_{i=1}^{5} \chi_{1i} y_{si}}{y_s}$$

$$\xi^U_{3,7} = -\xi^U_{4,5} = \xi^U_{5,11} = -\xi^U_{7,10} = \frac{\sum_{i=1}^{5} \chi_{2i} y_{si}}{y_s}$$

$$\xi^U_{3,14} = \xi^U_{4,12} = -\xi^U_{10,14} = \xi^U_{11,12} = \frac{\sum_{i=1}^{5} -\chi_{3i} y_{si}}{y_s}$$

$$\xi^U_{5,7} = \frac{\sum_{i=1}^{5} -\chi_{4i} y_{si}}{y_s} \qquad \xi^U_{5,14} = \xi^U_{7,12} = \frac{\sum_{i=1}^{5} \chi_{5i} y_{si}}{y_s} \qquad \xi^U_{12,14} = \frac{\sum_{i=1}^{5} -\chi_{6i} y_{si}}{y_s}$$

$$\xi^U_{6,7} = \frac{\sum_{i=1}^{5} -\chi_{4i} z_{si}}{z_s} \qquad \xi^U_{6,14} = \xi^U_{7,13} = \frac{\sum_{i=1}^{5} \chi_{5i} z_{si}}{z_s} \qquad \xi^U_{13,14} = \frac{\sum_{i=1}^{5} -\chi_{6i} z_{si}}{z_s}$$

$$\xi^U_{4,4} = \xi^U_{4,11} = \xi^U_{7,14} = \xi^U_{11,11}$$
$$= \frac{\sum_{i=1}^{5} \chi_{7i}\left(-\beta_{yi} + \beta_{zi}\right) + \sum_{i=1}^{5} \chi_{8i}\left(\beta_{yi} - \beta_{zi}\right) + 2\beta_\omega}{2\beta_\omega}$$

$$\xi^U_{4,7} = \xi^U_{7,11} = \frac{\sum_{i=1}^{5} \chi_{9i}\left(-\beta_{yi} + \beta_{zi}\right) + \sum_{i=1}^{5} \chi_{10i}\left(\beta_{yi} - \beta_{zi}\right) + \beta_\omega}{\beta_y - \beta_z + \beta_\omega}$$

$$\xi^U_{4,14} = \xi^U_{11,14} = \frac{\sum_{i=1}^{5} -\chi_{11i}\left(\beta_{yi} - \beta_{zi}\right) + \sum_{i=1}^{5} -\chi_{12i}\left(-\beta_{yi} + \beta_{zi}\right) + \beta_\omega}{-\beta_y + \beta_z + \beta_\omega}$$

$$\xi^U_{7,7} = \frac{\sum_{i=1}^{5} \chi_{13i}\left(-2\beta_{yi} + 2\beta_{zi}\right) + \sum_{i=1}^{5} \chi_{14i}\left(\beta_{yi} - \beta_{zi}\right) + 2\beta_\omega}{-\beta_y + \beta_z + 2\beta_\omega}$$

$$\xi^U_{14,14} = \frac{\sum_{i=1}^{5} \chi_{15i}\left(2\beta_{yi} - 2\beta_{zi}\right) + \sum_{i=1}^{5} \chi_{16i}\left(-\beta_{yi} + \beta_{zi}\right) + 2\beta_\omega}{\beta_y - \beta_z + 2\beta_\omega}$$

where, χ_{ki} are the coefficients for the modification matrix $\boldsymbol{\xi_U}$ given in Table 4.2**.**

Similarly, because the nodal displacements along the element length (u_1 and u_2 in Figure 4.5) are determined with reference to the cross-centroid axis, while other DOFs are defined relative to the shear center axis, a transformation matrix $\boldsymbol{\Gamma}$ should be introduced for the element tangent stiffness.

$$\boldsymbol{k_E} = \boldsymbol{\Gamma}(\boldsymbol{k_L} \odot \boldsymbol{\xi_L} + \boldsymbol{k_G} + \boldsymbol{k_U} \odot \boldsymbol{\xi_U})\boldsymbol{\Gamma}^T \tag{4.57}$$

where, $\boldsymbol{\Gamma}$ is given as,

$$\boldsymbol{\Gamma} = \begin{bmatrix} 1 & 0 & 0 & 0 & 0 & 0 & 0 & 0 & 0 & 0 & 0 & 0 & 0 & 0 \\ 0 & 1 & 0 & 0 & 0 & 0 & 0 & 0 & 0 & 0 & 0 & 0 & 0 & 0 \\ 0 & 0 & 1 & 0 & 0 & 0 & 0 & 0 & 0 & 0 & 0 & 0 & 0 & 0 \\ 0 & -z_{s\theta 1} & y_{s\theta 1} & 1 & 0 & 0 & 0 & 0 & 0 & 0 & 0 & 0 & 0 & 0 \\ 0 & 0 & 0 & 0 & 1 & 0 & 0 & 0 & 0 & 0 & 0 & 0 & 0 & 0 \\ 0 & 0 & 0 & 0 & 0 & 1 & 0 & 0 & 0 & 0 & 0 & 0 & 0 & 0 \\ 0 & 0 & 0 & 0 & 0 & 0 & 1 & 0 & 0 & 0 & 0 & 0 & 0 & 0 \\ 0 & 0 & 0 & 0 & 0 & 0 & 0 & 1 & 0 & 0 & 0 & 0 & 0 & 0 \\ 0 & 0 & 0 & 0 & 0 & 0 & 0 & 0 & 1 & 0 & 0 & 0 & 0 & 0 \\ 0 & 0 & 0 & 0 & 0 & 0 & 0 & 0 & 0 & 1 & 0 & 0 & 0 & 0 \\ 0 & 0 & 0 & 0 & 0 & 0 & 0 & 0 & -z_{s\theta 2} & y_{s\theta 2} & 1 & 0 & 0 & 0 \\ 0 & 0 & 0 & 0 & 0 & 0 & 0 & 0 & 0 & 0 & 0 & 1 & 0 & 0 \\ 0 & 0 & 0 & 0 & 0 & 0 & 0 & 0 & 0 & 0 & 0 & 0 & 1 & 0 \\ 0 & 0 & 0 & 0 & 0 & 0 & 0 & 0 & 0 & 0 & 0 & 0 & 0 & 1 \end{bmatrix} \tag{4.58}$$

in which, $z_{s\theta}$ and $y_{s\theta}$ are the coordinates of the shear centers, and the subscripts 1 and 2 denote the element starting and ending points, respectively.

4.4 Modified Updated Lagrangian Approach

The system global stiffness matrix needs to be assembled via the summation of the element stiffness matrix. The transformation matrix $\boldsymbol{L}$, per McGuire et al. (2000), is used to transform the element's local axes to a single global system before the assembly, which is updated during analysis at each load increment. Given that the transformation matrix $\boldsymbol{\Gamma}$ is utilised for transforming all DOFs to reference the centroidal axis, the global tangent stiffness matrix is expressed as

$$\boldsymbol{K_g} = \sum_{i=1}^{NELEM} \boldsymbol{L}\, \boldsymbol{k_{Ei}}\, \boldsymbol{L^T} \tag{4.59}$$

where $\boldsymbol{K_g}$ is the total global stiffness matrix, and NELEM is the total number of elements constructing the whole model. Afterwards, the node displacements are calculated, and the node coordinates as well as the element length are updated. As a sequence of the above, the element incremental force can be computed as

$$\Delta\boldsymbol{R}_G = \sum_{i=1}^{NELEM} \boldsymbol{k_E}\Delta\boldsymbol{u} \tag{4.60}$$

where $\boldsymbol{k_E}$ is the element tangent stiffness matrix, and $\Delta\boldsymbol{u}$ is the element’s end displacement. Then, the total element’s end forces are updated by

$$\boldsymbol{R}_G = \boldsymbol{R}_G + \Delta\boldsymbol{R}_G \tag{4.61}$$

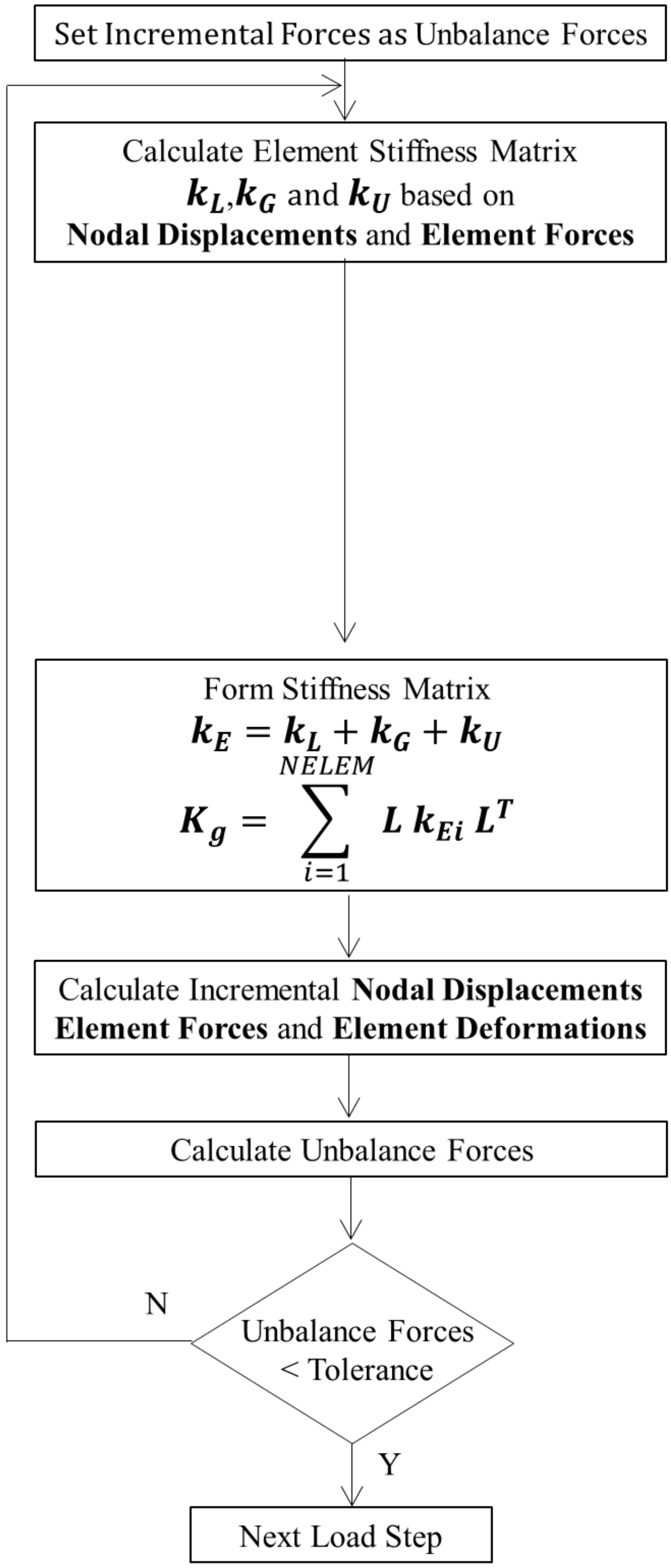

(a) Traditional UL approach

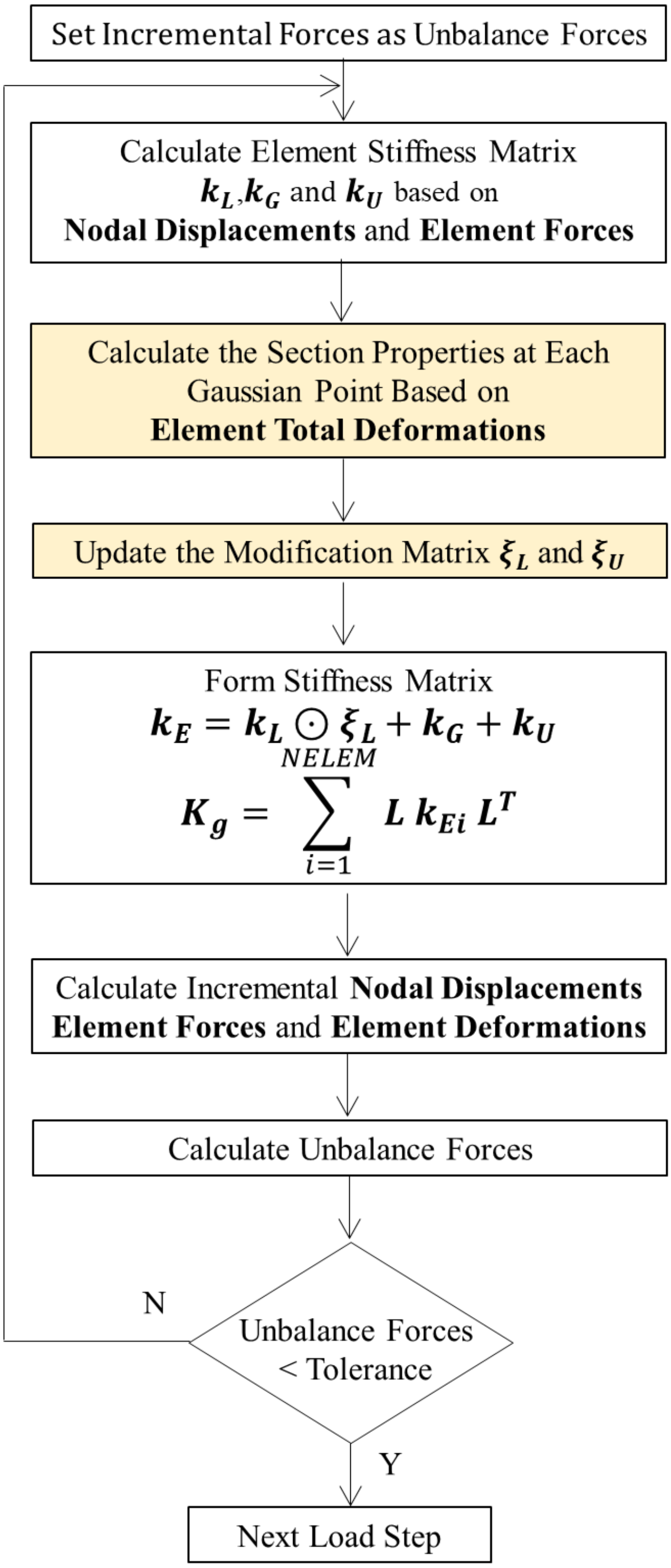

(b) Modified UL approach

Figure 4.8 The traditional UL and the proposed modified approaches

In this research, the traditional UL approach is adopted of the line element proposed in Section 4.2 and a modified UL method is proposed for the GLE element given in Section 4.3. Besides, an incremental-iterative analysis using Newton-Raphson method is used for tracing the large deflections of the beam-column element. In the traditional UL approach, the equilibrium conditions of each incremental step are based on the previous configuration during the analysis procedure. In each step, the stiffness matrix is updated based on the nodal displacements and element forces generated in the last step (Figure 4.8 a). Herein, when adopting the Gaussian quadrature method, the element deformations (twisting) are also taken into consideration to capture the large-deflection behavior of the elements (Figure 4.8 b). A comparison between the traditional UL approach and that presented in the current study is reflected in Figure 4.8.

4.5 Verification Examples

Two groups of examples are introduced to verify the accuracy and efficiency of the proposed refined warping line element and improved Gaussian line element. Lateral torsional buckling analyses of beams and large deflection analyses of members in different loading conditions are conducted. But one thing that should be noted is that this chapter focused on the new elements and the behaviors on the element level; more examples of the application of the proposed method for the space frames are given in Chapter 6.

4.5.1 Verification of the refined line element

Example 1: Lateral-torsional buckling of a beam subjected to uniform bending

This example is intended to provide results of lateral-torsional buckling (LTB) analyses of a series of simply-supported beams with a mono-symmetric-I section. Warping is assumed continuous along the length of the member and unrestrained (free) at its ends. The section dimensions are given in Figure 3.4 (a), and the section properties are taken from Table 3.1. Six beams with different lengths, including 2.0m, 3.0m, 4.0m, 5.0m, 6.0m, and 7.0m, under positive and negative bending moments are studied as shown Figure 4.9. The Young's and shear modulus are 210 GPa and 80.77 GPa, respectively. The closed-form solutions for computing the LTB bending moments are provided by Galambos (2016), and given by,

$$M_{cr}^{+} = \frac{\pi^2 E I_y}{L^2}\left\{\frac{\beta_z}{2} + \sqrt{\left(\frac{\beta_z}{2}\right)^2 + \left[\frac{I_\omega}{I_y} + \frac{GJL^2}{EI_y\pi^2}\right]}\right\} \tag{4.62}$$

$$M_{cr}^{-} = \frac{\pi^2 E I_y}{L^2}\left\{-\frac{\beta_z}{2} + \sqrt{\left(\frac{\beta_z}{2}\right)^2 + \left[\frac{I_\omega}{I_y} + \frac{GJL^2}{EI_y\pi^2}\right]}\right\} \tag{4.63}$$

Bifurcation analyses of this beam using 2 and 4 elements to model the member are conducted, and the buckling moments are compared with those calculated by the closed-form solutions. Results are given in Table 4.3 and Table 4.4 for the applied positive and negative bending moments, respectively. It is observed that the proposed element formulations can accurately predict the buckling strengths of this mono-symmetric-I section beam, where the error of using four elements to model the member is less than 0.1%. It is also encouraging to see percent errors within 0.75% when using only two elements.

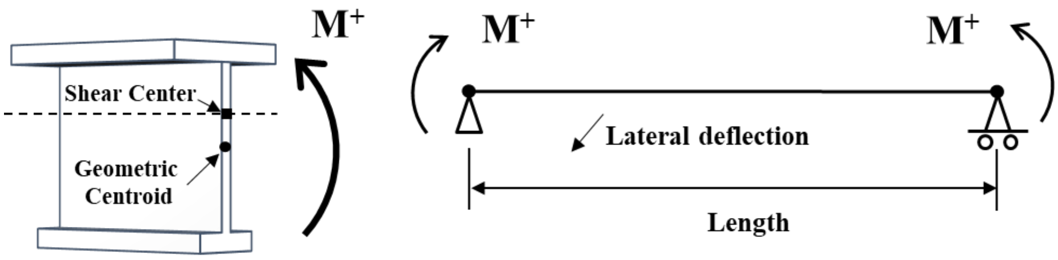

(a) Under positive bending moment

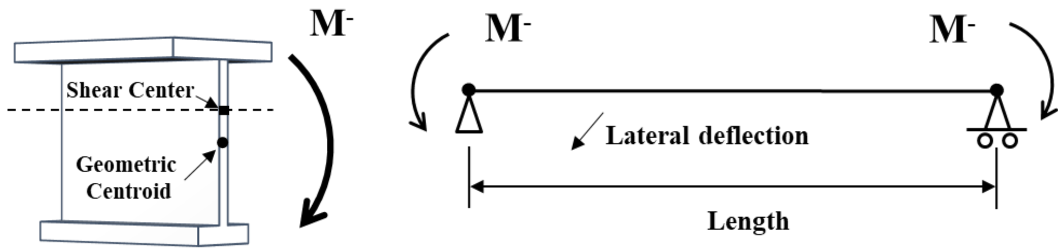

(b) Under negative bending moment

Figure 4.9 Simply-supported beams with mono-symmetric-I sections

Table 4.3 Buckling strengths under positive bending moment

Length (m)	***Theoretical Solution***	***Present Study***			
		2 Elements	**Difference**	**4 Elements**	**Difference**
	Moment (kNm)	**Moment (kNm)**		**Moment (kNm)**	
2.0	459.8	463.0	0.71%	460.0	0.057%
3.0	221.2	222.7	0.66%	221.3	0.053%
4.0	136.0	136.9	0.62%	136.1	0.050%
5.0	95.40	95.96	0.59%	95.44	0.047%
6.0	72.46	72.87	0.56%	72.49	0.044%
7.0	58.01	58.32	0.54%	58.04	0.042%

Table 4.4 Buckling strengths under negative bending moment

Length (m)	***Theoretical Solution***	***Present Study***			
		2 Elements	**Difference**	**4 Elements**	**Difference**
	Moment (kNm)	**Moment (kNm)**		**Moment (kNm)**	
2.0	94.52	94.97	0.48%	94.53	0.018%
3.0	58.85	59.07	0.38%	58.86	0.015%
4.0	44.71	44.86	0.38%	44.72	0.014%
5.0	36.96	37.07	0.30%	36.96	0.014%
6.0	31.88	31.97	0.29%	31.88	0.015%
7.0	28.19	28.28	0.29%	28.198	0.016%

Example 2: Lateral torsional buckling of a beam subjected to a concentrated force at mid-span

Three-dimensional analyses of the slender mono-symmetric-I-beam given in the previous example are conducted, in which a concentrated force P is applied at the mid-span of the beam. Two load directions are considered as shown in Figure 4.10, including downward (positive) and upward (negative). In both cases, the load is applied at the centroid of the section and is assumed to always remain vertical. The beam is modelled by ten of the proposed elements within the analyses. An out-of-plane initial imperfection, represented by a sine curve with an amplitude of $L/1000$, is included.

Plots of both the in-plane and out-of-plane deflections at the mid-span are provided in Figure 4.11 and Figure 4.12 for the downward and upward cases, respectively. Results generated by large-deflection warping-beam and shell element analyses from ADINA (Bathe 1999) are provided for comparison and validation. When the applied load is small, the results by all three methods are nearly identical.

When compared to the most accurate shell-element results at larger loads, however, the proposed element tends to produce more accurate predictions in buckling and post-buckling deformations than those given by the warping beam elements in ADINA. These comparisons are only intended to illustrate the accuracy and feasibility of using the proposed element in studying the behavior of slender members comprised of thin-walled sections. They are not intended to provide precise benchmark values and percent errors.

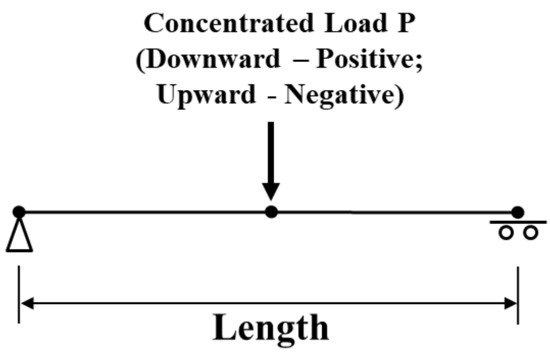

(a) Concentrated point load applied at the mid-span

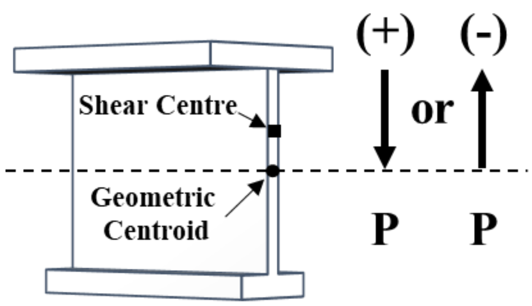

(b) Loads on the geometric centroid

Figure 4.10 The mono-symmetric-I-beam under a concentrated load

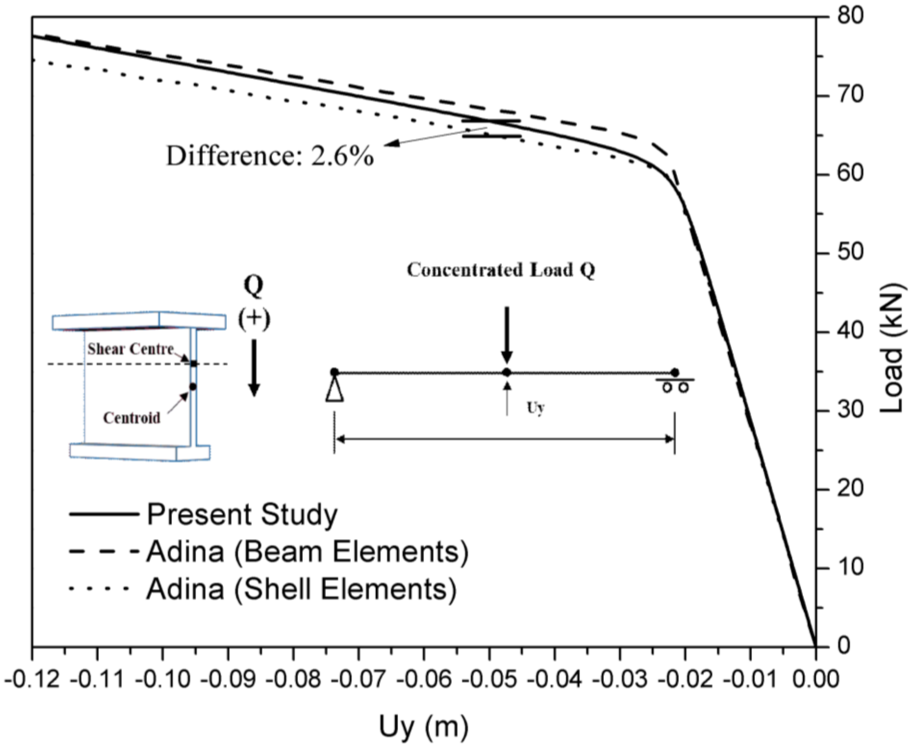

(a) In-plane deflection – Uy

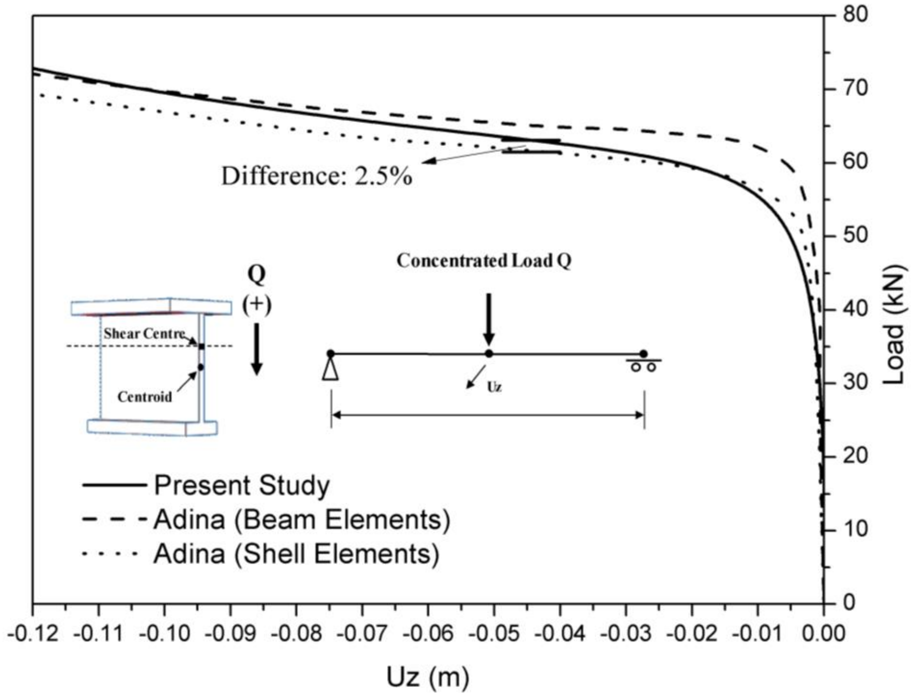

(b) Out-of-plane deflection – Uz

Figure 4.11 Comparison results of the mon-symmetric I-beam (Downward)

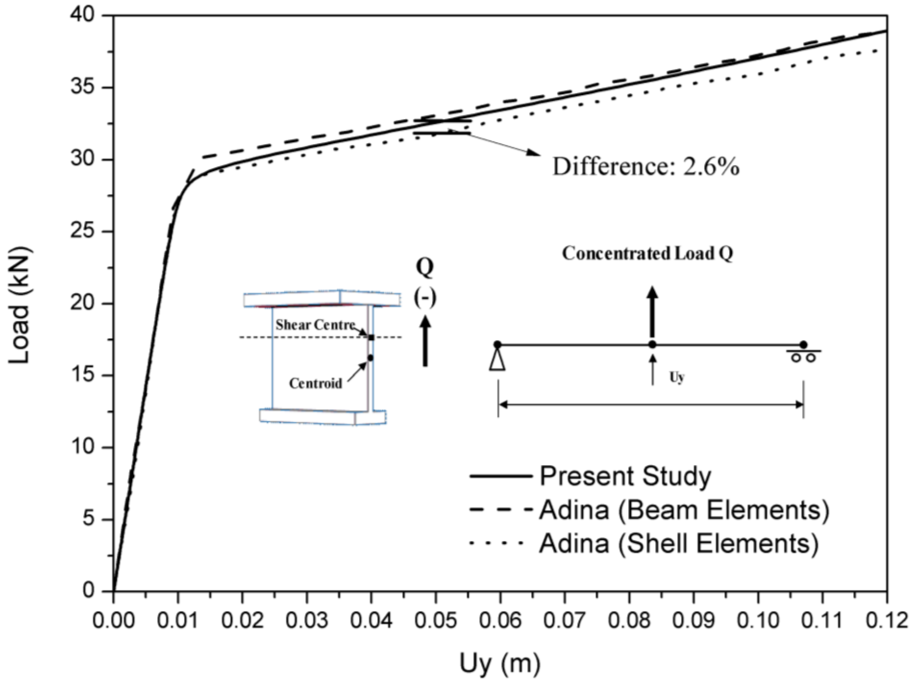

(a) In-plane deflection - Uy

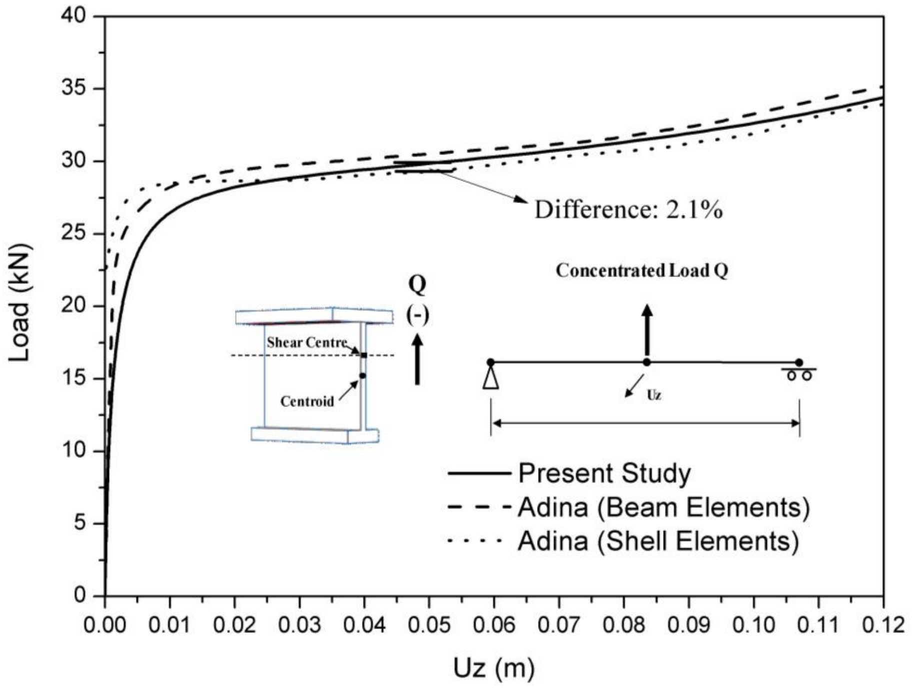

(b) Out-of-plane deflection - Uz

Figure 4.12 Comparison results of the non-symmetric I-beam (Upward)

Example 3: Large deflection analysis of a cantilevered beam

To validate the accuracy of the proposed method further in tracing the large-deflection behavior of slender, thin-walled members, a cantilevered beam constructed from a channel section is presented (Figure 4.13). The beam length is 9m with one end fully restrained (all 7 DOFs) and the other end free. Warping is assumed to be continuous along the length of the member, fixed at the supported end, and free at the other end. The material properties are E = 210 GPa and G = 80.77 GPa. A concentrated point load is applied at the centroid of the free end of the cantilevered beam. The beam is modelled by 20 of the proposed elements. The section properties, including the Wagner coefficients, are calculated by the above method and are given in Table 4.5. For comparison, analysis results employing the warping beam and shell elements within ADINA are provided. Based on load-displacement plots provided in Figure 4.14, the accuracy of the proposed element is further established.

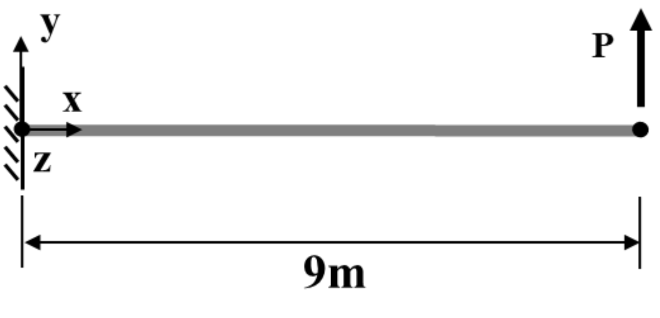

(a) Beam

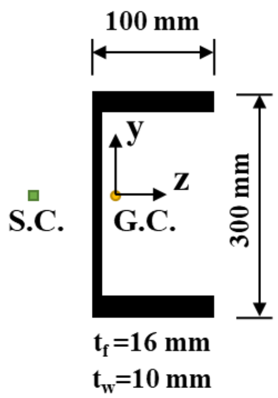

(b) Section

Figure 4.13 The cantilever column with channel section

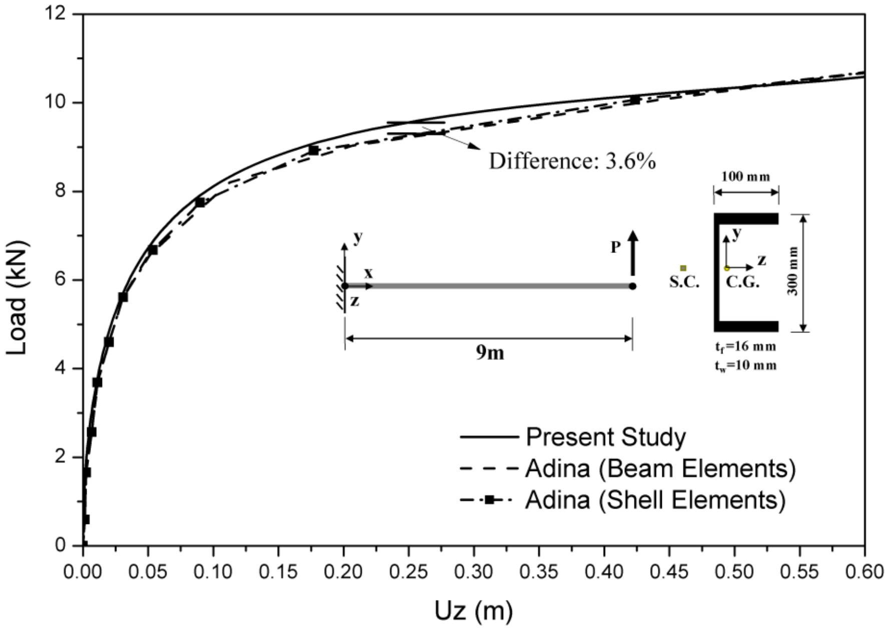

(a) Out-of-plane deflection - Uz

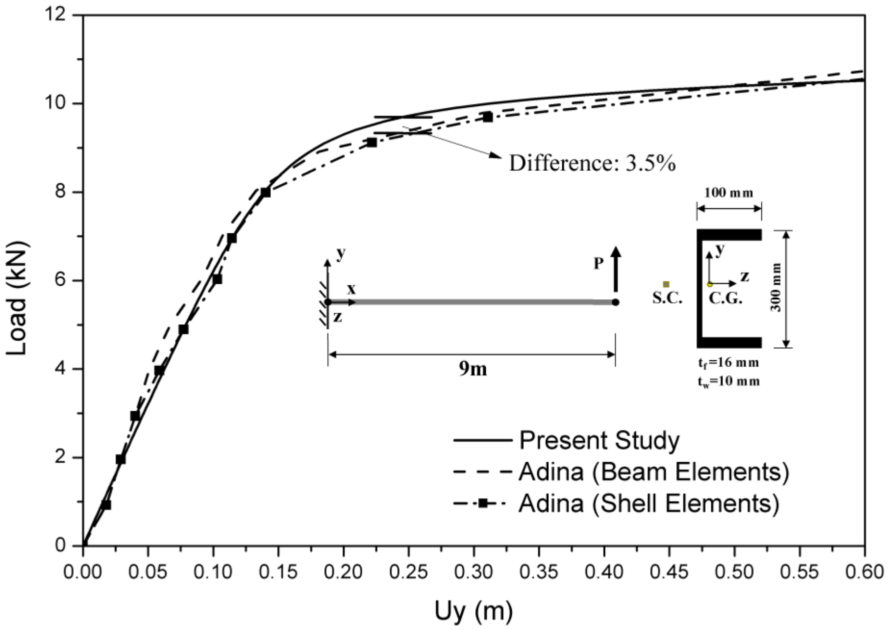

(b) In-plane deflection - Uy

Figure 4.14 Load-deflections of the cantilevered channel column

Table 4.5 Section properties of the channel section

A	Iy	Iz	J	I_w
m^2	m^4	m^4	m^4	m^6
5.88x10^{-3}	5.64 x10^{-6}	8.06 x10^{-5}	3.32 x10^{-7}	7.89 x10^{-8}
y_c	z_c	β_y	β_z	β_w
m	m	m	m	
0	-0.0607	0.315	0	0

4.5.2 Verification of the improved GLE element

To validate the accuracy and efficiency of the proposed GLE element, three groups of steel members with symmetric, monosymmetric, and nonsymmetric sections are studied. The Young's modulus and Poisson's ratio are 210 GPa and 0.3, respectively. An incremental-iterative scheme, utilizing Newton's method, is adopted for the analysis models. Consequently, results from the CWL element proposed by Liu et al. (2018) and those based on the proposed GLE element are given for comparison. The results obtained from the CWL element with 32 elements to model one member are considered representative solutions. Furthermore, the fourth example demonstrates the application of the proposed GLE element for frame analysis; accordingly, the large deflection effect at the structure level is successfully captured.

Example 1: Member with Symmetric Section

In the first example, a cantilever beam with symmetric I-section is studied. The depth is 200 mm, and the width 100 mm. The flange thickness and web thickness are 10 mm and 5 mm, respectively. The member length is 8 m, and the detailed boundary and loading conditions are shown in Figure 4.15. The analysis results generated by the CWL element using four, eight and 32 elements are generated for comparisons. Herein, results obtained from 32 CWL elements are provided as benchmark solutions, and consequently, Table 4.6 summarises the maximum displacements obtained from the CWL elements and proposed GLE elements.

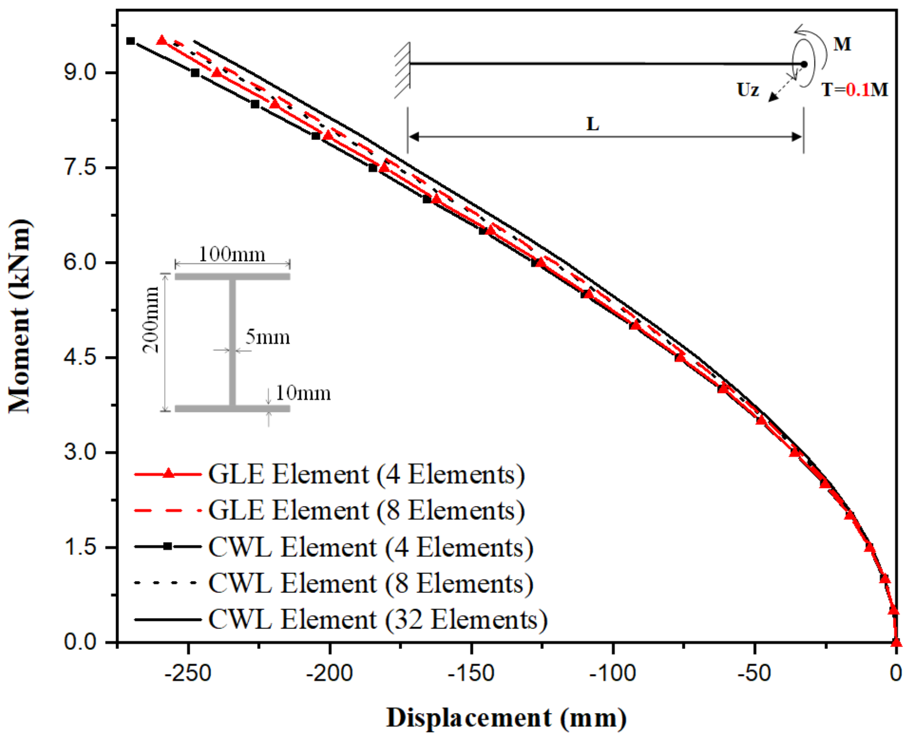

(a) *T/M*=0.1

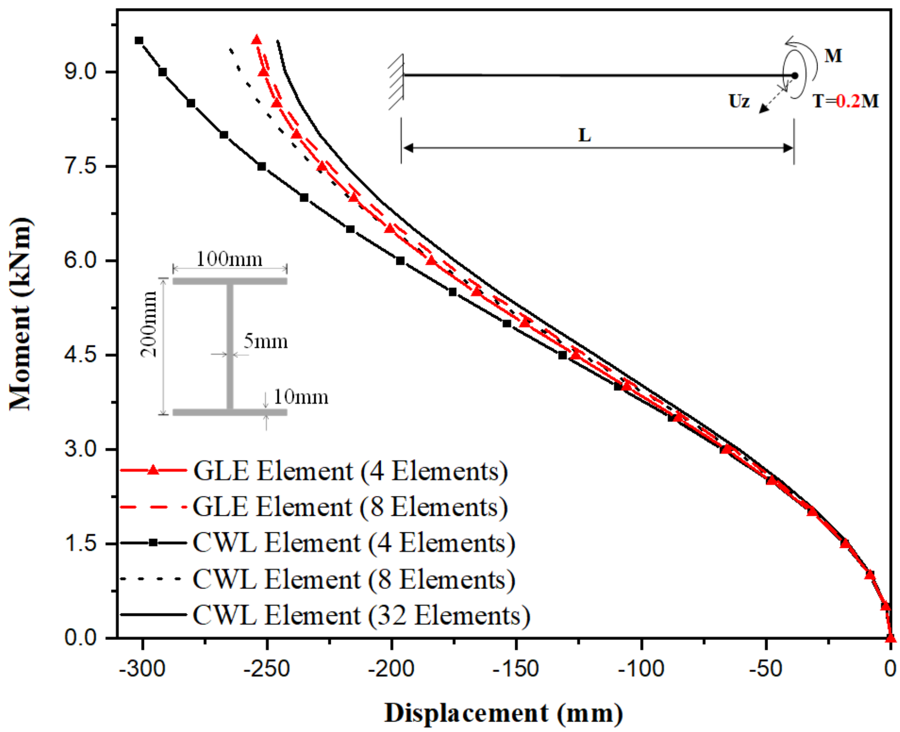

M
Uz
T=0.2M
L
100mm
200mm
5mm
10mm
GLE Element (4 Elements)
GLE Element (8 Elements)
CWL Element (4 Elements)
CWL Element (8 Elements)
CWL Element (32 Elements)
Moment (kNm)
Displacement (mm)

(b) *T/M*=0.2

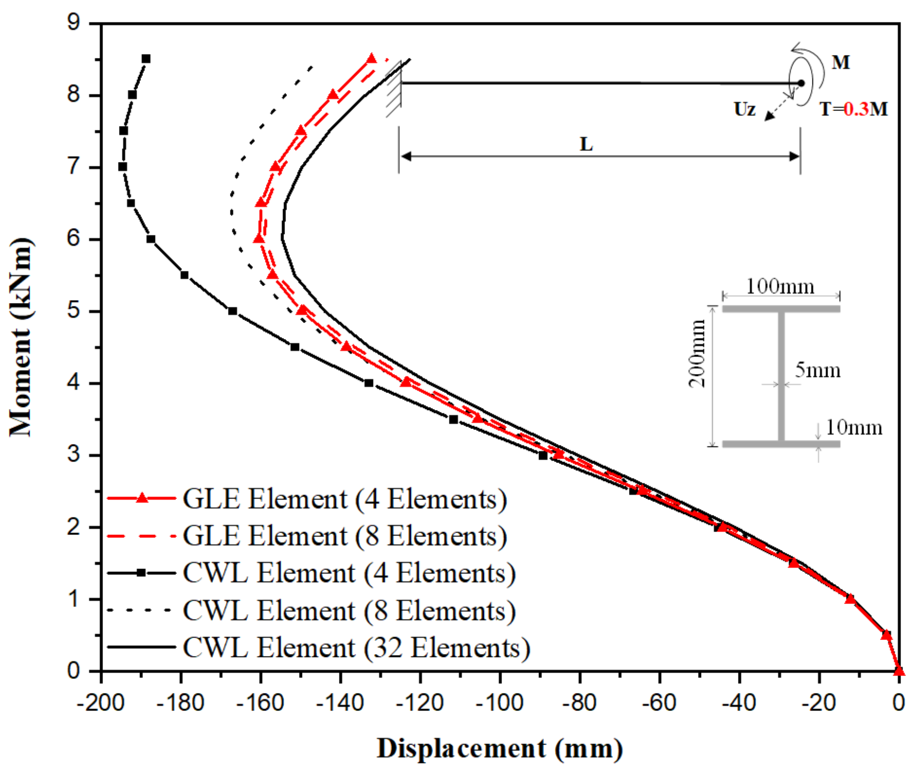

M
Uz
T=0.3M
L
100mm
200mm
5mm
10mm
GLE Element (4 Elements)
GLE Element (8 Elements)
CWL Element (4 Elements)
CWL Element (8 Elements)
CWL Element (32 Elements)
Moment (kNm)
Displacement (mm)

(c) *T/M*=0.3

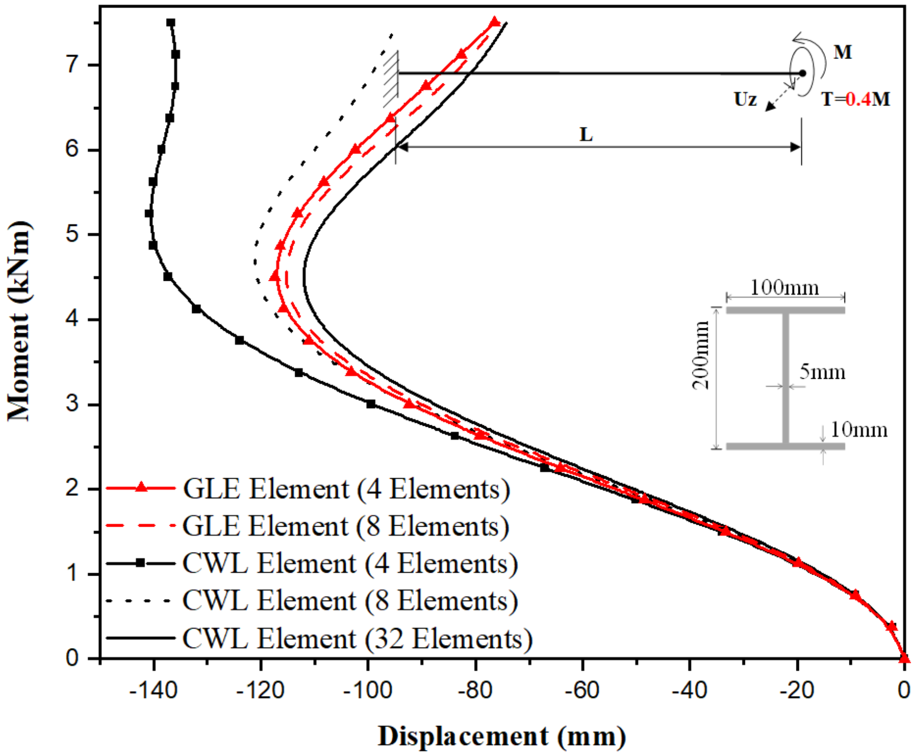

(d) *T/M*=0.4

Figure 4.15 Load-displacement curves for member with symmetric I section

From Figure 4.15 and Table 4.6, it is clearly seen that when the torsion moment is small ($T/M = 0.1$), both the CWL element and proposed GLE element can predict the member's behavior accurately using eight elements. Nevertheless, with the torsion moment increase, the proposed GLE element provides more accurate and closer results to 32 CWL elements. Even the results of four GLE elements are more reliable than those of eight CWL elements. In a word, adopting the proposed GLE element with only four elements to model the member can precisely capture both the small and large-deflection behavior of symmetric-section members. These comparisons indicate the robustness and accuracy of the proposed method in analysing a steel beam with combinations of bending moments and torsions.

Table 4.6 Results summary for the member with symmetric I section

T/M	Maximum Uz displacement (mm)								
	32 Elements	4 Elements				8 Elements			
	CWL	CWL		GLE		CWL		GLE	
			Diff.		Diff.		Diff.		Diff.
0.1	-248.0	-270.3	9.0%	-259.3	4.6%	-256.4	3.4%	-254.6	2.7%
0.2	-245.8	-301.2	22.5%	-254.4	3.5%	-266.1	8.2%	-252.6	2.7%
0.3	-154.6	-194.5	25.8%	-160.4	3.7%	-167.7	8.4%	-159.1	2.9%
0.4	-112.5	-140.7	25.1%	-117.4	4.4%	-121.3	7.9%	-115.8	2.9%

Note: *T* is the torsion moment, and M is the applied bending moment.

Example 2: Member with Mono-Symmetric Section

Two monosymmetric sections (channel and monosymmetric I-section) are studied under the loading conditions shown in Figure 4.16 and Figure 4.17. The channel section has a width of 100 mm and a depth of 300 mm, and the thicknesses of its flange and web are 16 mm and 10 mm, respectively. The widths of the monosymmetric I-section flanges are 150 mm and 75 mm; the depth of the I-section is 300 mm, and the flange thickness and web thickness are 10 mm and 5 mm, respectively. For the I-section beam, negative bending moments are adopted at the two ends, while a concentrated point load is applied at the free end of the cantilever channel section beam.

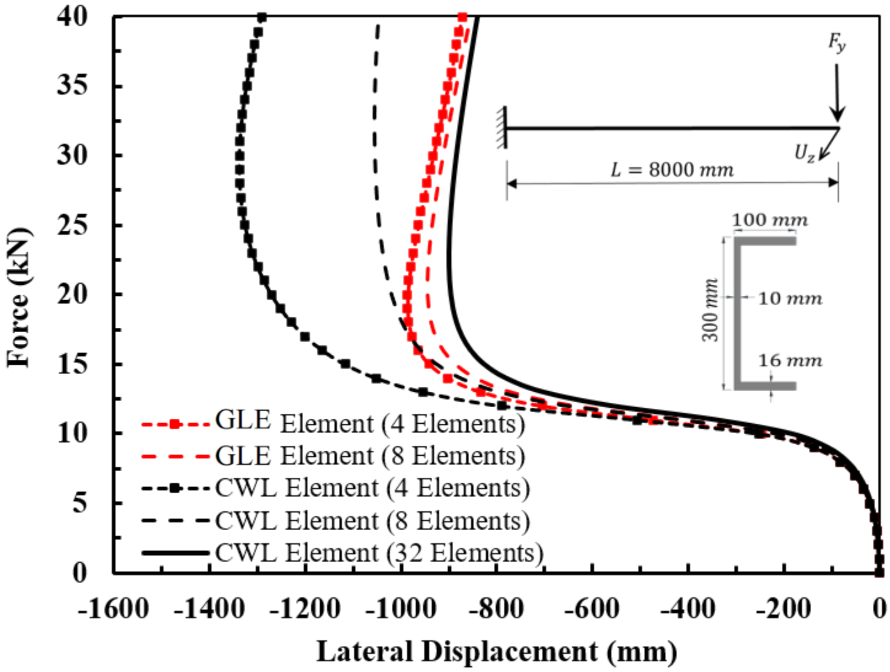

(a) $T/Fy = 0$

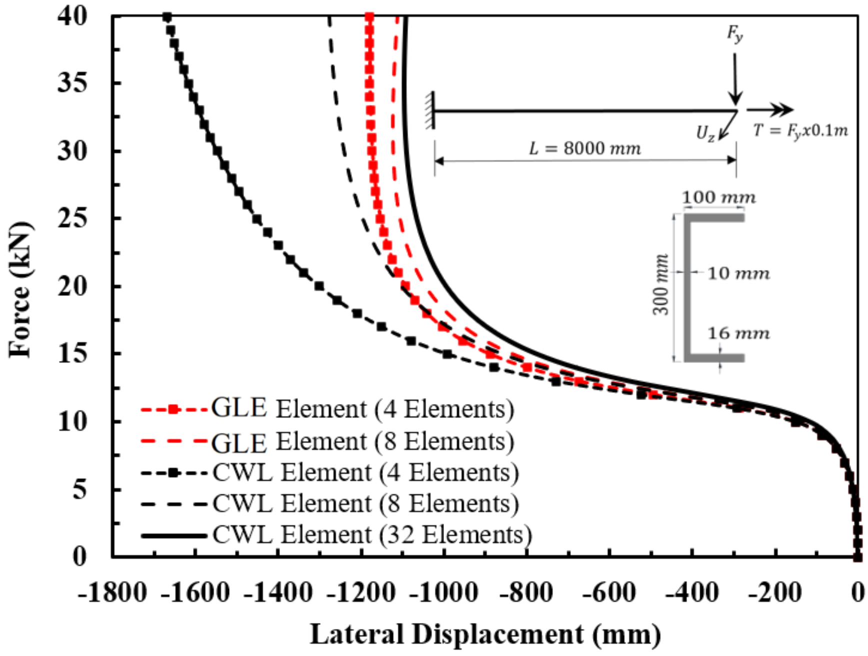

(b) $T/Fy = 0.1$m

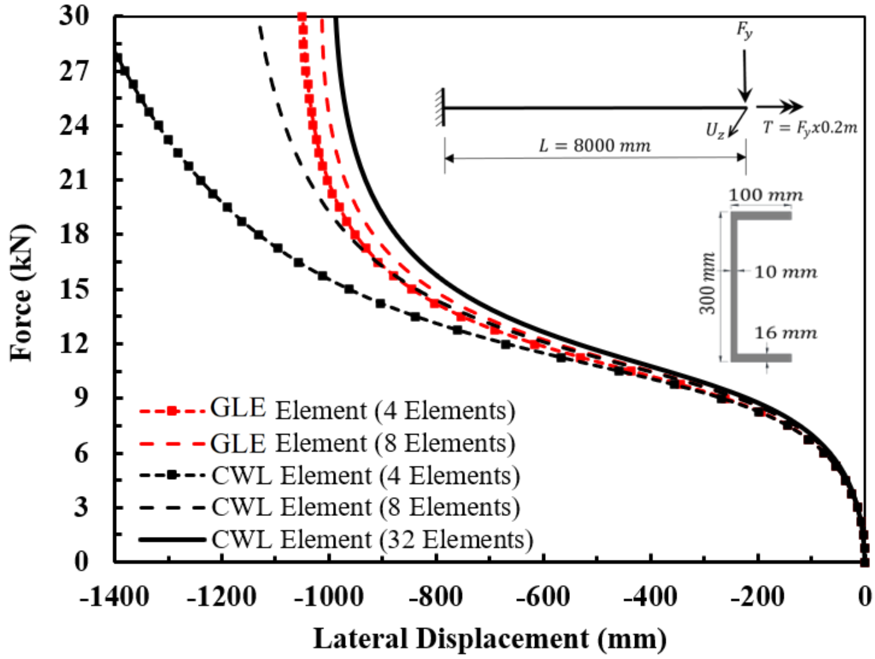

(c) $T/Fy = 0.2$m

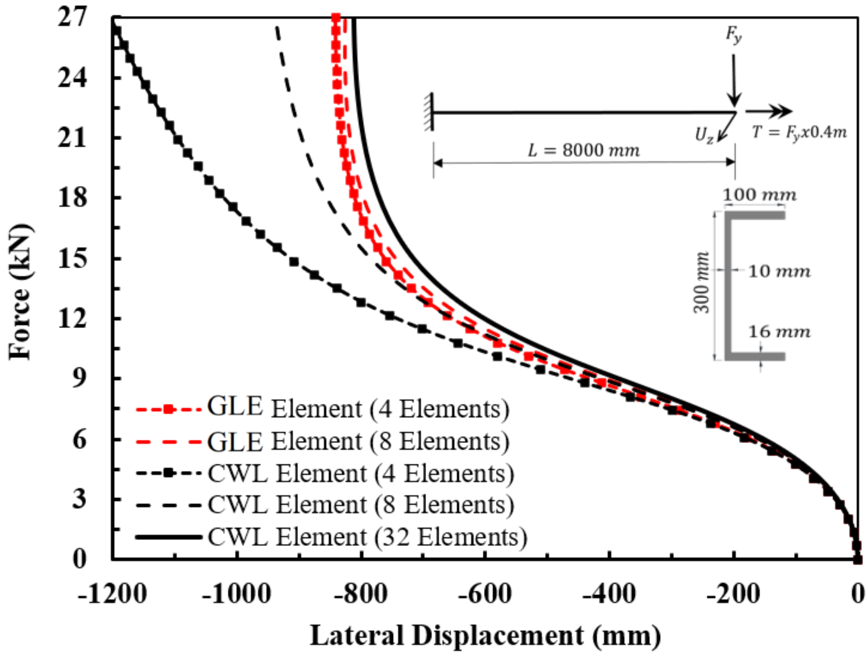

(d) $T/Fy = 0.4$m

Figure 4.16 Load-displacement curves for the member with channel section

As a sequel, a torsion moment is imposed with different twisting levels ($T/Fy = 0, 0.1\ m, 0.2\ m, and\ 0.4\ m$ for the cantilever beam and $T/M = 0.1\ and\ 0.3$ for the simply supported beam), where Fy is the applied vertical load and M is the applied bending moment. Consequently, the free-end and mid-span lateral displacement of the cantilever and simply supported beams are, respectively, plotted in Figure 4.16 and Figure 4.17. The maximum displacements from different methods are presented in Table 4.7.

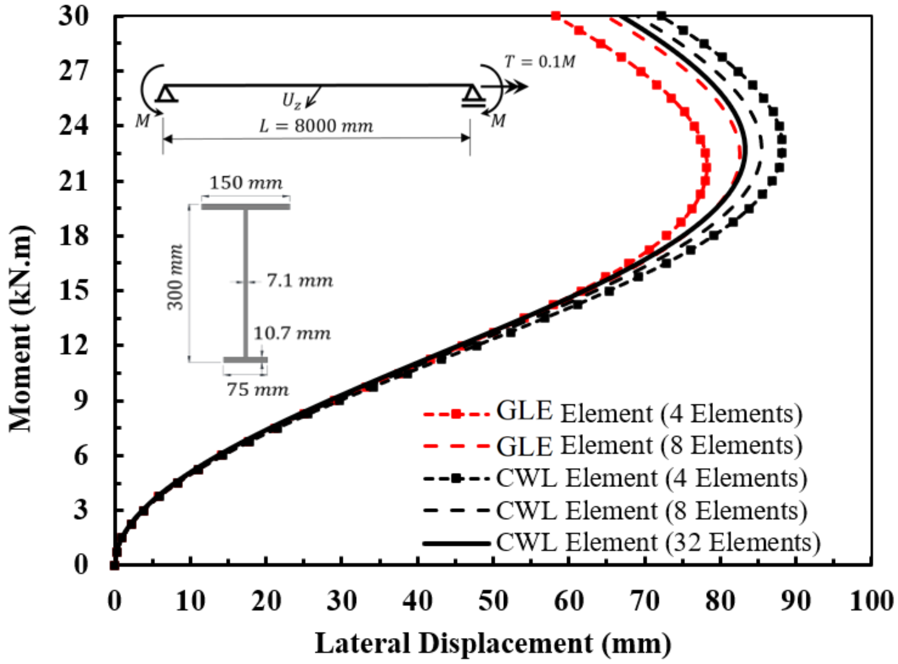

(a) T/M=0.1

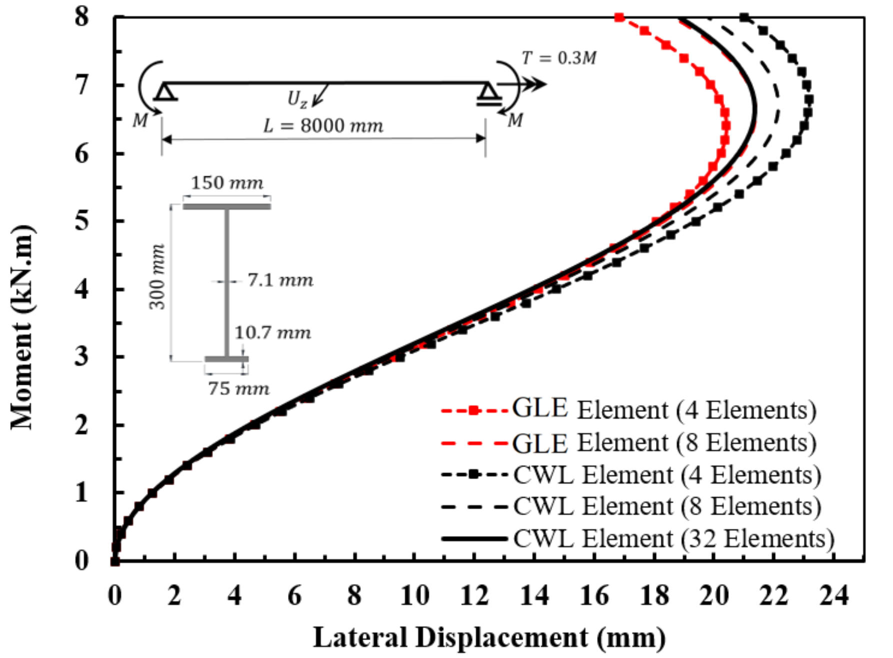

(b) T/M=0.3

Figure 4.17 Load-displacement curves for the member with mono-I section

As illustrated in the load versus deflections curves, the kinematics of large deflections of members with monosymmetric sections are further assessed. The results show that the GLE elements' response is theoretically more accurate than the CWL for large twisting problems. Due to the section's mono-symmetry, the differences between results from four or eight CWL elements versus 32 CWL elements are sizeable mainly when the torsion applied on the beam is large. Nevertheless, results from GLE elements are in line with those from 32 CWL elements under both small and large twisting. Even the results of four GLE elements are more accurate than those of eight CWL elements, and this further confirms the accuracy and efficiency of the proposed GLE element.

Table 4.7 Results summary for the member with channel section

T/M	Maximum Uz displacement (mm)								
	32 Elements	4 Elements				8 Elements			
	CWL element	CWL element		GLE element		CWL element		GLE element	
	(Benchmark)		Diff.		Diff.		Diff.		Diff.
0.1	-900.2	-1337.4	48.6%	-986.9	9.6%	-1055.2	17.2%	-943.9	4.9%
0.2	-1095.8	-1669.4	52.3%	-1179.6	7.6%	-1275.8	16.4%	-1124.7	2.6%
0.3	-988.0	-1430.6	44.8%	-1050.1	6.3%	-1132.1	14.6%	-1013.1	2.5%
0.4	-812.1	-1203.1	48.1%	-841.2	3.6%	-938.6	15.6%	-826.6	1.8%

Note: Fy is the applied shear force.

Example 3: Member with Nonsymmetric Section

This example is conducted further to examine the large-deflection behavior of members with nonsymmetric sections. Such members usually experience apparent warping, and the member twisting shows a noticeable influence on its behavior. The overall depth and width of the cross-section are 200 mm and 100 mm, and the flange thickness and web thickness are 10mm and 5mm, as shown in Figure 4.18. Once again, both simply supported beam and cantilever beam are studied, and the analysis results are plotted in Figure 4.18 and Figure 4.19 for the comparisons.

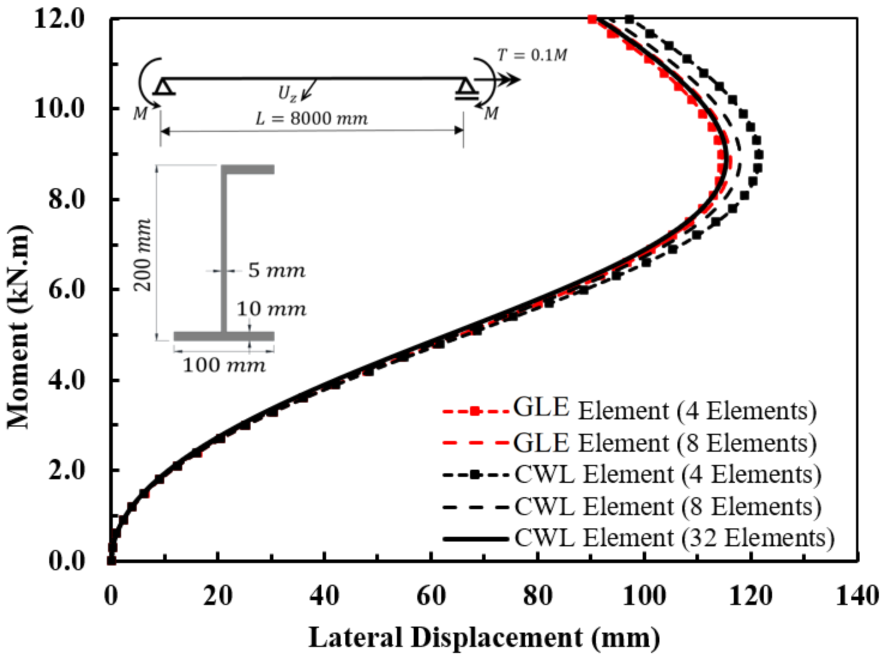

(a) *T/M*=0.1

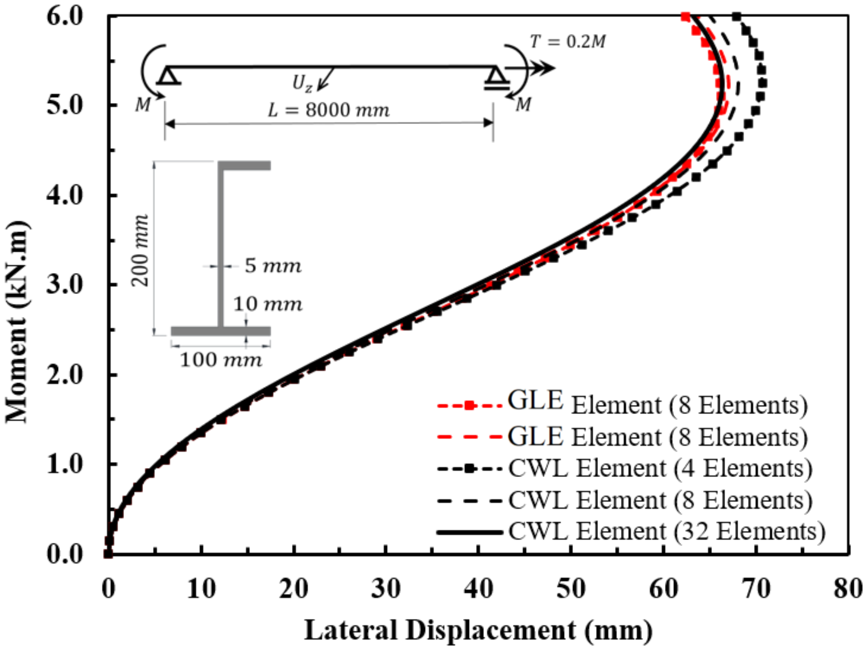
T = 0.2M
U_z
M
M
L = 8000 mm
200 mm
5 mm
10 mm
100 mm
GLE Element (8 Elements)
GLE Element (8 Elements)
CWL Element (4 Elements)
CWL Element (8 Elements)
CWL Element (32 Elements)
Moment (kN.m)
Lateral Displacement (mm)

(b) *T/M*=0.2

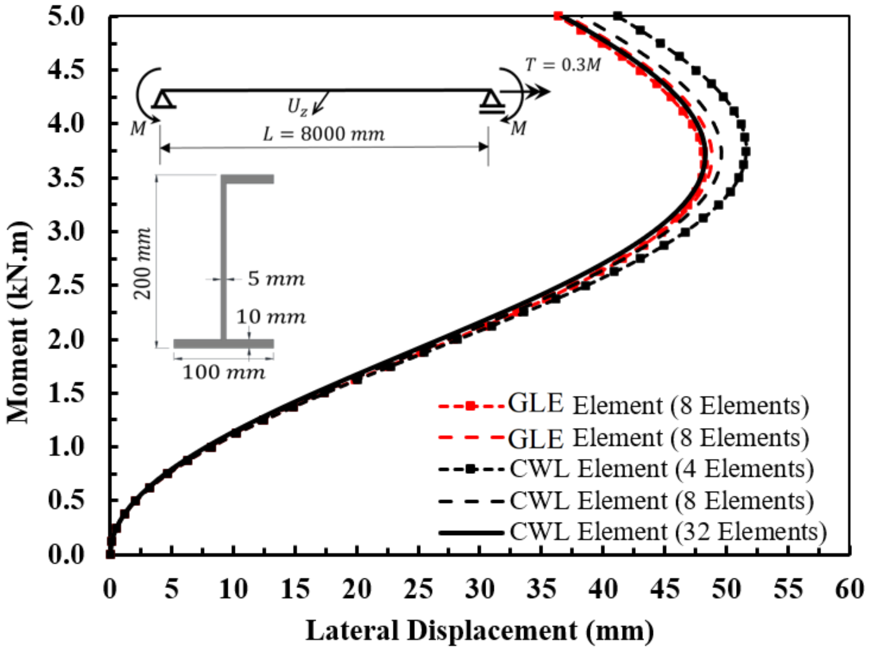
T = 0.3M
U_z
M
M
L = 8000 mm
200 mm
5 mm
10 mm
100 mm
GLE Element (8 Elements)
GLE Element (8 Elements)
CWL Element (4 Elements)
CWL Element (8 Elements)
CWL Element (32 Elements)
Moment (kN.m)
Lateral Displacement (mm)

(c) *T/M*=0.3

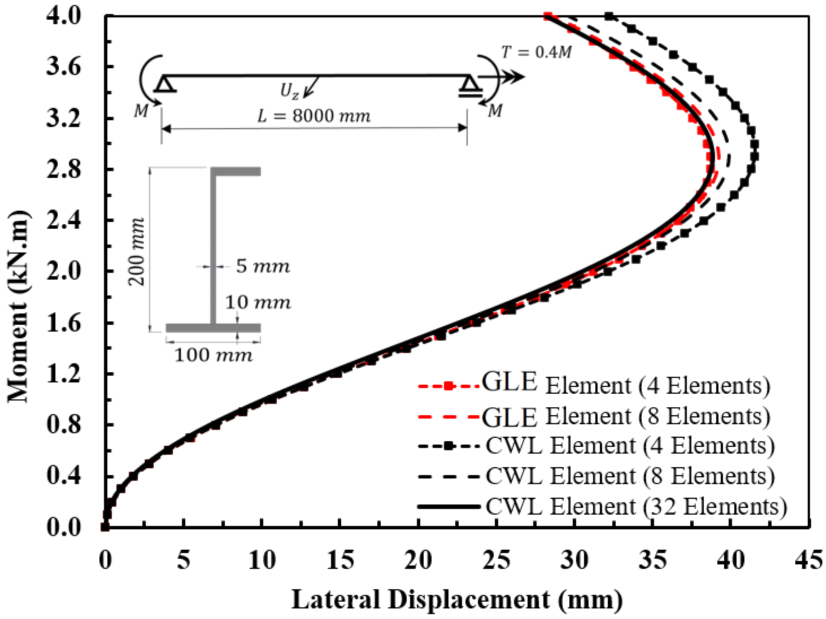

(d) *T/M*=0.4

Figure 4.18 Load-displacement curves for member with nonsymmetric section

From Figure 4.18 and Table 4.8, it is noted that when increasing the member twisting, the proposed GLE elements provide more accurate and closer results compared to the CWL elements. Results from four GLE elements are nearly identical (less than 1%) with those from 32 CWL elements under both small and large twisting. Moreover, the cantilever beam is subjected to bi-axial bending and torsion, thereby assessing the proposed element for more severe configurations. Herein, two vertical and horizontal concentrated forces together with the torsion are applied at the free end (Figure 4.19). Overall, four GLE elements provided comparable results and closely followed the trends from 32 CWL elements. As a result, the accuracy and persuasiveness of the proposed element are further established. It is believed that the proposed element can precisely and efficiently capture the second-order twist effects, thereby be used in a structural analysis of systems with nonsymmetric section members.

Table 4.8 Results summary for the member with nonsymmetric section

T/M	Maximum Uz displacement (mm)								
	32 Elements	4 Elements				8 Elements			
	CWL element (Benchmark)	CWL element	Diff.	GLE element	Diff.	CWL element	Diff.	GLE element	Diff.
0.1	115.4	121.5	5.3%	114.5	-0.7%	117.9	2.2%	116.2	0.7%
0.2	66.3	70.7	6.6%	66.2	-0.1%	68.1	2.7%	67.0	1.1%
0.3	48.3	51.6	6.9%	48.2	-0.2%	49.6	2.8%	48.8	1.0%
0.4	38.8	41.5	6.9%	38.7	-0.4%	39.9	2.7%	39.2	1.0%

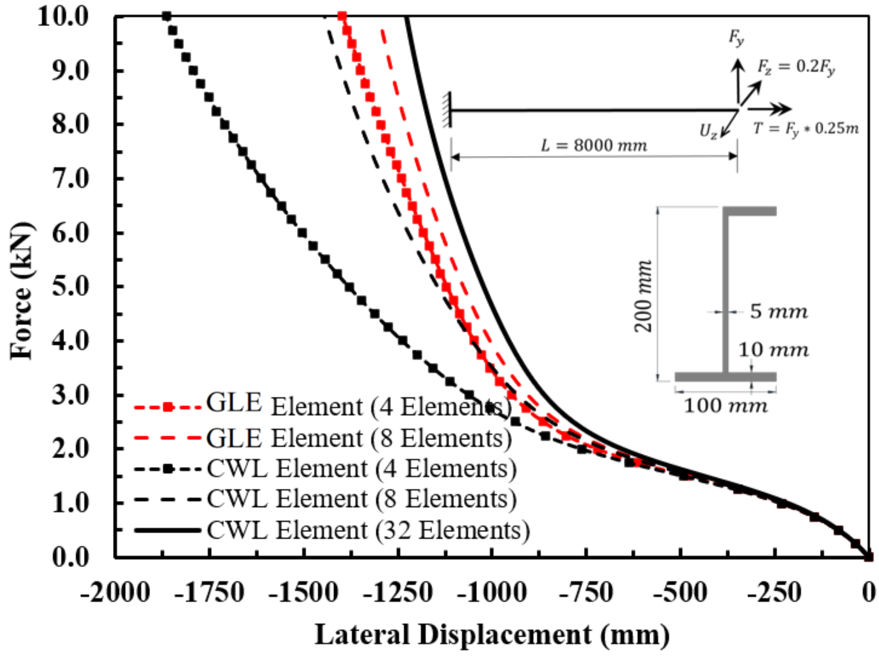

(a) $T/Fy = 0.25\text{m}$

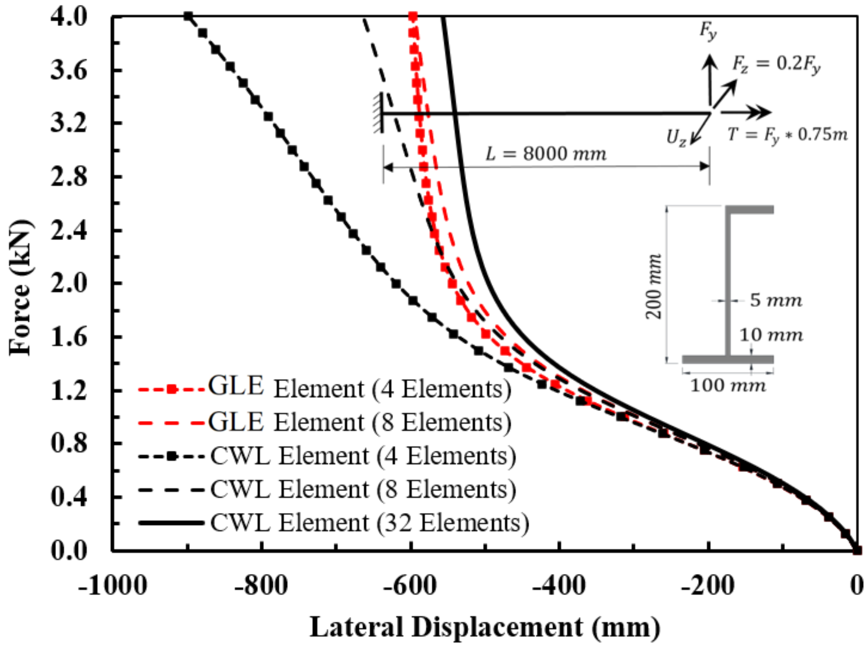

(b) $T/Fy = 0.75\text{m}$

Figure 4.19 Load-displacement curves for a member with nonsymmetric section

Example 4: Second-order analysis of a space frame.

This example is to conduct a second-order elastic analysis for an L-shaped frame, where the geometry and applied loads are plotted in Figure 4.20. The overall depth and width of the column's cross-section are 300 mm and 200 mm, and the flange thickness and web thickness are 15mm and 10mm, while the corresponding dimensions of the horizontal beam are, respectively, 200, 100, 10, and 5mm. The proposed GLE, utilizing 4 elements to model the column, is adopted for the frame analysis and the results are plotted in Figure 4.20**.** Results from 32 B31OS beam-element given by Chen et al. (2021) are introduced for comparison purposes. The lateral displacements in the Z-direction of the free-end node from the two models are plotted. This comparison, in which a large deflection level is achieved (U_z = 2300 mm) further validates the feasibility of the proposed element for large deflection analysis of steel frames, where the twisting behavior is significant.

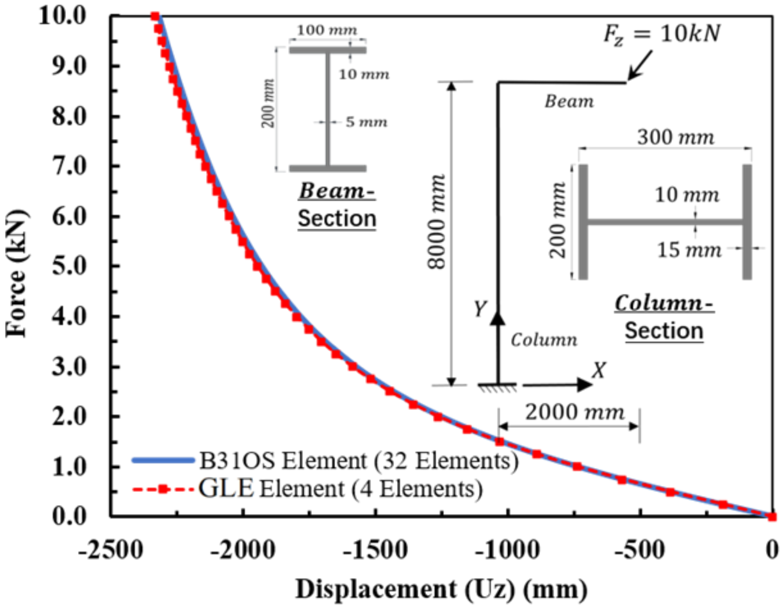

Figure 4.20 Load-displacement curves of the L-shaped frame

CHAPTER 5.

ELASTIC ANALYSIS OF STEEL MEMBERS WITH THICK-WALLED SECTIONS

5.1 Introduction

Chapter 4 proposed the LFEM for the steel frames with nonsymmetric thin-walled sections, where a line element with 14 DOFs and an improved Gaussian line element for the large-deflection analysis is given. Those line element formulations are based on Euler-Bernoulli beam theory, where the transverse shear deformations are neglected, leading to over-estimate the member stiffness of the thick-walled members. Existing approaches for the simulation of the nonsymmetric thick-walled members generally involve shell or solid elements, which are limited to single members due to high computational costs. This chapter proposes an improved Timoshenko line element (TLE) for the second-order analysis of nonsymmetric thick-walled members. The non-negligible shear deformation in nonsymmetric thick-walled members is considered by incorporating the shear deformation in the element stiffness matrices.

5.2 Line Element Based on Timoshenko Beam Theory

5.2.1 Element reference axes

The warping DOF is included in the proposed TLE element formulation. So, there are seven DOFs at each element node, and therefore, fourteen DOFs for an element (see Figure 4.2 (a)).

Therefore, the vector of the DOFs at one element end are given as,

$$\Delta = [x_i \quad \theta_i \quad \theta_b] \tag{5.1}$$

where $i=1,2,3$, $x_1 = u$, $x_2 = v$, and $x_3 = w$ are the translational DOFs, $\theta_1 = \theta_x$, $\theta_2 = \theta_v$, and $\theta_3 = \theta_w$ are the rotational DOFs, and θ_b is the warping DOF. As shown in Figure 4.2 (b), the corresponding forces at one element end are:

$$\boldsymbol{F} = [F_i \quad M_i \quad M_b] \tag{5.2}$$

5.2.2 Shape interpolation functions and shear deformations

In the TLE element, the lateral displacements along the element are composed of bending and shear deformations:

$$\epsilon_i(x) = \epsilon_{ib}(x) + \epsilon_{is}(x) \tag{5.3}$$

in which, $i=2,3,$ the subscripts b denotes the bending deformations, and the subscripts s denotes the shear deformations. Similarly, the rotational deformations along the element can be described by,

$$\frac{d\epsilon_i(x)}{dx} = \theta_{ib}(x) + \theta_{is}(x) \tag{5.4}$$

Based on the equilibrium condition, the relationship between the bending moments and the shear forces are:

$$\frac{dM_i}{dx} = V_j(x) \tag{5.5}$$

where $M_i = EI_i\left(\frac{\partial^2\theta_i(x)}{\partial x^2}\right)$ is the bending moments , $V_j(x) = \frac{GA\theta_{js}(x)}{k_j}$ is the shear forces, $i=2,3,$ and $j=3,2$. $k_2 = k_y$ and $k_3 = k_z$ are the section shear coefficients.

By substituting the Hermit interpolation function for the lateral deformations into equation (5.5), the bending deformations can be calculated by,

$$\theta_{ib}(x) = c_1 + 2c_2 x + \left(3x^2 + \frac{b_i L^2}{2}\right) c_3 \tag{5.6}$$

where, *i=2,3* and $b_i = 12EI_i k_i / GAL^2$. is the shear deformation factor

According to the boundary conditions, the element shape function along the element length can be described by interpolated polynomials as follows,

$$\epsilon_1(x) = (1-\eta)u_1 + \zeta u_2 \tag{5.7}$$

$$\begin{aligned}\epsilon_i(x) &= \left(1 - b_j\zeta_j\eta - 3\zeta_j\eta^2 + 2\zeta_j\eta^3\right)x_{i1} + \left(b_j\zeta_j\eta + 3\zeta_j\eta^2 - 2\zeta_j\eta^3\right)x_{i2} \\ &+\left(\left(2+b_j\right)\frac{\zeta_j}{2}\eta - \left(4+b_j\right)\frac{\zeta_j}{2}\eta^2 + \zeta_j\eta^3\right)L\theta_{j1} \\ &-\left(b_j\frac{\zeta_j}{2}\eta + (2-b_j)\frac{\zeta_j}{2}\eta^2 - \zeta_j\eta^3\right)L\theta_{j2}\end{aligned} \tag{5.8}$$

$$\begin{aligned}\theta_x(x) &= (\eta - 2\eta^2 + \eta^3)L\theta_{b1} + (-\eta^2 + \eta^3)L\theta_{b2} + (1 - 3\eta^2 + 2\eta^3)\theta_{x1} \\ &+(3\eta^2 - 2\eta^3)\theta_{x2}\end{aligned} \tag{5.9}$$

Where *i=2,3, j=3,2*, $\eta = x/L$ and $\zeta_j = 1/(1+b_j)$.

5.2.3 Strain descriptions and total potential energy function

Having the element shape function, the displacement field of the TLE element can be generated by:

$$\boldsymbol{X} = \begin{bmatrix} X_1(x_i) \\ X_2(x_i) \\ X_3(x_i) \end{bmatrix} = \begin{bmatrix} \epsilon_1(x_1) - x_2 \dfrac{\partial \epsilon_2(x_1)}{\partial x_1} - x_3 \dfrac{\partial \epsilon_3(x_1)}{\partial x_1} - \omega_n \dfrac{\partial \theta_x(x_1)}{\partial x_1} \\ \epsilon_2(x_1) - (x_3 - z_s)\theta_x(x_1) \\ \epsilon_3(x_1) + (x_2 - y_s)\theta_x(x_1) \end{bmatrix} \tag{5.10}$$

where z_s and y_s are the coordinates of the shear center.

The Green-Lagrange strain tensor can be calculated by,

$$\varepsilon_{ij} = \frac{1}{2}\left(\frac{\partial X_i}{\partial x_j} + \frac{\partial X_j}{\partial x_i} + \frac{\partial X_k}{\partial x_i}\frac{\partial X_k}{\partial x_j}\right) \tag{5.11}$$

This research adopts the minimal total potential energy principle to get the element stiffness matrix. The total potential energy function is expressed as,

$$\Pi = U - V \tag{5.12}$$

where V is the external work; and U is the strain energy stored by the element, which can be expressed as,

$$U = \frac{1}{2}\int_V \boldsymbol{\sigma}^{\boldsymbol{T}} \boldsymbol{\varepsilon}\, dv = \frac{1}{2}\int_V \boldsymbol{\varepsilon}^T \boldsymbol{D}\boldsymbol{\varepsilon}\, dv \tag{5.13}$$

in which, $\boldsymbol{D}$ is the constitutive matrix relating the stresses and strains by Hooke's law and is written as,

$$\boldsymbol{D} = \begin{bmatrix} E & 0 & 0 \\ 0 & G & 0 \\ 0 & 0 & G \end{bmatrix} \tag{5.14}$$

By substituting equations (5.7) - (5.10) into equation (5.13), replacing some stress tensor with the express of nodal forces and ignoring the high-order terms, the potential strain equation can be written as,

$$
\begin{aligned}
U \approx\ & \frac{1}{2}\int_0^L \left[EA\left(\frac{\partial\epsilon_1(x)}{\partial x}\right)^2 + EI_z\left(\frac{\partial^2\epsilon_2(x)}{\partial x^2}\right)^2 + EI_y\left(\frac{\partial^2\epsilon_3(x)}{\partial x^2}\right)^2\right]dx \\
& + \frac{1}{2}\int_0^L \left[EI_\omega\left(\frac{\partial^2\theta_x(x)}{\partial x^2}\right)^2 + GJ\left(\frac{\partial\theta_x(x)}{\partial x}\right)^2\right]dx \\
& + \frac{1}{2}\int_0^L P\left[\left(\frac{\partial\epsilon_2(x)}{\partial x}\right)^2 + \left(\frac{\partial\epsilon_3(x)}{\partial x}\right)^2\right]dx + \frac{1}{2}\int_0^L Pr^2\left(\frac{\partial\theta_x(x)}{\partial x}\right)^2 dx \\
& + \frac{1}{2}\int_0^L P\left[2y_s\frac{\partial\epsilon_3(x)}{\partial x} - 2z_s\frac{\partial\epsilon_2(x)}{\partial x}\right]\frac{\partial\theta(x)}{\partial x}dx \\
& + \frac{1}{2}\int_0^L M_b\beta_\omega\left(\frac{\partial\theta_x(x)}{\partial x}\right)^2 dx \\
& + \frac{GA}{k_y}\left[\left(\theta_z(x)\right)^2 + \left(\frac{\partial\epsilon_2(x)}{\partial x}\right)^2 - 2\theta_z(x)\frac{\partial\epsilon_2(x)}{\partial x}\right]dx \\
& + \frac{GA}{k_z}\left[\left(\theta_y(x)\right)^2 + \left(\frac{\partial\epsilon_3(x)}{\partial x}\right)^2 - 2\theta_y(x)\frac{\partial\epsilon_3(x)}{\partial x}\right]dx \\
& + \int_0^L M_{y1}\frac{L-x}{L}\frac{\partial\theta_x(x)}{\partial x}\left[\frac{\partial\epsilon_2(x)}{\partial x} + \frac{1}{2}\beta_y\frac{\partial\theta_x(x)}{\partial x}\right]dx \\
& - \int_0^L M_{y2}\frac{x}{L}\frac{\partial\theta_x(x)}{\partial x}\left[\frac{\partial\epsilon_2(x)}{\partial x} + \frac{1}{2}\beta_y\frac{\partial\theta_x(x)}{\partial x}\right]dx \\
& + \int_0^L M_{z1}\frac{L-x}{L}\frac{\partial\theta_x(x)}{\partial x}\left[\frac{\partial\epsilon_3(x)}{\partial x} + \frac{1}{2}\beta_z\frac{\partial\theta_x(x)}{\partial x}\right]dx \\
& - \int_0^L M_{z2}\frac{x}{L}\frac{\partial\theta_x(x)}{\partial x}\left[\frac{\partial\epsilon_3(x)}{\partial x} + \frac{1}{2}\beta_z\frac{\partial\theta_x(x)}{\partial x}\right]dx \\
& + \int_0^L V_y\left(\theta_x(x)\frac{\partial\epsilon_3(x)}{\partial x} - \frac{\partial\epsilon_1(x)}{\partial x}\frac{\partial\epsilon_2(x)}{\partial x}\right)dx \\
& - \int_0^L V_z\left(\theta_x(x)\frac{\partial\epsilon_2(x)}{\partial x} + \frac{\partial\epsilon_1(x)}{\partial x}\frac{\partial\epsilon_3(x)}{\partial x}\right)dx
\end{aligned}
\tag{5.15}
$$

where P is the axial force, $r^2 = [I_y + I_z]/A$.

5.2.4 Tangent stiffness matrix

The element stiffness matrices of the TLE element can be generated by the second variation of the total potential energy Π,

$$\delta^2\Pi = \frac{\partial^2\Pi}{\partial u_i\,\partial u_j}\delta u_i\delta u_j = \left(\frac{\partial F_i}{\partial u_j} + \frac{\partial F_i}{\partial q}\frac{\partial q}{\partial u_j}\right)\delta u_i\delta u_j = \boldsymbol{K_e}\Delta\boldsymbol{u} - \Delta\boldsymbol{f} = 0 \tag{5.16}$$

$(i, j =$1-14)

The tangent stiffness matrix can be written as,

$$\boldsymbol{k_E} = \boldsymbol{k_{Ls}}\boldsymbol{\alpha} + \boldsymbol{k_G} + \boldsymbol{k_U} \tag{5.17}$$

in which $\boldsymbol{k_E}$ is the element tangent stiffness matrix; $\boldsymbol{k_G}$ and $\boldsymbol{k_U}$ is the well-established geometric stiffness matrix given above; and $\boldsymbol{k_{Ls}}$ and $\boldsymbol{\alpha}$ is the linear stiffness matrix and transformation matrix given below.

$$\boldsymbol{\alpha} = \begin{bmatrix}
1 & 0 & 0 & 0 & 0 & 0 & 0 & 1 & 0 & 0 & 0 & 0 & 0 & 0 \\
 & \alpha_z & 0 & 0 & 0 & \alpha_z & 0 & 0 & \alpha_z & 0 & 0 & 0 & \alpha_z & 0 \\
 & & \alpha_y & 0 & \alpha_y & 0 & 0 & 0 & 0 & \alpha_y & 0 & \alpha_y & 0 & 0 \\
 & & & 1 & 0 & 0 & 1 & 0 & 0 & 0 & 1 & 0 & 0 & 1 \\
 & & & & \alpha_y & 0 & 0 & 0 & 0 & \alpha_y & 0 & \alpha_y & 0 & 0 \\
 & & & & & \alpha_z & 0 & 0 & \alpha_z & 0 & 0 & 0 & \alpha_z & 0 \\
 & & & & & & 1 & 0 & 0 & 0 & 1 & 0 & 0 & 1 \\
 & & S. & & & & & 1 & 0 & 0 & 0 & 0 & 0 & 0 \\
 & & & Y. & & & & & \alpha_z & 0 & 0 & 0 & \alpha_z & 0 \\
 & & & & M. & & & & & \alpha_y & 0 & \alpha_y & 0 & 0 \\
 & & & & & & & & & & 1 & 0 & 0 & 1 \\
 & & & & & & & & & & & \alpha_y & 0 & 0 \\
 & & & & & & & & & & & & \alpha_z & 0 \\
 & & & & & & & & & & & & & 1
\end{bmatrix} \tag{5.18}$$

where, $\alpha_y = \frac{I_y + I_z + (I_y - I_z)\cos 2\varphi + 2I_{yz}\sin 2\varphi}{2I_y}$ and $\alpha_z = \frac{I_y + I_z - (I_y - I_z)\cos 2\phi - 2I_{yz}\sin 2\phi}{2I_z}$.

$$\boldsymbol{k_{Ls}} = \begin{bmatrix}
\frac{EA}{L} & 0 & 0 & 0 & 0 & 0 & 0 & -\frac{EA}{L} & 0 & 0 & 0 & 0 & 0 & 0 \\
 & \vartheta_z & 0 & 0 & 0 & \frac{L\vartheta_z}{2} & 0 & 0 & -\vartheta_z & 0 & 0 & 0 & \frac{L\vartheta_z}{2} & 0 \\
 & & \vartheta_y & 0 & -\frac{L\vartheta_y}{2} & 0 & 0 & 0 & 0 & -\vartheta_y & 0 & -\frac{L\vartheta_y}{2} & 0 & 0 \\
 & & & \frac{\kappa_1 + 6\kappa_2}{5L^3} & 0 & 0 & \frac{\kappa_1 + \kappa_2}{10L^2} & 0 & 0 & 0 & -\frac{\kappa_1 + 6\kappa_2}{5L^3} & 0 & 0 & \frac{\kappa_1 + \kappa_2}{10L^2} \\
 & & & & \vartheta_y\left(\frac{L^2}{3} + \varpi_z\right) & 0 & 0 & 0 & 0 & -\frac{L\vartheta_y}{2} & 0 & \vartheta_y\left(\frac{L^2}{6} - \varpi_z\right) & 0 & 0 \\
 & & & & & \vartheta_z\left(\frac{L^2}{3} + \varpi_y\right) & 0 & 0 & -\frac{\vartheta_z L}{2} & 0 & 0 & 0 & \vartheta_z\left(\frac{L^2}{6} - \varpi_y\right) & 0 \\
 & S. & & & & & \frac{\kappa_1 + 2\kappa_2}{15L} & 0 & 0 & 0 & -\frac{\kappa_1 + \kappa_2}{15L^2} & 0 & 0 & \frac{\kappa_1 - \kappa_2}{30L} \\
 & & & & & & & \frac{EA}{L} & 0 & 0 & 0 & 0 & 0 & 0 \\
 & & & Y. & & & & & \vartheta_z & 0 & 0 & 0 & -\frac{\vartheta_z L}{2} & 0 \\
 & & & & & & & & & \vartheta_y & 0 & \frac{L\vartheta_y}{2} & 0 & 0 \\
 & & & & & M. & & & & & \frac{\kappa_1 + 6\kappa_2}{5L^3} & 0 & 0 & -\frac{\kappa_1 + \kappa_2}{10L^2} \\
 & & & & & & & & & & & \vartheta_y\left(\frac{L^2}{3} + \varpi_z\right) & 0 & 0 \\
 & & & & & & & & & & & & \vartheta_z\left(\frac{L^2}{3} + \varpi_y\right) & 0 \\
 & & & & & & & & & & & & & \frac{\kappa_1 + 2\kappa_2}{15L}
\end{bmatrix} \tag{5.19}$$

where,

$$\varpi_y = \frac{EI_y}{k_y} AG \tag{5.20}$$

$$\varpi_z = \frac{EI_z}{k_z} AG \tag{5.21}$$

$$\vartheta_z = \frac{12EI_z}{L^3 + 12\varpi_y L} \tag{5.22}$$

$$\vartheta_y = \frac{12EI_y}{L^3 + 12\varpi_z L} \tag{5.23}$$

$$\kappa_1 = 60EI_\omega \tag{5.24}$$

$$\kappa_2 = GJL^2 \tag{5.25}$$

5.3 Verification Examples

Example 1: Simply supported beams

Simply supported beams with different cross-section will be analyzed with proposed method. Detailed loading and boundary conditions of the beams are given in Figure 5.1. This is a classic example been widely studied. The deflection along the beams can be calculated by the theoretical solutions given by Gere and Timoshenko (Gere and Timoshenko 1991),

$$\epsilon_y(x) = \epsilon_{yb}(x) + \epsilon_{ys}(x) = \frac{VL^3 x}{48EIL}\left(3 - 4\frac{x^2}{L^2}\right) + \frac{Vx}{2GAk_y} \tag{26}$$

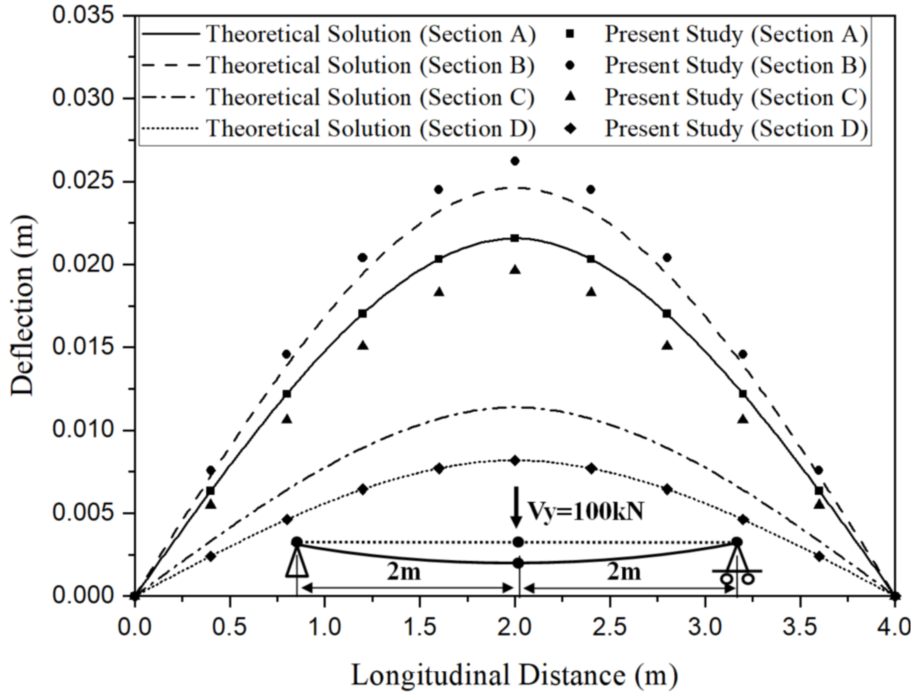

Figure 5.1 The deflection along the beams

The beams modeled with 10 TLE elements each are analyzed to get the member deflections at each element nodes. The cross-sections given in Figure 3.7 with 20mm wall thicknesses are adopted, and the results are plotted in Figure 5.1. The member deflection predicted by the proposed TLE elements are inline with those from the theoretical solutions for the beams with Section A and D. However, large differences can be observed from the results of the beams with Section B and C. This is because Section B and C are nonsymmetric sections. The theoretical solutions given by Gere and Timoshenko (Gere and Timoshenko 1991) is based on the symmetric-section assumption, which is no longer applicable for members with nonsymmetric sections.

Example 2: Fix-pin Column

As shown in Figure 5.2, a fix-pin steel column firstly studied by Tang et al. (Tang et al. 2019) is analyzed with proposed TLE element. The cross-section is a circular hollow section with dimensions given in Figure 5.2, and the shear coefficients of the section generated by the proposed CST elements is 0.4996, which is very close to the theoretical value, 0.5. The Young's modulus and Poisson's ratio of the material are taken as 200000MPa and 0.3. The second-order analysis of the column under different load combinations are conducted, where a compression force $P = \pi^2 EI/L^2$ is applied with the end moments $M = mP$.

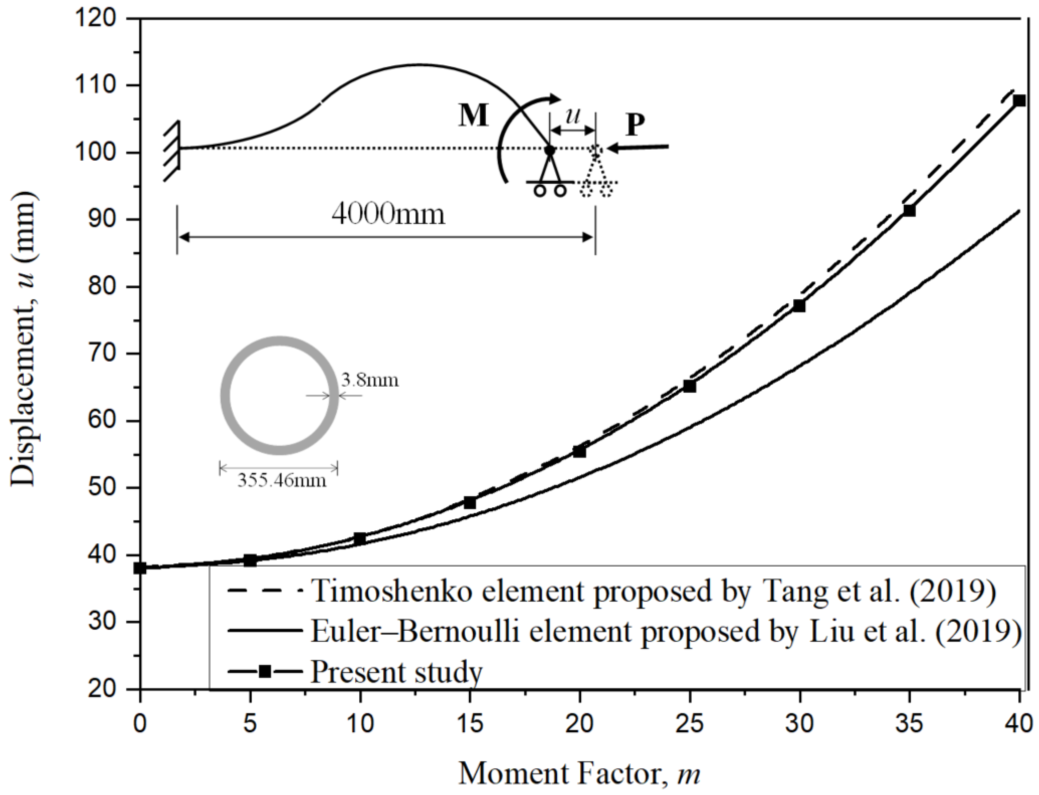

Figure 5.2 Load versus displacement curves for the member under compression

The relationship between the column axial displacement and the moment factor m is given in Figure 5.2, where the results from the Timoshenko element for symmetric sections proposed by Tang et al. (Tang et al. 2019) are given as the benchmark. The results from the Euler-Bernoulli element for nonsymmetric sections proposed by Liu er al. (Liu et al. 2019b) are also given for comparation. From Figure 5.2, it can be seen that large differences can be observed when the shear deformation has been ignored (Euler-Bernoulli element). While, the differences between the results from present study and those from Tang et al. (Tang et al. 2019) are relatively small showing the accuracy of the proposed method.

Example 3: Cantilever beams

In this example, the second-order analysis of a series of cantilever beams with different cross sections are investigated by the proposed method and the shell finite-element (FE) analysis method. The FE models are established based on the software ANSYS version 14.0 (Ansys 2011) using the SHELL93 element. SHELL93 is an 8-node structural finite element that has six degrees of freedom at each node: translations in the nodal x, y, and z directions and rotations about the nodal x, y, and z-axes. Shear deflections are included in this element, and the element has plasticity, stress stiffening, large deflection, and large strain capabilities.

Based on the mesh sensitivity studies, the maximum element size of about 20 mm is adopted, and the length-to-width ratio of the shell element is constrained to be not greater than 2. The material modelling is assumed to be linear elastic. The material Young's modulus and Poisson's ratio are taken as 210000MPa and 0.3. Four different cross sections, namely, the I section, channel section, lipped channel section, and nonsymmetric box section, are adopted. The section properties and shear coefficients of those sections are listed in Table 5.1. The results from the sophisticated shell FE models are provided in Figure 5.3-Figure 5.6 and taken as the benchmark solutions. The loading conditions, member length, and the dimensions of the cross sections for each case are also given in the figures. The results generated by the conventional Timoshenko element based on symmetric sections assumptions and the Euler-Bernoulli element for members with nonsymmetric sections proposed by Liu er al. (Liu et al. 2019b) are also given for comparison.

From those results, the Euler-Bernoulli element is not suitable for the analysis of those thick beams under shear loading. Large differences can be observed when analyzing the members with nonsymmetric open sections with conventional Timoshenko symmetric elements (Figure 5.4a, Figure 5.5a), showing the importance of the present study. However, the conventional Timoshenko symmetric element can relatively accurately predict the members' behaviors with nonsymmetric close sections (Figure 5.6). This is because members with close sections have a large resistance to torsion, making the torsion-related Wagner effects of the nonsymmetric section non-significant. The differences between results from the proposed line element and those from the FE model are small in all the cases given above, showing the accuracy of the proposed Timoshenko line element for members with symmetric or nonsymmetric sections. One thing should be mentioned is that the computation time required for using the FE method is 5-8 minutes, while the computation time required for using the proposed line element is about 10 seconds, showing the efficiency of the proposed method.

Table 5.1 Section properties and shear coefficients of the sections

Section	***I section***	***channel section***	***lipped channel section***	***nonsymmetric box section***
$\boldsymbol{A}$	5.446×10^{3} mm^{2}	1.920×10^{4} mm^{2}	2.040×10^{4} mm^{2}	1.144×10^{5} mm^{2}
$\boldsymbol{I_y}$	7.136×10^{6} mm^{4}	7.305×10^{7} mm^{4}	8.857×10^{7} mm^{4}	4.550×10^{9} mm^{4}
$\boldsymbol{I_z}$	5.931×10^{7} mm^{4}	2.541×10^{8} mm^{4}	2.767×10^{8} mm^{4}	6.458×10^{9} mm^{4}
$\boldsymbol{J}$	2.186×10^{5} mm^{4}	5.779×10^{6} mm^{4}	6.233×10^{6} mm^{4}	4.346×10^{9} mm^{4}
$\boldsymbol{I_w}$	9.948×10^{10} mm^{6}	9.607×10^{11} mm^{6}	1.188×10^{12} mm^{6}	4.765×10^{13} mm^{6}
$\boldsymbol{y_c}$	0	0	-1.024×10^{1} mm	8.176×10^{1} mm
$\boldsymbol{z_c}$	0	-1.248×10^{2} mm	-1.388×10^{2} mm	2.639×10^{1} mm
$\boldsymbol{\beta_y}$	0	3.619×10^{2} mm	3.794×10^{2} mm	-1.604×10^{2} mm
$\boldsymbol{\beta_z}$	0	0	2.835×10^{1} mm	-1.662×10^{2} mm
$\boldsymbol{\beta_\omega}$	0	0	7.108×10^{-2} mm	-3.227×10^{-1} mm
$\boldsymbol{k_y}$	3.250×10^{-1}	3.462×10^{-1}	3.167×10^{-1}	4.956×10^{-1}
$\boldsymbol{k_z}$	5.764×10^{-1}	4.392×10^{-1}	4.322×10^{-1}	3.102×10^{-1}

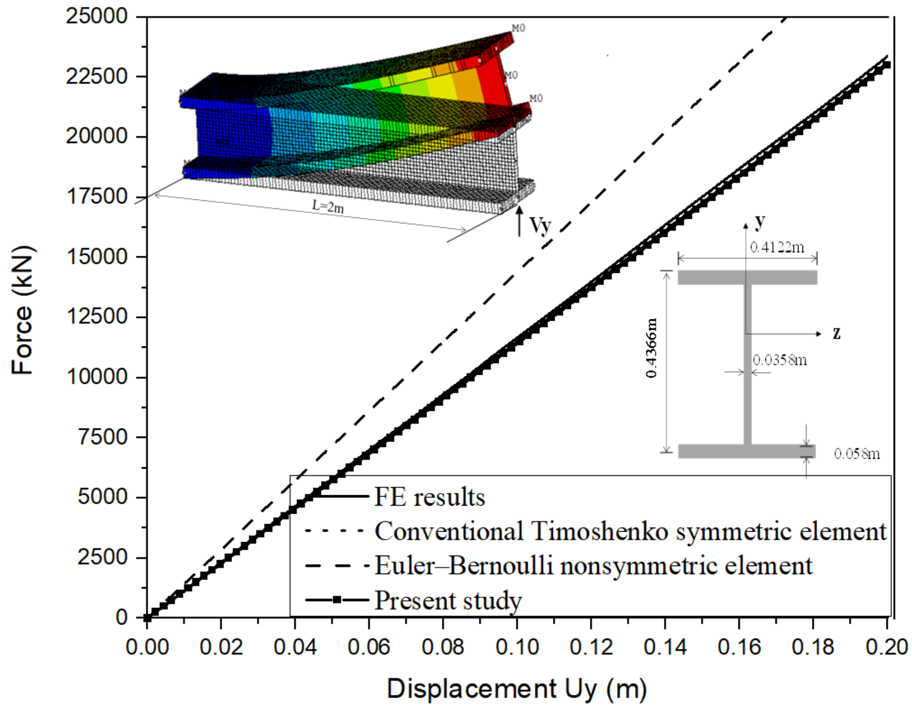

(a) Shear force along y axis

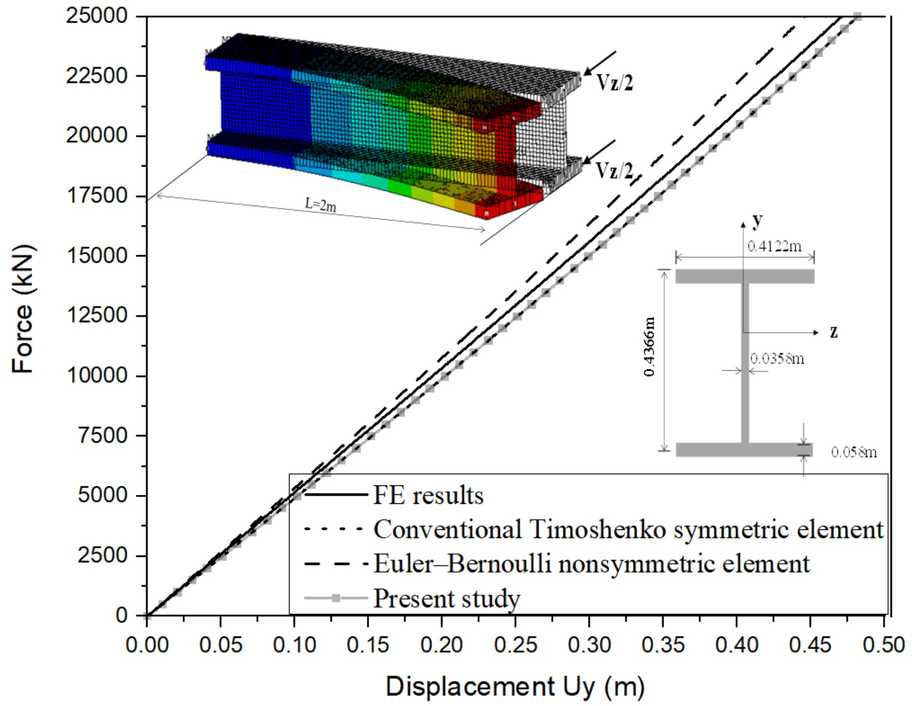

(b) Shear forces along z axis

Figure 5.3 Load-displacement curve for the cantilever beam with I section

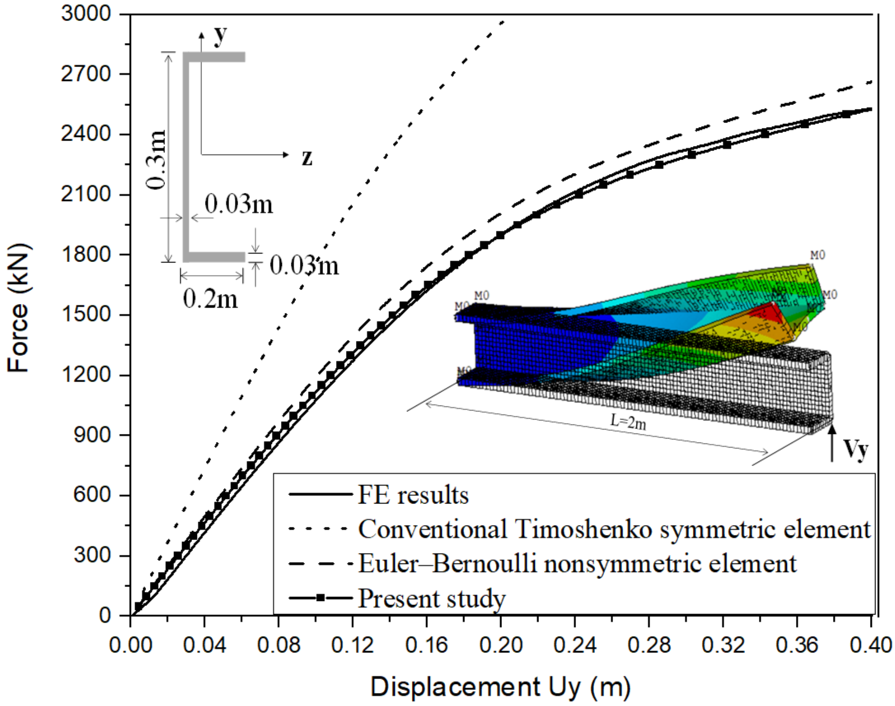

(a) Shear force along y axis

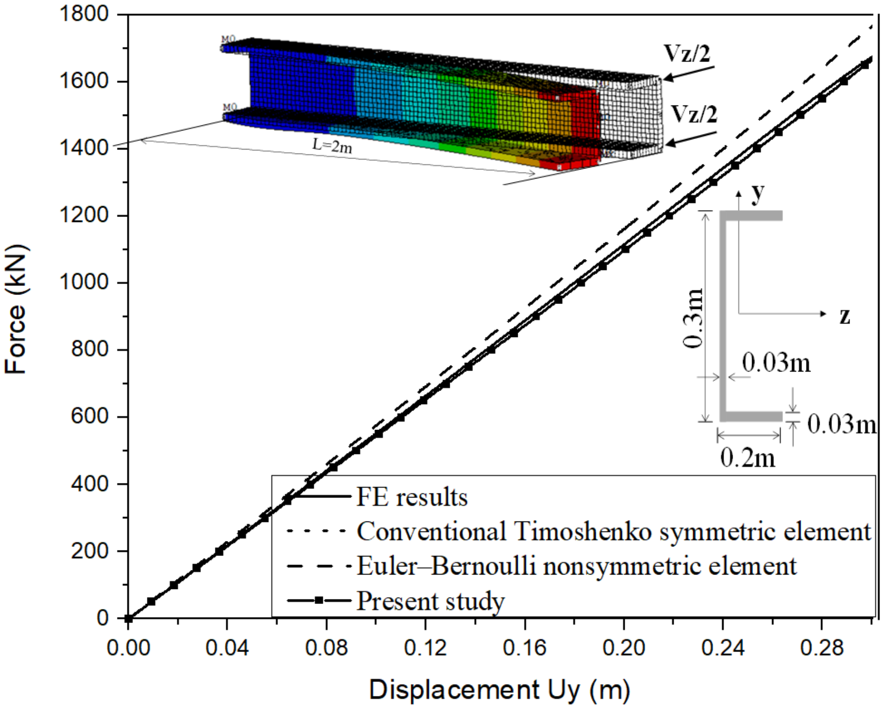

(b) Shear forces along z axis

Figure 5.4 Load-displacement curve for the cantilever beam with channel section

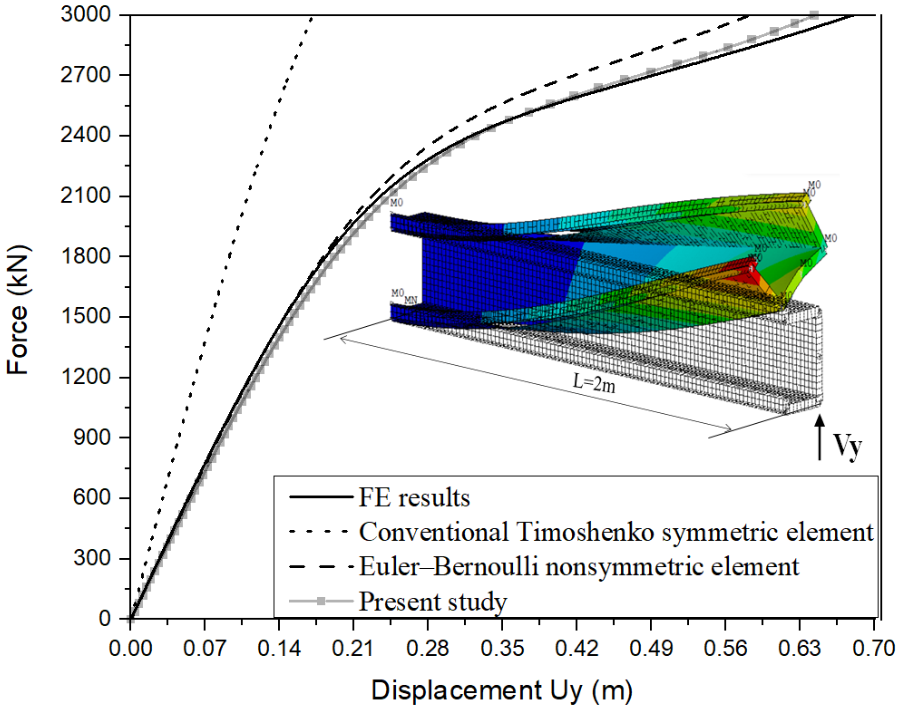

(a) Shear force along y axis

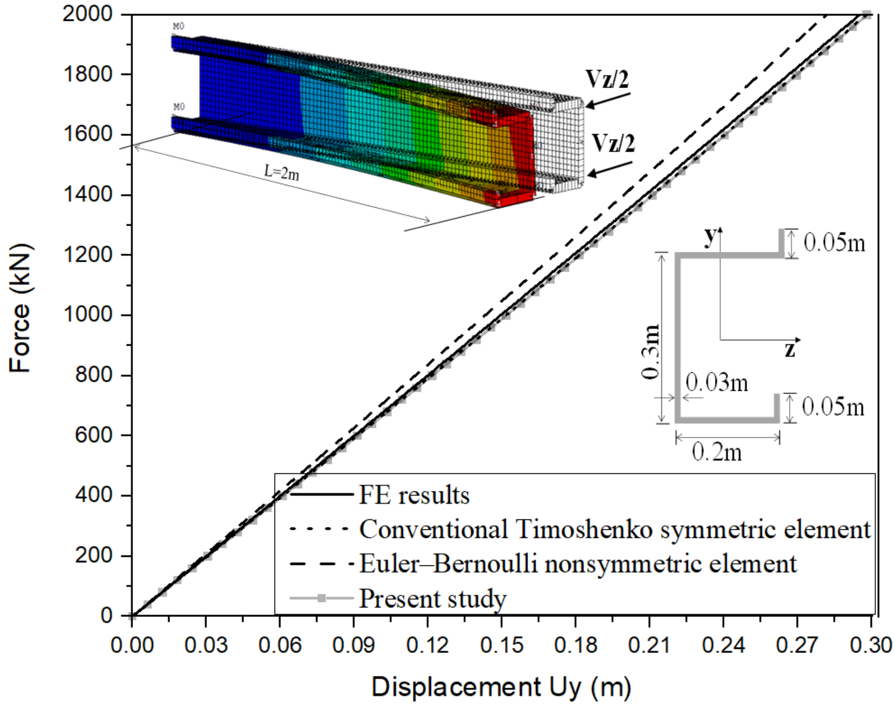

(b) Shear forces along z axis

Figure 5.5 Load-displacement curve for the beam with lipped channel section

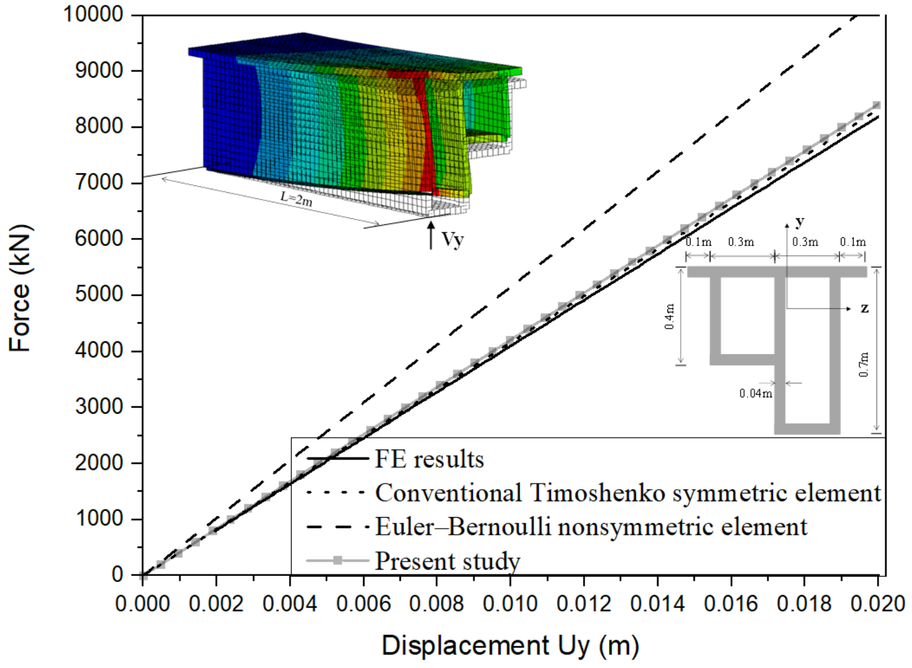

(a) Shear force along y axis

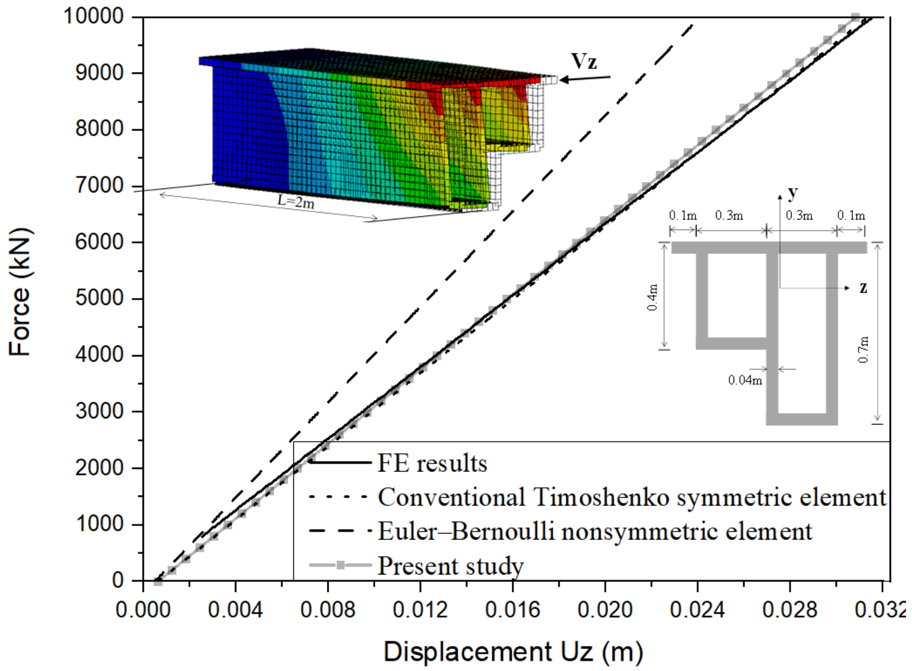

(b) Shear forces along z axis

Figure 5.6 Load-displacement curve for the beam with nonsymmetric box section

CHAPTER 6.

INELASTIC ANALYSIS

6.1 Introduction

An inelastic analysis method for the steel frames with nonsymmetric sections is proposed in this chapter. The concentrated plasticity (CP) model is integrated into the line element formulation given in Chapter 4, and the modified tangent modulus (MTM) approach is adopted to represent partial material yielding, which may be accentuated by the residual stresses. A yield surface, describing the full yield capacity of a section resisting axial force and major-axis bending and/or minor-axis bending, is also given.

The successful structural design for steel structures requires a realistic assessment of the ultimate strength capacity of a structure under extreme loading conditions, such as super-typhoon and seismic events, to ensure structural safety. As such, nonlinear analysis method, which include geometric (second-order) and material (inelastic) nonlinear effects, is crucial and has been extensively studied over the past 65 years (Driscoll 1965; Porter and Powell 1971; King et al. 1992; Ziemian et al. 1992; Chen and Chan 1995; Liew et al. 2000; Thai and Kim 2011; Liu et al. 2014b). The research presented herein mostly adopts the concentrated plasticity (plastic hinge) analysis method for inelastic simulation, aiming for practical application via efficient computational procedures. The modified tangent modulus (MTM) approach, proposed by Ziemian and McGuire (2002), is an implementation of plastic hinge analysis methods that have been used widely for nearly two decades, thereby establishing its robustness and effectiveness. This method has been used in designing systems of steel members with symmetric section shapes and is now expanded in the present study to promote its application for systems of nonsymmetric steel section members.

When analyzing steel members with nonsymmetric sections, another dominant consideration is using line-elements for frame analysis that can simulate the offset between the shear center and the centroid of the cross-section. The line-element formulation given in Chapter 4 is employed in this research.

In this chapter, the concentrated plasticity (CP) model is integrated into the element tangent stiffness matrix, and the MTM approach is adopted to represent partial material yielding, which may be accentuated by the residual stresses. A yield surface, describing the full yield capacity of a section resisting axial force and major-axis bending and/or minor-axis bending, will be required. A matrix describing the gradients at all points on the yield surface will be used to control the plastic flow.

This chapter first presents the assumptions of this research and a brief formulation of the line-element employed for modeling nonsymmetric section. After providing the approach to implement the CP-MTM approach, a divergence-free cross-section analysis algorithm using the fiber section model is proposed to evaluate the full-yield criterion. Finally, the inelastic response and validation are elaborated.

6.2 Assumptions

The following assumptions are made: (1) material remains elastic in the element; however, the deformation due to material yielding is concentrated at potential plastic hinges at the element ends; (2) Plane sections remain plane after deformation; (3) the applied loads are conservative; (4) shear strain is not included, but warping deformation is considered; (5) strain within the element is small, whereas the element deformation can be moderately large via the Updated-Lagrangian formulation used; (6) local buckling and distortional buckling are not considered; and (7) the material's constitutive model for steel is taken as linearly elastic-perfectly plastic.

6.3 Line Element Formulation

The line-element formulation given in Chapter 4 is employed in this chapter. When analyzing steel members with nonsymmetric sections, the dominant features using line-elements for frame analysis include: (1) the Wagner effects; and (2) the noncoincidence of the shear center and centroid of a nonsymmetric section should be considered. This element can capture the nonlinear and buckling behaviors of members with nonsymmetric sections, evidenced by the extensive validations. This chapter extends its application for the geometric and material nonlinear analysis by integrating the CP model into the element tangent stiffness matrix.

As introduced in Chapter 4, the element stiffness matrix $\boldsymbol{k_E}$ can be calculated by,

$$\boldsymbol{k_E} = \boldsymbol{T}(\boldsymbol{k_L} + \boldsymbol{k_G} + \boldsymbol{k_U})\boldsymbol{T}^T \tag{6.1}$$

where $\boldsymbol{k_L}$ has been well established and documented by McGuire et al. (2000); $\boldsymbol{k_G}$ and $\boldsymbol{k_U}$ are geometric stiffness matrices for symmetric and nonsymmetric sections, respectively; $\boldsymbol{T}$ are the transformation matrices.

6.4 Modified Tangent Modulus (MTM) Method

This research extends the application of the line-element formulation given above by integrating the CP model into the element tangent stiffness matrix. The zero-length plastic hinges at the element ends will be used to account for the material nonlinearity. In addition, the MTM approach, which is a straightforward extension of the CP model, is adopted to represent partial material yielding of the cross-section.

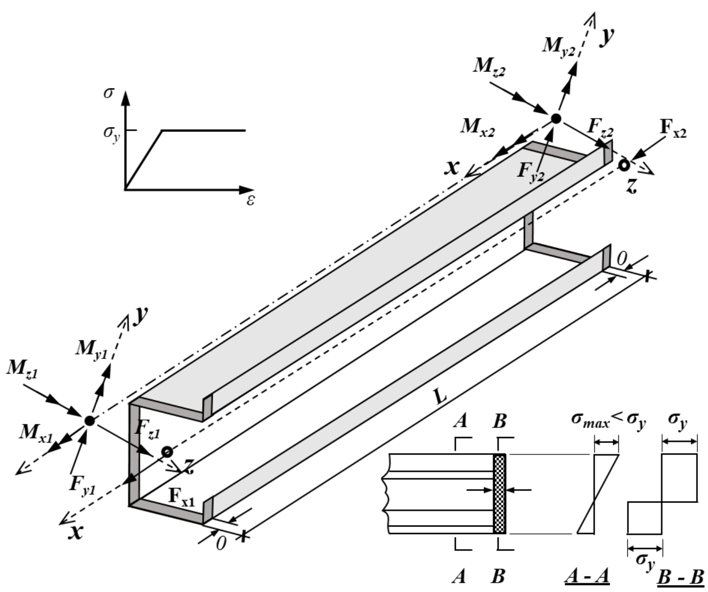

Figure 6.1 Concentrated plasticity (CP) model

6.4.1 Concentrated plasticity (CP) model

The CP model is adopted to consider the material nonlinearity in this research. The total plastic flexural deformation is represented by a zero-length hinge located at one or both ends of the element. The illustration of a CP model with elastic-perfectly-plastic material constitutive is shown in Figure 6.1. Using the CP model can avoid complicated and tedious stress resultant formulation, which is more effective and acceptable when performing the inelastic analysis for massive practical structures.

6.4.2 Implementation

The MTM approach is a straightforward extension of the CP method, which has been used widely for nearly two decades. This research adopts the MTM method to represent partial material yielding, which may be accentuated by the residual stresses. In the MTM method, a reduction factor τ is given for reducing the element tangent stiffness, which is expressed as,

$$E_{tm} = \tau E \; with \; \tau = min\begin{cases} 1.0 \\ (1+2p)\left(1-p-\alpha_y m_y - \alpha_z m_z^2\right) \end{cases} \tag{6.2}$$

in which, $p = |P/P_x|$, $m_y = |M_y/M_{py}|$, and $m_z = |M_z/M_{pz}|$. α_y and α_z are the empirical factors and the values, 0.65 and 1.0, given by Ziemian and McGuire (2002), are adopted.

The factor τ is related to the p, m_y, and m_z values. The corresponding relationships between τ and those values in some general cases are shown in Figure 6.2.

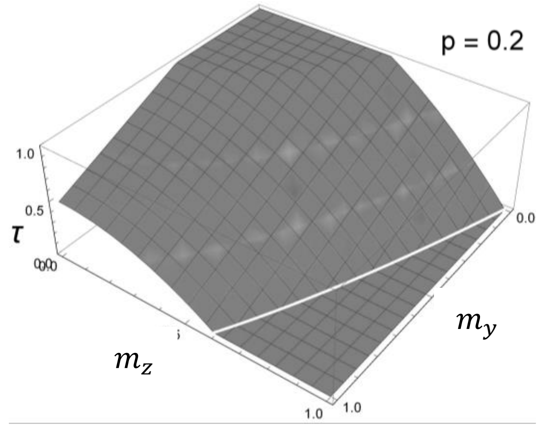

(a) When p = 0.2

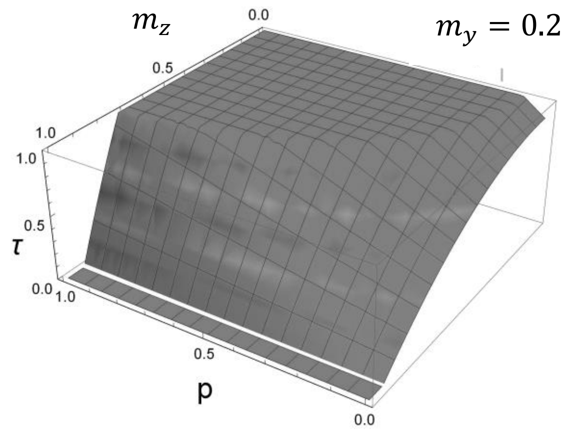

(b) When m_y = 0.2

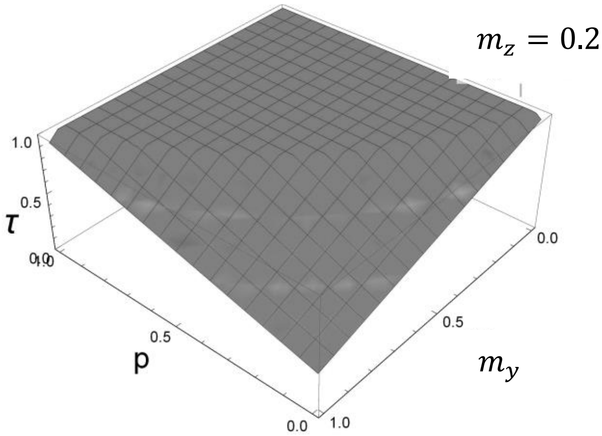

(c) When m_z = 0.2

Figure 6.2 Plots of the τ factor.

The stiffness along the element can be generated by,

$$E(x) = [(1 - x/L)a + b\,x/L]E \tag{6.3}$$

where, a and b are the reduction factors given by,

$$a = E_{tm,1}/E;\, b = E_{tm,2}/E \tag{6.4}$$

in which, $E_{tm,1}$ and $E_{tm,2}$ are the reduced material Young's modulus at the element ends, and the element tangent stiffness matrix given in Equation (6.1) can be rewritten as.

$$\boldsymbol{k_E} = \boldsymbol{T}(\boldsymbol{\rho_{et}} \odot \boldsymbol{k_L} + \boldsymbol{k_G} + \boldsymbol{k_U})\boldsymbol{T}^T \tag{6.5}$$

where $\odot$ represents the Hadamard product, $\boldsymbol{\rho_{et}}$ is the reduction matrix, which can be calculated by,

$$
\boldsymbol{\rho_{et}} =
\begin{bmatrix}
\frac{(a+b)}{2} & 1 & 1 & 1 & 1 & 1 & 1 & \frac{(a+b)}{2} & 1 & 1 & 1 & 1 & 1 & 1 \\
 & \frac{(a+b)}{2} & 1 & 1 & 1 & \frac{(2a+b)}{3} & 1 & 1 & \frac{(a+b)}{2} & 1 & 1 & 1 & \frac{(a+2b)}{3} & 1 \\
 & & \frac{(a+b)}{2} & 1 & \frac{(2a+b)}{3} & 1 & 1 & 1 & 1 & \frac{(a+b)}{2} & 1 & \frac{(a+2b)}{3} & 1 & 1 \\
 & & & 1 & 1 & 1 & 1 & 1 & 1 & 1 & 1 & 1 & 1 & 1 \\
 & & & & \frac{(3a+b)}{4} & 1 & 1 & 1 & 1 & \frac{(2a+b)}{3} & 1 & \frac{(a+b)}{2} & 1 & 1 \\
 & & & & & \frac{(3a+b)}{4} & 1 & 1 & \frac{(2a+b)}{3} & 1 & 1 & 1 & \frac{(a+b)}{2} & 1 \\
 & & & & & & 1 & 1 & 1 & 1 & 1 & 1 & 1 & 1 \\
 & & & & & & & \frac{(a+b)}{2} & 1 & 1 & 1 & 1 & 1 & 1 \\
 & & S & & & & & & \frac{(a+b)}{2} & 1 & 1 & 1 & \frac{(a+2b)}{3} & 1 \\
 & & & & & & & & & \frac{(a+b)}{2} & 1 & 1 & 1 & 1 \\
 & & & & Y & & & & & & 1 & 1 & 1 & 1 \\
 & & & & & & & & & & & \frac{(a+3b)}{4} & 1 & 1 \\
 & & & & & & M & & & & & & \frac{(a+3b)}{4} & 1 \\
 & & & & & & & & & & & & & 1
\end{bmatrix}
\tag{6.6}
$$

6.5 Full-yield Criterion Using a Yield Surface

The plastic hinge will eventually form at the ends of the member with the increment of applied forces. This research adopts the full-yield criterion using a yield surface that describes the full yield capacity of a section resisting axial force and major-axis moment and minor-axis moment.

6.5.1 Full-yield criterion

The basic concepts of the full-yield criterion using yield surface are: (1) sections with force points lie within the yield surface are elastic; (2) sections for which the force points on the yield surface are fully plastic; and (3) points outside the yield surface are not admissible because the material's constitutive model for steel is assumed to be linearly elastic-perfectly plastic. This research proposed a numerical method to estimate whether a force point, like N [P, M_y, M_z], is located inside the yield surface or not. As shown in Figure 6.3, there is a spatial yield surface with the origin point O. When a section internal forces are P, My, and Mz, which can be denoted as point N, there will be an intersection point, N_1 [P_1, M_{y1}, M_{z1}], between the extended line of OP and the yield surface, as shown in Figure 6.3. One thing should be noted is that the bi-moments, M_b, are not considered in the yield surface. This is because the bi-moments are self-equilibrating actions, like the residual stress, they will have no influence on the yield surface.

The corresponding loading ratio L_r will be calculated by,

$$L_r = d/d_1 \tag{6.7}$$

where d and d_1 are the norm of the vector [P, M_y, M_z] and [P_1, M_{y1}, M_{z1}], respectively.

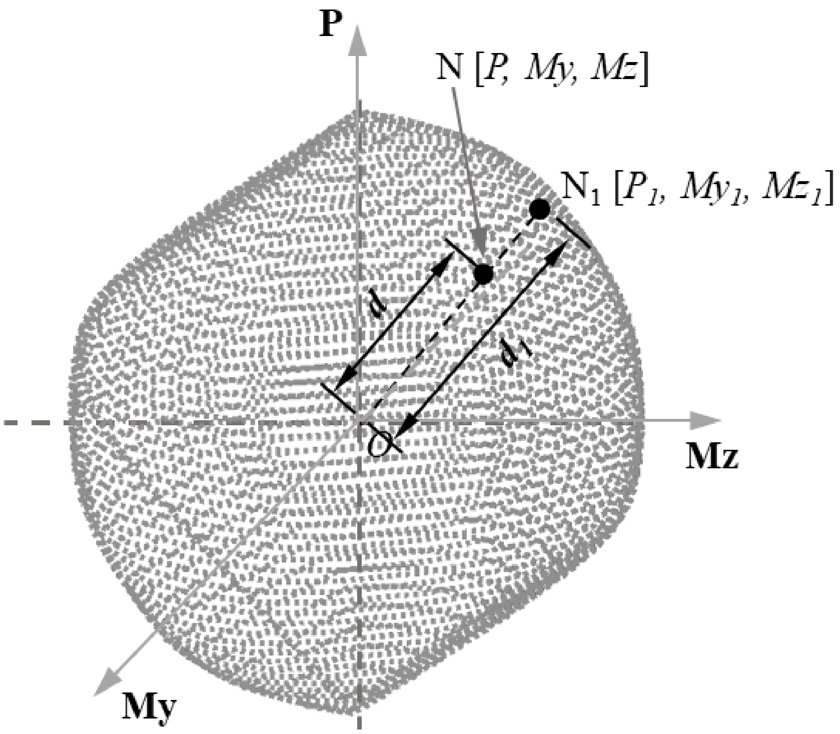

Figure 6.3 A spatial yield surface

When $L_r < 1.0$ indicates that the point N is located inside the yield surface and the related section is elastic. When $L_r = 1.0$, the point N is on the yield surface, and the corresponding section will be regarded as fully plastic. And if $L_r > 1.0$, the point N is outside the yield surface, which is not admissible, a correction of the resisting forces will be conducted.

A spatial yield surface (Figure 6.3), describing the ultimate strength capacity of a section for the axial force and major-axis moment and minor-axis moment, is required and essential for the yield criterion. For the sections with doubly symmetric section shapes, the yield surface can be easily calculated with the equations given by AISC (2016) or McGuire et al. (2000), where the yield surfaces are also symmetric in shape.

Nevertheless, the yield surfaces are nonsymmetric for nonsymmetric sections, which cannot be generated by the conventional equations. Apart from deriving the curve-fitted equations, a rigorous analysis method to calculate the yield surfaces for any section shapes is developed based on the work introduced by Liu et al. (2012).

6.5.2 Cross-section modelling

A cross-section modelling approach has been proposed for the calculation of the yield surfaces. The cross-section will be modelled by nodes and segments, as shown in Figure 6.4, where the segments are the centerline of the section plate, and the nodes are the starting, ending, and intersection of the segments. Each segment is defined by two nodes and a thickness, and the initial coordinates of the nodes are given based on a global Z-O-Y coordinate system.

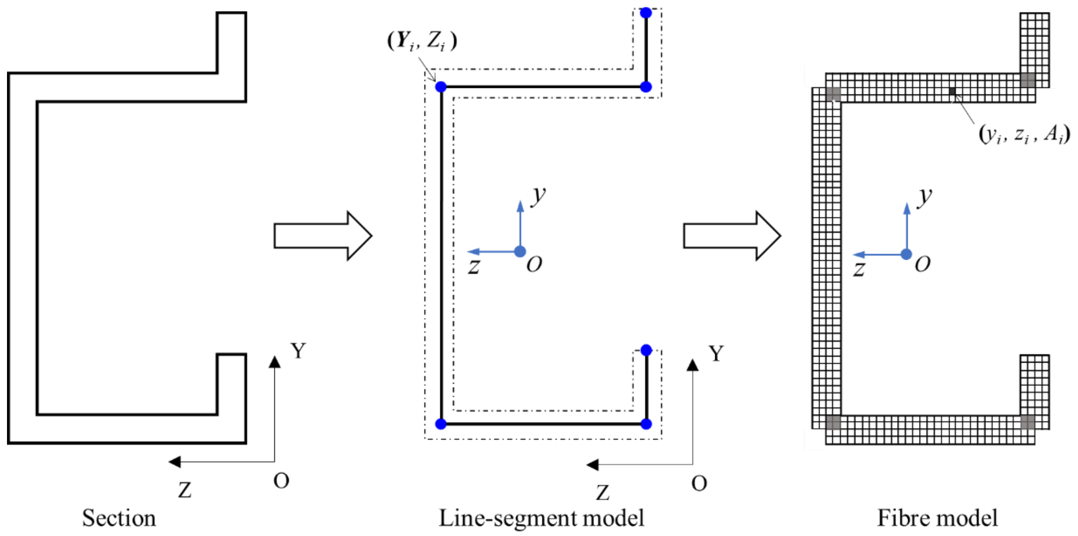

Figure 6.4 Cross-section modelling

The coordinate of the cross-section centroid and some other basic section properties like I_y and I_y can be computed using the cross-section analysis method given above. Then, as shown in Figure 6.4, the segments of the section will be further meshed into small fibers. Each fiber is described by the coordinates of its centroid (y_i, z_i), referring to z-o-y system, and the fiber area (A_i).

6.5.3 Yield surface generation

As shown in Figure 6.5, the strain is linearly distributed in the cross-section according to the Euler-Bernoulli hypothesis. The stress at each fiber can be determined based on the strain level. By referring to the y-z axis system, the overall section capacity can be calculated by the equations as follows to get one data point of the yield surface.

$$P = \sum_{i=1}^{nf} \sigma_i(\varepsilon_i) A_i \tag{6.8}$$

$$M_y = -\sum_{i=1}^{nf} \sigma_i(\varepsilon_i) A_i z_i \tag{6.9}$$

$$M_z = \sum_{i=1}^{nf} \sigma_i(\varepsilon_i) A_i y_i \tag{6.10}$$

where P, M_y and M_z are the section ultimate axial and bending capacities, respectively, n_f is the total number of fibers, y_i and z_i are the coordinates, and σ_i represents the i^{th} fiber's stress generated from constitutive models, and ε_i is i^{th} fiber's strain, which can be calculated by,

$$\varepsilon_i = \varepsilon_u \frac{d_i}{d_n} \tag{6.11}$$

in which, ε_u is the strain of the topmost fiber, which equals to the material ultimate strain, d_n is the location of the neutral axis (Figure 6.5), and d_i is the location of the i^{th} fiber, whose value will be negative if the i^{th} fiber is on the other side of the neutral axis.

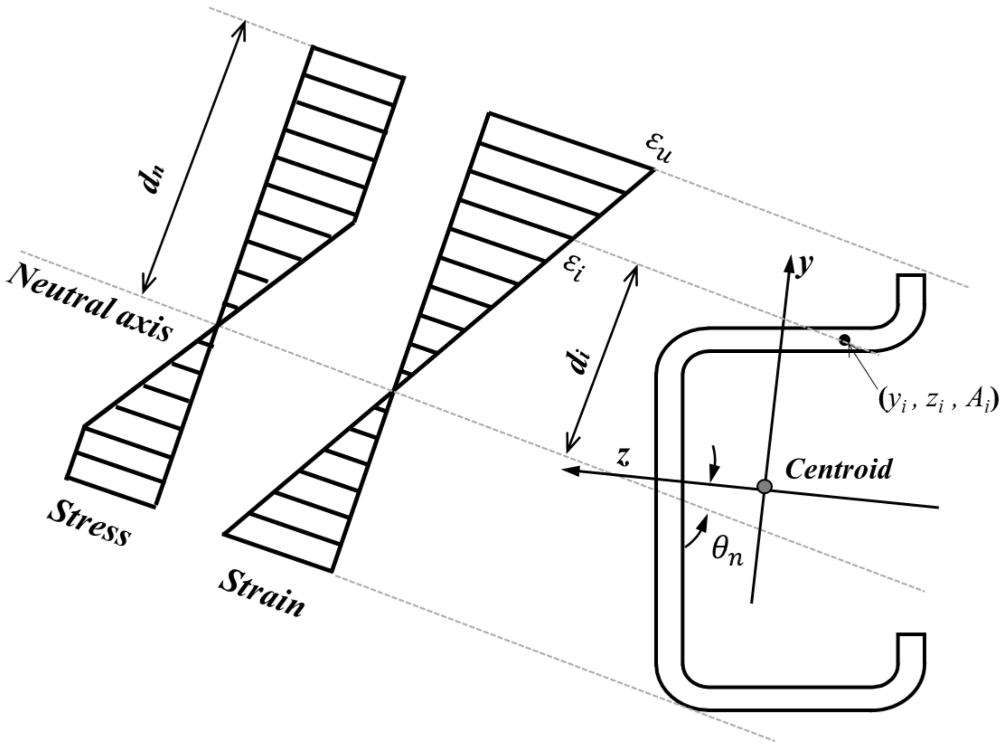

Figure 6.5 Strain and stress over the cross-section

The complete yield surface of any sections can be generated by changing the axial load P_a from the minimum axial strength (tension capacity) to the maximum axial strength (compression capacity) and rotating the inclined angle between the neutral axis and the section axis θ_n (Figure 6.5) from 0 to 2π at each axial load P_a. At a certain angle

θ_n, the strain of the topmost fiber will be assumed to be the ultimate strain ε_u, then the location of the neutral axis d_n will be calculated using the Quasi-Newton algorithm.

$$d_n^{k+1} = d_L^k + \frac{d_U^k - d_L^k}{P_U^k - P_L^k}\left(P_a - P_L^k\right) \tag{6.12}$$

where d_n^{k+1} is the location of the current neutral axis; d_U^k is the location of neutral axis with the axial force P_U^k larger than P_a; and d_L^k is the location of neutral axis with the axial force P_L^k smaller than P_a. Detailed iteration procedure can be found in reference paper given by Chen et al. (2017). Once the location of the updated neutral axis is determined, one data point of the yield surface can be generated with Equation (6.8). The analysis flowchart for the generation of the complete yield surface is elaborated in Figure 6.6. The calculation procedure will give a series of data points, which will form a complete yield surface, as shown in Figure 6.6.

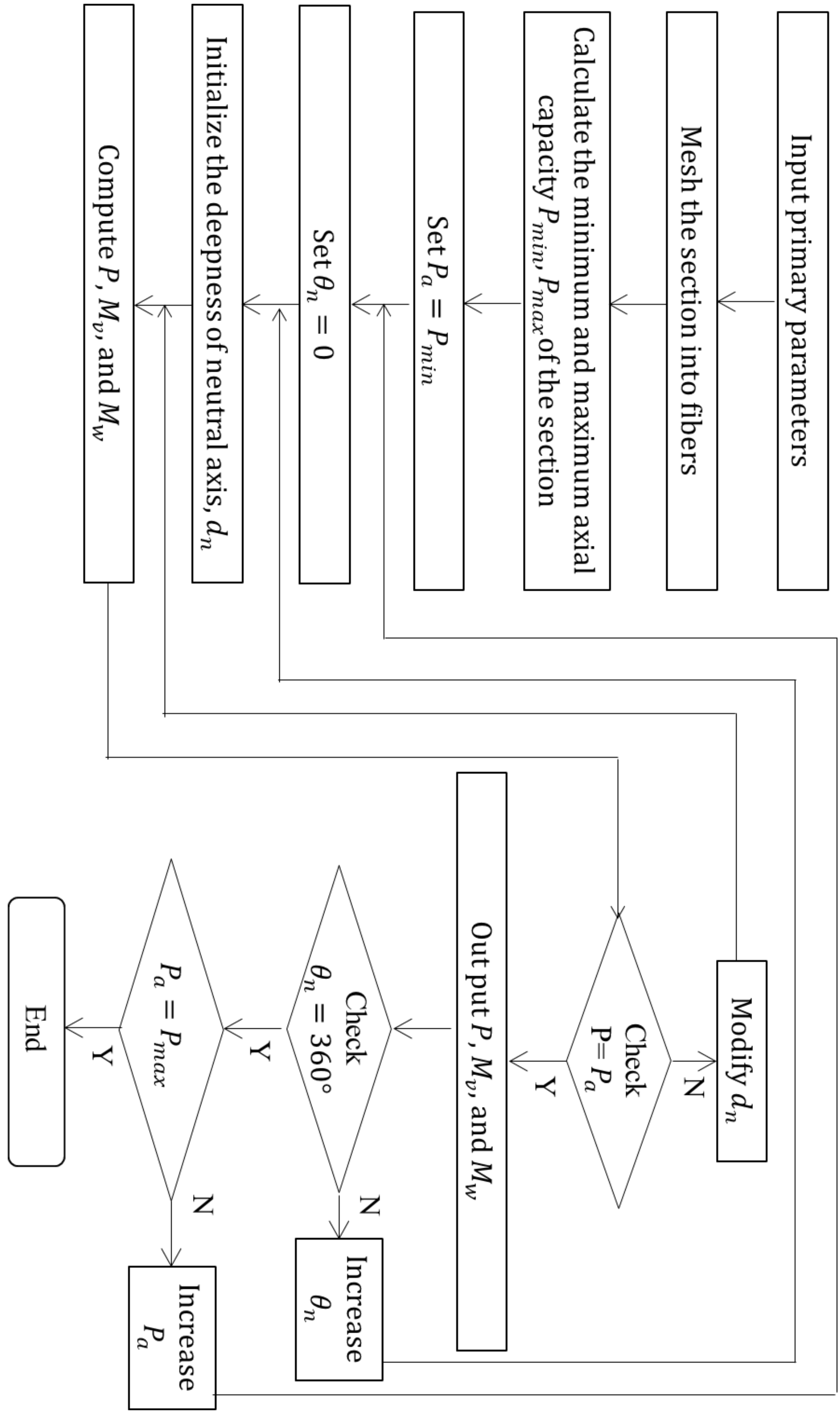

Figure 6.6 A flowchart to generate the complete yield surface

6.6 Post Yielding Behavior

According to the assumption, the plastic deformation will be only concentrated on the end of an element in the CP model. Once the internal member forces point has reached the yield surface, the member may either remain plastic with the force point moving along the yield surface or unload elastically with the force point moving into the yield surface. In this research, the gradient matrix describing the gradients to the yield surface will be calculated to control the plastic flow.

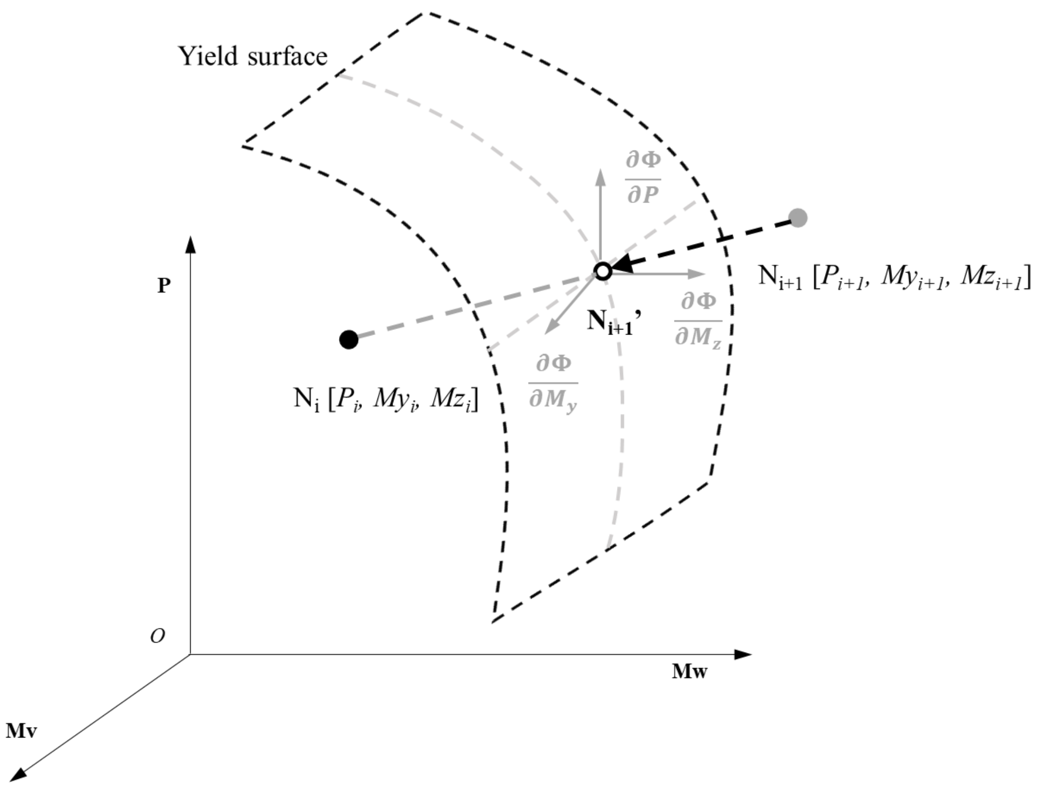

Figure 6.7 Correction of force point outside the yield surface

6.6.1 Correction of force point outside the yield surface

When the loading ratio L_r from Equation (6.7) is larger than 1.0, it indicates that the force point lies outside the failure surface, which is not admissible. As shown in Figure 6.7, at the i^{th} load step, the element end forces are assumed as N_i [P_i, M_{yi}, M_{zi}]. This force point is inside the yield surface, which shows that there is no plastic deformation. While in the next load increment, the force point is increased to N_{i+1} [P_{i+1}, M_{yi+1}, M_{zi+1}], which is outside the yield surface. There are millions of paths to bring this force point back onto the yield surface. In this research, the path connecting N_i and N_{i+1} is chosen and the new equilibrium force point will be N_{i+1}', as shown in Figure 6.7. The coordinate of the N_{i+1}' will be taken as the new resisting forces.

6.6.2 The plastic reduction matrix

The incremental displacement at a plastic hinge can be divided into two parts: the elastic and a plastic displacement:

$$\boldsymbol{d\Delta} = \boldsymbol{d\Delta_e} + \boldsymbol{d\Delta_p} \tag{6.13}$$

As shown in Figure 6.8, since the increment of plastic deformation must be normal to the yield surface, the plastic deformation $\boldsymbol{d\Delta_p}$ can be acquired by the gradients to the yield surface:

$$\boldsymbol{d\Delta_{p1}} = \lambda_1 \boldsymbol{G_1} \tag{6.14}$$

$$\boldsymbol{G_1} = \begin{bmatrix} \dfrac{\partial \Phi}{\partial P_1} \\ \dfrac{\partial \Phi}{\partial M_{y1}} \\ \dfrac{\partial \Phi}{\partial M_{z1}} \end{bmatrix} \tag{6.15}$$

where Φ represents the function of the entire yield surface obtained by the proposed method and $\boldsymbol{G_1}$ is the gradient to it; and λ_1 is the magnitude of the plastic deformation.

Since both ends of the element have the possibility of plastification, the element's plastic deformation can be expressed as:

$$\boldsymbol{d\Delta_p} = \begin{bmatrix} \boldsymbol{d\Delta_{p1}} \\ \boldsymbol{d\Delta_{p2}} \end{bmatrix} = \begin{bmatrix} \boldsymbol{G_1} & \boldsymbol{0} \\ \boldsymbol{0} & \boldsymbol{G_2} \end{bmatrix} \begin{bmatrix} \boldsymbol{\lambda_1} \\ \boldsymbol{\lambda_2} \end{bmatrix} = \boldsymbol{G\lambda} \tag{6.16}$$

in which, $\boldsymbol{G}$ is a matrix and a vital component of the derivation of the plastic reduction matrix. The matrix $\boldsymbol{G}$ contains nonzero elements only when the element ends in the plasticized situation. The primary purpose of this matrix is to reduce axial and rotational resistance.

The linearly elastic-perfectly plastic constitutive model is adopted for steel. Therefore, all the force points located on the yield surface will remain plastic, with the force points moving along the yield surface. Consequently, any incremental of the force vector at those points must follow the elastic relationship:

$$\boldsymbol{dF} = \boldsymbol{k_e d\Delta_e} \tag{6.17}$$

in which $\boldsymbol{d\Delta_e}$ is the incremental elastic deformation.

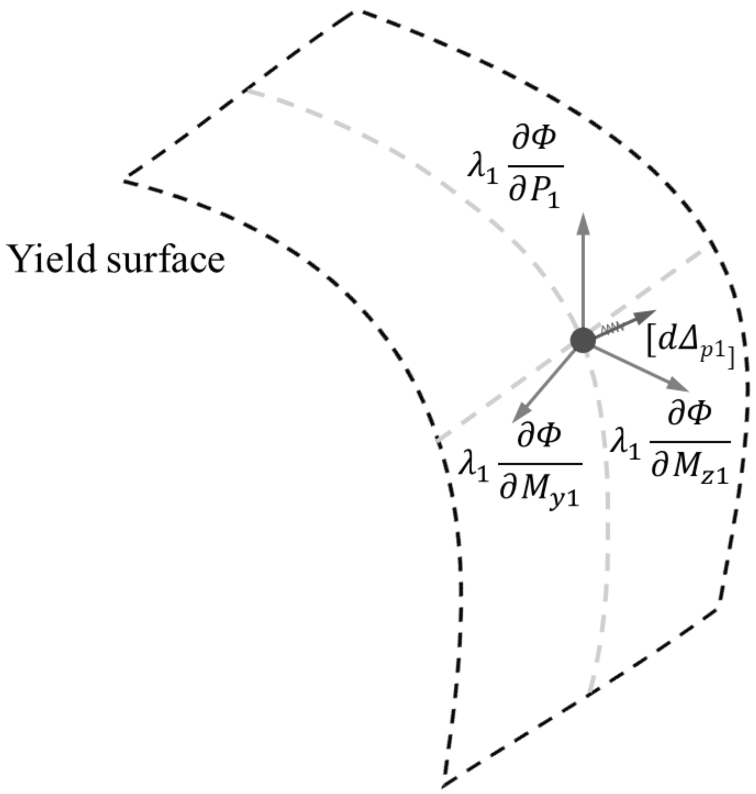

Figure 6.8 Plastic deformation

When the plastic deformation has been accessed by Equation (6.15), the plastic deformation and the incremental force vectors will be orthometric and the following expression can be attained:

$$\boldsymbol{d\Delta_p dF} = \boldsymbol{\lambda G^T dF} = 0 \tag{6.18}$$

Since $\boldsymbol{\lambda}$ is arbitrary, the above expression can be simplified as,

$$\boldsymbol{G^T dF} = 0 \tag{6.19}$$

Using Equations (6.7), (6.15), (6.16), and (6.18), and solving for $\boldsymbol{\lambda}$, the solution can be got:

$$\boldsymbol{\lambda} = [\boldsymbol{G}^{\boldsymbol{T}}\boldsymbol{k_e}\boldsymbol{G}]^{-\mathbf{1}}\boldsymbol{G}^{\boldsymbol{T}}\boldsymbol{k_e}\boldsymbol{d\Delta} \tag{6.20}$$

Similarly, using Equations (6.7), (6.15), (6.16), and (6.19) and solving for $\boldsymbol{dF}$ results in

$$\boldsymbol{dF} = [\boldsymbol{k_e} + \boldsymbol{k_m}]\boldsymbol{d\Delta} \tag{6.21}$$

in which, $\boldsymbol{k_m}$ is the element plastic reduction matrix, which can be generated by,

$$\boldsymbol{k_m} = -\boldsymbol{k_e}\boldsymbol{G}[\boldsymbol{G}^{\boldsymbol{T}}\boldsymbol{k_e}\boldsymbol{G}]^{-\mathbf{1}}\boldsymbol{G}^{\boldsymbol{T}}\boldsymbol{k_e} \tag{6.22}$$

6.6.3 Gradients to the yield surface

For tracing the plastic deformations, the gradients to the yield surface need to be calculated. The yield surface generated by the proposed numerical method consists of a series of discrete data points, as shown in Figure 6.9**.** This yield surface is too complicated to be described with curve-fitted equations. Therefore, a numerical method that is reasonable and practical for computing the gradients to the discrete point on the yield surface has been proposed.

The gradient on a data point of the yield surface will be calculated by,

$$\boldsymbol{\Phi}'(N) = \frac{\boldsymbol{n_1} + \boldsymbol{n_2} + \boldsymbol{n_3} + \boldsymbol{n_4}}{|\boldsymbol{n_1} + \boldsymbol{n_2} + \boldsymbol{n_3} + \boldsymbol{n_4}|} \tag{6.23}$$

in which, $\boldsymbol{n_1}$, $\boldsymbol{n_2}$, $\boldsymbol{n_3}$, and $\boldsymbol{n_4}$ are the normal vectors of the areas around the data point (Figure 6.9). The gradients to each data point on the yield surface will be calculated with the above equation and used to control the plastic flow.

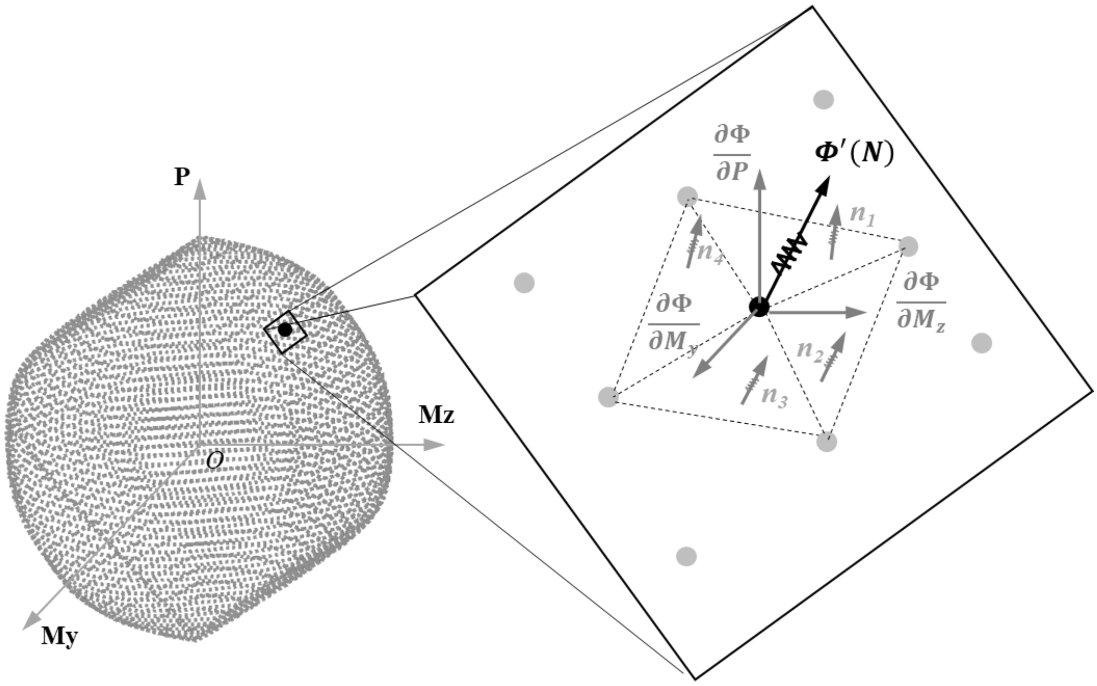

Figure 6.9 Yield surface and the gradient on it

6.7 Numerical Procedure

In present study, an incremental stiffness method based on the Updated-Lagrangian (UL) approach is employed to account for the influence of large deflections on the distribution of internal forces. The UL method is efficient and robust, especially when the element formulation involves large deformations.

6.7.1 Global stiffness matrix and element resistant forces

In the proposed incremental stiffness method, the global stiffness matrix will be assembled by,

$$\boldsymbol{K_E} = \sum_{\boldsymbol{m}=\boldsymbol{1}}^{\boldsymbol{NE}} \boldsymbol{\Gamma^T}[\boldsymbol{k_e} + \boldsymbol{k_m}]\boldsymbol{\Gamma} \tag{6.24}$$

where $\boldsymbol{k_e}$ is the element tangent stiffness matrix generated by Equation (6.5), $\boldsymbol{k_m}$ is the element plastic reduction matrix calculated by Equation (6.22), *NE* represents the total number of elements, and $\boldsymbol{\Gamma}$ is the transformation matrix given by McGuire et al. (2000).

With the element global stiffness matrix, the element incremental forces can be calculated by,

$$\boldsymbol{\Delta R_e^i} = \boldsymbol{K_E}^{\boldsymbol{i}} \boldsymbol{\Delta u_e^i} \tag{6.25}$$

where the superscript *i* denotes the *ith* incremental step, Δu_e^i is the element incremental displacement without rigid body movement. And, then the element total forces can be updated by,

$$\boldsymbol{R_e^{i+1}} = \boldsymbol{R_e^i} + \boldsymbol{\Delta R_e^i} \tag{6.26}$$

6.7.2 Analysis procedure

The flowchart of the numerical analysis procedure for the proposed geometric and material nonlinear analysis is given in Figure 6.10. Firstly, the basic information, including the geometries of the analytical model and cross-section dimension, material parameters, boundary conditions, and the like, are inputted into the program. Then, the section properties, yield surface, and gradients to the yield surface are calculated. Later, the second-order elastic analysis is conducted to get the initial element forces. The reduction factor $\boldsymbol{\tau}$ for Young's modulus E is determined by the MTM method, following which the updated element stiffness and element forces can be obtained. The element end forces will be checked at each step. If the force point is not located inside the yield surface, it indicates that a plastic hinge is formed in the element ends, and the element plastic reduction matrix will be included in the element stiffness matrix. In this research, a nonlinear solution named Predictor-Corrector is adopted to trace the load-displacement path. This solution has been widely employed by serval researchers, such as Ziemian et al. (2021) and Yang et al. (2019), and it is a reliable numerical method.

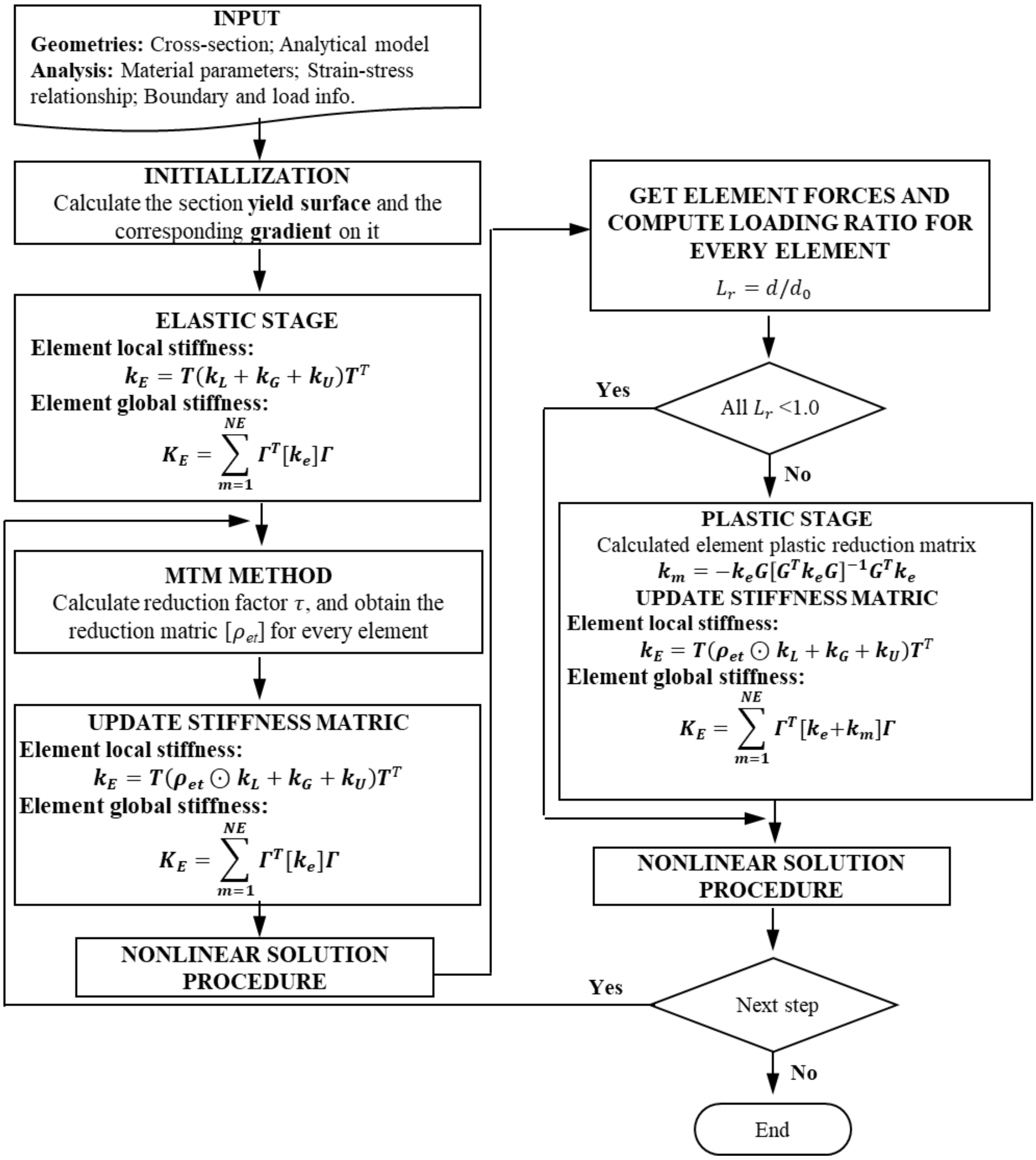

Figure 6.10 Flowchart of numerical analysis procedure

6.8 Verification Examples

Two groups of verification examples are provided to validate the accuracy of the yield surface generation method and the proposed CP-MTM analysis method. In the first example, two sets of cross-sections, doubly symmetric sections and non-symmetric sections, are studied. The yield surfaces generated by the proposed rigorous cross-section analysis method are validated via the analytical solutions and the well-developed computational method. Then the geometric and material nonlinear analyses for steel members with I-section, Channel section, and non-symmetric cross-section under different boundary and loading conditions are conducted.

6.8.1 Verification of the yield surfaces generation

Example 1: Symmetric sections

This example verifies the accuracy of the yield surface generation for symmetrical cross-sections, including a wide flange I-section, a double web section, and a circular hollow section. The dimensions of the cross-sections are given in Figure 6.11. Those cross-sections were studied by Chen and Atsuta (1972). They provided accurate results of the M_y vs M_z curve under different axial force levels. Same My vs M_z curves are calculated and provided in Figure 6.12. The load values were normalized to obtain a more general cross-sectional load relationship. Since the sections are doubly symmetric and the full M_y vs M_z curve will also be doubly symmetric, only one-quarter of the resulting curves are given.

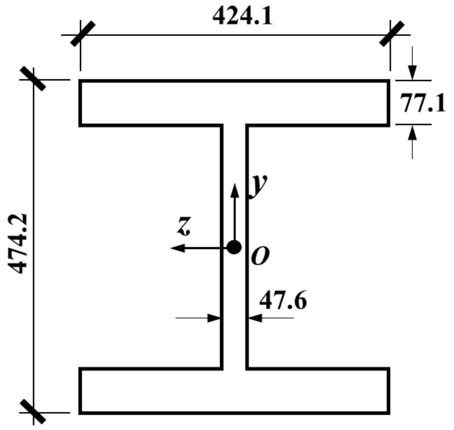

(a) Wide flange I-section

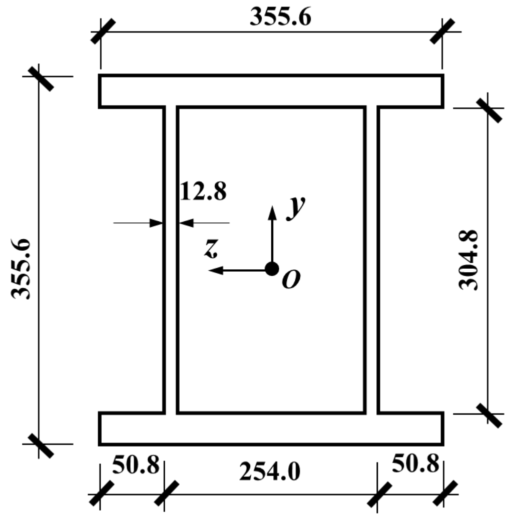

(b) Double web section

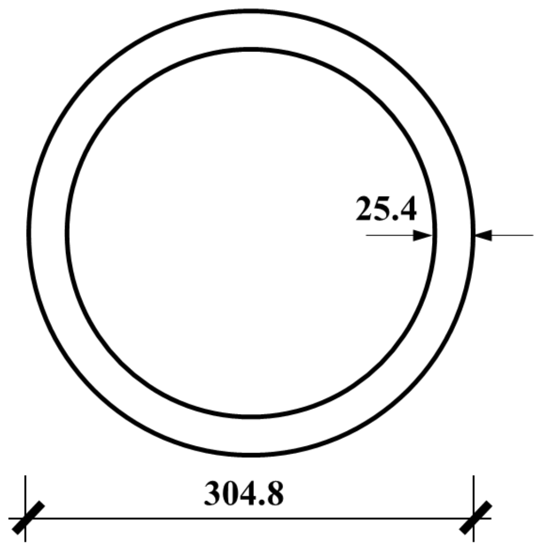

(c) Circular Hollow section

Figure 6.11 Doubly symmetric sections (Unit: mm)

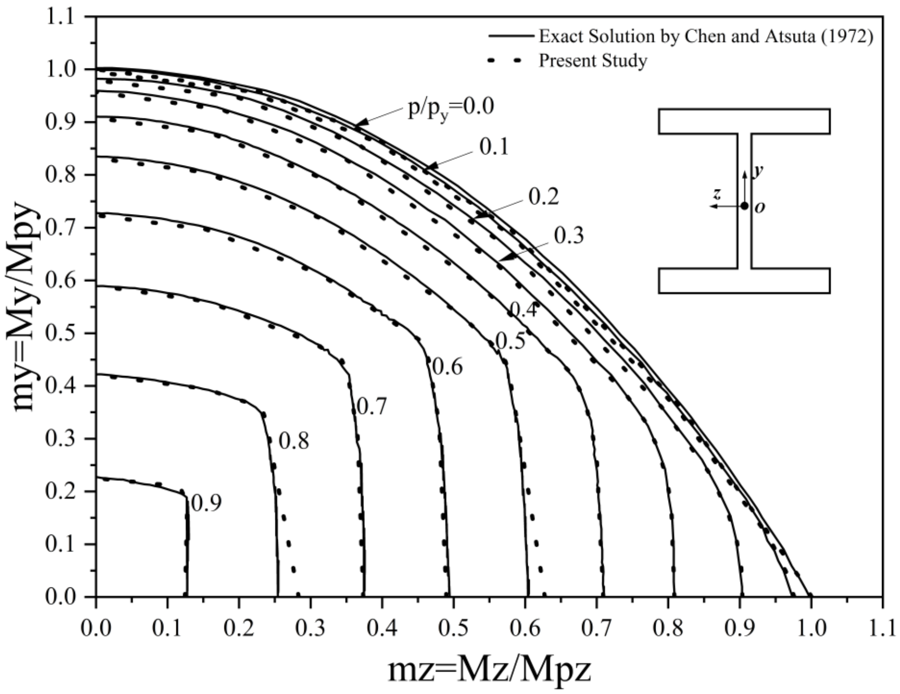

(a) Wide flange section

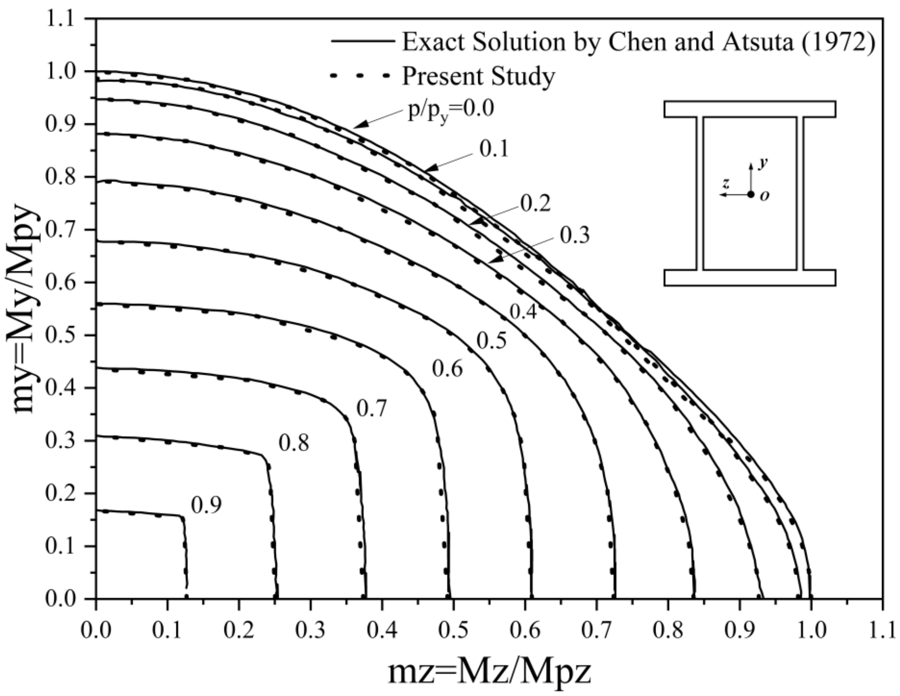

(b) Double web steel section

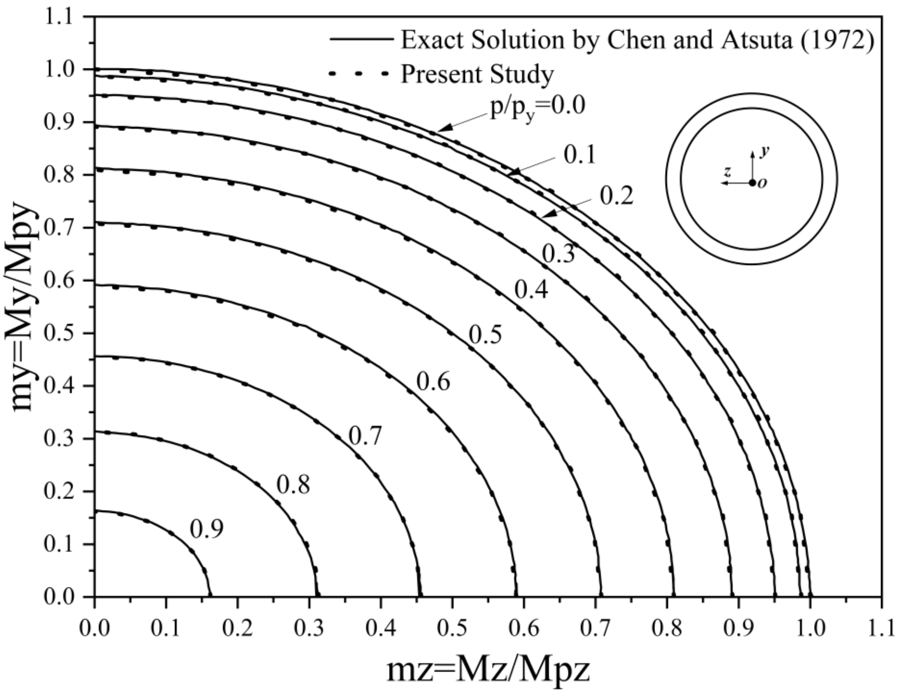

(c) Hollow steel section

Figure 6.12 Comparison results for the doubly symmetric sections

The solid lines plotted in Figure 6.12 are the close-formed solutions provided by Chen and Atsuta (1972), and the dotted points depict the results from the proposed approach. The results agree with each other well, verifying the validity of the yield surface generation for symmetrical cross-section.

Example 2: Nonsymmetric sections

This example is given to verify the reliability of the proposed yield surface generation method for nonsymmetric sections. Four nonsymmetric sections (Figure 6.13), including an angle section, a T-section, a nonsymmetric lipped channel section, and a highly irregular section, are studied. The *P-My*, *P-Mz*, *P-Mv*, *P-Mw*, *My–Mz*, and *Mv–Mw* curves (*v-w* is the section principal axis) generated from the proposed yield surface generation algorithm are compared with those given by the advanced cross-sectional analysis method invented by Liu et al. (2012). Results from the calculation methods recommended by AISC (2016) and McGuire et al. (2000) are also plotted in Figure 6.14 to Figure 6.17.

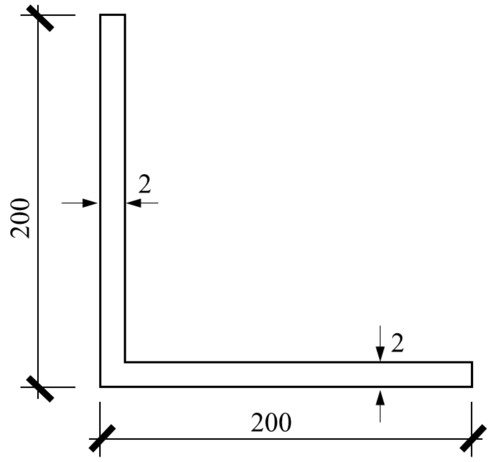

(a) Section A

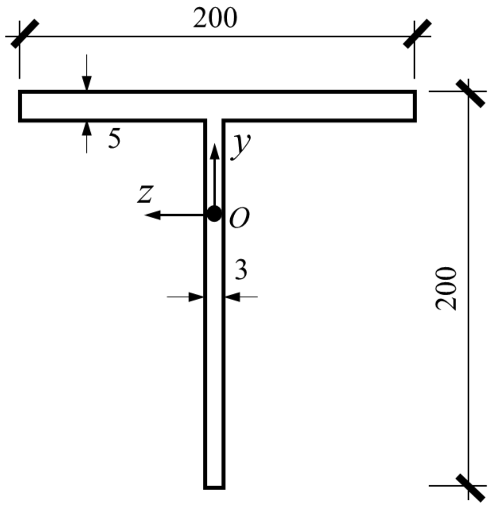

(b) Section B

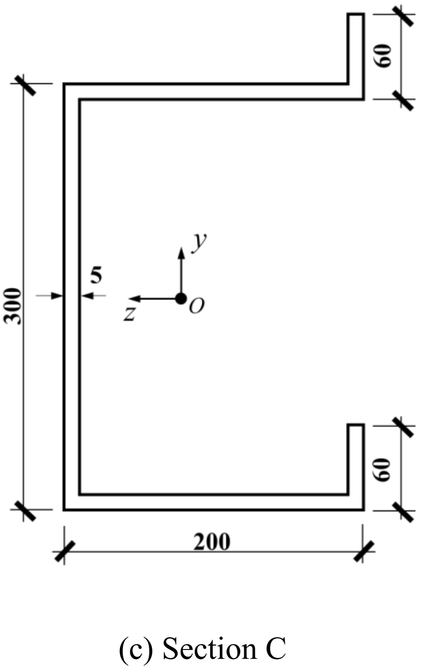

(c) Section C

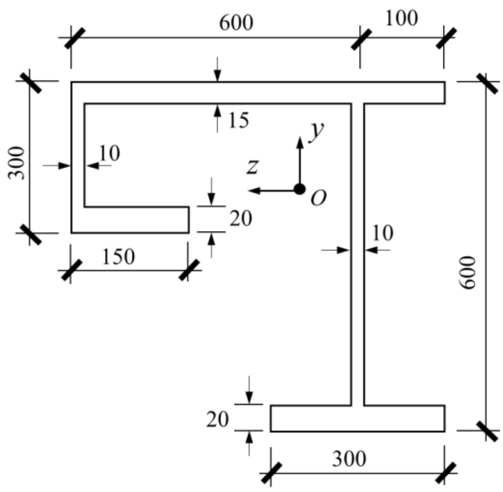

(d) Section D

Figure 6.13 Nonsymmetric sections (Unit: mm)

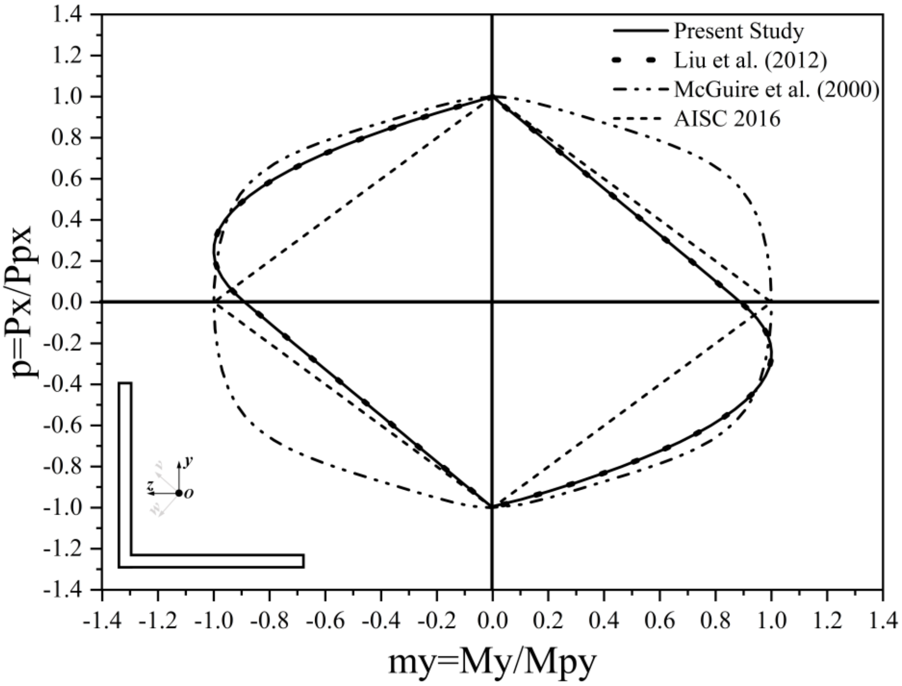

(a) Interaction curve of p vs m_y of section A

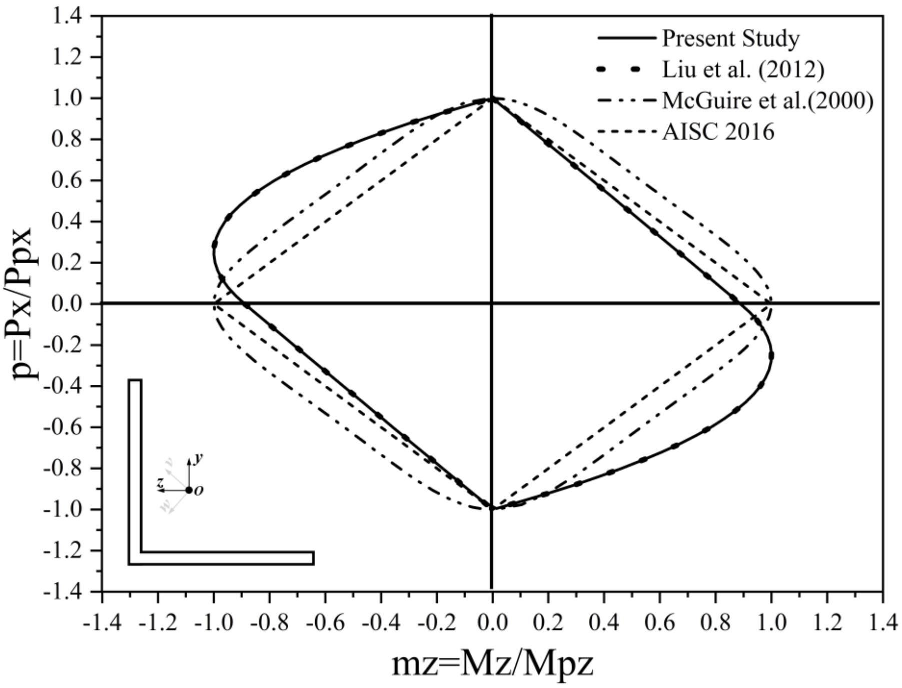

(b) Interaction curve of p vs m_z of section A

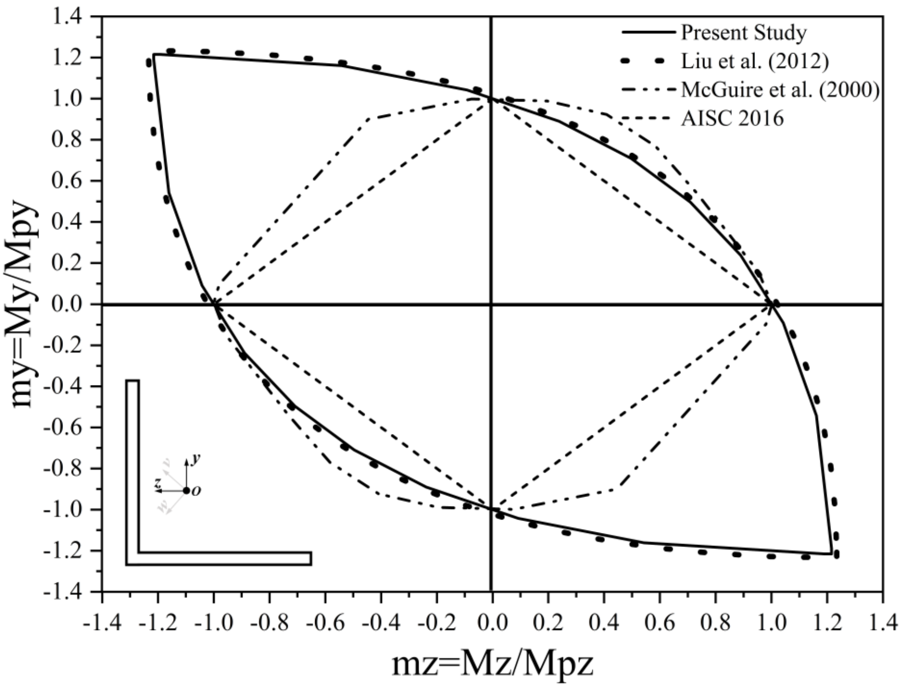

(c) Interaction curve of m_y vs m_z of section A

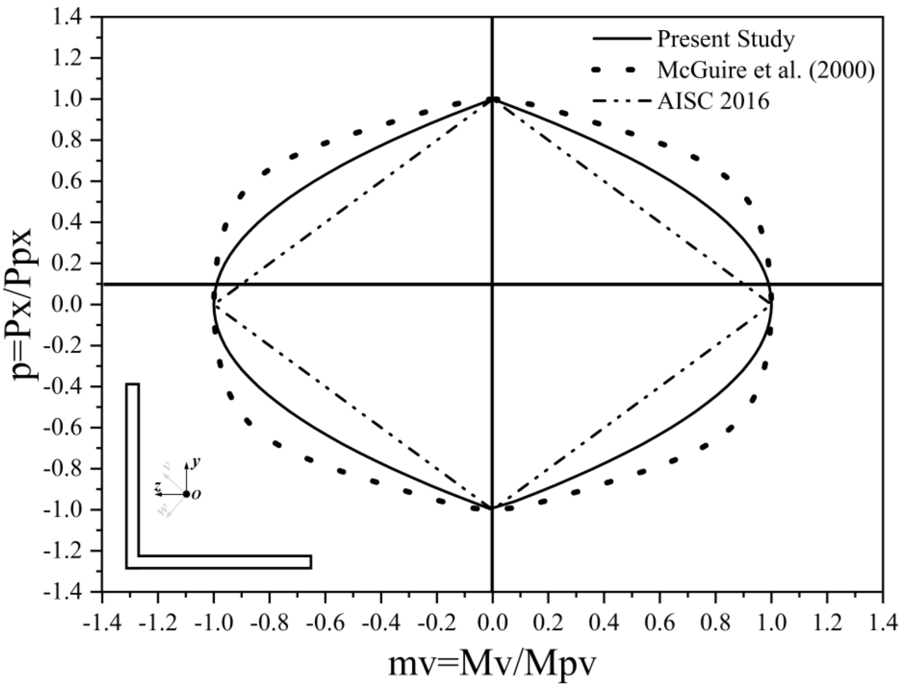

(d) Interaction curve of p vs m_v of section A

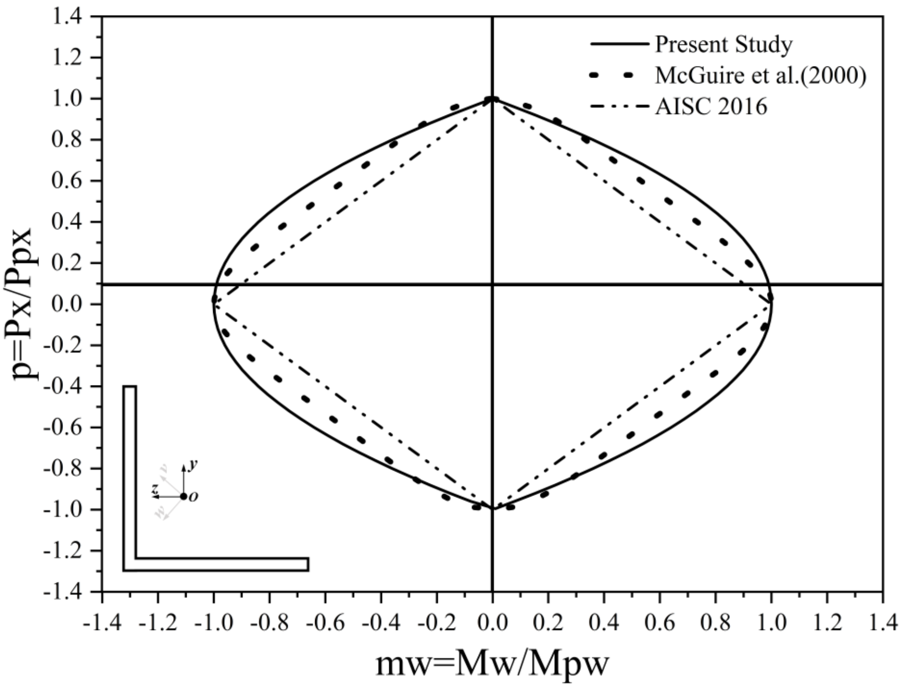

(e) Interaction curve of p vs m_w of section A

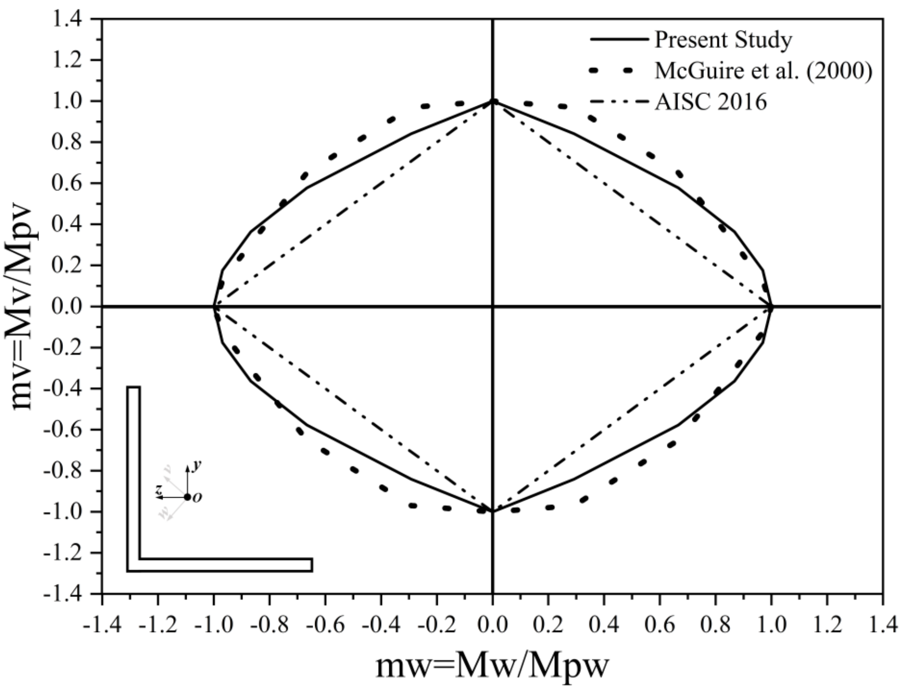

(f) Interaction curve of m_v vs m_w of section A

Figure 6.14 Comparison results for section A

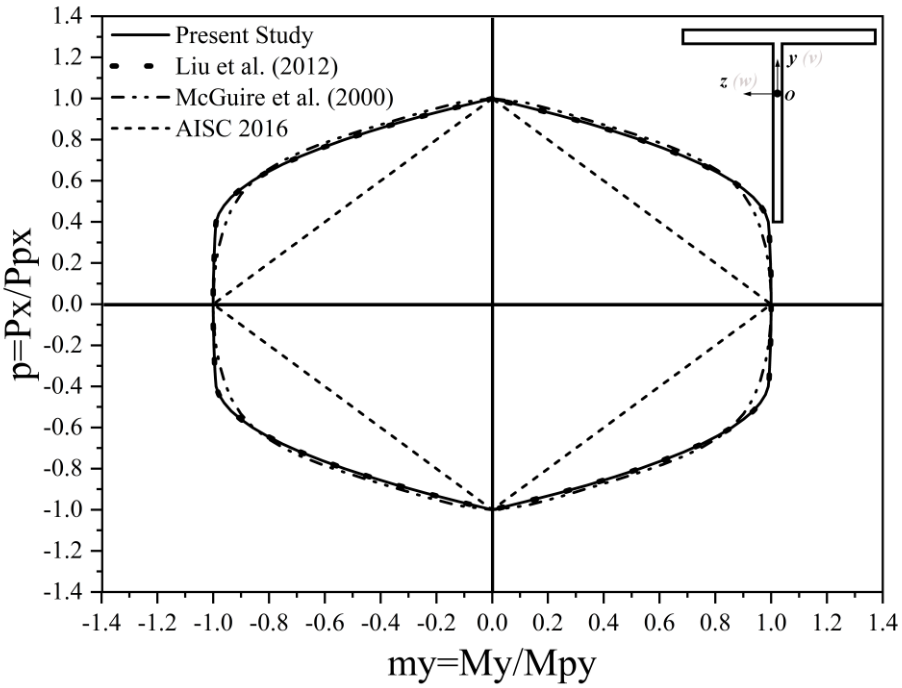

(a) Interaction curve of p vs m_y of section B

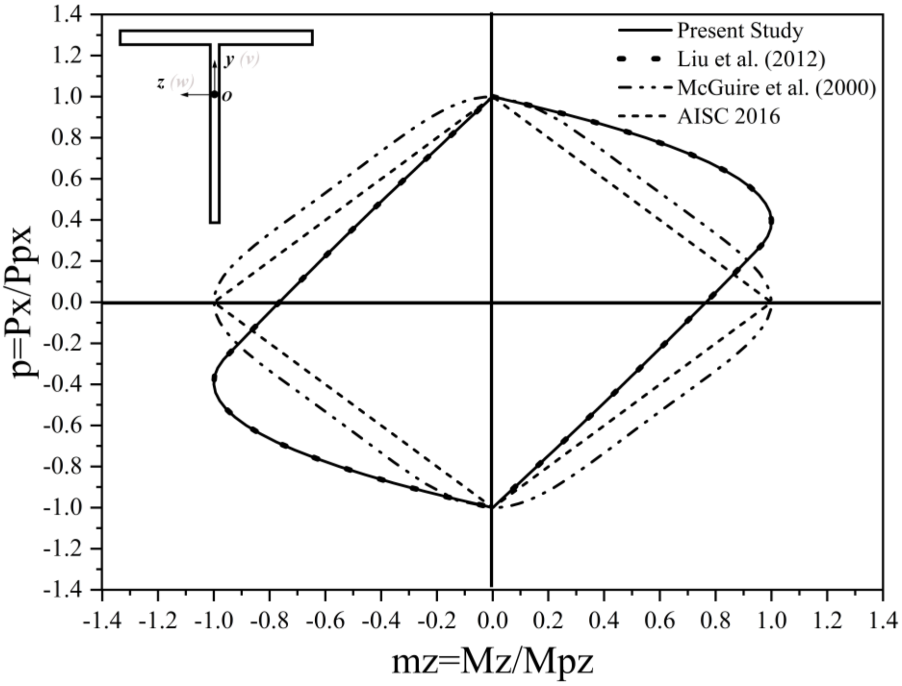

(b) Interaction curve of p vs m_z of section B

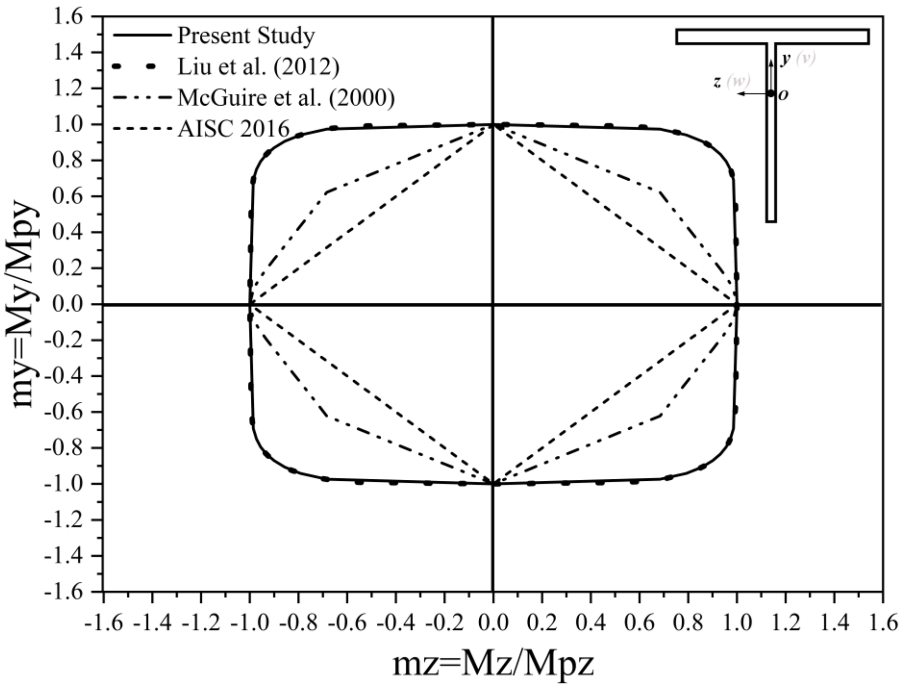

(c) Interaction curve of m_y vs m_z of section B

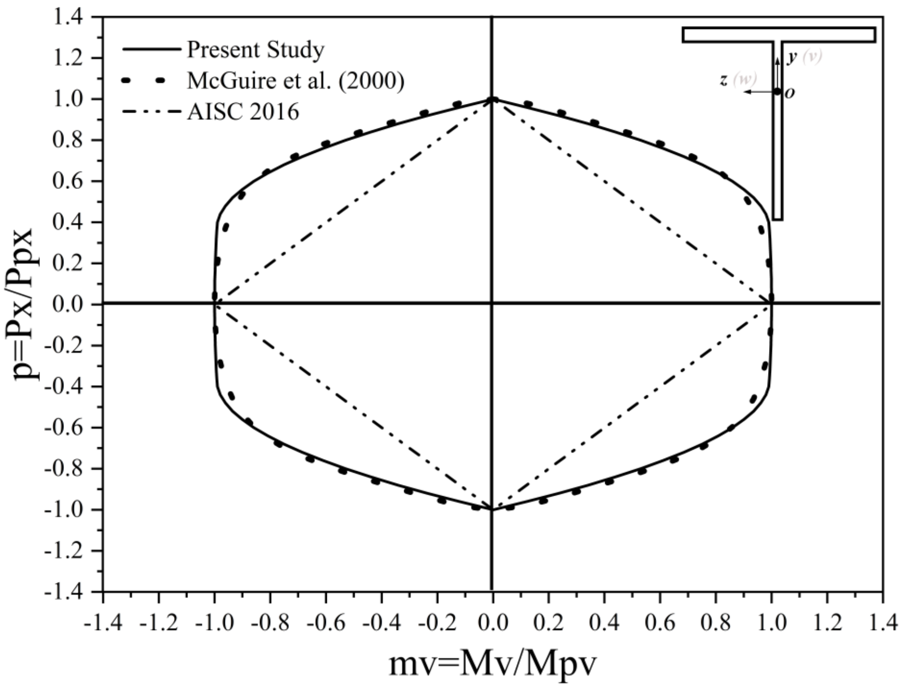

(d) Interaction curve of p vs m_v of section B

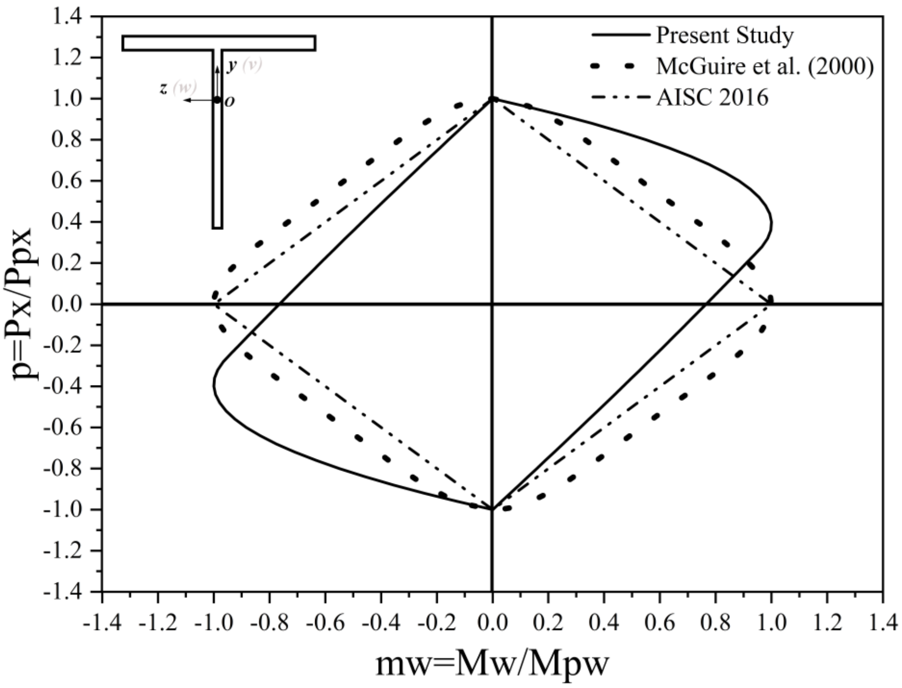

(e) Interaction curve of p vs m_w of section B

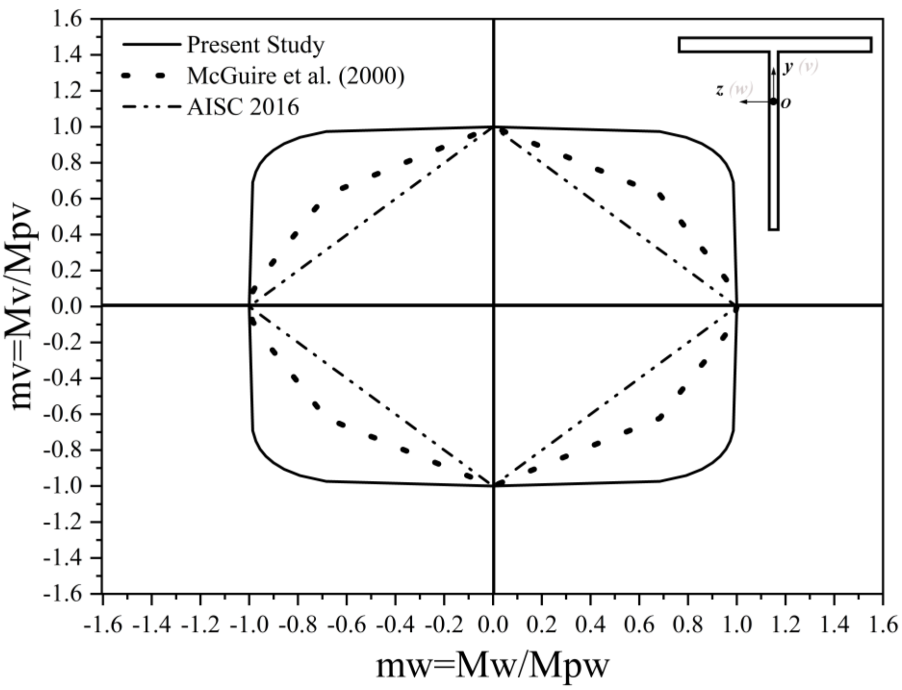

(f) Interaction curve of m_v vs m_w of section B

Figure 6.15 Comparison results for section B

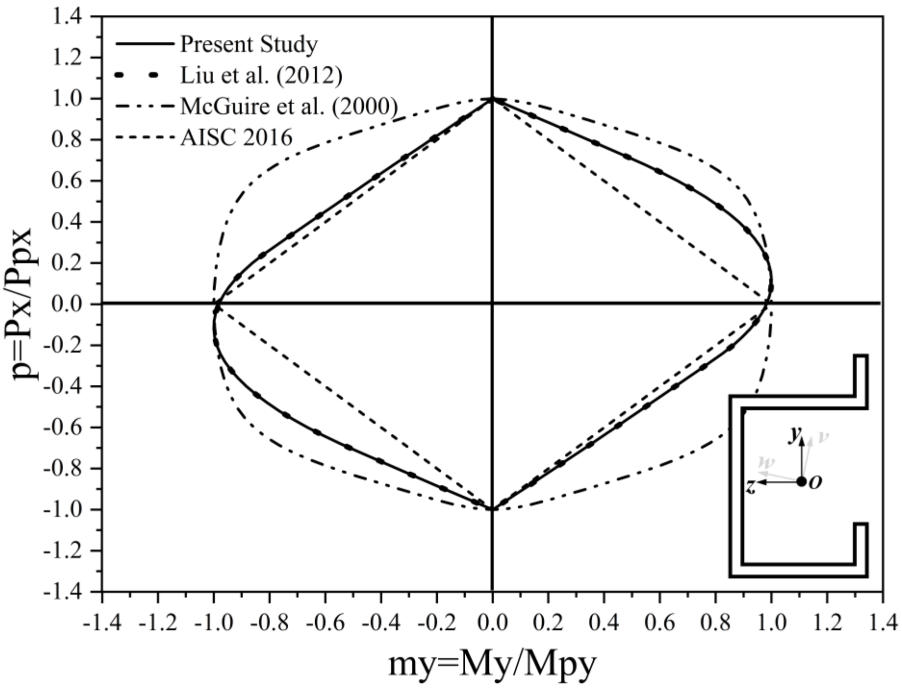

(a) Interaction curve of p vs m_y of section C

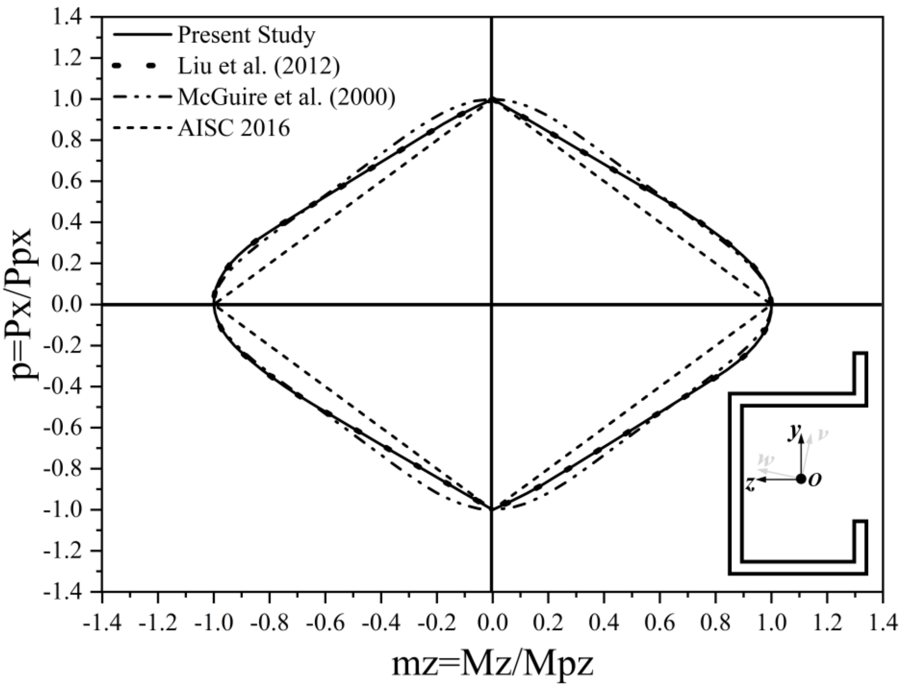

(b) Interaction curve of p vs m_z of section C

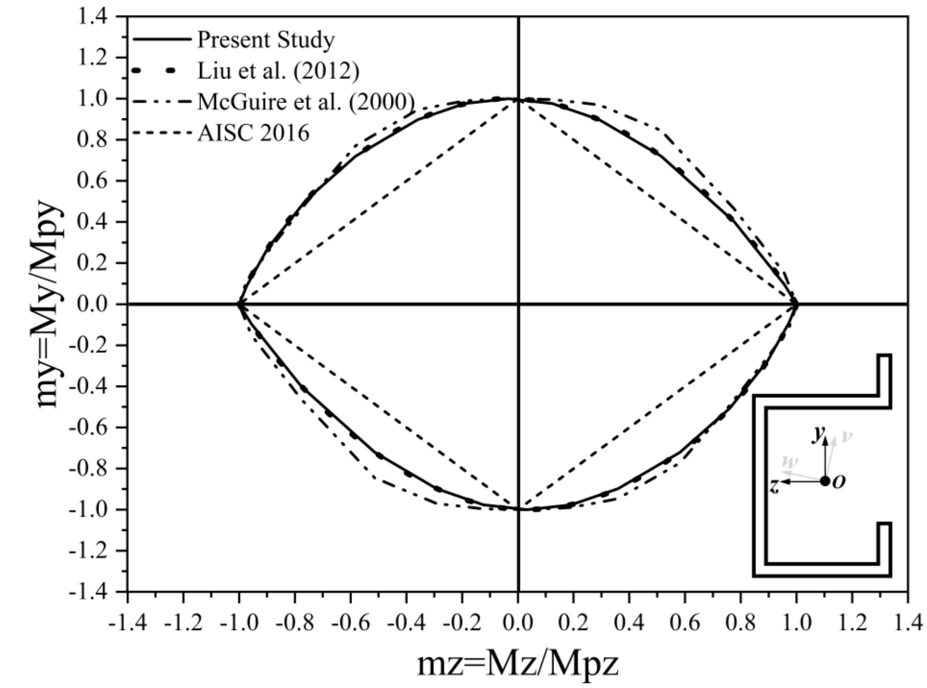

(c) Interaction curve of m_y vs m_z of section C

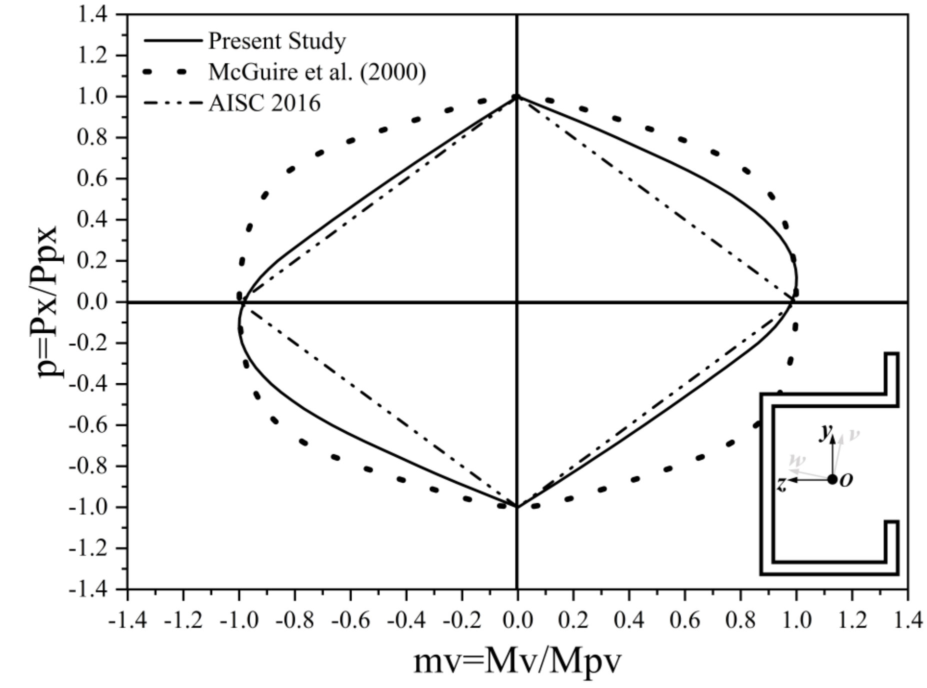

(d) Interaction curve of p vs m_v of section C

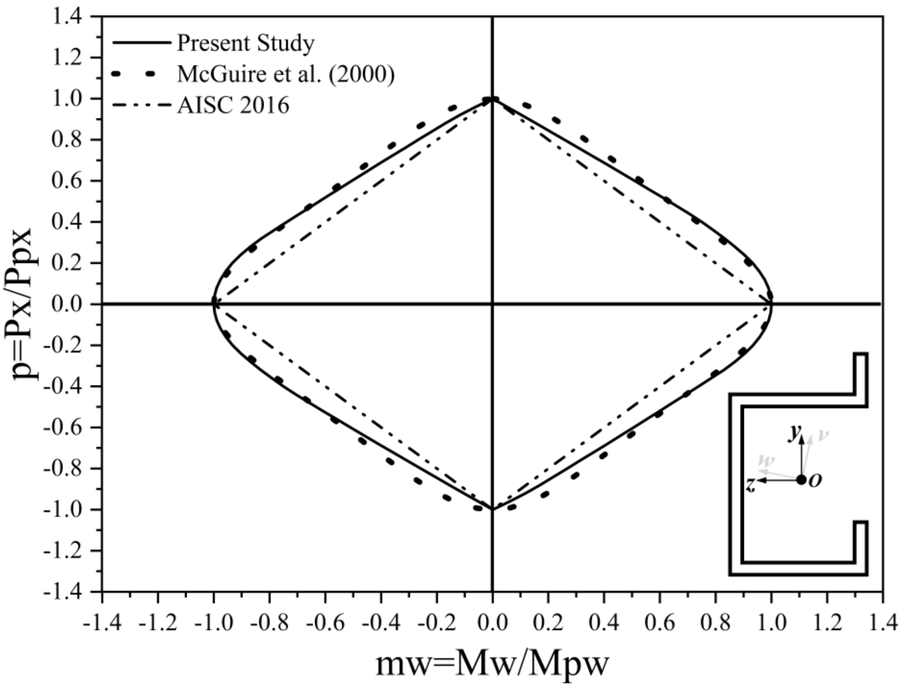

(e) Interaction curve of p vs m_w of section C

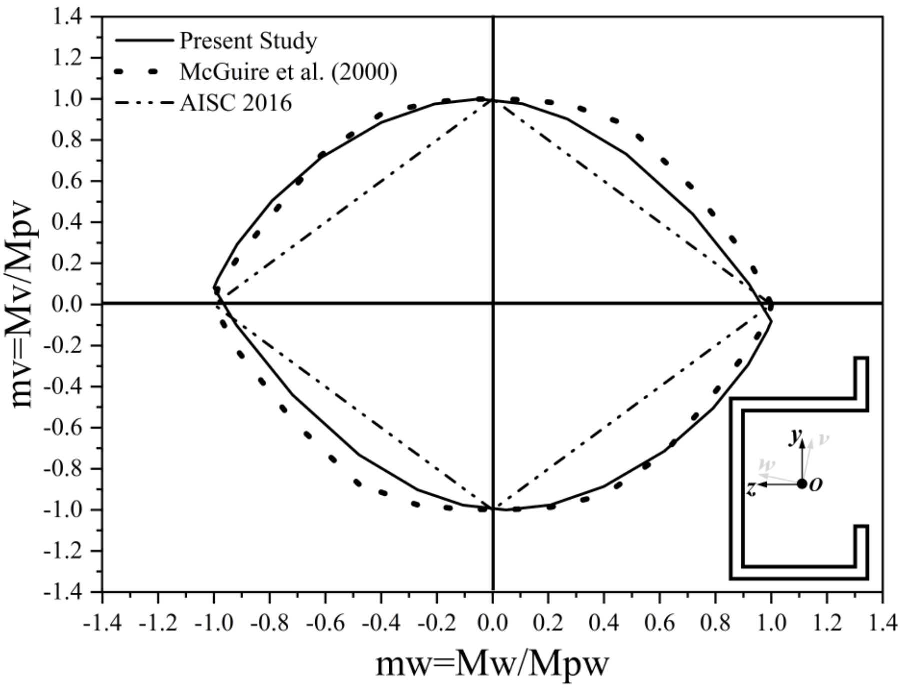

(f) Interaction curve of m_v vs m_w of section C

Figure 6.16 Comparison results for section C

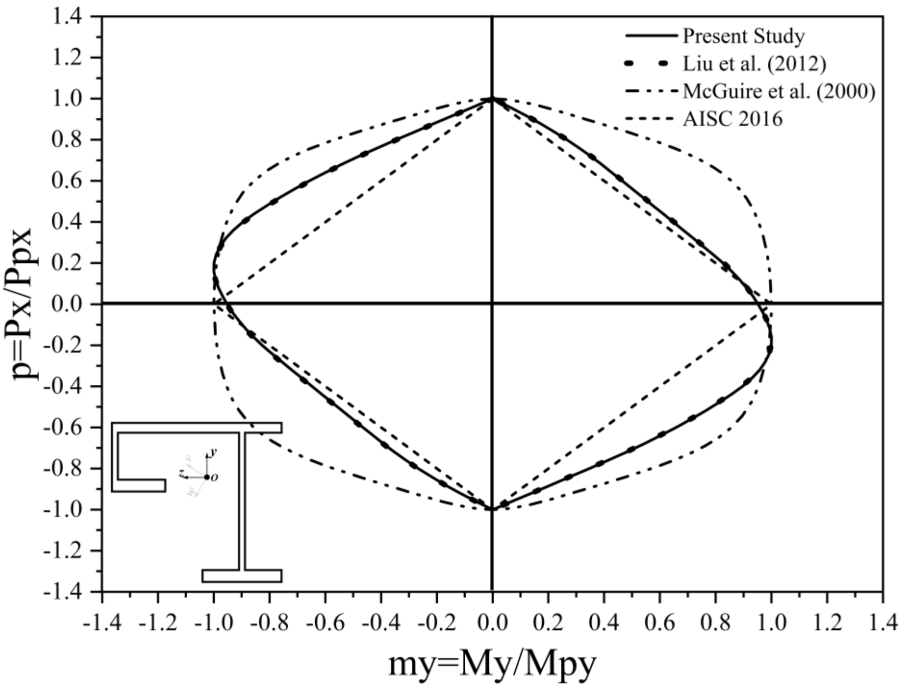

(a) Interaction curve of p_x vs m_y of section D

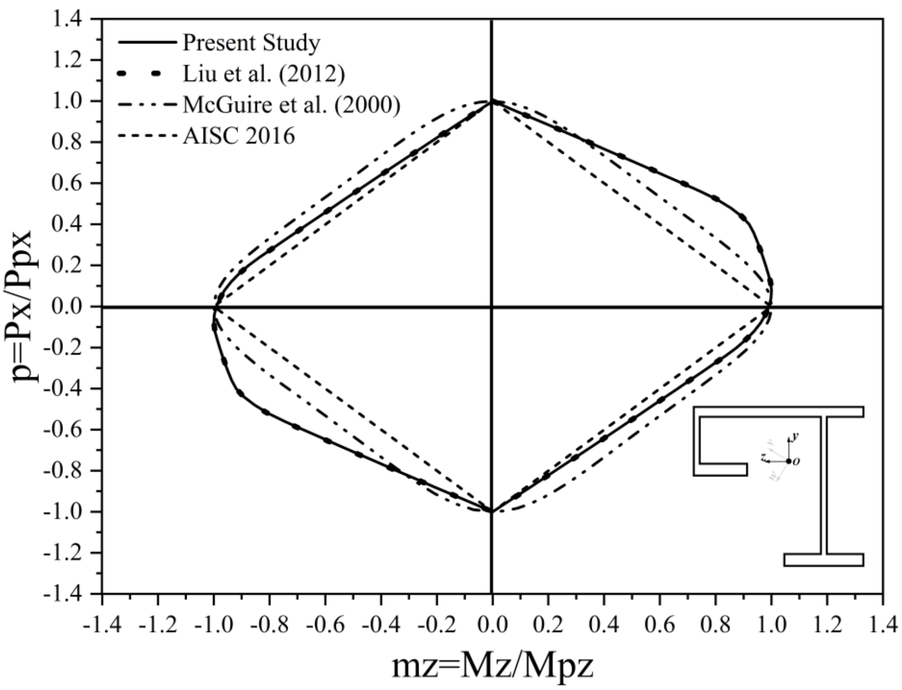

(b) Interaction curve of p_x vs m_z of section D

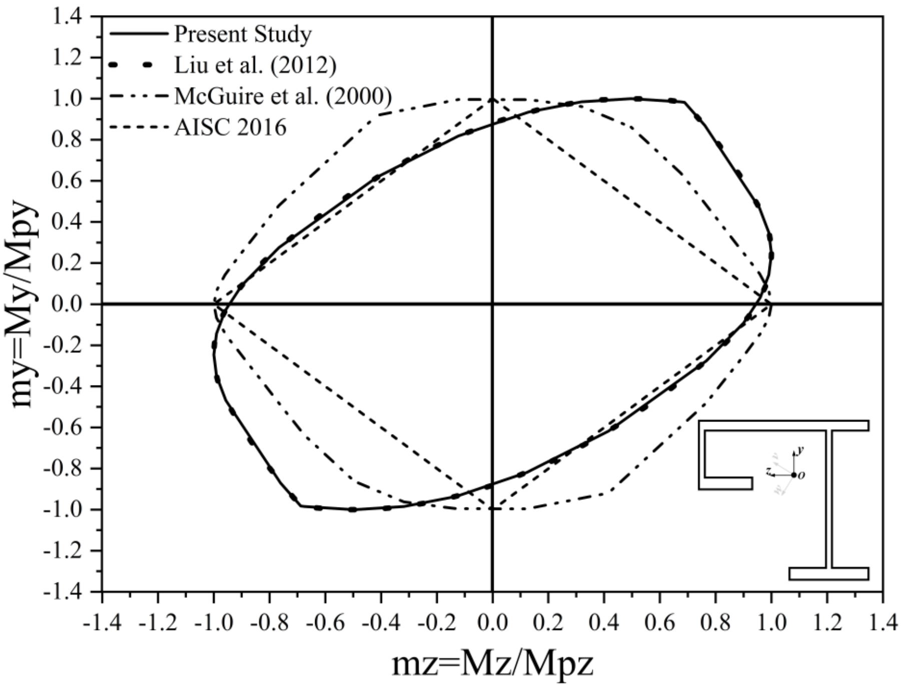

(c) Interaction curve of m_y vs m_z of section D

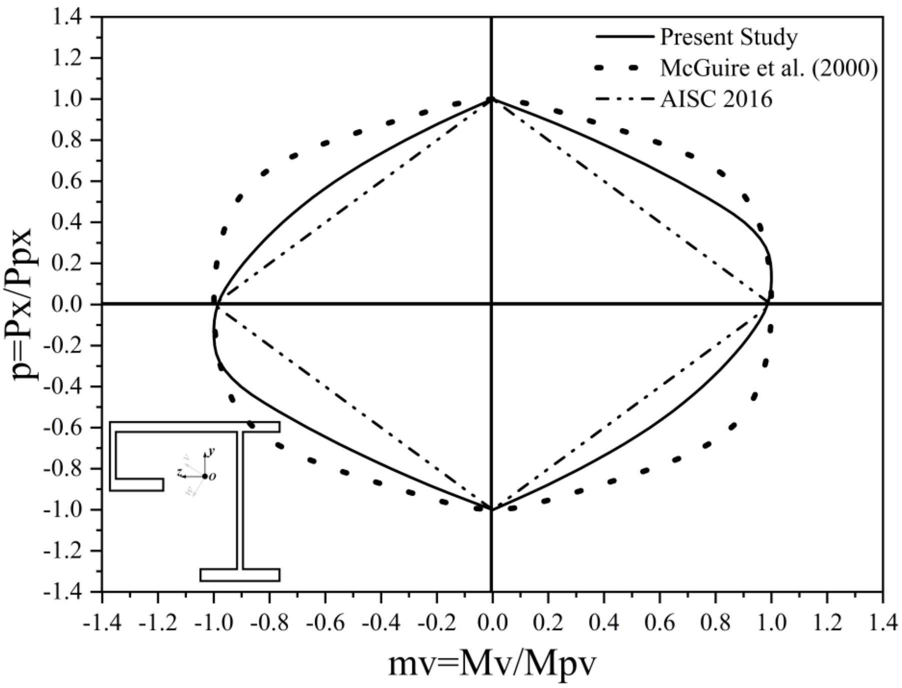

(d) Interaction curve of p_x vs m_v of section D

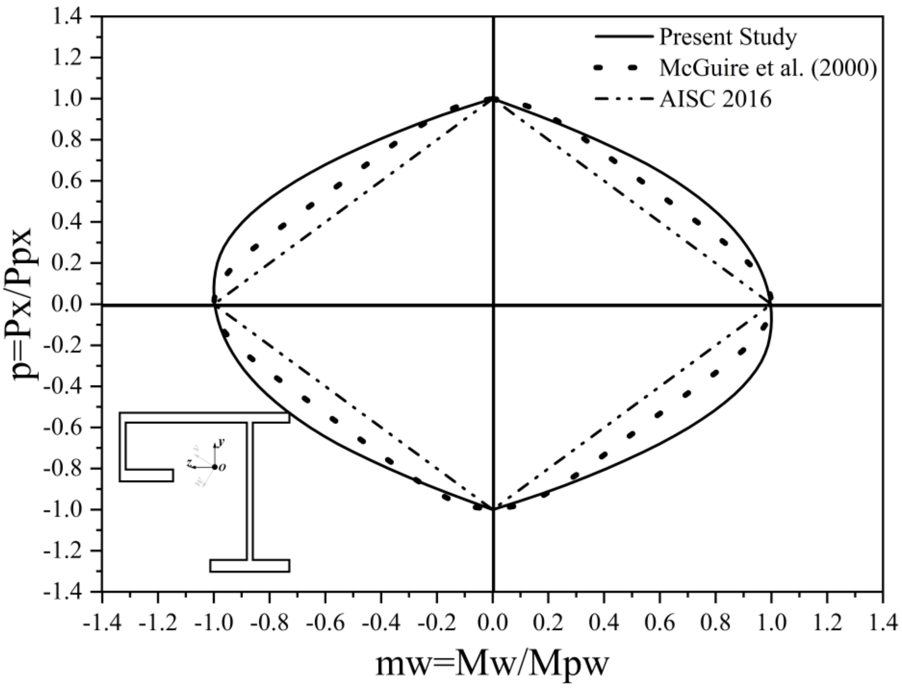

(e) Interaction curve of p_x vs m_w of section D

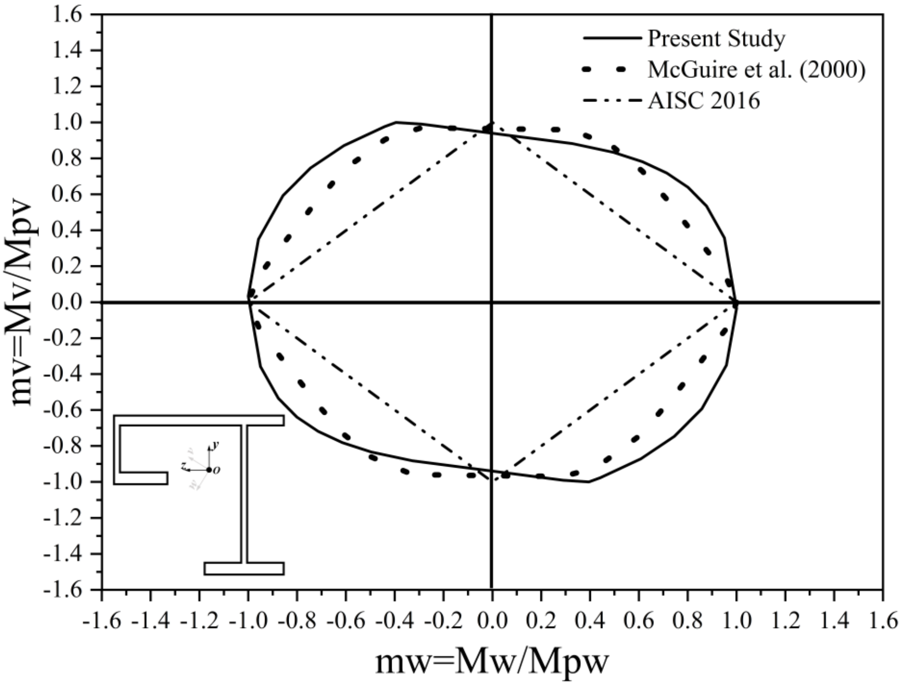

(f) Interaction curve of m_v vs m_w of section D

Figure 6.17 Comparison results for section D

From Figure 6.14, the results from the proposed algorithm are in line with those from the advanced cross-sectional analysis method given by Liu et al. (2012). While the calculation methods recommended by AISC (2016) and McGuire et al. (2000) are no longer suitable for the yield surface generation of nonsymmetric sections. The yield surfaces predicted by the calculation method recommended by AISC (2016) are linear, and most of the yield surfaces are inside the yield surfaces obtained by Liu et al. (2012), which means they are safe and conservative. Some figures (Figure 6.16 a, Figure 6.17 a) show that the section capacities predicted by the equation given by McGuire et al. (2000) are overestimated. This example shows the accuracy of the proposed yield surface generation algorithm for nonsymmetric sections and proves that the traditional yield surface calculation methods, such as those equations given by AISC (2016) and McGuire et al. (2000), are not suitable for nonsymmetric sections.

6.8.2 Nonlinear analysis of steel members

The geometric and material nonlinear analysis for a series of members is conducted to verify the reliability of the proposed CP-MTM analysis method. Members with I-section, Channel section, and nonsymmetric sections under different boundary and loading conditions are investigated. Results from the proposed method and those from other researchers are provided.

Example 1: I-section beam under bending

A simply supported beam under pure bending has been studied in this example. The beam was initially investigated by Rinchen et al. (2020). The member cross-section and relevant dimensions, the applied forces, and the boundary conditions are given in Figure 6.18. The boundary conditions at both ends are symmetric. The warping deformations at each end are free, and an additional axial restrain has been employed at the midspan of the beam. The beam has a length of 4.0m, and the material Young's modulus and Poisson's ratio are taken as 200000MPa and 0.3. The material yield stress is 300MPa. The member's initial imperfection has been added by applying a small torque, +970Nmm, about the central axis at the midspan of the beam.

The numerical analysis model is built with ten line-elements. There is no residual stress included in this example, and the steel hardening process after firstly reaching yielded is also not considered. The moment-rotation response curves generated by the proposed method and shell elements model proposed by Rinchen et al. (2020) are given in Figure 6.18. The results from Rinchen et al. (2020) are taken as benchmarks. Results from the second-order elastic analysis introduced by Liu et al. (2019) and those from the conventional approach using the yield surface given by McGuiore et al. are also provided for comparison. From Figure 6.18, large differences will occur when the second-order elastic analysis is adopted. Meanwhile, a slight increase of end moments will cause significant rotation at the end of the curves, indicating that the beam has formed a plastic hinge. The results generated by inelastic analyses are in line with each other, showing the accuracy of the proposed CP-MTM analysis method.

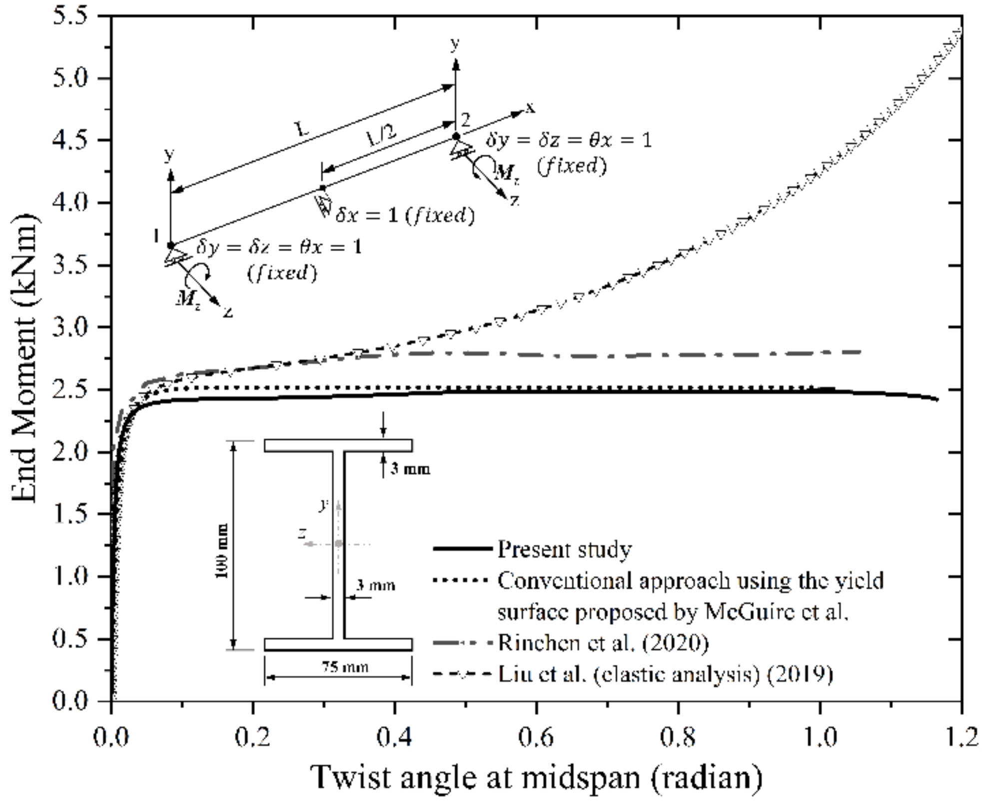

Figure 6.18 Post-buckling behavior of the beam.

Example 2: I-section beam under shear

To further test the accuracy of the proposed method, a fixed-ended beam with I-section is studied. The dimensions of the I-section and the boundary and loading conditions of the beam are given in Figure 6.19. The beam length is 2743.2 mm, and the Young's modulus and Poisson's ratio of the material are 200,000MPa and 0.3. The material yield strength is 248MPa, and the material hardening stress is ignored. This example was formerly studied by Thai and Kim (2011), in which the finite element method and line-element with fiber section model are employed. This research created a line-element model, where the beam is modelled with eight elements.

The load-displacement curves generated by the present study, the conventional approach (using the yield surface given by McGuire et al. (2000)), and Thai and Kim (2011) are plotted in Figure 6.19. The results given by the sophisticated finite element model built by Thai and Kim (2011) are regarded as the benchmark. The comparison of ultimate load factors is listed in Table 6.1. The ultimate load factor calculated by the proposed method has rarely differenced from the benchmark. It is clear Figure 6.19 that the proposed method can get a reliable result. Only slight differences are observed at the elastoplastic stage, which can be eliminated by adjusting the empirical factors $\alpha_v$and α_w in the MTM method. Therefore, the proposed method has good accuracy and is applicable for practical applications.

Table 6.1 Comparison of the predicted ultimate load factor of the beam.

Methods	Ultimate load factor	Difference (%)
Thai and Kim (2011) (Shell element)	9.079	-
Thai and Kim (2011) (Line-element)	9.003	-0.84
Present	8.932	-1.62

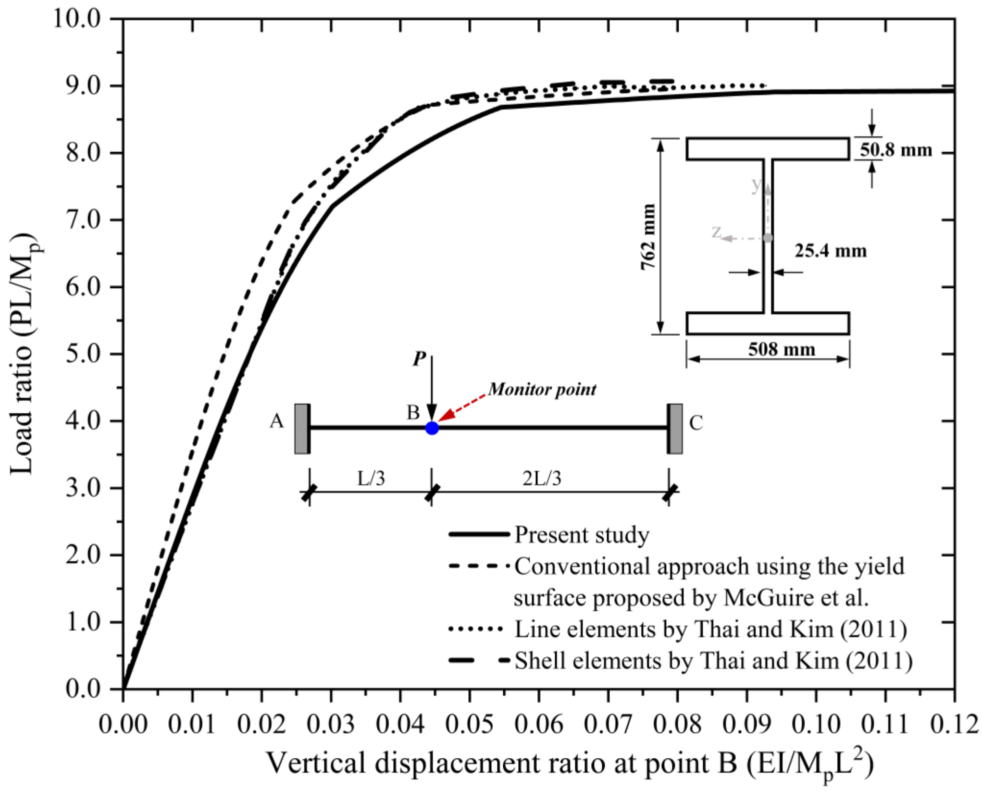

Figure 6.19 Load-deflection curve of fixed-ended beam.

Example 3: Lipped channel section member under bending

In this example, a 4.0m long member with channel cross-section under major axis bending is investigated. The dimensions of the cross-section, and the applied forces and the boundary conditions of the member are given in Figure 6.20. A torque of +400Nmm is applied at the mid-span of the member as the initial imperfection. The material Young's modulus and Poisson's ratio are 200,000MPa and 0.3. The material yield strength is 500MPa.

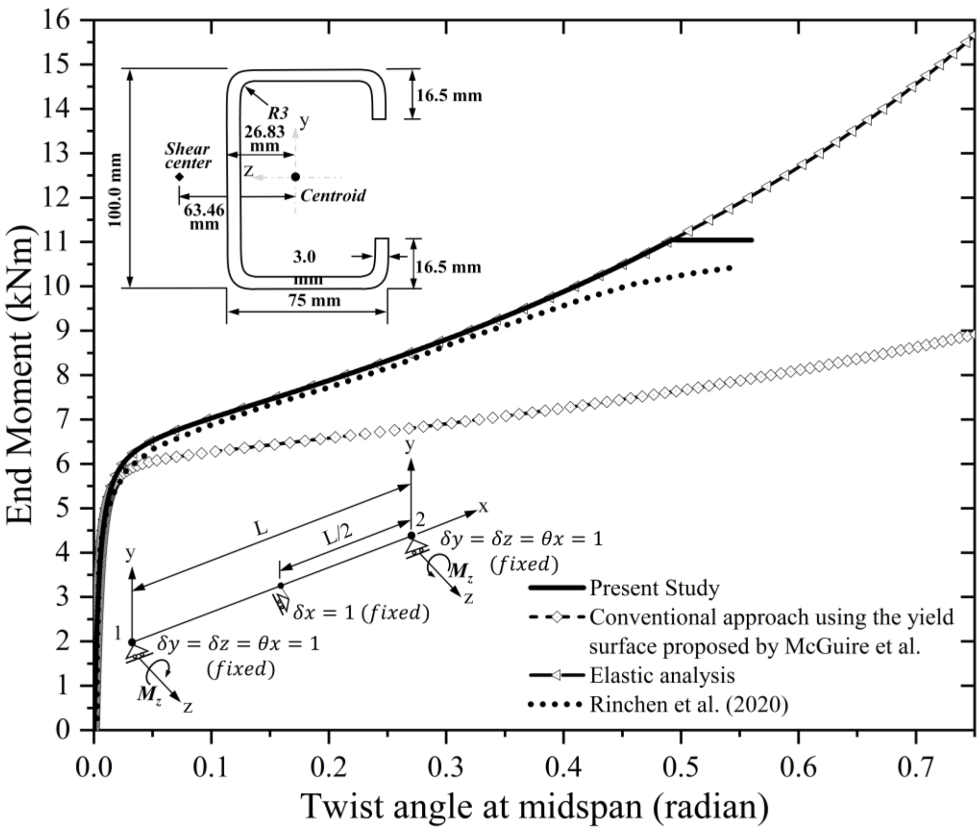

Figure 6.20 Post-buckling behavior of the channel member.

This example is firstly studied by Rinchen et al. (2020). The moment-rotation response curves from the shell element model proposed by Rinchen et al. (2020) are given in Figure 6.20 as benchmarks. Results from the second-order elastic analysis introduced by Liu et al. (2019) and those from the conventional approach (using the yield surface given by McGuire et al. (2000)) are also provided for comparison. From Figure 6.20, the second-order elastic analysis introduced by Liu et al. (2019) can predict the elastic and buckling behavior of the member, but large differences will occur when the member enters the elastoplastic stage. Besides, the conventional approach, which is based on the doubly symmetric section assumption, is no longer suitable for the nonlinear analysis of steel members with nonsymmetric sections.

To further validate the reliability of the proposed method, a nonsymmetric lipped channel section member is investigated. The analytical model is the same as the former example, and the cross-section dimensions are shown in Figure 6.21. The material yield stress is 300MPa, and the initial imperfection is implemented at the mid-span by applying a small twist displacement (+0.007 radians) in this case.

The moment-rotation response curves from the shell element model proposed by Rinchen et al. (2020) are given in Figure 6.21 as benchmarks. The results have further validated that the conventional approach is no longer suitable for the nonlinear analysis of steel members with nonsymmetric sections. They also show that the proposed method can predict the elastoplastic behaviors of nonsymmetric cross-section members accurately.

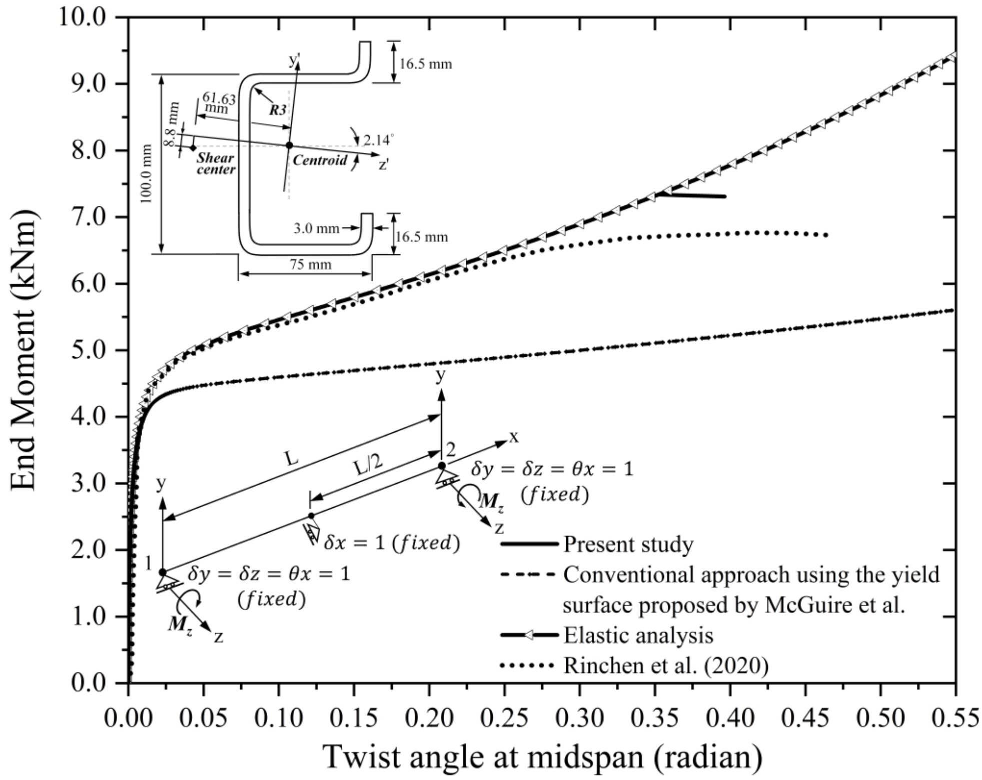

Figure 6.21 Post-buckling behavior of the nonsymmetric member.

Example 4: Angle section column under compression

In this example, four columns with unequal-leg angles, which were investigated by Dinis et al. (2015) and Liu et al. (2019), have been studied. The material of the columns is steel with ASTM A36 – Grade50, and the Young's modulus and Poisson's ratio are adopted as 205.2Gpa and 0.3. The basic information about the measurement of cross-section dimensions and member lengths can be found in reference literature (Dinis et al. 2015). As shown in Figure 6.22, one end of the column is fixed with all degrees of freedoms restrained, and the other end of the column is free in the axial direction with the axial loads applied at the centroid. The initial imperfections and the section properties given by Liu et al. (2019) are adopted. Those columns are simulated with ten line-elements each, to capture the nonlinear behaviors.

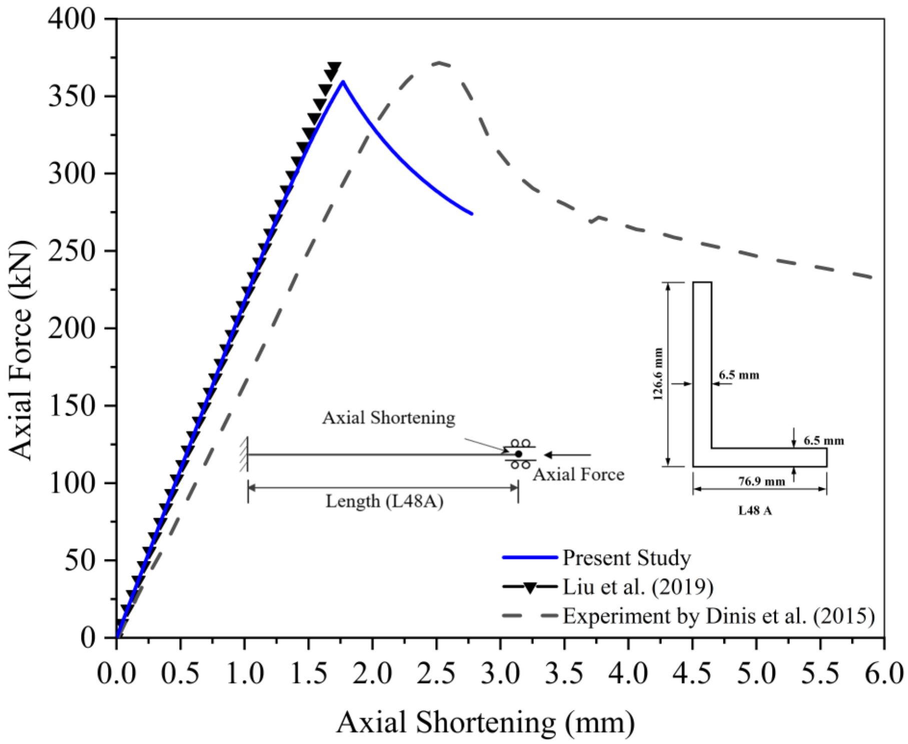

(a) L48A

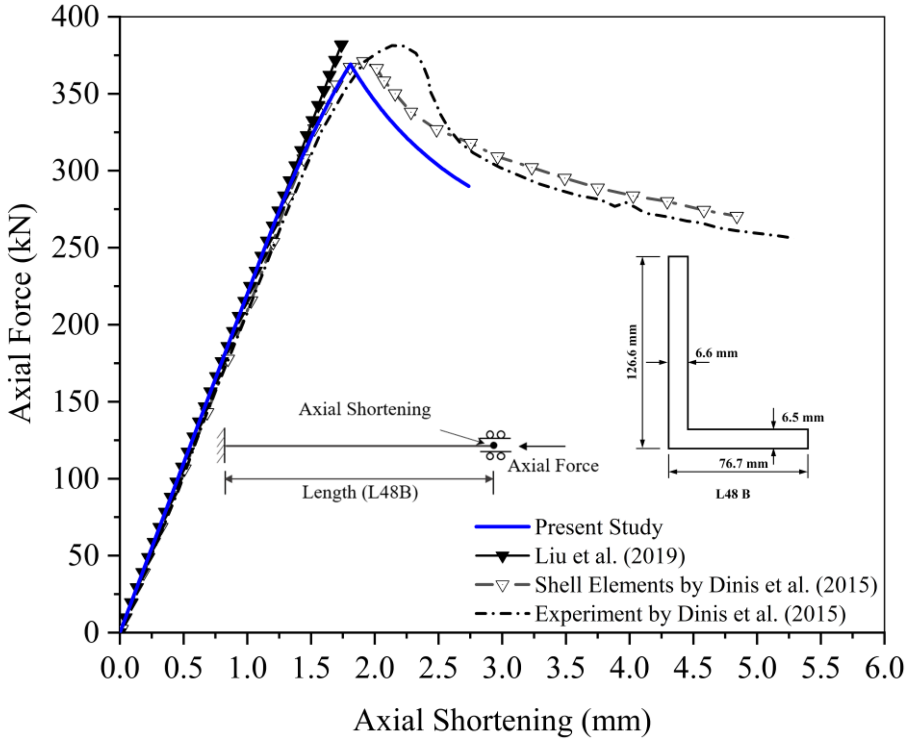
Axial Force (kN)
Axial Shortening (mm)
Axial Shortening
Axial Force
Length (L48B)
126.6 mm
6.6 mm
6.5 mm
76.7 mm
L48 B
Present Study
Liu et al. (2019)
Shell Elements by Dinis et al. (2015)
Experiment by Dinis et al. (2015)

(b) L48B

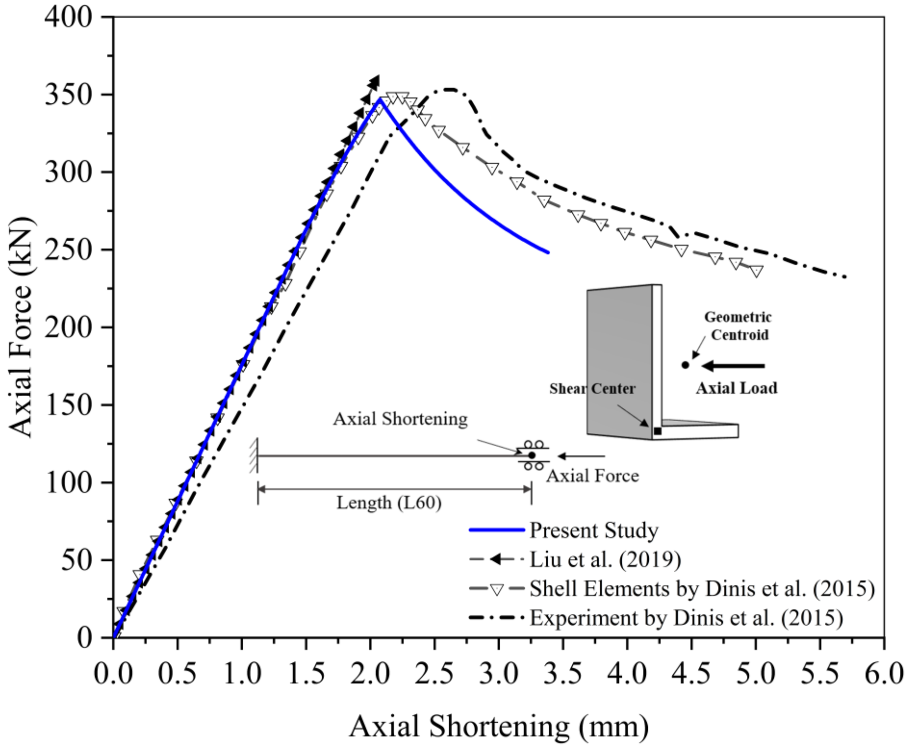
Axial Force (kN)
Axial Shortening (mm)
Geometric Centroid
Shear Center
Axial Load
Axial Shortening
Axial Force
Length (L60)
Present Study
Liu et al. (2019)
Shell Elements by Dinis et al. (2015)
Experiment by Dinis et al. (2015)

(c) L60

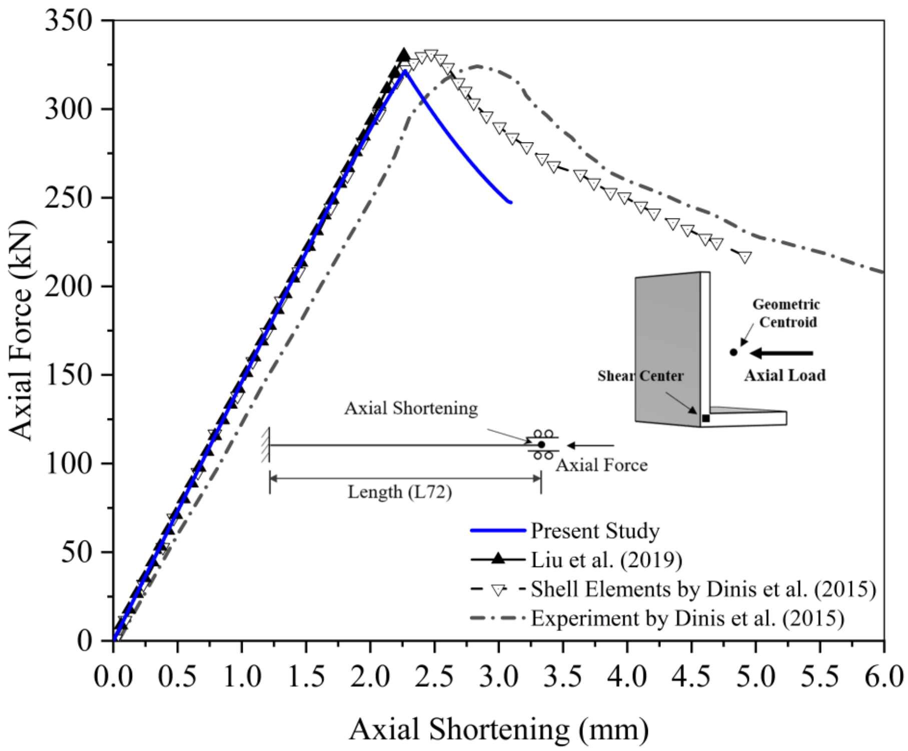

(d) L72

Figure 6.22 Load-deflections of the columns

From Figure 6.22, discrepancies between the predictions by the proposed method and the experimental results can be observed. There might be several reasons that caused the discrepancies. The first reason might be the strengthening of the steel materials. In the numerical simulation, the elastic-perfectly-plastic but in the experiment, there might be material strength. This could explain why the ultimate load from the experiment a little bit is higher than the numerical prediction. The second reason might be the end conditions of the experiment. In the numerical simulation, the end conditions of the members are perfectly rigid. But in the real experiment, there might be semi-rigid at the member ends. This could explain why the stiffness given by the experiment is smaller than the numerical simulation.

6.8.3 Nonlinear analysis of planar frames

In this section, groups of application cases for the analysis of planar frames are provided to verify the accuracy and practicability of the proposed method. A portal frame proposed by Thai and Kim (2011), a two-story frame extensively investigated by several researchers, such as Ziemian and McGuire (2002), Du et al. (2017), and a six-story frame firstly studied by Vogel (1985), are analyzed using the proposed method.

Example 1: Portal frame with a solid rectangular section

This example aims to validate the accuracy of the proposed method for the portal frame. A portal frame with a solid rectangular section has been studied by several researchers to test their theory for elastic-plastic analysis. For instance, Thai and Kim (2011) have conducted the plastic-zone analysis using the line-element with fiber models. The geometry of the portal frame is illustrated in Figure 6.23, where the overall breadth and depth are 10.0m. The cross-section shape of all members in this frame is a solid rectangle with 0.4 m width and 0.2m depth. The corresponding section properties are given in Table 6.2. A pair of gravity load P and a horizontal force H is applied at the top of the frame, whose values are 300kN. The material Young's modulus, Poisson's ratio, and yield strength are 19613MPa, 0.3, and 98MPa, respectively.

Table 6.2 Section properties of the solid rectangle

A (m^2)	I_y (m^4)	I_z (m^4)	J (m^4)	I_ω (m^6)	y_c (m)
8.000 x10^{-2}	1.067 x10^{-3}	2.666 x10^{-4}	1.067 x10^{-3}	1.422 x10^{-5}	0
z_c (m)	β_y (m)	β_z (m)	β_ω	z_y (m^3)	z_z (m^3)
0	0	0	0	8.000 x10^{-3}	4.000 x10^{-3}

The frame members are modeled with four elements each. Results from the FE model and beam-column element proposed by Thai and Kim (2011) and the proposed method are provided for comparison. The predicted ultimate load factors are listed in Table 6.3, and the equilibrium paths of the monitor point are plotted in Figure 6.23. From Table 6.3, it can be seen that the ultimate load factor predicted by the proposed method is close to the benchmark (results from the FE model by Thai and Kim). In Figure 6.23, those curves are kept in great consistency with each other in the entire loading process, demonstrating that the method in this study is accurate for the second-order inelastic analysis of the portal frame.

Table 6.3 Comparison of ultimate load factor of portal frame.

Method	Ultimate load factor	Difference (%)
FE model by Thai and Kim (2011) (20 elements per member)	0.826	-
Line-element by Thai and Kim (2011) (1 element per member)	0.825	-0.12
Present study (4 elements per member)	0.818	-0.97

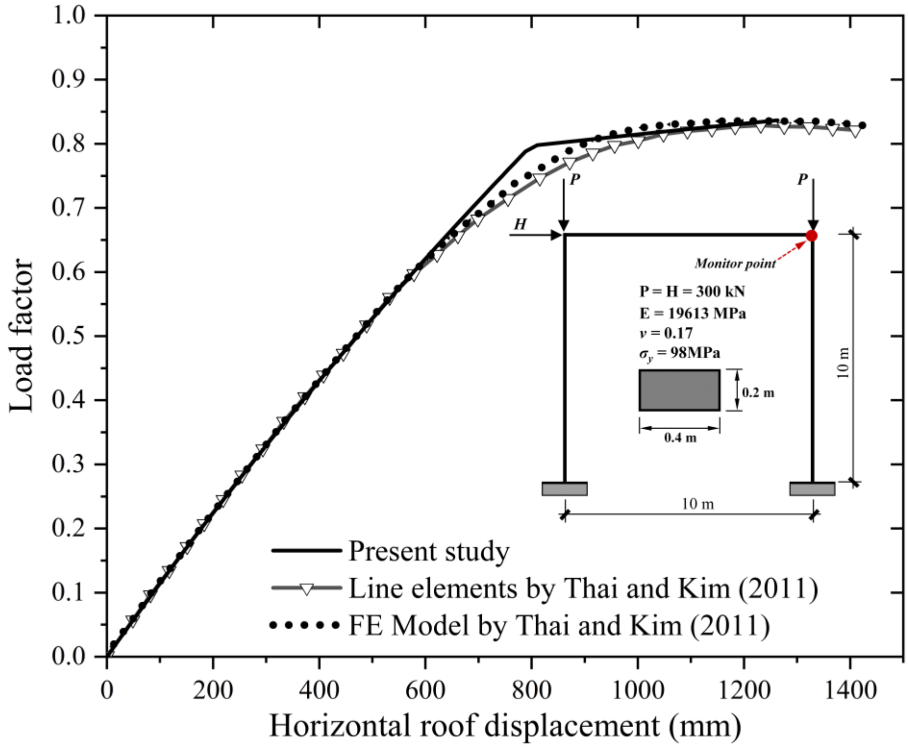

Figure 6.23 Load-deflection curve of portal frame.

Example 2: Portal frame with a lipped channel section

To further validate the accuracy of the proposed method for frames with nonsymmetric sections, a portal frame composed of lipped channel sections has been investigated. This example shares the basic information, such as the frame geometric, the loading conditions, and the boundary conditions, with the former example. But in this example, the material yield strength and Young's modulus are 355MPa and 206000MPa, respectively. The dimensions of the lipped channel section are given in Figure 6.25, and the section properties of the section are listed in Table 6.4.

Table 6.4 Section properties of the lipped channel section

A (m^2)	I_y (m^4)	I_z (m^4)	J (m^4)
2.220 x10^{-2}	1.064 x10^{-4}	2.782 x10^{-4}	6.660 x10^{-6}
I_ω (m^6)	y_c (m)	z_c (m)	β_y (m)
2.375 x10^{-6}	0	1.656 x10^{-1}	-3.921 x10^{-2}
β_z (m)	β_ω	z_y (m^3)	z_z (m^3)
0	0	1.380 x10^{-3}	2.323 x10^{-3}

To validate the accuracy of the present study, the sophisticated FE model is established using the Solid185 element in ANSYS version 14.0 (Ansys 2011), as shown in Figure 6.24. The FE model is composed of more than 15000 elements with the orientation of the beam and column accurately depicted. The material constitutive relationships are assumed elastic-perfectly-plastic with no hardened stress. Load-deflection curves of the monitor point generated by the FE model and proposed method are plotted in Figure 6.25. A similar tendency of the whole load-deflection cure can be obtained. Only a slight discrepancy can be found at the elastoplastic stage, which may be caused by the empirical factors $\alpha_v$and α_w in the MTM method. But the method in this paper is much more efficient, with only 12 elements used. Therefore, the proposed method can be conveniently used for the design of steel frames.

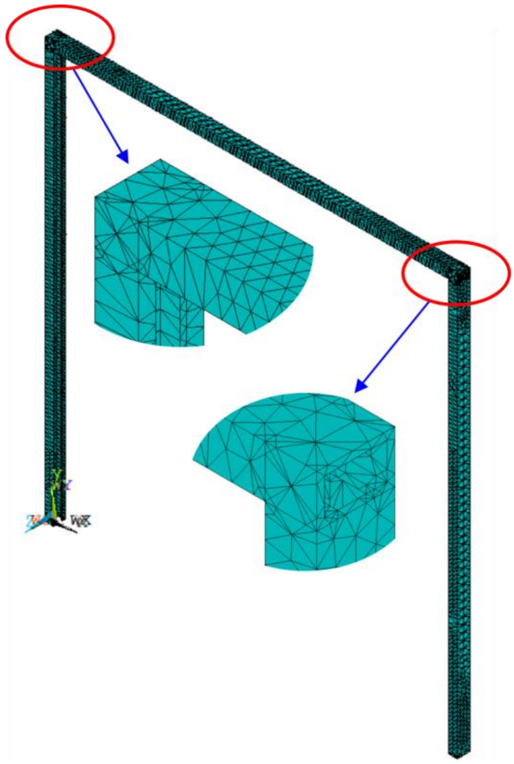

(a) Finite element model

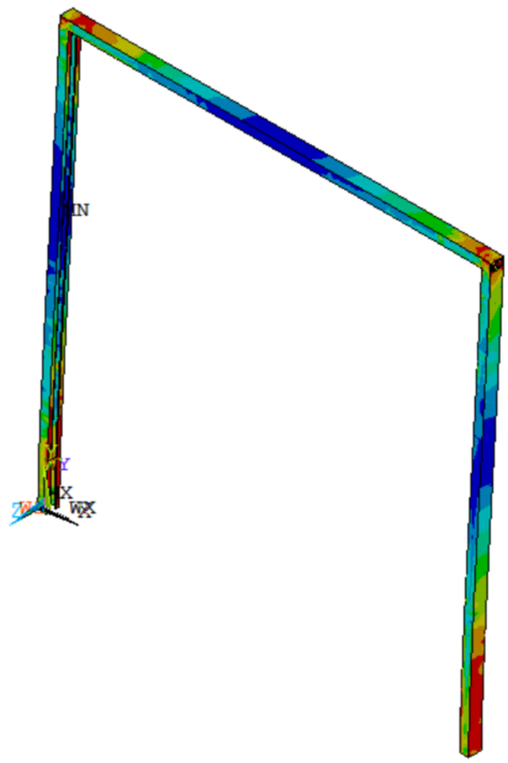

(b) The stress contour

Figure 6.24 Sophisticated Finite element model

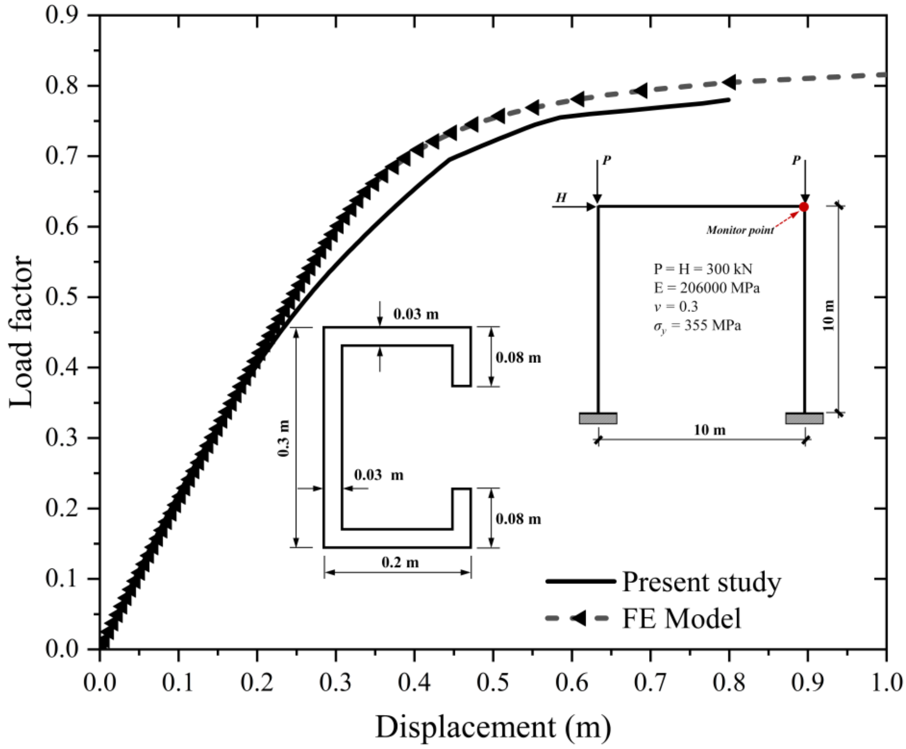

Figure 6.25 Load-deflection curve of nonsymmetric portal frame.

Example 3: Two-story Ziemian frame

In this example, a two-story frame, namely the Ziemian frame, is studied. It is a classical benchmark example extensively investigated by several researchers, such as Ziemian (2002) and Du et al. (2017). The basic geometry and loading conditions of this frame are given in Figure 6.26. All members' orientations are consistent with Ziemian's model, in which beams are orientated in major axis bending, and columns are orientated in minor axis bending. The material Young's modulus of the steel is taken as 205Gpa, and Poisson's ratio is 0.3. The yield strength is 345MPa. One thing that should be mentioned is that Ziemian has conducted a series of parametric studies for this frame, and the selected frame covered more types of common I-section and likely had more obvious material nonlinearities.

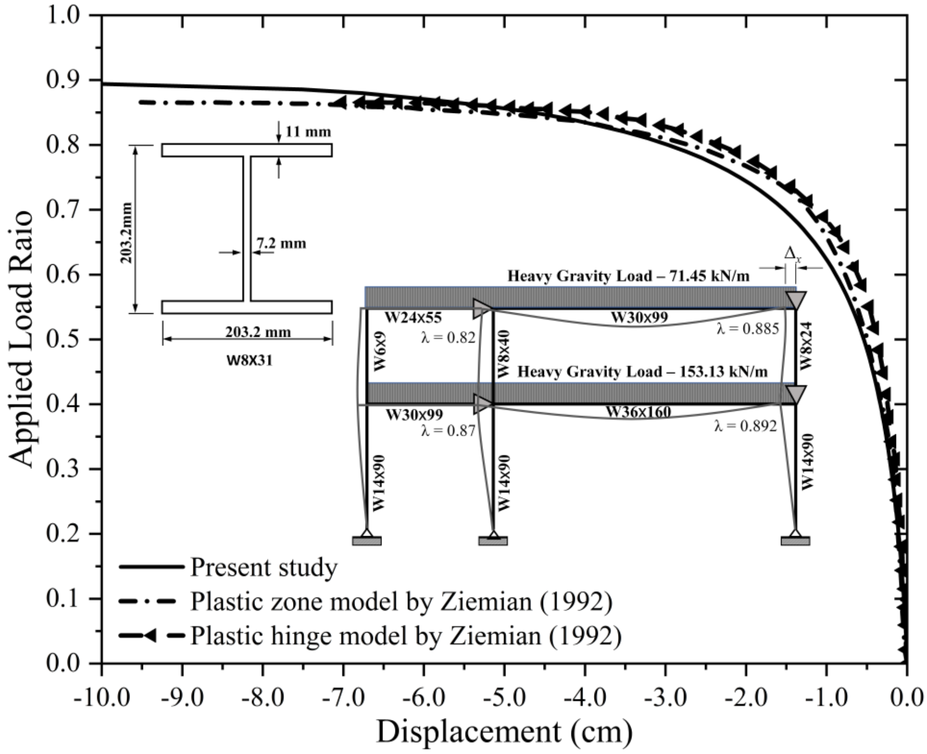

Figure 6.26 Response curves for Ziemian frame.

Results obtained by Ziemian using the plastic-zone and plastic hinge method and those from the present study are plotted in Figure 6.26. There are only slight differences between the result from the proposed method and comparison consequences showing that the present study has a good performance in capturing the elastic-plastic behavior of steel frames composed by commonly used sections.

Example 4: Six-story Vogel frame

To further test the accuracy of the proposed method, Vogel's six-story planar frame made of a series of members with European calibration sections is studied. Distributed gravity loads are applied on the beams, and concentrated horizontal forces are applied at the top of each floor. Detailed geometric and boundary conditions are given in Figure 6.27. In this frame, there is global out-of-plumb straightness φ equals 1/300. The material for all members is steel. The Young's modulus and Poisson's ratio are 205 Gap and 0.3, respectively, and the yield strength is 235MPa. This frame was firstly studied by Vogel (1985) using the plastic zone method to trace the load-deflection path in 1985. Subsequently, Liu et al. (2014b) investigated this frame with an Arbitrarily-located-plastic-hinge (ALH) element. In the ALH element, the plastic hinge can locate everywhere, not merely at the mid-span. In this paper, the Vogel frame is modeled with four elements per member to investigate its geometrical and material nonlinear behaviors. The comparison results are plotted in Figure 6.27.

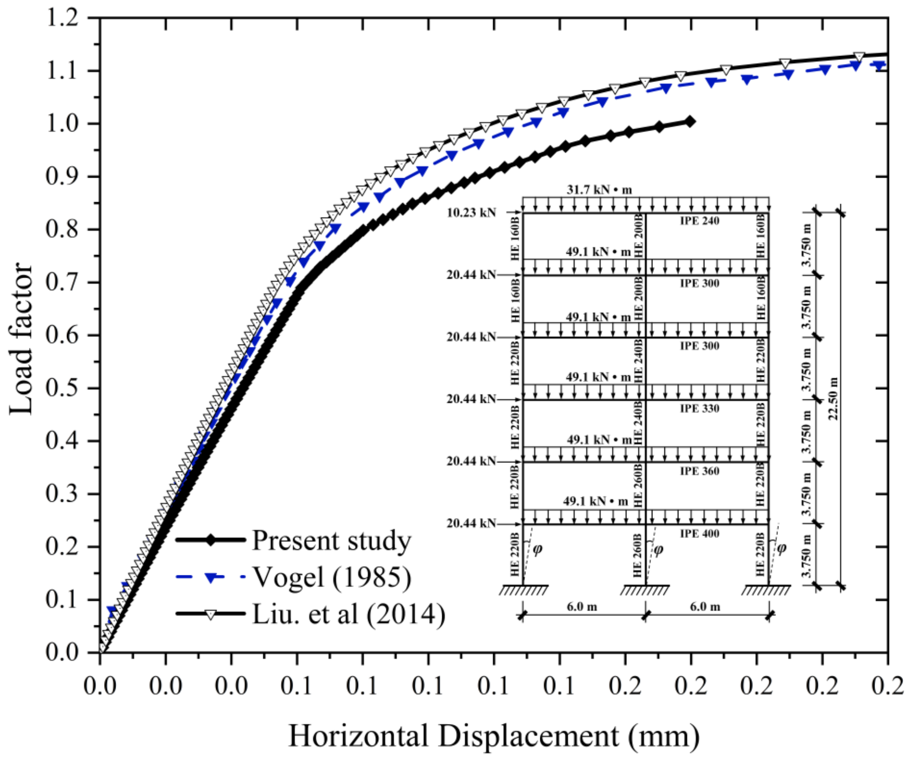

Figure 6.27 Load deflection behavior of six-story frame

As shown in Figure 6.27, all members stay in an elastic situation in the first stage. The load-deflection curves obtained by Vogel (1985), Liu et al. (2014), and the proposed method are kept consistent with each other. However, the ultimate load factors obtained by Vogel and Liu et al. are 1.112 and 1.152, respectively, while the corresponding load factor by the proposed method is 1.004. Nonetheless, around 10% discrepancy is formed between different methods, but a more conservative and more likely safer consequence could get for complex practical structural calculation process. Also, the proposed method is more efficient than the plastic zone method.

6.8.4 Nonlinear analysis of spatial frames

In this section, two spatial frames are investigated to verify the accuracy and practicability of the proposed method. A two-story space frame first analyzed by Argyris (1982) and then studied by De Souza (2000) and Thai and Kim (2011) is modeled with four elements per member. Then, a twenty-story space frame with 460 members and 210 joints studied by Liew et al. (2000) and Liu et al. (2014a) is analyzed.

Example 1: Two story spatial frame

The two-story space frame, as shown in Figure 6.28, was first analyzed by Argyris (1982) and then studied by De Souza (2000) using the force-based element with fiber model. Recently, a similar investigation was conducted by Thai and Kim (2011), where the refined plastic hinge method is used. The Young's Modulus, Poisson's ratio, and yield stress for the steel are 19613MPa, 0.3, and 98MPa, respectively. The frame geometric information and the load locations are depicted in Figure 6.28. The spatial frame is modeled with four elements per member.

Table 6.5 Ultimate load of two-story space frame.

Method	*Ultimate load (kN)*	*Difference*
De Souza (2000)	128.05	--
Thai and Kim (2011)	128.50	0.35%
Proposed	128.00	-0.04%

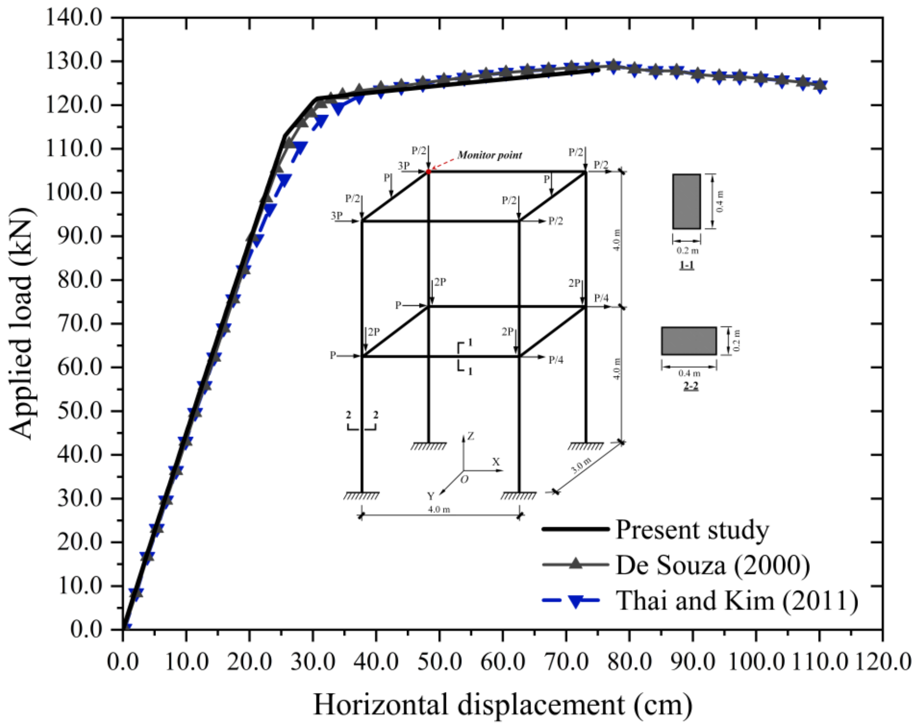

Figure 6.28 Load deflection behavior of two-story space frame

Table 6.5 gives the ultimate load predicted by De Souza (2000), Thai and Kim (2011), and the proposed method, where De Souza’s result from the force-based element with fiber model is taken as the benchmark. It is clear from the table that the proposed method can get an accurate result. Besides, the horizontal displacement of the monitor point has been traced, and the load-deflection curves accessed by different methods are plotted in Figure 6.28. From the comparison, the three curves also agree well with each other, which proves that the proposed method has excellent accuracy.

Example 2: Twenty story spatial frame

In this example, a twenty-story space frame first studied by Liew et al. (2000) and then investigated by Liu et al. (2014a) is modeled and analyzed in. This spatial steel frame with 460 members and 210 joints has a structural size closer to a practical one. The geometry and the section assignments of the frame are illustrated in Figure 6.29. The steel of the twenty-story frame is A50 steel with yield stress equal to 344.8 MPa. The gravity load on all the floors is 4.8 kN/m2, and concentrated joint loads are applied to the top of the columns. A wind load of 0.96 kN/m2 is applied to the beam-column joints. All members are modeled by one element per member in the present analysis.

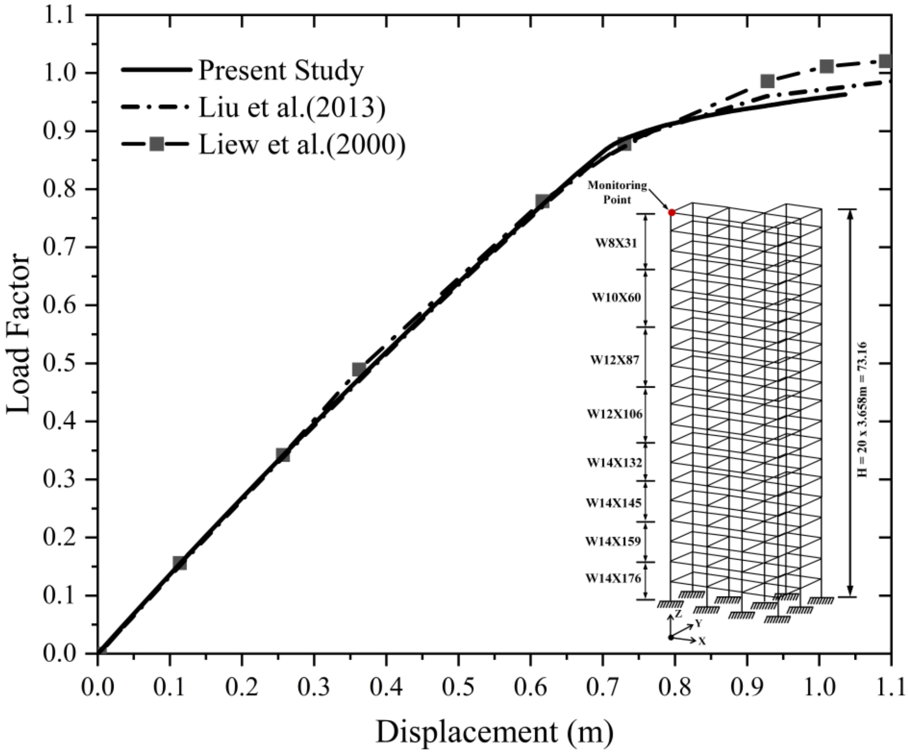

Figure 6.29 Twenty-story space frame

The results generated from the present study and those given by Liew et al. (2000) and Liu et al. (2014a) are plotted in Figure 6.29 for comparison. The curves in the figure are identical in the elastic range, while the differences are also small in the partial yield stage, which shows the accuracy of the proposed method.

CHAPTER 7.

SECOND-ORDER ELASTIC ANALYSIS UNDER FIRE

7.1 Introduction

In this chapter, the analysis methods of the steel frames with nonsymmetric cross-sections under fire condition are introduced. Steel structures are sensitive to fires and elevated temperatures because the thermal effects will rapidly deteriorate the strength and stiffness of steel material (Wang and Moore 1995; C. K. and Chan 2004; Wang et al. 2013). Fire safety engineering is required to examine the behaviors of steel members under fire conditions. The related design approaches (Eurocode-3 2005 and Hong Kong steel codes 2011) can be categorized into two types, such as the prescriptive (De Sanctis et al. 2014; Qureshi et al. 2020) and the performance-based approaches (Liew et al. 2002; Parkinson et al. 2009; Dwaikat and Kodur 2011), where the former is an element-based approach using experimental results from standard fire tests. At the same time, the latter is a system-based approach that relies on sophisticated analysis of checking global and local stabilities of structures. Adopting the performance-based design method is attractive because it could reduce or eliminate the usage of expensive fire-resistant coating materials. However, the practicability of this design method relies on the robustness of the analysis method, which should be able to predict the nonlinear behaviors of steel structures at elevated temperatures and under fire conditions.

With the advancement in manufacturing techniques, robotic welding machines and advanced cold-forming processes are gradually used in modern steel constructions, eliminating the constraints of fabricating nonsymmetric sections. Innovative structural forms with nonsymmetric sections are recently proposed. Unlike in the past old days when robotic welding was unavailable, steel members can be tailored made to suit architectural requirements and structural efficiency. Nevertheless, the members with nonsymmetric sections may be susceptible to lateral-torsional or flexural-torsional buckling due to the offset between the shear center and the centroid in the cross-section (Liu et al. 2019a; Chen et al. 2021). Regarding fire conditions, the steel members may exhibit a temperature gradient. Under this circumstance, the twisting may be induced if its cross-section is nonsymmetric (see Figure 2.5), which may lead to lateral-torsional buckling. The buckling behaviors of these steel members are usually complex, making their buckling design difficult, especially at elevated temperatures.

To investigate the structural behaviors of the steel member with nonsymmetric sections in fire, several experimental investigations and numerical simulations using Finite Elements (FE) were conducted. For example, Wang and his colleagues (2002; 2003; 2003a; 2003b) studied the structural behaviors of cold-formed thin-walled steel channels under non-uniform temperatures, where more than 50 short channel columns were tested and studied to develop the design methods. Kim *et al.* (2015) investigated the buckling behavior of cold-formed steel channel-section beams at elevated temperatures using a two-dimensional FE heat transfer analysis and found that the buckling modes of the beam with temperature variation in its section are quite different from that of the beam with a uniform temperature in its section. Recently, Laím *et al.* (2013; 2014; 2015; 2016) conducted experiments and numerical analysis of cold-formed steel members in the fire, where the beams with lipped C, compound C, Sigma, and compound Sigma sections were studied and noticed that the lateral-torsional buckling is the primary failure mode. These investigations provided some basic understanding of the buckling behaviors of steel members with nonsymmetric sections at elevated temperatures. However, they are too complicated and time-consuming to conduct physical tests and numerical FE simulations. A more convenient analysis method, namely the beam-column analysis method, is preferred and suitable for extensive studies and practical designs.

Several beam-column elements have been proposed in the literature for the nonlinear analysis of steel members at elevated temperatures. For example, Li and Jiang (1999) derived a beam-column element considering the temperature variation across the cross-section. Iu and Chan (2005) developed a beam-column element formulation to simulate the large deflection and inelastic behavior of steel members in fire. Huang and Tan (2007) proposed an element formulation with the warping degree of freedom (DOF) to study the responses of a steel frame at elevated temperatures. However, these element formulations are mostly proposed for the conventional steel members with symmetric sections, which are inapplicable for the use of nonsymmetric sections.

Recently, refined beam-column element formulations for members with nonsymmetric sections have been proposed by Liu and his colleagues (Gao et al. 2021; Liu et al. 2018). Both the warping DOF and Wagner effects are included in these element formulations, which are based on the updated-Lagrangian (UL) method to establish the equilibrium conditions based on the previously known deformed status. However, this element is unsuitable for analyzing steel members exposed to fires because the material stiffness degradation could destroy the previous equilibrium conditions. The total-Lagrangian (TL) method, in which the equilibrium conditions are established based on the originally undeformed statuses, can be used for studying steel members in fire (Xia et al. 2012; Jiang et al. 2014). But the TL method requires starting-over computation at every temperature increment, which is time-consuming and inapplicable for practical analyses. To this, a new beam-column element formulation using the co-rotational (CR) method for nonsymmetric section members is proposed, which could be an effective and efficient solution for the analysis problems of steel members in fire. In the CR method, the location of the element axis is continuously updated during the analysis, but the element resistances are computed by referring to the original undeformed configuration. As a result, the proposed CR beam-column element formulation can conveniently consider the material degradation and the thermal expansion when the temperature rises. The new equilibrium conditions can be determined without repeating the loading procedure as it in the TL method.

This chapter proposed a new CR beam-column element formulation for the steel member with nonsymmetric sections at elevated temperatures. The element formulation has been derived based on the nonsymmetric section assumption, explicitly modeling the offsets between the shear center and the centroid. The warping degree of freedom (DOF) is included. In this case, the lateral-torsional and flexural-torsional buckling of the nonsymmetric section members can be determined directly. The detailed derivation procedure of the element formulation is given, and a refined Newton-Raphson-typed numerical method for the analysis at elevated temperatures is also proposed and elaborated. Finally, several examples are provided for verifying the accuracy and examining the robustness of the proposed method.

7.2 Assumptions

In this chapter, the following assumptions are adopted: (1) the material is elastic and homogeneous; (2) shear strain is not included, but warping deformation is considered; (3) the loads applied on elements are conservative; and (4) the strain is assumed to be small, but the deflections and displacements might be large; (5) the section local and cross-section distortional buckling is not considered; and (6) the temperature distribution in the member cross-section is the combination of a uniform distribution and a temperature gradient, as shown in Figure 7.1 (b).

7.3 Co-rotational (CR) Formulation

The element axis is chosen as the reference framework in the CR method, the location of the element axis is continuously updated during the analysis, and the element resistances are computed by referring to the original undeformed configuration. As a result, the CR beam-column element formulation can directly calculate the element resisting forces using the total element deformations.

7.3.1 Element local reference axes and shape functions

There are eight degrees of freedom (DOFs) for an element at the local axes as shown in Figure 7.1 (a) and given as,

$$\boldsymbol{u} = \left[e\ \gamma_{y1}\ \gamma_{z1}\ \theta_{b1}\ \gamma_x\ \gamma_{y2}\ \gamma_{z2}\ \theta_{b2}\right]^T \tag{7.1}$$

where, $\boldsymbol{u}$ is the element basic deformational vector, referring to the shear center axis after removing the rigid body movement; e is the axial deformation, γ_x, γ_y and γ_z are the rotations about the element axis; and θ_b is the warping deformation. The subscript 1 and 2 stand for the element start and end nodes, respectively.

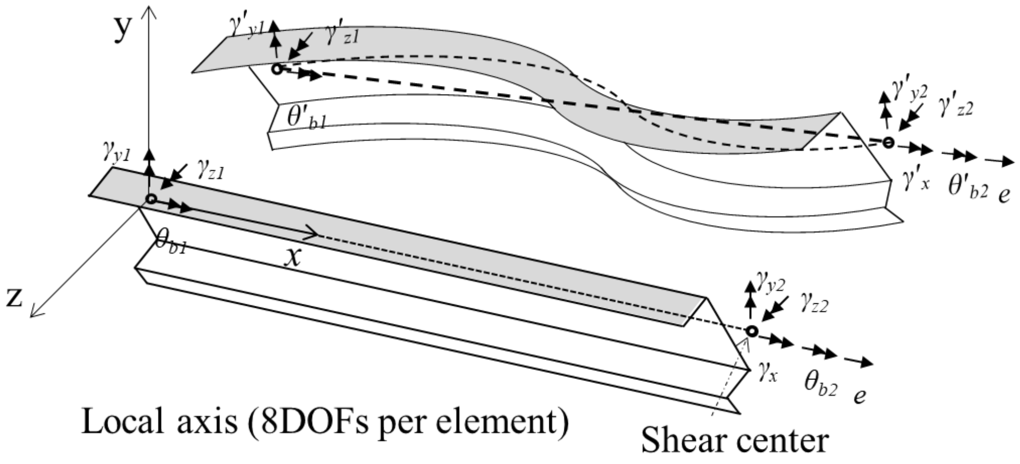

(a) Element local degrees of freedom

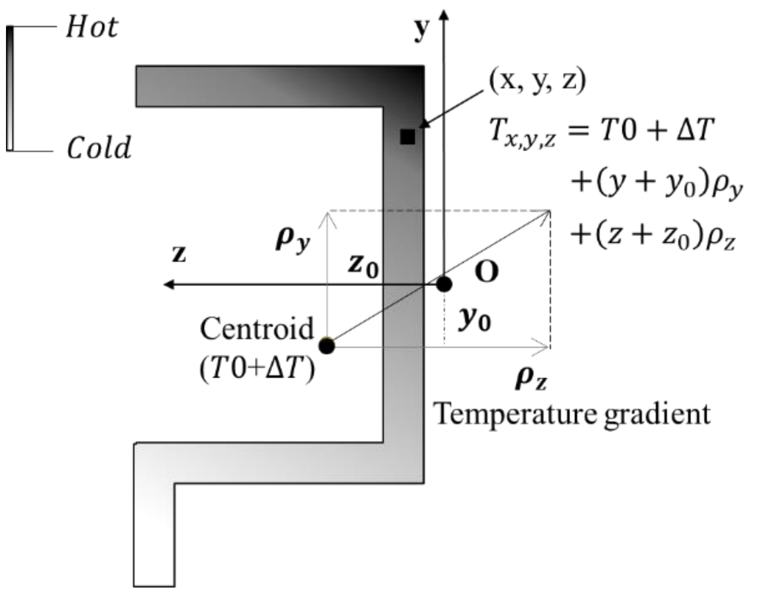

(b) Temperature distribution

Figure 7.1 Element local DOF and temperature distribution in the cross-section

The corresponding nodal force vector is,

$$\boldsymbol{F} = [P \ M_{y1} \ M_{z1} \ M_{b1} \ M_x \ M_{y2} \ M_{z2} \ M_{b2}] \tag{7.2}$$

The polynomial interpolations are used for describing the deformations along the element length, and the following shape functions are adopted,

$$\boldsymbol{f} = \boldsymbol{B}\boldsymbol{u}^{\boldsymbol{T}} \tag{7.3}$$

in which, $\boldsymbol{f}$ is the shape functions, giving as follows,

$$\boldsymbol{f} = [f_x(x) \ \ f_y(x) \ \ f_z(x) \ \ f_{\theta x}(x)]^{\boldsymbol{T}} \tag{7.4}$$

where, $f_x(x)$ is the axial displacement along the x-axis; $f_y(x)$ and $f_z(x)$ are the lateral displacements along y- and z-axes, respectively; and $f_{\theta x}(x)$ is the torsional rotation along the element length. $\boldsymbol{B}$ is the shape function matrix which can be written as,

$$\boldsymbol{B} = \begin{bmatrix} B_1 & 0 & 0 & 0 & 0 & 0 & 0 & 0 \\ 0 & 0 & B_2 & 0 & 0 & 0 & B_3 & 0 \\ 0 & B_2 & 0 & 0 & 0 & B_3 & 0 & 0 \\ 0 & 0 & 0 & B_2 & B_4 & 0 & 0 & B_3 \end{bmatrix} \tag{7.5}$$

where,

$$B_1 = \frac{x}{L} \tag{7.6}$$

$$B_2 = x - \frac{2x^2}{L} + \frac{x^3}{L^2} \tag{7.7}$$

$$B_3 = -\frac{x^2}{L} + \frac{x^3}{L^2} \tag{7.8}$$

$$B_4 = \frac{3x^2}{L} - \frac{2x^3}{L^2} \tag{7.9}$$

in which, L is the length of the element and x is the distance along the element length.

7.3.2 Strain definitions

The total strain of steel at elevated temperatures can be divided into two parts: the force-related strain $\boldsymbol{\varepsilon_\sigma}$ and the thermal-related strain $\boldsymbol{\varepsilon}_T$.

$$\boldsymbol{\varepsilon} = \boldsymbol{\varepsilon_\sigma} + \boldsymbol{\varepsilon}_T \tag{7.10}$$

The displacements u_x, u_y, and u_z at any place of the element, like the point (*x*, *y*, *z*) given in Figure 7.1 (b), can be calculated using the shape functions,

$$u_x(x,y,z) = f_x(x) - (y + y_0)\frac{\partial f_y(x)}{\partial x} - (z + z_0)\frac{\partial f_z(x)}{\partial x} - \omega_n \frac{\partial f_{\theta x}(x)}{\partial x} \tag{7.11}$$

$$u_y(x,y,z) = f_y(x) - z f_{\theta x}(x) \tag{7.12}$$

$$u_z(x,y,z) = f_z(x) + y f_{\theta x}(x) \tag{7.13}$$

where, y_0 and z_0 are the coordinates of the centroid as shown in Figure 7.1 (b), and ω_n is the normalized unit warping constant.

The total strain $\boldsymbol{\varepsilon}$ can be calculated by,

$$\boldsymbol{\varepsilon} = \begin{bmatrix} \varepsilon_{xx} \\ \varepsilon_{xy} \\ \varepsilon_{xz} \end{bmatrix} = \begin{bmatrix} \dfrac{\partial u_x}{\partial x} + \dfrac{1}{2}\left[\left(\dfrac{\partial u_x}{\partial x}\right)^2 + \left(\dfrac{\partial u_y}{\partial x}\right)^2 + \left(\dfrac{\partial u_z}{\partial x}\right)^2\right] \\ \dfrac{1}{2}\left(\dfrac{\partial u_x}{\partial y} + \dfrac{\partial u_y}{\partial x}\right) + \dfrac{1}{2}\left(\dfrac{\partial u_x}{\partial x}\dfrac{\partial u_x}{\partial y} + \dfrac{\partial u_y}{\partial x}\dfrac{\partial u_y}{\partial y} + \dfrac{\partial u_z}{\partial x}\dfrac{\partial u_z}{\partial y}\right) \\ \dfrac{1}{2}\left(\dfrac{\partial u_x}{\partial z} + \dfrac{\partial u_z}{\partial x}\right) + \dfrac{1}{2}\left(\dfrac{\partial u_x}{\partial x}\dfrac{\partial u_x}{\partial z} + \dfrac{\partial u_y}{\partial x}\dfrac{\partial u_y}{\partial z} + \dfrac{\partial u_z}{\partial x}\dfrac{\partial u_z}{\partial z}\right) \end{bmatrix} \tag{7.14}$$

Figure 7.1 (b) shows the nonsymmetric section with the thermal gradient. In which, $T0$ is the room temperature, ΔT is the average temperature increment at the centroid, ρ_y and ρ_z are the temperature gradients along the y and z axes, respectively. Figure 7.1, the thermal-related strain of a fiber on the cross-section can be express as,

$$\boldsymbol{\varepsilon}_T = \begin{bmatrix} \alpha\left[\Delta T + \rho_y(y + y_0) + \rho_z(z + z_0)\right] \\ \mathbf{0} \\ \mathbf{0} \end{bmatrix} \tag{7.15}$$

where, α is thermal expansion coefficient.

7.3.3 Total potential energy

The equilibrium equation can be constructed according to the total potential energy function given by,

$$\Pi = U - V \tag{7.16}$$

in which, Π is the total potential energy function, U is the strain energy; and $V = \boldsymbol{F}\Delta\boldsymbol{u}$ is the work done by the external forces.

The strain energy U can be given by,

$$U = \int_V \boldsymbol{\varepsilon}^{\boldsymbol{T}}\boldsymbol{\sigma} dV = \int_V (\boldsymbol{\varepsilon}_{\boldsymbol{\sigma}} + \boldsymbol{\varepsilon}_T)^{\boldsymbol{T}}\boldsymbol{\sigma} dV = \int_V \boldsymbol{\varepsilon}_{\boldsymbol{\sigma}}{}^{\boldsymbol{T}}\boldsymbol{\sigma} dV + \int_V \boldsymbol{\varepsilon}_T{}^{\boldsymbol{T}}\boldsymbol{\sigma} dV$$
$$= U_\sigma + U_T \tag{7.17}$$

where, U_σ is the force-related potential energy, and U_T is the thermal-related potential energy.

The elasticity matrix for describing the relations between the stress and the strain at the evaluated temperature can be expressed as,

$$\boldsymbol{D} = \begin{bmatrix} E(T) & 0 & 0 \\ 0 & G(T) & 0 \\ 0 & 0 & G(T) \end{bmatrix} \tag{7.18}$$

where, $E(T)$ and $G(T)$ indicate the material Young's and shear moduli with respect to the specified temperature T.

The force-related strain energy U_σ can be integrated as,

$$U_\sigma = \int_V \boldsymbol{\varepsilon_\sigma}^{\boldsymbol{T}} \boldsymbol{\sigma} dV \approx \int_V (\boldsymbol{\varepsilon_L}^{\boldsymbol{T}} \boldsymbol{D} \boldsymbol{\varepsilon_L} + 2\boldsymbol{\sigma}^{\boldsymbol{T}} \boldsymbol{\varepsilon_N})\, dV \tag{7.19}$$

where, $\boldsymbol{\varepsilon_L}$ and $\boldsymbol{\varepsilon_N}$ are the first-order and second-order parts of the strain tensor given in Chapter 4, and $\boldsymbol{\sigma}$ is the stress tensor which can be expressed in terms of the nodal forces and given as,

$$\boldsymbol{\sigma} = \begin{bmatrix} \sigma_{xx} \\ \tau_{xy} \\ \tau_{xz} \end{bmatrix}$$

$$= \begin{bmatrix} \frac{P}{A} + \left[M_{y1}\left(1 - \frac{x}{L}\right) - M_{y2}\frac{x}{L}\right]\frac{z + z_0}{I_y} + \left[M_{z1}\left(1 - \frac{x}{L}\right) - M_{z2}\frac{x}{L}\right]\frac{y + y_0}{I_z} + M_B\frac{\omega_n}{I_\omega} \\ -(M_{z1} + M_{z2})/AL \\ \left(M_{y1} + M_{y2}\right)/AL \end{bmatrix} \tag{7.20}$$

where, A is the cross-section area; I_y and I_z are the second moment of areas about the y- and z-axes; I_ω is the warping section constant.

By substituting equations (7.11)-(7.14), (7.18), and (7.20) into equation (7.19) and ignoring some high-order terms, the strain energy U_σ becomes,

$$U_\sigma \approx \frac{1}{2}\int_0^L \left[E(T)A\left(\frac{\partial f_x(x)}{\partial x}\right)^2\right] dx + \frac{1}{2}\int_0^L \left[E(T)I_z\left(\frac{\partial^2 f_y(x)}{\partial x^2}\right)^2\right] dx$$

$$+\frac{1}{2}\int_0^L \left[E(T)I_y\left(\frac{\partial^2 f_z(x)}{\partial x^2}\right)^2\right] dx + \frac{1}{2}\int_0^L P\left[\left(\frac{\partial f_y(x)}{\partial x}\right)^2 + \left(\frac{\partial f_z(x)}{\partial x}\right)^2\right] dx$$

$$+\frac{1}{2}\int_0^L \left[E(T)I_\omega\left(\frac{\partial^2 f_{\theta x}(x)}{\partial x^2}\right)^2\right]dx+\frac{1}{2}\int_0^L\left[G(T)J\left(\frac{\partial f_{\theta x}(x)}{\partial x}\right)^2\right]dx$$

$$+\frac{1}{2}\int_0^L P\left[-2y_0\frac{\partial f_z(x)}{\partial x}+2z_0\frac{\partial f_y(x)}{\partial x}\right]\frac{\partial f_{\theta x}(x)}{\partial x}dx+\frac{1}{2}\int_0^L Pr^2\left(\frac{\partial f_{\theta x}(x)}{\partial x}\right)^2 dx$$

$$+\frac{1}{2}\int_0^L M_b\beta_\omega\left(\frac{\partial f_{\theta x}(x)}{\partial x}\right)^2 dx+\int_0^L M_{y1}\frac{L-x}{L}\frac{\partial f_{\theta x}(x)}{\partial x}\left[\frac{\partial f_y(x)}{\partial x}+\frac{1}{2}\beta_y\frac{\partial f_{\theta x}(x)}{\partial x}\right]dx$$

$$-\int_0^L M_{y2}\frac{x}{L}\frac{\partial f_{\theta x}(x)}{\partial x}\left[\frac{\partial f_y(x)}{\partial x}+\frac{1}{2}\beta_y\frac{\partial f_{\theta x}(x)}{\partial x}\right]dx$$

$$+\int_0^L M_{z1}\frac{L-x}{L}\frac{\partial f_{\theta x}(x)}{\partial x}\left[\frac{\partial f_z(x)}{\partial x}+\frac{1}{2}\beta_z\frac{\partial f_{\theta x}(x)}{\partial x}\right]dx$$

$$-\int_0^L M_{z2}\frac{x}{L}\frac{\partial f_{\theta x}(x)}{\partial x}\left[\frac{\partial f_z(x)}{\partial x}+\frac{1}{2}\beta_z\frac{\partial f_{\theta x}(x)}{\partial x}\right]dx$$

(7.21)

where, J is the torsional rigidity; β_y, β_z, and β_ω are the Wagner coefficients; and $r^2 = (I_y + I_z)/A$. The thermal-related strain energy can be calculated as,

$$U_T=\int_V \boldsymbol{\varepsilon_T}^{\boldsymbol{T}}\boldsymbol{\sigma}dV=\int_V \boldsymbol{\varepsilon_T}^{\boldsymbol{T}}\boldsymbol{D}\boldsymbol{\varepsilon}dV \tag{7.22}$$

When substituting equations (7.11)-(7.15), and (7.18) into equation (7.22) and ignoring some high-order term, the thermal-related energy U_T can be expressed as,

$$U_T\approx E(T)\alpha\Delta TA\int_0^L\left[\frac{1}{2}({y_0}^2+{z_0}^2)\left(\frac{\partial f_{\theta x}(x)}{\partial x}\right)^2\right]dx$$

$$+E(T)\alpha\Delta TA\int_0^L\left[\left(y_0\frac{\partial f_z(x)}{\partial x}-z_0\frac{\partial f_y(x)}{\partial x}\right)\frac{\partial f_{\theta x}(x)}{\partial x}\right]dx$$

$$+E(T)\alpha\Delta TA\int_0^L\left[\frac{\partial f_x(x)}{\partial x}+\frac{1}{2}\left(\left(\frac{\partial f_y(x)}{\partial x}\right)^2+\left(\frac{\partial f_z(x)}{\partial x}\right)^2\right)\right]dx$$

$$+\frac{1}{2}E(T)\alpha\Delta T\left(I_y+I_z\right)\int_0^L\left(\frac{\partial f_{\theta x}(x)}{\partial x}\right)^2dx$$

$$+E(T)I_z\rho_y\int_0^L\left[y_0\left(\frac{\partial f_{\theta x}(x)}{\partial x}\right)^2-\frac{\partial^2 f_y(x)}{\partial x^2}+\left(\frac{\partial f_{\theta x}(x)}{\partial x}\right)\left(\frac{\partial f_z(x)}{\partial x}\right)\right]dx$$

$$+E(T)I_y\rho_z\int_0^L\left[z_0\left(\frac{\partial f_{\theta x}(x)}{\partial x}\right)^2-\frac{\partial^2 f_z(x)}{\partial x^2}-\left(\frac{\partial f_{\theta x}(x)}{\partial x}\right)\left(\frac{\partial f_y(x)}{\partial x}\right)\right]dx$$

(7.23)

7.3.4 Secant relations

According to the minimum potential energy principle, the secant relations can be obtained by the first variation of the potential energy function as,

$$\delta\Pi=\frac{\partial\Pi}{\partial u_i}+\frac{\partial\Pi}{\partial q}\frac{\partial q}{\partial u_i}=0 \tag{7.24}$$

where u_i stands for the element DOFs given in (7.1), and *i*=1-8.

The equations for the calculation of element nodal forces given in equation (7.2) can be get by submitting equations (7.17), (7.21), (7.23) in to equation (7.24),

$$P=P_\sigma+P_T \tag{7.25}$$

$$M_{y1}=M_{\sigma y1}+M_{Ty1} \tag{7.26}$$

$$M_{z1}=M_{\sigma z1}+M_{Tz1} \tag{7.27}$$

$$M_{b1}=M_{\sigma b1}+M_{Tb1} \tag{7.28}$$

$$M_x = M_{\sigma x} + M_{Tx} \tag{7.29}$$

$$M_{y2} = M_{\sigma y2} + M_{Ty2} \tag{7.30}$$

$$M_{z2} = M_{\sigma z2} + M_{Tz2} \tag{7.31}$$

$$M_{b2} = M_{\sigma b2} + M_{Tb2} \tag{7.32}$$

where, the subscripts σ denotes the force-related element nodal forces generated from equation (7.21), and the subscripts T denotes the thermal-related element nodal forces generated from equation (7.23).

The force-related element nodal forces can be calculated by the following equations.

$$P_\sigma = \frac{E(T)A}{L} e \tag{7.33}$$

$$\begin{aligned} M_{\sigma y1} &= \frac{4E(T)Iy}{L}\gamma_{y1} + \frac{2E(T)Iy}{L}\gamma_{y2} + \frac{2LP}{15}\gamma_{y1} - \frac{LP}{30}\gamma_{y2} \\ &+ \frac{3LM_{z1} - LM_{z2}}{30}\theta_{b1} - \frac{LM_{z1}}{30}\theta_{b2} + \frac{M_{z1} + 2M_{z2}}{10}\gamma_x - \frac{2LPy_0}{15}\theta_{b1} \\ &+ \frac{LPy_0}{30}\theta_{b2} + \frac{Py_0}{10}\gamma_x \end{aligned} \tag{7.34}$$

$$\begin{aligned} M_{\sigma z1} &= \frac{4E(T)Iz}{L}\gamma_{z1} + \frac{2E(T)Iz}{L}\gamma_{z2} + \frac{2LP}{15}\gamma_{z1} - \frac{LP}{30}\gamma_{z2} \\ &+ \frac{3LM_{y1} - LM_{y2}}{30}\theta_{b1} - \frac{LM_{y1}}{30}\theta_{b2} + \frac{M_{y1} + 2M_{y2}}{10}\gamma_x + \frac{2LPz_0}{15}\theta_{b1} \\ &- \frac{LPz_0}{30}\theta_{b2} - \frac{Pz_0}{10}\gamma_x \end{aligned} \tag{7.35}$$

$$M_{\sigma b1} = -\left[\frac{G(T)J}{10} + \frac{6E(T)Iw}{L^2}\right]\gamma_x + \left[\frac{4E(T)Iw}{L} + \frac{2G(T)JL}{15}\right]\theta_{b1}$$

$$+\left[\frac{2E(T)Iw}{L} - \frac{G(T)JL}{30}\right]\theta_{b2} + \frac{3LM_{z1} - LM_{z2}}{30}\gamma_{y1} + \frac{3LM_{y1} - LM_{y2}}{30}\gamma_{z1}$$

$$+\frac{LM_{z2}}{30}\gamma_{y2} + \frac{LM_{y2}}{30}\gamma_{z2} + \frac{2LPr^2}{15}\theta_{b1} - \frac{LPr^2}{30}\theta_{b2} - \frac{Pr^2}{10}\gamma_x - \frac{2LPy_0}{15}\gamma_{y1}$$

$$+\frac{2LPz_0}{15}\gamma_{z1} + \frac{LPy_0}{30}\gamma_{y2} - \frac{LPz_0}{30}\gamma_{z2} - \frac{\beta_\omega M_b + \beta_z M_{y2} - \beta_y M_{z2}}{10}\gamma_x \tag{7.36}$$

$$+\frac{1}{30}\left(4\beta_\omega LM_b - 3\beta_z LM_{y1} + \beta_z LM_{y2} + 3\beta_y LM_{z1} - \beta_y LM_{z2}\right)\theta_{b1}$$

$$+\frac{1}{60}\left(-2\beta_\omega LM_b + \beta_z LM_{y1} - \beta_z LM_{y2} - \beta_y LM_{z1} + \beta_y LM_{z2}\right)\theta_{b2}$$

$$M_{\sigma x} = \left[\frac{12E(T)Iw}{L^3} + \frac{6G(T)J}{5L}\right]\gamma_x - \left[\frac{G(T)J}{10} + \frac{6E(T)Iw}{L^2}\right](\theta_{b1} + \theta_{b2})$$

$$+\left(\frac{M_{z1} + 2Mz2 + Py_0}{10}\right)\gamma_{y1} - \frac{Pz_0}{10}\gamma_{z2}\left(\frac{M_{y1} + 2M_{y2} - Pz_0}{10}\right)\gamma_{z1}$$

$$-\frac{2M_{z1} + M_{z2}}{10}\gamma_{y2} - \frac{2M_{y1} + M_{y2}}{10}\gamma_{z2} - (\theta_{b1} + \theta_{b2})\frac{Pr^2}{10} + \frac{6Pr^2}{5L}\gamma_x \tag{7.37}$$

$$+\frac{Py_0}{10}\gamma_{y2} + \frac{-\beta_\omega LM_b - \beta_z LM_{y2} + \beta_y LM_{z2}}{10L}\theta_{b1}$$

$$+\frac{-\beta_\omega LM_b + \beta_z LM_{y1} - \beta_y LM_{z1}}{10L}\theta_{b2}$$

$$+\frac{6\beta_\omega M_b + 3\beta_z(-M_{y1} + M_{y2}) + 3\beta_y(M_{z1} - M_{z2})}{5L}\gamma_x$$

$$M_{\sigma y2} = \frac{2E(T)Iy}{L}\gamma_{y1} + \frac{4E(T)Iy}{L}\gamma_{y2} - \frac{LP}{30}\gamma_{y1} + \frac{2LP}{15}\gamma_{y2} + \frac{LM_{z2}}{30}\theta_{b1} \tag{7.38}$$

$$+\frac{LM_{z1}-3LM_{z2}}{30}\theta_{b2}-\frac{2M_{z1}+M_{z2}}{10}\gamma_x+\frac{LPy_0}{30}\theta_{b1}-\frac{2LPy_0}{15}\theta_{b2}+\frac{Py_0}{10}\gamma_x$$

$$M_{\sigma z2}=\frac{2E(T)Iz}{L}\gamma_{z1}+\frac{4E(T)Iz}{L}\gamma_{z2}-\frac{LP}{30}\gamma_{z1}+\frac{2LP}{15}\gamma_{z2}+\frac{LM_{y2}}{30}\theta_{b1}$$

(7.39)

$$+\frac{LM_{y1}-3LM_{y2}}{30}\theta_{b2}-\frac{2M_{y1}+M_{y2}}{10}\gamma_x-\frac{LPz_0}{30}\theta_{b1}+\frac{2LPz_0}{15}\theta_{b2}-\frac{Pz_0}{10}\gamma_x$$

$$M_{\sigma b2}=-\left[\frac{G(T)J}{10}+\frac{6E(T)Iw}{L^2}\right]\gamma_x+\left[\frac{2E(T)Iw}{L}-\frac{G(T)JL}{30}\right]\theta_{b1}$$

$$+\left[\frac{4E(T)Iw}{L}+\frac{2G(T)JL}{15}\right]\theta_{b2}-\frac{LM_{z1}}{30}\gamma_{y1}-\frac{LM_{y1}}{30}\gamma_{z1}$$

$$+\frac{LM_{z1}-3LM_{z2}}{30}\gamma_{y2}+\frac{LM_{y1}-3LM_{y2}}{30}\gamma_{z2}-\frac{LPr^2}{30}\theta_{b1}+\frac{2LPr^2}{15}\theta_{b2}$$

$$-\frac{Pr^2}{10}\gamma_x+\frac{LPy_0}{30}\gamma_{y1}-\frac{LPz_0}{30}\gamma_{z1}-\frac{2LPy_0}{15}\gamma_{y2}+\frac{2LPz_0}{15}\gamma_{z2} \tag{7.40}$$

$$+\frac{1}{60}\left(-2\beta_\omega LM_b+\beta_z LM_{y1}-\beta_z LM_{y2}-\beta_y LM_{z1}+\beta_y LM_{z2}\right)\theta_{b1}$$

$$+\frac{1}{30}\left(4\beta_\omega LM_b-\beta_z LM_{y1}+3\beta_z LM_{y2}+\beta_y LM_{z1}-3\beta_y LM_{z2}\right)\theta_{b2}$$

$$-\frac{\beta_\omega M_b-\beta_z M_{y1}+\beta_y M_{z1}}{10}\gamma_x$$

The thermal-related element nodal forces can be generated by:

$$P_{Tx}=-E(T)\alpha\Delta TA \tag{7.41}$$

$$M_{Ty1}=-\alpha E(T)I_y\rho_z+\frac{\alpha E(T)\left(I_z\rho_y+\Delta TAy_0\right)}{10}\gamma_x-\frac{2\alpha\Delta TE(T)AL}{15}\gamma_{y1}$$

(7.42)

$$+\frac{\alpha\Delta TE(T)AL}{30}\gamma_{y2}-\frac{\alpha E(T)\left(2I_zL\rho_y+2\Delta TALy_0\right)}{15}\theta_{b1}$$

$$-\frac{\alpha E(T)\left(-I_z L\rho_y - \Delta TALy_0\right)}{30}\theta_{b2}$$

$$M_{Tz1} = -\alpha E(T)I_z\rho_y - \frac{\alpha E(T)\left(3I_y\rho_z + 3\Delta TAz_0\right)}{30}\gamma_x - \frac{2\alpha\Delta TE(T)AL}{15}\gamma_{z1}$$

$$+\frac{\alpha\Delta TE(T)AL}{30}\gamma_{z2} + \frac{\alpha E(T)\left(2I_y L\rho_z + 2\Delta TALz_0\right)}{15}\theta_{b1} \tag{7.43}$$

$$+\frac{\alpha E(T)\left(-I_y L\rho_z - \Delta TALz_0\right)}{30}\theta_{b2}$$

$$M_{Tb1} = +\frac{\alpha E(T)\left(I_z L\rho_y + \Delta TALy_0\right)}{30}\gamma_{y2} + \frac{\alpha E(T)\left(I_y L\rho_z - \Delta TALz_0\right)}{30}\gamma_{z2}$$

$$\frac{\alpha E(T)\left(-2I_z L\rho_y - 2\Delta TALy_0\right)}{15}\gamma_{y1} + \frac{\alpha E(T)\left(2I_y L\rho_z + 2\Delta TALz_0\right)}{15}\gamma_{z1}$$

$$+\frac{\alpha E(T)\left[\Delta TI_y + Iz\left(\Delta T + 2\rho_y y_0\right) + 2I_y\rho_z z_0 + \Delta TA({y_0}^2 + {z_0}^2)\right]}{10}\gamma_x$$

$$+\frac{\alpha E(T)\left(-4I_z L\rho_y y_0 - 2\Delta TAL{y_0}^2 - 4I_y L\rho_z z_0 - 2\Delta TAL{z_0}^2\right)}{15}\theta_{b1} \tag{7.44}$$

$$+\frac{\alpha E(T)\left(-2\Delta TI_y L - 2\Delta TI_z L\right)}{15} + \frac{\alpha E(T)\left(\Delta TI_y L + \Delta TI_z L\right)}{30}$$

$$+\frac{\alpha E(T)\left(2I_z L\rho_y y_0 + \Delta TAL{y_0}^2 + 2I_y L\rho_z z_0 + \Delta TAL{z_0}^2\right)}{30}\theta_{b2}$$

$$M_{Tx} = \frac{\alpha E(T)\left(I_z L\rho_y + \Delta TALy_0\right)}{10L}\gamma_{y1} + \frac{\alpha E(T)\left(-I_y L\rho_z - \Delta TALz_0\right)}{10L}\gamma_{z1}$$

$$+\frac{\alpha E(T)\left(I_z L\rho_y + \Delta TALy_0\right)}{10L}\gamma_{y2} + \frac{\alpha E(T)\left(I_y L\rho_z + \Delta TALz_0\right)}{10L}\gamma_{z2} \tag{7.45}$$

$$+\frac{\alpha E(T)\left[\Delta T\left(I_y + I_z\right)L + 2I_z L\rho_y y_0 + 2I_y L\rho_z z_0 + \Delta TAL({y_0}^2 + {z_0}^2)\right]}{10L}\theta_{b1}$$

$$+\frac{\alpha E(T)\left[\Delta T\left(I_y+I_z\right)L+2I_zL\rho_y y_0+2I_yL\rho_z z_0+\Delta TAL({y_0}^2+{z_0}^2)\right]}{10L}\theta_{b2}$$

$$+\frac{\alpha E(T)\left[-6\Delta T\left(I_y+I_z\right)-12I_z\rho_y y_0-12I_y\rho_z z_0-6\Delta TA({y_0}^2+{z_0}^2)\right]}{5L}\gamma_x$$

$$M_{Ty2}=\alpha E(T)I_y\rho_z+\frac{\alpha E(T)\left(I_z\rho_y-\Delta TAy_0\right)}{10}\gamma_x-\frac{2\alpha\Delta TE(T)AL}{15}\gamma_{y2}$$

$$+\frac{\alpha\Delta TE(T)AL}{30}\gamma_{y1}+\frac{\alpha E(T)\left(-2I_zL\rho_y-2\Delta TALy_0\right)}{15}\theta_{b2} \tag{7.46}$$

$$+\frac{\alpha E(T)\left(I_zL\rho_y+\Delta TALy_0\right)}{30}\theta_{b1}$$

$$M_{Tz2}=\alpha E(T)I_z\rho_y+\frac{\alpha E(T)\left(-I_y\rho_z-\Delta TAz_0\right)}{10}\gamma_x-\frac{2\alpha\Delta TE(T)AL}{15}\gamma_{z2}$$

$$+\frac{\alpha\Delta TE(T)AL}{30}\gamma_{z1}+\frac{\alpha E(T)\left(2I_yL\rho_z+2\Delta TALz_0\right)}{15}\theta_{b2} \tag{7.47}$$

$$+\frac{\alpha E(T)\left(-I_yL\rho_z-\Delta TALz_0\right)}{30}\theta_{b1}$$

$$M_{Tb2}=2\alpha E(T)\left[\frac{\left(-I_zL\rho_y-\Delta TALy_0\right)}{15}\gamma_{y2}+\frac{\left(I_yL\rho_z+\Delta TALz_0\right)}{15}\gamma_{z2}\right]$$

$$+\frac{\alpha E(T)\left(I_zL\rho_y+\Delta TALy_0\right)}{30}\gamma_{y1}+\frac{\alpha E(T)\left(-I_yL\rho_z-\Delta TALz_0\right)}{30}\gamma_{z1}$$

$$+\frac{\alpha E(T)\left(-4I_zL\rho_y y_0-2\Delta TAL{y_0}^2-4I_yL\rho_z z_0-2\Delta TAL{z_0}^2\right)}{15}\theta_{b2} \tag{7.48}$$

$$+\frac{\alpha E(T)\left(-2\Delta TI_yL-2\Delta TI_zL\right)}{15}+\frac{\alpha E(T)\left(\Delta TI_yL+\Delta TI_zL\right)}{30}$$

$$+\frac{\alpha E(T)\left(2I_zL\rho_y y_0+\Delta TAL{y_0}^2+2I_yL\rho_z z_0+\Delta TAL{z_0}^2\right)}{30}\theta_{b1}$$

$$+\frac{\alpha E(T)\left[\Delta TI_y + Iz\left(\Delta T + 2\rho_y y_0\right) + 2I_y\rho_z z_0 + \Delta TA({y_0}^2 + {z_0}^2)\right]}{10}\gamma_x$$

7.3.5 Tangent stiffness and transformation matrices

The element stiffness matrices can be generated by the second variation of the potential energy,

$$\delta^2\Pi = \frac{\partial^2\Pi}{\partial u_i\,\partial u_j}\delta u_i\delta u_j = \left(\frac{\partial F_i}{\partial u_j} + \frac{\partial F_i}{\partial q}\frac{\partial q}{\partial u_j}\right)\delta u_i\delta u_j = \boldsymbol{k_E}\Delta\boldsymbol{u} - \Delta\boldsymbol{f} \tag{7.49}$$

$(i, j =$1-8)

Therefore, the element tangent stiffness can be determined and written in terms of four parts,

$$\boldsymbol{k_E} = \frac{E(T)}{E_0}\boldsymbol{k_L} + \boldsymbol{k_G} + \boldsymbol{k_U} + \boldsymbol{k_T} \tag{7.50}$$

where, $E(T)$ and E_0 are the material Young's modulus at the evaluated temperature and the room temperature; $\boldsymbol{k_L}$ and $\boldsymbol{k_G}$ are linear stiffness matrices and geometric stiffness matrices; $\boldsymbol{k_U}$ is the additional geometric stiffness matrix for the element with nonsymmetric section; and $\boldsymbol{k_T}$ is the thermal-related geometric stiffness given below.

$$\boldsymbol{k_T} = \begin{bmatrix} 0 & 0 & 0 & 0 & 0 & 0 & 0 & 0 \\ 0 & \dfrac{-2\alpha E(T)AL\Delta T}{15L} & 0 & k_{T2,4} & k_{T2,5} & \dfrac{\alpha E(T)A\Delta TL}{30} & 0 & k_{T2,8} \\ 0 & 0 & \dfrac{-2\alpha E(T)AL\Delta T}{15L} & k_{T3,4} & k_{T3,5} & 0 & \dfrac{\alpha E(T)A\Delta TL}{30} & k_{T3,8} \\ 0 & k_{T2,4} & k_{T3,4} & k_{T4,4} & k_{T4,5} & k_{T4,6} & k_{T4,7} & k_{T4,8} \\ 0 & k_{T2,5} & k_{T3,5} & k_{T4,5} & k_{T5,5} & k_{T5,6} & k_{T5,7} & k_{T5,8} \\ 0 & \dfrac{\alpha E(T)A\Delta TL}{30} & 0 & k_{T4,6} & k_{T5,6} & \dfrac{-2\alpha E(T)A\Delta TL}{15} & 0 & k_{T6,8} \\ 0 & 0 & \dfrac{\alpha E(T)A\Delta TL}{30} & k_{T4,7} & k_{T5,7} & 0 & \dfrac{-2\alpha E(T)A\Delta TL}{15} & k_{T7,8} \\ 0 & k_{T2,8} & k_{T3,8} & k_{T4,8} & k_{T5,8} & k_{T6,8} & k_{T7,8} & k_{T8,8} \end{bmatrix} \tag{7.51}$$

in which,

$$k_{T4,4} = \frac{\alpha L\left[-4\Delta T E(T)\left(I_y + I_z\right) - 8E(T)I_z\rho_y y_0 - 8E(T)I_y\rho_z z_0 - 4E(T)A\Delta T({y_0}^2 + {z_0}^2)\right]}{30}$$

$$k_{T4,5} = \frac{\alpha\left[\Delta T E(T)\left(I_y + I_z\right) + 2E(T)I_z\rho_y y_0 + 2E(T)I_y\rho_z z_0 + E(T)A\Delta T({y_0}^2 + {z_0}^2)\right]}{10}$$

$$k_{T4,8} = \frac{\alpha L\left[\Delta T E(T)\left(I_y + I_z\right) + 2E(T)I_z\rho_y y_0 + 2E(T)I_y\rho_z z_0 + E(T)A\Delta T({y_0}^2 + {z_0}^2)\right]}{30}$$

$$k_{T5,5} = \frac{\alpha\left[-12\Delta T E(T)\left(I_y + I_z\right) - 24E(T)I_z\rho_y y_0 - 24E(T)I_y\rho_y z_0 - 12E(T)A\Delta T({y_0}^2 + {z_0}^2)\right]}{10L}$$

$$k_{T5,8} = \frac{\alpha\left[\Delta T E(T)\left(I_y + I_z\right) + 2E(T)I_z\rho_y y_0 + 2E(T)I_y\rho_z z_0 + E(T)A\Delta T({y_0}^2 + {z_0}^2)\right]}{10L}$$

$$k_{T8,8} = \frac{\alpha L\left[-4\Delta T E(T)\left(I_y + I_z\right) - 8E(T)I_z\rho_y y_0 - 8E(T)I_y\rho_z z_0 - 4E(T)A\Delta T({y_0}^2 + {z_0}^2)\right]}{30}$$

$$k_{T2,4} = \frac{\alpha\left[-4E(T)I_z L\rho_y - 4E(T)A\Delta T L y_0\right]}{30}$$

$$k_{T2,5} = \frac{\alpha\left[E(T)I_z\rho_y - E(T)A\Delta T y_0\right]}{10}$$

$$k_{T2,8} = \frac{\alpha E(T)\left(I_z L\rho_y + A\Delta T L y_0\right)}{30}$$

$$k_{T3,4} = \frac{\alpha E(T)\left(4I_y L\rho_z + 4A\Delta T L z_0\right)}{30}$$

$$k_{T3,5} = \frac{\alpha E(T)\left(-I_y\rho_z - A\Delta T z_0\right)}{10}$$

$$k_{T3,8} = \frac{\alpha E(T)\left(-I_y L\rho_z - A\Delta T L z_0\right)}{30}$$

$$k_{T6,8} = -\frac{4\alpha E(T)\left(I_z L\rho_y + A\Delta T L y_0\right)}{30}$$

$$k_{T4,6} = \frac{\alpha E(T)\left(I_z L\rho_y + A\Delta T L y_0\right)}{30}$$

$$k_{T4,7} = \frac{\alpha E(T)\left(-I_y\rho_z - A\Delta T z_0\right)}{10L}$$

$$k_{T5,6} = \frac{\alpha E(T)\left(I_z\rho_y + A\Delta T y_0\right)}{10L}$$

$$k_{T5,7} = \frac{\alpha E(T)\left(-I_y\rho_z - A\Delta T z_0\right)}{10L}$$

$$k_{T7,8} = \frac{4\alpha E(T)\left(I_y L\rho_z + A\Delta T L z_0\right)}{30}$$

A transformation matric is adopted to transform the element local independent eight DOFs (Figure 7.1 (a)) to the 14 DOFs in the element coordinate. This transformation matric is generate based on the relations between end moments and shear forces and given by Liu *et al*. (2014a),

$$\boldsymbol{F_e} = \boldsymbol{TF} \tag{7.52}$$

The element nodal force in global axis can be generated by,

$$\boldsymbol{F_g} = \boldsymbol{L}^T\boldsymbol{F_e} \tag{7.53}$$

where, $\boldsymbol{L}$ is the matrix that transfers the DOFs from the element local to global axis given by Chan and Chui (2009).

The element stiffness matrix in global axis then can be calculated by,

$$\boldsymbol{k_g} = \boldsymbol{L}^T(\boldsymbol{T}\boldsymbol{k_E}\boldsymbol{T}^T + \boldsymbol{N})\boldsymbol{L} \tag{7.54}$$

in which, $\boldsymbol{k_g}$ is the element stiffness matrices in global axis, $\boldsymbol{k_e}$ is the element stiffness matrices in local coordinates, and $\boldsymbol{N}$ is the matrix for the consideration of rigid body movement given by Liu *et al*. (2014a). The global stiffness matrices then can be assembled by,

$$\boldsymbol{K_g} = \sum_{i=1}^{NELE} \boldsymbol{k_{gi}} \tag{7.55}$$

in which, $NELE$ stands for the total number of the elements.

7.4 Numerical Procedure

A Newton–Raphson-typed incremental-iterative procedure introduced as per Iu and Chan (2004; 2005) is adopted for the structural analysis at elevated temperatures. The CR description will be used to determine the equilibrium conditions. Detailed analysis procedures are briefly described as follows.

Establishment of equilibrium condition at room temperature $\boldsymbol{T0}$:

Step 1.: Assemble the global stiffness matrices $\boldsymbol{K_g}$ using equations (7.50), (7.54), and (7.55).

Step 2.: Calculate the global incremental displacement using the global stiffness matrices and the unbalanced force vector,

$$\Delta \boldsymbol{U}^i_{\boldsymbol{g},T0} = \Delta \boldsymbol{F}^i_{\boldsymbol{g},T0} {\boldsymbol{K}^i_{\boldsymbol{g},T0}}^{-1} \tag{7.56}$$

where, $\Delta \boldsymbol{F_g}$ is the unbalanced force vector, $\Delta \boldsymbol{U_g}$ is the global incremental displacement vector, the subscripts *T0* denotes the room temperature, and *i* stands for the *i*th iterations.

Step 3.: Update the total displacement,

$$\boldsymbol{U}_{\boldsymbol{g},T0}^{i} = \boldsymbol{U}_{\boldsymbol{g},T0}^{i-1} + \Delta\boldsymbol{U}_{\boldsymbol{g},T0}^{i} \tag{7.57}$$

Step 4.: Extract the incremental element displacement $\Delta\boldsymbol{u}_{\boldsymbol{g},T0}^{i}$ from the global incremental displacement $\Delta\boldsymbol{U}_{\boldsymbol{g},T0}^{i}$, then transform it into the element local incremental displacement

$$\Delta\boldsymbol{u}_{\boldsymbol{e},T0}^{i} = \boldsymbol{L}^{T}\Delta\boldsymbol{u}_{\boldsymbol{g},T0}^{i} \tag{7.58}$$

Step 5.: Update the total element displacement in the local axis,

$$\boldsymbol{u}_{\boldsymbol{e},T0}^{i} = \boldsymbol{u}_{\boldsymbol{e},T0}^{i-1} + \Delta\boldsymbol{u}_{\boldsymbol{e},T0}^{i} \tag{7.59}$$

Step 6.: Extract the total element deformation $\boldsymbol{u}_{T0}^{i}$ by removing the rigid body movement from the element total displacement $\boldsymbol{u}_{\boldsymbol{e},T0}^{i}$, and calculate the element local reaction force $\boldsymbol{r}_{T0}^{i}$ using the secant relations given in equation (7.25)-(7.48).

Step 7.: Assemble the total reaction force vector,

$$\boldsymbol{R}_{T0}^{i} = \sum_{i=1}^{NELE} \boldsymbol{L}^{T}\left(\boldsymbol{T}\boldsymbol{r}_{T0}^{i}\right) \tag{7.60}$$

Step 8.: Calculate the new unbalanced force by,

$$\Delta\boldsymbol{F}_{\boldsymbol{g},T0}^{i+1} = \boldsymbol{F}_{\boldsymbol{a}} - \boldsymbol{R}_{T0}^{i} \tag{7.61}$$

where, $\boldsymbol{F}_{\boldsymbol{a}}$ is the applied load vector.

Step 9.: Repeat Steps 1. - 8. until equilibrium measured by norms is achieved. To this end, in order to obtain an accurate analysis for both forces and displacements, the convergence criteria are checked using the unbalanced forces and displacements as,

$$\Delta \boldsymbol{U_g}^T \Delta \boldsymbol{U_g} < Tol \times \boldsymbol{U_g}^T \boldsymbol{U_g} \tag{7.62}$$

$$\Delta \boldsymbol{F_g}^T \Delta \boldsymbol{F_g} < Tol \times \boldsymbol{F_a}^T \boldsymbol{F_a} \tag{7.63}$$

in which, Tol is the convergence tolerance.

When the temperature starts to elevate:

Step 10.: Get the total element deformation $\boldsymbol{u}_{Tj-1}$ by removing the rigid body movement from the total element displacement $\boldsymbol{u}_{e,Tj-1}$, and calculate the new element local reaction force $\boldsymbol{r}_{Tj}$ using the secant relations given in equation (7.25)-(7.48). *Tj* stands for the *j*th temperature step.

Step 11.: Assemble the new total reaction force vector by,

$$\boldsymbol{R}_{Tj}^{i} = \sum_{i=1}^{NELE} \boldsymbol{L}^T \left(\boldsymbol{T} \boldsymbol{r}_{Tj}^{i} \right) \tag{7.64}$$

Step 12.: Calculate the new unbalanced force by,

$$\Delta \boldsymbol{F}_{\boldsymbol{g},Tj}^{i+1} = \boldsymbol{F_a} - \boldsymbol{R}_{Tj}^{i} \tag{7.65}$$

Step 13.: Repeat Steps 1. - 9. until the equilibrium is achieved, and then go to Step 10. to increase the temperature to the next temperature step.

The incremental procedure will be repeated till the target temperature is achieved or the structure becomes unstable.

7.5 Verification Examples

To validate the accuracy and the efficiency of the proposed method, five sets of examples, which are: columns with L section, beams with mono-symmetric I-section, cantilever beams with channel section, beams with nonsymmetric section, and star frames with T section, are studied. The Young's and shear moduli for steel at room temperature are adopted as 210 GPa and 80.77 GPa, respectively. The reduction factors for the Young's modulus with respect to the temperature provided by Eurocode 3 (2005) are adopted (Figure 7.2).

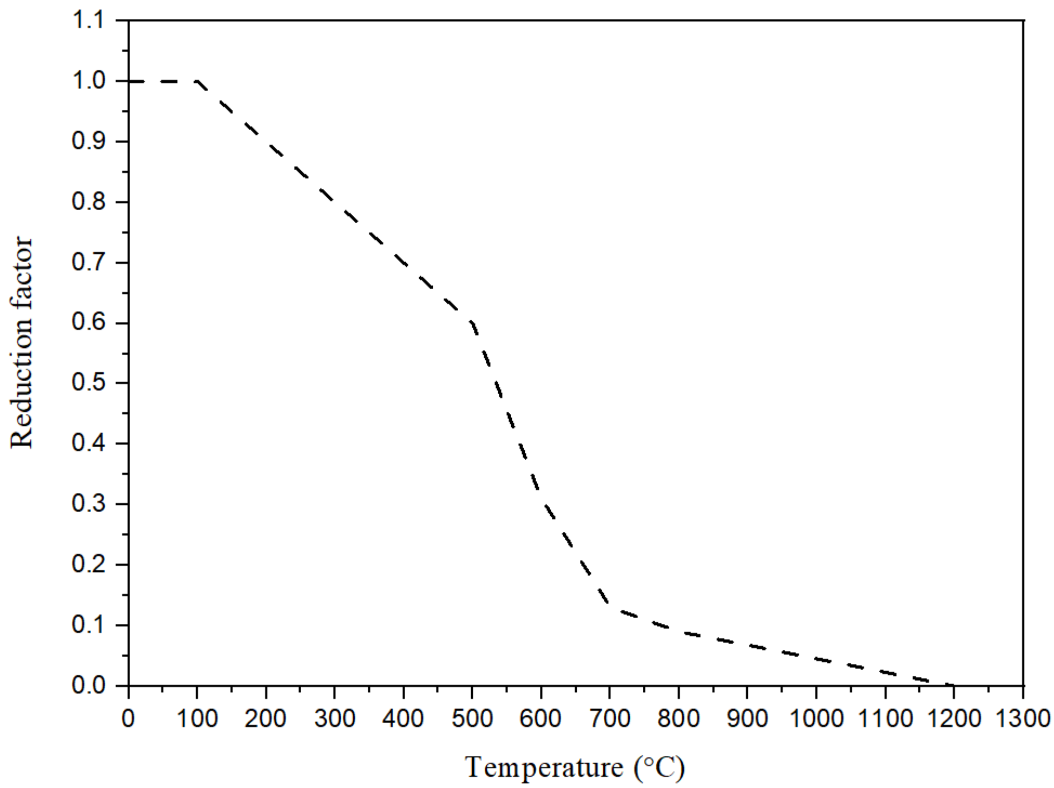

Figure 7.2 The reduction factors for the Young's modulus

Example 1: Thermal buckling analysis of columns with L section

In this example, the buckling behaviors of a series of columns due to thermal expansion are computed by the analytical solutions, and the corresponding results will be used as benchmarks for validating the proposed method. Ziemian (2010) has provided the closed-formed solution for the calculation of buckling strength for columns with L sections as given by,

$$P_{cr}^3(r^2 - y_0^2 - z_0^2) - P_{cr}^2\left[\left(P_y + P_z + P_r\right)r^2 - P_z y_0^2 - P_y z_0^2\right]$$
$$+P_{cr}r^2\left(P_y P_z + P_r P_z + P_y P_r\right) - \left(P_y P_z P_r r^2\right) = 0 \quad (7.66)$$

where,

$$P_y = \frac{\pi^2 E I_y}{L^2} \quad (7.67)$$

$$P_z = \frac{\pi^2 E I_z}{L^2} \quad (7.68)$$

$$P_r = \frac{GJ + \pi^2 E I_\omega / L^2}{y_0^2 + z_0^2 + \left(I_y + I_z\right)/A} \quad (7.69)$$

The axial force caused by the thermal expansion in an axial restrained column (Figure 7.3) can be calculated by,

$$P_T = \int_A (T - T_0)\alpha E(T) dA \quad (7.70)$$

in which T_0 is the room temperature, T is the temperature of the columns. The analytical solution to compute the critical buckling temperatures of a column under thermal expansion can be generated by,

$$P_T = P_{cr} \quad (7.71)$$

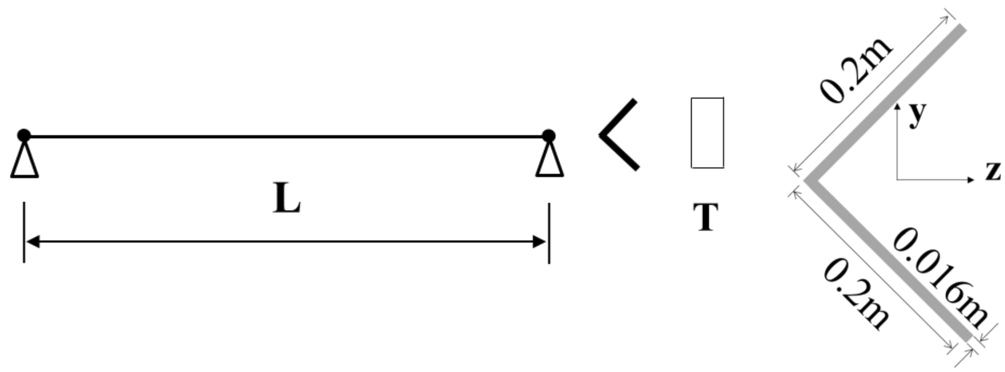

Figure 7.3 Section dimensions and member boundary conditions

Table 7.1 Critical buckling temperatures of the columns with L section

Relative slenderness λ_y	***Theoretical*** (℃)	***Present Study*** (℃)	***Differences***
50	933.9	924.2	-1.0%
60	426.2	421.8	-1.0%
70	248.5	246.1	-0.9%
80	166.2	164.7	-0.9%
90	121.5	120.5	-0.8%
100	94.6	93.8	-0.8%

A series of columns with L section are investigated. The detailed section dimensions and member boundary conditions are given in Figure 7.3. All the columns are warping-continuous along the length of the member. The nonlinear buckling analysis for those columns is conducted, and the temperature-displacement cures for the middle points of the columns are given in Figure 7.4. The theoretical buckling temperatures of the columns calculated with equation (7.70) and those generated by the proposed method are given in Table 7.1 for comparison. It is clearly seen that the proposed method can predict the buckling behaviors of simply supported columns at elevated temperatures accurately regardless of the relative slenderness.

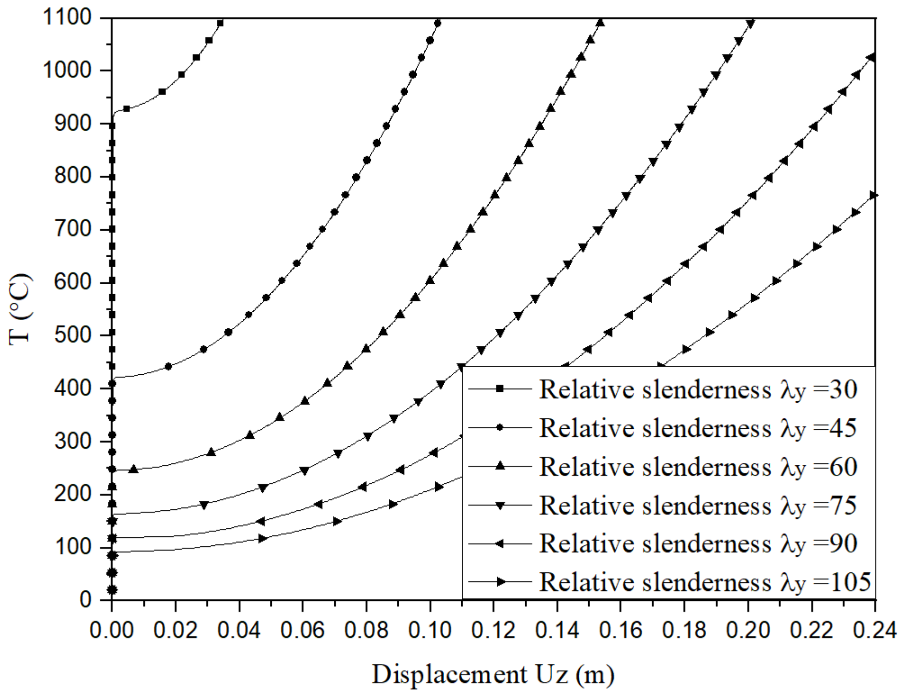

Figure 7.4 Temperature-displacement cures for the middle points of the columns

Example 2: Thermal buckling analysis of beams with mono-symmetric I-section

This example gives results of the thermal buckling analysis of beams in different temperature gradients. The cross-section of those beams is the mono-symmetric I-section. As shown in Figure 7.5, the width of the I-section flanges are 0.15 m and 0.075 m, the depth of the I-section is 0.3 m, and the flange thickness and web thickness are 0.0107 m and 0.0071 m, respectively. The boundary conditions of the beams are also given in Figure 7.5.

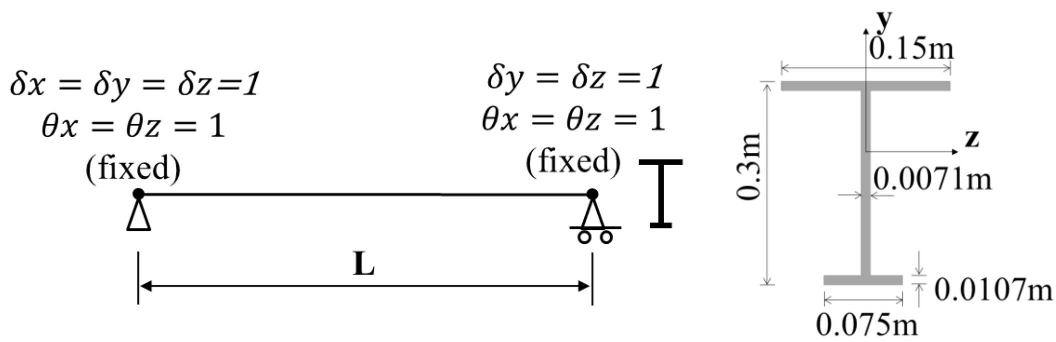

Figure 7.5 Section dimensions and boundary conditions

A series of beams with different lengths are studied to investigate the influence of the temperature gradients. The buckling behaviors of all the beams under positive and negative temperature gradients are studied. Based on the closed-formed solution given by Galambos (2016), the critical lateral-torsional buckling moment for those beams can be calculated by,

$$M_{cr}^{\pm} = \frac{\pi^2 E(T) I_y}{L^2}\left\{\pm\frac{\beta_z}{2} + \sqrt{\left(\frac{\beta_z}{2}\right)^2 + \left[\frac{I_\omega}{I_y} + \frac{G(T) J L^2}{E(T) I_y \pi^2}\right]}\right\} \tag{7.72}$$

The thermal-induced moment caused by the temperature gradients in a rotation restrained beam as shown in Figure 7.6 can be calculated by,

$$M_T = \int_A \alpha \rho_y E(T) y^2 dA = \alpha \rho_y E(T) I_z \tag{7.73}$$

where, $\rho_y = \frac{T_t - T_b}{H}$, and T_t and $T_b$are temperatures at the top and bottom of the cross-section, respectively; H is the depth of the cross-section. The analytical solution to compute the critical buckling temperatures of the beams under temperature gradients can be generated by,

$$M_T = M_{cr} \tag{7.74}$$

Table 7.2 Critical buckling temperatures of the beams (under negative temperature gradient)

L	***Theoretical***	***Present Study***		***Present Study (Elements with Doubly-symmetric-section Assumption)***	
(m)	(°C)	(°C)	Differences	(°C)	Differences
2	182.4	180.9	-0.81%	402.2	120.6%
3	113.6	112.8	-0.66%	220.1	93.9%
4	86.3	85.8	-0.55%	150.5	74.4%
5	71.3	71.1	-0.29%	114.6	60.7%
6	61.5	61.4	-0.20%	92.7	50.8%
7	54.4	54.3	-0.18%	78.0	43.4%

Table 7.3 Critical buckling Temperatures of the beams (under positive temperature gradient)

L	***Theoretical***	***Present Study***		***Present Study (Elements with Doubly-symmetric-section Assumption)***	
(m)	(°C)	(°C)	Differences	(°C)	Differences
2	887.1	857.7	-3.32%	402.2	-54.7%
3	426.8	414.0	-2.99%	220.1	-48.4%
4	262.5	255.6	-2.61%	150.5	-42.7%
5	184.1	180.0	-2.21%	114.6	-37.8%
6	139.8	137.1	-1.94%	92.7	-33.7%
7	111.9	110.1	-1.63%	78.0	-30.3%

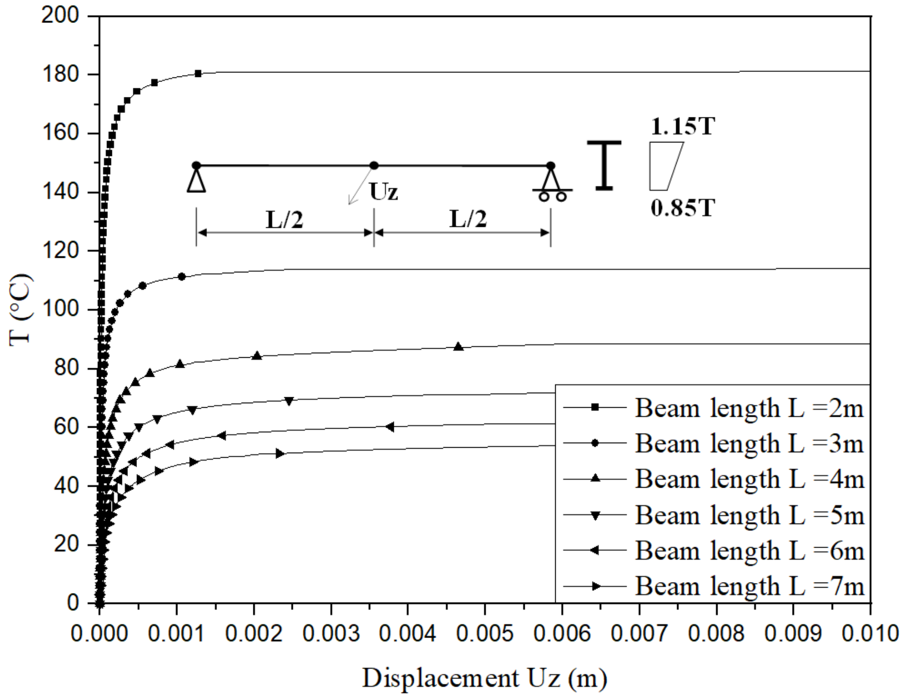

(a) Under negative temperature gradient

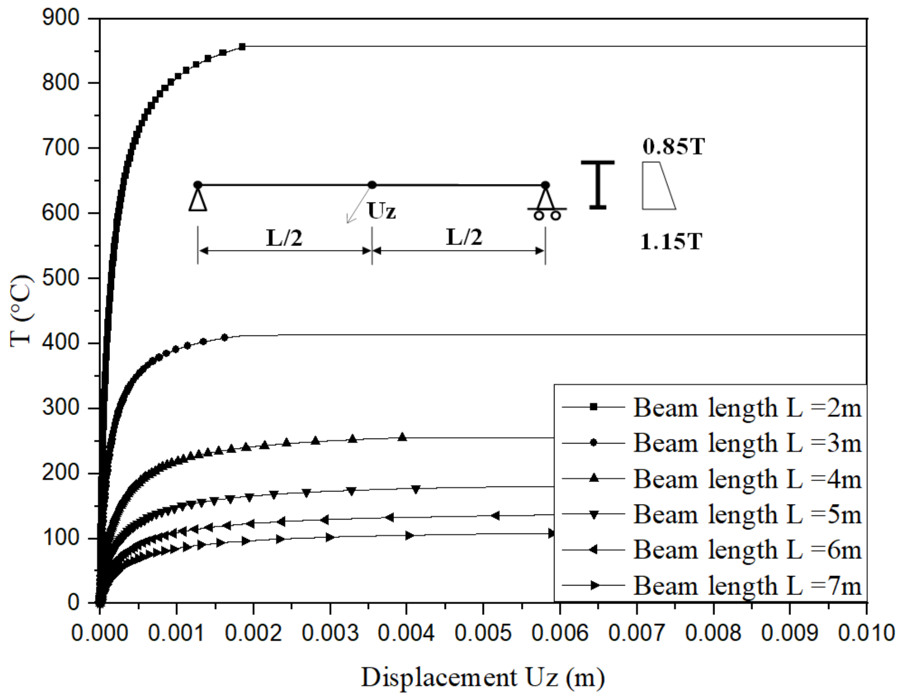

(b) Under positive temperature gradient

Figure 7.6 Temperature-displacement cures for the middle points of the beams

Results from the theoretical solution and ten proposed CR beam-column elements are given in Table 7.2 and Table 7.3, and Figure 7.6. Results generated by ten conventional beam-column elements with doubly-symmetric-section assumption are also presented, where the coordinates of the shear center and the Wagner coefficients will be taken as zero in the element formulations given above. It is clearly seen that the proposed method can predict the lateral-torsional buckling behaviors of the beam in fire, and the doubly-symmetric-section assumption can cause significant differences.

Example 3: Large deflection analysis of a cantilever beam with channel section

A cantilever beam with a channel section is studied in this example. This example was proposed and tested at ambient temperature by Battini (2002) and Gruttmann *et al.* (2000; 1998). Then, Possidente *et al.* (2020) investigated the structural behaviors of this beam at elevated temperatures. Detailed boundary and loading conditions are given in Figure 7.7. The width of the channel section flanges is 0.1 m, the depth of the section is 0.3 m, and the flange thickness and web thickness are 0.016 m and 0.01 m, respectively.

A constant load P=3kN is applied at the bottom of the section web, which is not in line with the shear center, causing a twisting moment at the end of the beam. Results from Possidente *et al.* (2020) generated from shell elements with 2101 nodes and ten proposed CR beam-column elements with eleven nodes are given in Figure 7.7 for comparison. Results generated by ten conventional beam-column elements with doubly-symmetric-section assumption are also presented. From Figure 7.7, it is clear that ten proposed beam-column elements are capable of predicting the nonlinear behaviors of members at elevated temperatures, and if the doubly-symmetric-section assumption is adopted for the nonsymmetric section, large differences will be observed.

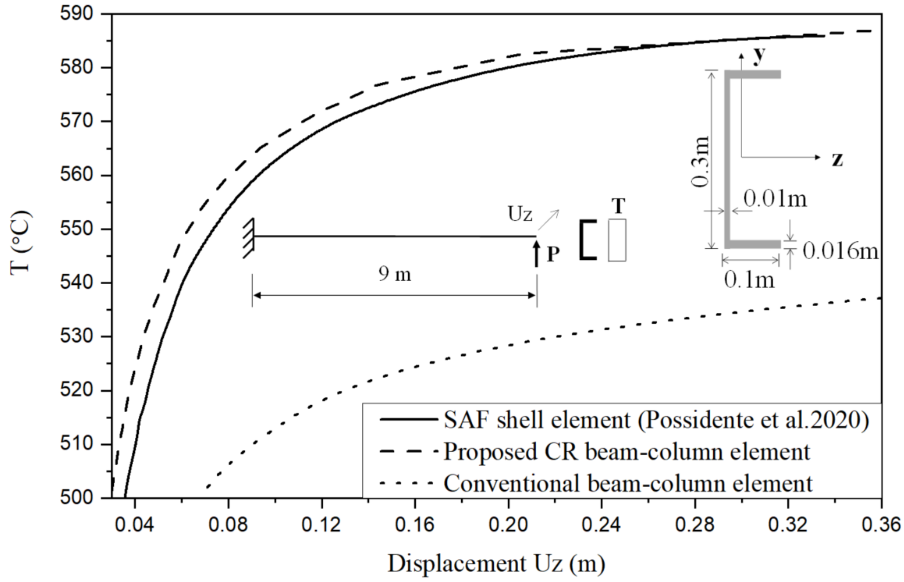

(a) Out-of-plane displacement

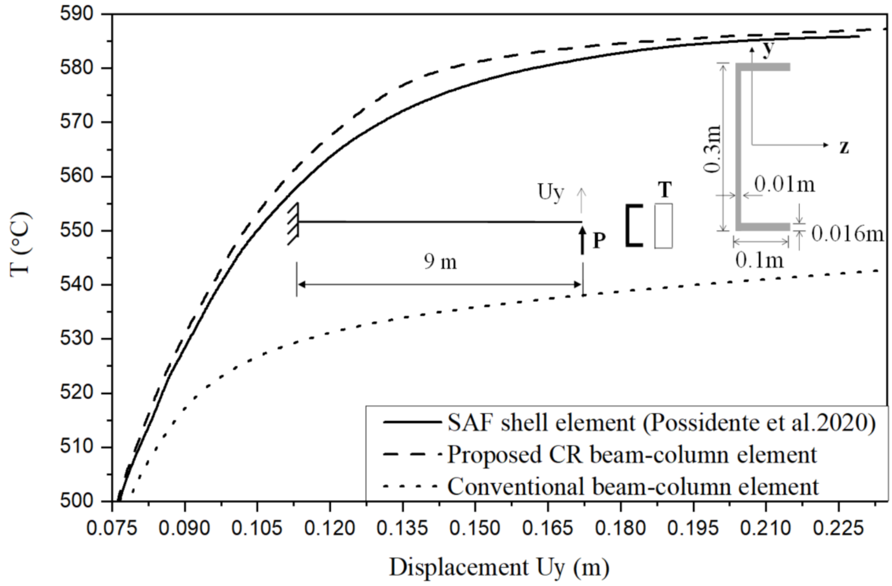

(b) In-plane displacement

Figure 7.7 Temperature-displacement cures for the cantilever beam

Example 4: Nonlinear analysis of steel beams with nonsymmetric section

A FE model is established to further validate the accuracy of the proposed numerical method. The FE Analysis software version 14.0 (Ansys 2011) is employed for the simulation. A simply supported beam is meshed using a coupled-field element – SOLID226, which has twenty nodes and can be used for Structural-Thermal coupling analysis. The FE model and detailed boundary conditions are given in Figure 7.8. The cross-section dimensions are given in Figure 7.9, and the temperature around the beam is assumed to be uniform. After a series of mesh sensitivity studies, a maximum size of 0.01 m is adopted. The FE model is composed of 52345 SOLID226 elements.

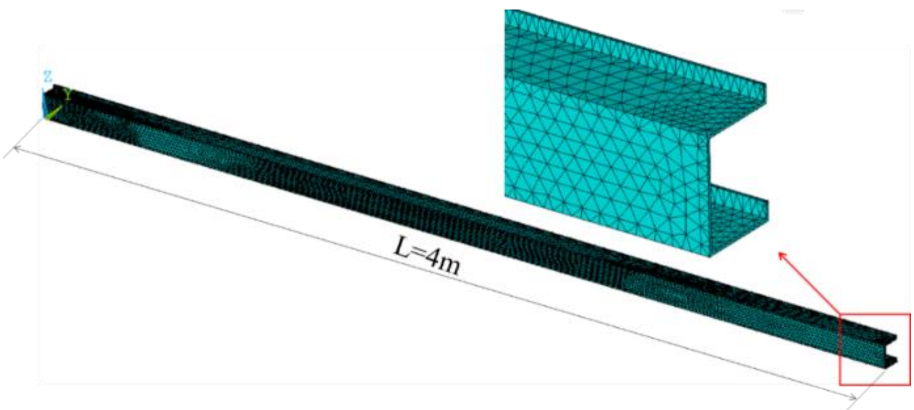

(a) FE model with 52345 solid elements

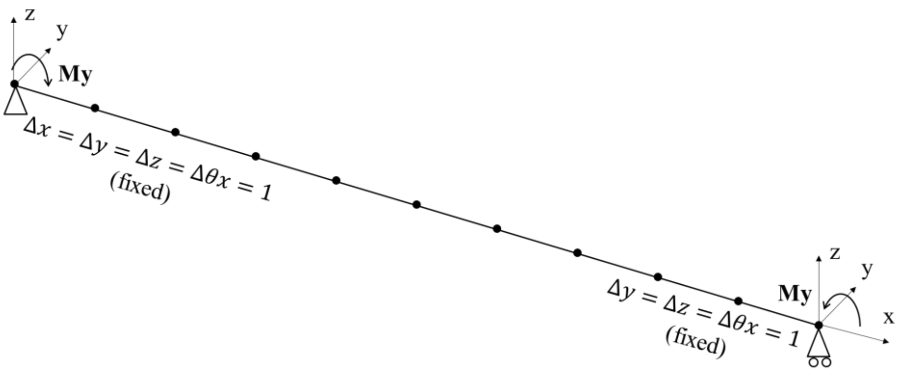

(b) Model with 10 proposed CR elements

Figure 7.8 Model for the nonlinear analysis of the nonsymmetric steel beams

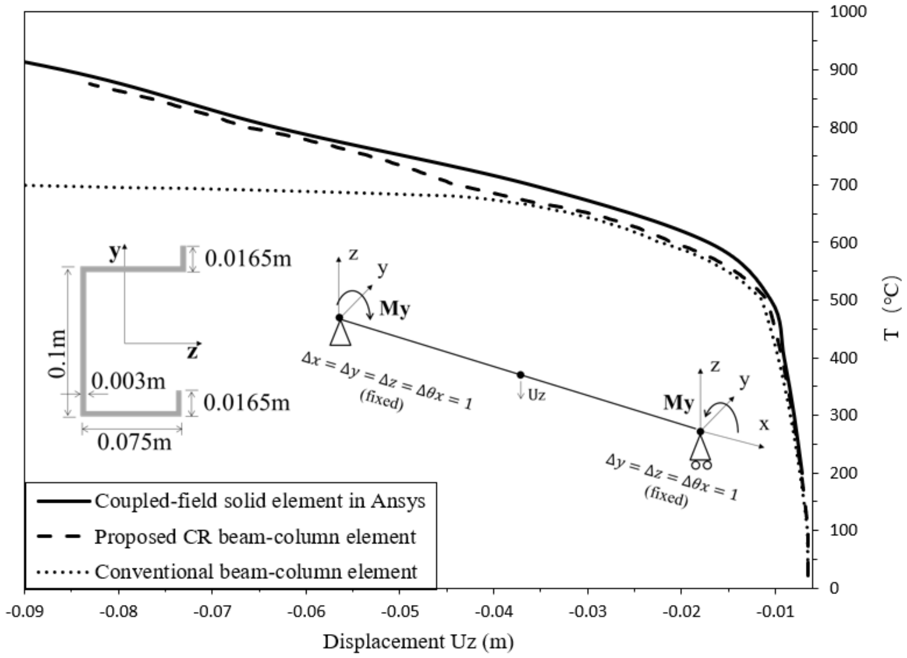

Figure 7.9 Temperature-displacement cures of the nonsymmetric steel beams

Results from the sophisticated FE model, ten proposed CR beam-column elements, and ten conventional beam-column elements with doubly-symmetric-section assumption are given in Figure 7.9 for comparison. The temperature-displacement curve generated from the FE model is taken as the benchmark. From Figure 7.9, large differences can be observed between the results from the conventional beam-column elements and those from the FE model, showing the necessity of the proposed method. While the temperature-displacement curves from the proposed method and the FE model are kept in line with each other in the entire heating process, demonstrating that the proposed method is accurate for the nonlinear analysis of steel members with nonsymmetric sections at elevated temperatures.

Example 5: Nonlinear analysis of a star frame with T section

In this example, a star frame is studied. The boundary and loading conditions of the star frame are given in Figure 7.10. The frame is under a constant load P=3kN and has six pin supports with thermal expansion restrained. The span and height of the frame are 8m and 0.4m, respectively. There are six beams with a T shape section in the star frame. The width and depth of the T section are 0.1 m, and the flange thickness and web thickness are 0.011 m.

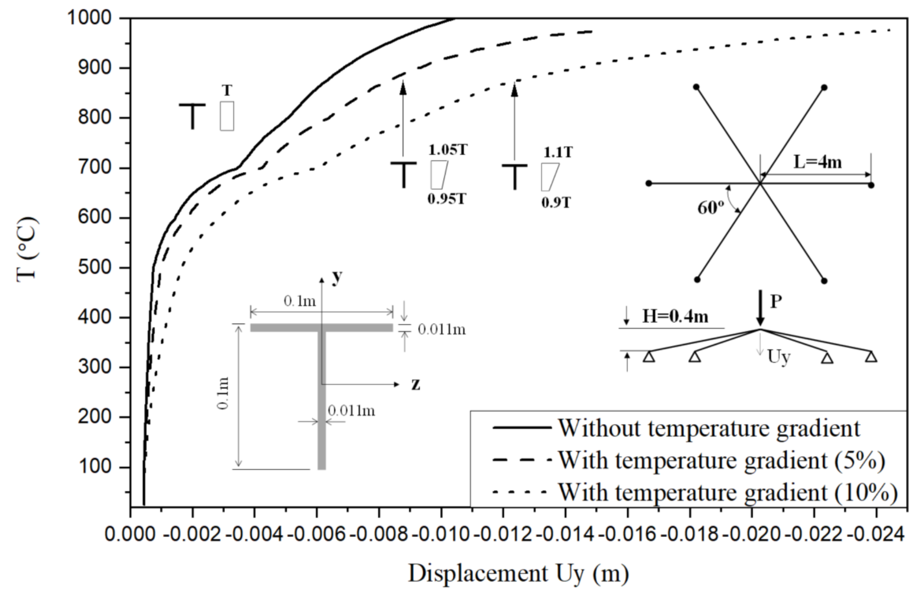

Figure 7.10 Temperature-displacement at the middle span of the star frame

The temperature-displacement cures of the star frame under three different thermal conditions, uniformly elevated temperatures, elevated temperatures with a 5% temperature gradient, and elevated temperatures with a 10% temperature gradient, are given in Figure 7.10. The results show that the applied load is relatively small, with only 0.004m initial displacement. However, with the temperature rise, a more significant displacement will occur. Since the deterioration rate of the material Young's modulus will change dramatically at 700℃, there is a kink on the temperature-displacement cure when the temperature reaches 700℃. It is also worth noting that only a slight temperature gradient (5%) can significantly reduce the structural capacity as expected since the softened material reduces stiffness considerably. Further, analysis without consideration of temperature gradient is insufficiently accurate.

CHAPTER 8.

CONCLUSIONS AND RECOMMENDATIONS

8.1 Conclusions

In this thesis, a second-order analysis framework for modern steel frames with nonsymmetric cross-sections is proposed. Cross-section analysis methods are given to calculate the section properties of nonsymmetric thin- and thick-walled sections. Besides, an LFEM with several line element formulations and an inelastic analysis method is developed.

The main findings and contributions of this research are summarized as follows:

1) Comprehensive cross-section analysis methods are proposed to calculate the section properties of nonsymmetric sections. A Coordinate Method (CM) is introduced for the thin-walled sections, while a 2D Finite Element (FE) method is given for the thick-walled sections. Five special section properties for the nonsymmetric sections, including the coordinates of the shear center (zs and ys) and the Wagner coefficients (βy, βz, and βω), and the shear coefficients of nonsymmetric thick-walled sections can be generated accordingly.
2) The LFEM for the second-order analysis of members with nonsymmetric cross-sections is further developed. A refined line element and an improved line element are proposed for members with nonsymmetric thin-walled sections. The element formulations are derived based on the nonsymmetrical section assumption. The Wagner effects and the noncoincidence of the shear

center and centroid of the nonsymmetric sections are directly considered, and therefore, the lateral-torsional and flexural-torsional of nonsymmetric section members can be captured robustly.

3) An improved Timoshenko line element for the second-order analysis of nonsymmetric thick-walled members is derived. The non-negligible shear deformation in nonsymmetric thick-walled members is considered by incorporating the shear deformation in the element stiffness matrices.
4) An inelastic analysis method for the members with nonsymmetric cross-sections is proposed, where the concentrated plasticity (CP) model is integrated into the line element formulation, and the modified tangent modulus (MTM) approach is adopted to represent partial material yielding. A yield surface, describing the full yield capacity of a nonsymmetric section, is given to evaluate the full-yield condition, and the gradients to the yield surfaces are calculated and used to control the plastic flow.
5) An analysis method for the members with nonsymmetric sections under fire conditions is introduced. A novel line element formulation based on the co-rotational (CR) method is developed. The proposed CR line element can conveniently consider the material degradation and the thermal expansion. A Newton-Raphson-typed numerical procedure for the analysis at elevated temperatures is proposed and elaborated.

8.2 Recommendations for Future Work

This thesis proposes a second-order analysis framework for the modern steel frames with nonsymmetric cross-sections, including cross-section analysis methods, line elements allowing for warping effects, shear deformation, and material yielding. A second-order elastic analysis method for the nonsymmetric members under fire conditions is also proposed. Some studies, however, are needed to be conducted in the future.

a) To extend the framework for dynamic analysis. Structural dynamic analysis is essential for the design of steel structures in some extreme scenarios, such as earthquakes. The behaviors of steel frames with nonsymmetric cross-sections need to be further investigated.
b) To incorporate plastic analysis into the second-order analysis method for the nonsymmetric members under fire conditions. Steel structures subjected to fire typically undergo plastic deformations. The consideration of the material nonlinearity is important for steel structures subjected to fire.
c) To consider the effects of semi-rigid joints. In this research, all member connections are assumed pinned or rigid. However, the member connections are neither rigid nor pinned in the practical structures, and therefore, the effects of semi-rigid joints should be considered.
d) To consider the member local buckling. Local buckling is a failure mode commonly observed in thin-walled steel structural members. The such effect should be considered in further research.
e) To consider the distortion of the cross-section. In this research, the cross-section shape of a member is assumed to be sustained when exposed to loads and deformations, which may be inconsistent with the actual structural behaviors. The distortion of the cross-section should be considered in further studies.

f) To extend the framework for the nonsymmetric built-up members. The built-up cold-formed steel members with bolted interconnections are more commonly used in modern structures. The structural behaviors of such members need to be further investigated.

REFERENCES

Abdelrahman, AHA, Liang Chen, Si-Wei Liu, and Ronald D Ziemian. 2022. 'Timoshenko line-element for stability analysis of tapered I-section steel members considering warping effects', *Thin-Walled Structures*, 175: 109198.

Ádány, Sándor, and Benjamin W Schafer. 2014. 'Generalized constrained finite strip method for thin-walled members with arbitrary cross-section: Primary modes', *Thin-Walled Structures*, 84: 150-69.

AISC. 2016. 'ANSI/AISC 360-16: Specification for structural steel buildings'. American Institute of Steel Construction.

Alsafadie, R, Mohammed Hjiaj, and J-M Battini. 2010. 'Corotational mixed finite element formulation for thin-walled beams with generic cross-section', *Computer Methods in Applied Mechanics and Engineering*, 199: 3197-212.

Ansys. 2011. Version 14.0, 'ANSYS users manual', *Ansys Inc*. http://www.ansys.com

Arboleda-Monsalve, Luis G, David G Zapata-Medina, and J Dario Aristizabal-Ochoa. 2008. 'Timoshenko beam-column with generalized end conditions on elastic foundation: Dynamic-stiffness matrix and load vector', *Journal of Sound and Vibration*, 310: 1057-79.

Argyris, John. 1982. 'An excursion into large rotations', *Computer Methods in Applied Mechanics and Engineering*, 32: 85-155.

Bai, Rui, Wen-Long Gao, Si-Wei Liu, and Siu-Lai Chan. 2020. "Innovative high-order beam-column element for geometrically nonlinear analysis with one-element-per-member modelling method." In *Structures*, 542-52. Elsevier.

Bathe, KJ. 1999. 'ADINA–Automatic Dynamic Incremental Nonlinear Analysis System', *ADINA Engineering, Watertown, MA*.

Bathe, Klaus-Jürgen. 2006. *Finite element procedures* (Klaus-Jurgen Bathe).

Bathe, Klaus-Jürgen. 2007. 'Finite element method', *Wiley encyclopedia of computer science and engineering*: 1-12.

Bathe, Klaus-Jürgen, and Said Bolourchi. 1979. 'Large displacement analysis of three-dimensional beam structures', *International journal for numerical methods in engineering*, 14: 961-86.

Battini, J. M. 2002. 'Co-rotational beam elements in instability problems', *Natural ences*.

Bian, Guanbo, Kara D Peterman, Shahabeddin Torabian, and Benjamin W Schafer. 2016. 'Torsion of cold-formed steel lipped channels dominated by warping response', *Thin-Walled Structures*, 98: 565-77.

Bleich, Friedrich. 1952. *Buckling strength of metal structures* (McGraw-Hill).

Bourihane, Oussama, Aberrahmane Ed-Dinari, Bouazza Braikat, Mohammad Jamal, Foudil Mohri, and Noureddine Damil. 2016. 'Stability analysis of thin-walled beams with open section subject to arbitrary loads', *Thin-Walled Structures*, 105: 156-71.

Bradford, Mark A, and Gregory J Hancock. 1984. 'Elastic interaction of local and lateral buckling in beams', *Thin-Walled Structures*, 2: 1-25.

Bradford, Mark A., and Peter E. Cuk. 1988. 'Elastic Buckling of Tapered Monosymmetric I‐Beams', *Journal of Structural Engineering*, 114: 977-96.

Bradford, Mark Andrew. 1986. 'Inelastic distortional buckling of I-beams', *Computers & structures*, 24: 923-33.

Bradford, Mark Andrew, and Hamid Reza Ronagh. 1997. 'Generalized Elastic Buckling of Restrained I-Beams by FEM', *Journal of Structural Engineering*, 123: 1631-37.

Caillerie, Denis, Panagiotis Kotronis, and Robert Cybulski. 2015. 'A Timoshenko finite element straight beam with internal degrees of freedom', *International Journal for Numerical and Analytical Methods in Geomechanics*, 39: 1753-73.

Chan, Siu-Lai, and S. Kitipornchai. 1987. 'Geometric nonlinear analysis of asymmetric thin-walled beam-columns', *Engineering Structures*, 9: 243-54.

Chan, Siu-Lai, and Jian-Xin Gu. 2000. 'Exact tangent stiffness for imperfect beam-column members', *Journal of structural engineering*, 126: 1094-102.

Chan, Siu-Lai, and SH Cho. 2008. 'Second-order analysis and design of angle trusses Part I: Elastic analysis and design', *Engineering Structures*, 30: 616-25.

Chan, Siu-Lai, and PPT Chui. 2009. 'Non-linear static analysis allowing for plastic hinges and semi-rigid joints', *Non-Linear Static and Cyclic Analysis of Steel Frames with Semi-Rigid Connections, SLCPT Chui, Elsevier Science Ltd, Oxford*: 123-94.

Chen, Liang, AHA Abdelrahman, Si-Wei Liu, Ronald D Ziemian, and Siu-Lai Chan. 2021. 'Gaussian Beam–Column Element Formulation for Large-Deflection Analysis of Steel Members with Open Sections Subjected to Torsion', *Journal of Structural Engineering*, 147: 04021206.

Chen, Liang, Si-Wei Liu, and Siu-Lai Chan. 2017. 'Divergence-free algorithms for moment-thrust-curvature analysis of arbitrary sections', *Steel and Composite Structures*, 25: 557-69.

Chen, Wai-Fah, and Toshio Atsuta. 2007. *Theory of beam-columns, volume 2: space behavior and design* (J. Ross Publishing).

Chen, Wai-Fah, and Eric M Lui. 1987. 'Effects of joint flexibility on the behavior of steel frames', *Computers & Structures*, 26: 719-32.

Chen, Wai F, and Toshio Atsuta. 1972. 'Interaction equations for biaxially loaded sections', *Journal of the Structural Division*, 98: 1035-52.

Chen, WF, and Siu-Lai Chan. 1995. 'Second-order inelastic analysis of steel frames using element with midspan and end springs', *Journal of Structural Engineering*, 121: 530-41.

Connor Jr, Jerome J, Robert D Logcher, and Shing-Ching Chan. 1968. 'Nonlinear analysis of elastic framed structures', *Journal of the Structural Division*, 94: 1525-47.

CoPHK. 2011. "Code of Practice for the Structural Use of Steel 2011." In.: Buildings Department Hong Kong SAR Government.

Craveiro, Helder D., Joao Paulo C. Rodrigues, and Luis Laim. 2014. 'Cold-formed steel columns made with open cross-sections subjected to fire', *Thin-Walled Structures*, 85: 1–14.

Davies, Mfcwm. 2003. 'Structural behavior of cold-formed thin-walled short steel channel columns at elevated temperatures. Part 1: experiments', *Thin-Walled Structures*.

Davis, R, RD Henshell, and GB Warburton. 1972. 'A Timoshenko beam element', *Journal of Sound and Vibration*, 22: 475-87.

De Sanctis, Gianluca, Mario Fontana, and Michael H Faber. 2014. "Assessing the level of safety for performance based and prescriptive structural fire design of steel structures." In *Proceedings of the 11th International Symposium on Fire Safety Science*. ETH-Zürich.

Ding, Yang, and TL Zhang. 2019. 'Research on influence of member initial curvature on stability of single-layer spherical reticulated domes', *Adv. Steel Constr*, 15: 9-15.

Dinis, Pedro B, Dinar Camotim, Kostas Belivanis, Colter Roskos, and Todd Helwig. 2015. "On the Buckling, Post-Buckling and Strength Behavior of Thin-Walled Unequal-Leg Angle Columns." In *Proceedings of the Annual Stability Conference Structural Stability Research Council: Structural Stability Research Council Nashville, Tennessee*.

Driscoll, George C. 1965. *Plastic design of multi-story frames* (Fritz Engineering Laboratory).

Du, Zuo-Lei, Yao-Peng Liu, and Siu-Lai Chan. 2017. 'A second-order flexibility-based beam-column element with member imperfection', *Engineering Structures*, 143: 410-26.

Dwaikat, MMS, and VKR Kodur. 2011. 'A performance based methodology for fire design of restrained steel beams', *Journal of Constructional Steel Research*, 67: 510-24.

Edem, Ini B. 2006. 'The exact two-node Timoshenko beam finite element using analytical bending and shear rotation interdependent shape functions', *International Journal for Computational Methods in Engineering Science and Mechanics*, 7: 425-31.

El Masri, Omar Y, and Eric M Lui. 2019. 'Cross-section properties and elastic lateral-torsional buckling capacity of steel delta girders', *International Journal of Steel Structures*, 19: 914-31.

Elkaimbillah, Ahmed, Bouazza Braikat, Foudil Mohri, and Noureddine Damil. 2021. 'A one-dimensional model for computing forced nonlinear vibration of thin-walled composite beams with open variable cross-sections', *Thin-Walled Structures*, 159: 107211.

Feng, De-Cheng, and Jian-Ying Wu. 2020. 'Improved displacement-based Timoshenko beam element with enhanced strains', *Journal of structural engineering*, 146: 04019221.

Feng, M., Y. C. Wang, and J. M. Davies. 2003a. 'Structural behavior of cold-formed thin-walled short steel channel columns at elevated temperatures. Part 2: Design calculations and numerical analysis', *Thin-Walled Structures*, 41: 571-94.

Feng, M., W. Yong, and J. M. Davies. 2002. 'Behavior of cold-formed thin-walled steel short columns with service holes at elevated temperatures'.

Feng, Min, Yu-Chun Wang, and JM Davies. 2003b. 'Axial strength of cold-formed thin-walled steel channels under non-uniform temperatures in fire', *Fire Safety Journal*, 38: 679-707.

Framecad, 2019. How Cold Formed Steel Opens up Design Flexibility. https://blog.framecad.com/blog/how-cold-formed-steel-opens-up-design-flexibility

Friedman, Z, and John B Kosmatka. 1993. 'An improved two-node Timoshenko beam finite element', *Computers & Structures*, 47: 473-81.

Galambos, Theodore V. 2016. *Structural members and frames* (Courier Dover Publications).

Gao, W. L., Aha Abdelrahman, S. W. Liu, and R. D. Ziemian. 2021. 'Second-order dynamic time-history analysis of beam-columns with nonsymmetrical thin-walled steel sections', *Thin-Walled Structures*, 160: 107367.

Gere, James M, and Stephen P Timoshenko. 1991. 'Mechanics of Materials, 3rd SI ed', *Nelson Thornes Ltd*.

Gonçalves, Rodrigo, Manuel Ritto-Corrêa, and Dinar Camotim. 2010. 'A new approach to the calculation of cross-section deformation modes in the framework of generalized beam theory', *Computational Mechanics*, 46: 759-81.

Gruttmann, F, R Sauer, and W Wagner. 2000. 'Theory and numerics of three-dimensional beams with elastoplastic material behavior', *International journal for numerical methods in engineering*, 48: 1675-702.

Gruttmann, F, RAWW Sauer, and W Wagner. 1998. 'A geometrical nonlinear eccentric 3D-beam element with arbitrary cross-sections', *Computer Methods in Applied Mechanics and Engineering*, 160: 383-400.

Gruttmann, F, and W Wagner. 2001. 'Shear correction factors in Timoshenko's beam theory for arbitrary shaped cross-sections', *Computational mechanics*, 27: 199-207.

Hancock, Gregory J, and Kim JR Rasmussen. 2016. 'Formulation and Implementation of General Thin-Walled Open-Section Beam-Column Elements in Opensees (No. R961)'.

Hancock, Gregory J, and Kim JR Rasmussen. 2020. 'Geometric and material nonlinear analysis of thin-walled members with arbitrary open cross-section', *Thin-Walled Structures*, 153: 106783.

Herrmann, Leonard R. 1965. 'Elastic torsional analysis of irregular shapes', *Journal of the Engineering Mechanics Division*, 91: 11-19.

Hsiao, Kuo Mo, and Wen Yi Lin. 2000. 'A co-rotational formulation for thin-walled beams with monosymmetric open section', *Computer methods in applied mechanics and engineering*, 190: 1163-85.

Huang, Z. F., and K. H. Tan. 2007. 'FE SIMULATION OF SPACE STEEL FRAMES IN FIRE WITH WARPING EFFECT', *Advanced Steel Construction*, 3: 652-67.

Iu, Chi Kin, and Siu Lai Chan. 2004. 'A simulation-based large deflection and inelastic analysis of steel frames under fire', *Journal of constructional steel research*, 60: 1495-524.

Iu, Chi Kin, Siu Lai Chan, and Xiao Xiong Zha. 2005. 'Nonlinear pre-fire and post-fire analysis of steel frames', *Engineering Structures*, 27: 1689-702.

Izzuddin, BA, and D Lloyd Smith. 1996. 'Large-displacement analysis of elastoplastic thin-walled frames. 1. Formulation and implementation'.

Jiang, Jian, Asif Usmani, and Guo-Qiang Li. 2014. 'Modelling of steel-concrete composite structures in fire using OpenSees', *Advances in Structural Engineering*, 17: 249-64.

Kathir, 2017. STEEL STRUCTURE. https://civilsnapshot.com/classification-steel-structures/

Kim, Boksun, Long-yuan, Cheng, and Shanshan. 2015. 'Buckling analysis of cold-formed steel channel-section beams at elevated temperatures', *Journal of Constructional Steel Research*.

Kim, MY, SP Chang, and SB Kim. 1996. 'Spatial stability analysis of thin-walled space frames', *International journal for numerical methods in engineering*, 39: 499-525.

Kim, Nam-Il, and Moon-Young Kim. 2005. 'Exact dynamic/static stiffness matrices of non-symmetric thin-walled beams considering coupled shear deformation effects', *Thin-Walled Structures*, 43: 701-34.

Kim, Sung Bo, and Moon Young Kim. 2000. 'Improved formulation for spatial stability and free vibration of thin-walled tapered beams and space frames', *Engineering Structures*, 22: 446-58.

King, WS, DW White, and WF Chen. 1992. 'Second-order inelastic analysis methods for steel-frame design', *Journal of Structural Engineering*, 118: 408-28.

Kitipornchai, Sritawat, and Nicholas S Trahair. 1972. 'Elastic stability of tapered I-beams', *Journal of the Structural Division*, 98.

Kitipornchai, Sritawat, and Nicholas Snowden Trahair. 1975. 'Elastic behavior of tapered monosymmetric I-beams', *Journal of the Structural Division*, 101.

Krahula, Joseph L, and Gerald F Lauterbach. 1969. 'A finite element solution for Saint-Venant torsion', *AIAA Journal*, 7: 2200-03.

Laím, L, Joo P C Rodrigues, and L. S. Silva. 2013. "NUMERICAL ANALYSIS OF COLD-FORMED STEEL BEAMS IN FIRE." In *International Conference Fire & Materials*.

Laim, Luis, Joao Paulo C Rodrigues, and Helder D Craveiro. 2016. 'Flexural behavior of axially and rotationally restrained cold-formed steel beams subjected to fire', *Thin-Walled Structures*, 98: 39-47.

Laim, Luis, Joao Paulo C. Rodrigues, and Helder David Craveiro. 2015. 'Flexural behavior of beams made of cold-formed steel sigma-shaped sections at ambient and fire conditions', *Thin-Walled Structures*, 87: 53-65.

Li, Guo-Qiang, and Shou-Chao Jiang. 1999. 'Prediction to nonlinear behavior of steel frames subjected to fire', *Fire Safety Journal*, 32: 347-68.

Liew, J. Y. Richard, H. Chen, N. E. Shanmugam, and W. F. Chen. 2000. 'Improved nonlinear plastic hinge analysis of space frame structures', *Engineering Structures*, 22: 1324-38.

Liew, J. Y. Richard, W. F. Chen, and H. Chen. 2000. 'Advanced inelastic analysis of frame structures', *Journal of Constructional Steel Research*, 55: 245-65.

Liew, JY Richard, H Chen, and NE Shanmugam. 1999. 'Stability functions for second-order inelastic analysis of space frames', *Light-Weight Steel and Aluminium Structures*: 19-26.

Liew, JY Richard, LK Tang, and YS Choo. 2002. 'Advanced analysis for performance-based design of steel structures exposed to fires', *Journal of Structural Engineering*, 128: 1584-93.

Liu, S. W., W. L. Gao, and R. D. Ziemian. 2019a. 'Improved line-element formulations for the stability analysis of arbitrarily- shaped open-section beam-columns', *Thin-Walled Structures*, 144: 106290.

Liu, S. W., R. D. Ziemian, C. Liang, and Siu-Lai Chan. 2018. 'Bifurcation and large-deflection analyses of thin-walled beam-columns with non-symmetric open-sections', *Thin-Walled Structures*, 132: 287-301.

Liu, Si-Wei, Wen-Long Gao, and Ronald D Ziemian. 2019b. 'Improved line-element formulations for the stability analysis of arbitrarily-shaped open-section beam-columns', *Thin-Walled Structures*, 144: 106290.

Liu, Si-Wei, Yao-Peng Liu, and Siu-Lai Chan. 2012. 'Advanced analysis of hybrid steel and concrete frames: Part 1: Cross-section analysis technique and second-order analysis', *Journal of Constructional Steel Research*, 70: 326-36.

Liu, Si-Wei, Yao-Peng Liu, and Siu-Lai Chan. 2014a. 'Direct analysis by an arbitrarily-located-plastic-hinge element—part 2: spatial analysis', *Journal of Constructional Steel Research*, 103: 316-26.

Liu, Si-Wei, Yao-Peng Liu, and Siu-Lai Chan. 2014b. 'Direct analysis by an arbitrarily-located-plastic-hinge element — Part 1: Planar analysis', *Journal of Constructional Steel Research*, 103: 303-15.

Liu, Si-Wei, Ronald D Ziemian, Liang Chen, and Siu-Lai Chan. 2018. 'Bifurcation and large-deflection analyses of thin-walled beam-columns with non-symmetric open-sections', *Thin-Walled Structures*, 132: 287-301.

Machado, Sebastián P. 2008. 'Non-linear buckling and postbuckling behavior of thin-walled beams considering shear deformation', *International Journal of Non-Linear Mechanics*, 43: 345-65.

Magalhaes de Souza, R. 2000. 'Force-based finite element for large displacement inelastic analysis of frames', *University of California, Berkeley*.

Martins, André Dias, Dinar Camotim, and Pedro Borges Dinis. 2018. 'Distortional-global interaction in lipped channel and zed-section beams: Strength, relevance and DSM design', *Thin-Walled Structures*, 129: 289-308.

Mason Jr, William E, and Leonard R Herrmann. 1968. 'Elastic shear analysis of general prismatic beams', *Journal of the Engineering Mechanics Division*, 94: 965-83.

McGuire, William, Richard H Gallagher, and Ronald D Ziemian. 2000. *Matrix structural analysis*.

Mohri, F, A Brouki, and JC Roth. 2003. 'Theoretical and numerical stability analyses of unrestrained, mono-symmetric thin-walled beams', *Journal of Constructional Steel Research*, 59: 63-90.

Murín, J, M Aminbaghai, V Kutiš, V Královič, T Sedlár, V Goga, and H Mang. 2014. 'A new 3D Timoshenko finite beam element including non-uniform torsion of open and closed cross sections', *Engineering Structures*, 59: 153-60.

Neuenhofer, Ansgar, and Filip C Filippou. 1997. 'Evaluation of nonlinear frame finite-element models', *Journal of structural engineering*, 123: 958-66.

Park, Kyoungsoo, Hyungtae Kim, and Dae-Jin Kim. 2019. 'Generalized finite element formulation of fiber beam elements for distributed plasticity in multiple regions', *Computer-Aided Civil and Infrastructure Engineering*, 34: 146-63.

Parkinson, David L, Venkatesh Kodur, and Paul D Sullivan. 2009. "Performance-Based Design of Structural Steel for Fire Conditions: A Calculation Methodology." In.: American Society of Civil Engineers USA.

Pi, Y-L, and MA Bradford. 2001. 'Effects of approximations in analyses of beams of open thin-walled cross-section—part I: Flexural–torsional stability', *International journal for numerical methods in engineering*, 51: 757-72.

Porter, Frank L, and Graham H Powell. 1971. *Static and dynamic analysis of inelastic frame structures* (University of California, College of Engineering, Earthquake Engineering …).

Possidente, L., N. Tondini, and J. M. Battini. 2020. '3D Beam Element for the Analysis of Torsional Problems of Steel-Structures in Fire', *Journal of Structural Engineering*, 146.

Prokić, A. 1993. 'Thin-walled beams with open and closed cross-sections', *Computers & structures*, 47: 1065-70.

Qureshi, Ramla, Ruben Van Coile, Danny Hopkin, Thomas Gernay, and Negar Elhami Khorasani. 2020. "A practical tool for evaluating fire induced failure probability of steel columns designed based on US prescriptive standards." In *Proceedings of the 11th International Conference on Structures in Fire (SiF2020)*.

Rasmussen, Kim J. R., Xi Zhang, and Hao Zhang. 2016a. 'Beam-element-based analysis of locally and/or distortionally buckled members: Theory', *Thin-Walled Structures*, 98: 285-92.

Rinchen, Gregory J. Hancock, and Kim J. R. Rasmussen. 2020. 'Geometric and material nonlinear analysis of thin-walled members with arbitrary open cross-section', *Thin-Walled Structures,* 153: 106783.

Saadé, Katy, Bernard Espion, and Guy Warzée. 2004. 'Non-uniform torsional behavior and stability of thin-walled elastic beams with arbitrary cross sections', *Thin-walled structures*, 42: 857-81.

Saleeb, AF, TYP Chang, and AS Gendy. 1992. 'Effective modelling of spatial buckling of beam assemblages, accounting for warping constraints and rotationdependency of moments', *International journal for numerical methods in engineering*, 33: 469-502.

Salvadori, Mario G. 1956. 'Lateral buckling of eccentrically loaded I-columns', *Transactions of the American Society of Civil Engineers*, 121: 1163-78.

Schafer, Benjamin W, and Teoman Peköz. 1998. 'Computational modeling of cold-formed steel: characterizing geometric imperfections and residual stresses', *Journal of constructional steel research*, 47: 193-210.

Schafer, BW. 2002. 'Local, distortional, and Euler buckling of thin-walled columns', *Journal of structural engineering*, 128: 289-99.

Schramm, Uwe, Levent Kitis, Weize Kang, and Walter D Pilkey. 1994. 'On the shear deformation coefficient in beam theory', *Finite Elements in Analysis and Design*, 16: 141-62.

Seaburg P A, Carter C J. Torsional analysis of structural steel members. No. D809 (5M297). 1997.

Shakourzadeh, H, YQ Guo, and J-L Batoz. 1995. 'A torsion bending element for thin-walled beams with open and closed cross sections', *Computers & Structures*, 55: 1045-54.

So, Andrew Kwok Wai, and Siu-Lai Chan. 1991. 'Buckling and geometrically nonlinear analysis of frames using one element/member', *Journal of constructional steel research*, 20: 271-89.

Standard, British. 1998. "BS 5950–5: Structural Use of Steelworks in Building. Part 5. Code of Practice for Design of Cold-Formed Thin Gauge Sections." In.: British Standards Institution London, UK.

SteelConstruction.info. Modular construction. https://www.steelconstruction.info

Tang, Yi-Qun, Yao-Peng Liu, Siu-Lai Chan, and Er-Feng Du. 2019. 'An innovative co-rotational pointwise equilibrating polynomial element based on Timoshenko beam theory for second-order analysis', *Thin-Walled Structures*, 141: 15-27.

Tang, YQ, YP Liu, and Siu-Lai Chan. 2018. 'A co-rotational framework for quadrilateral shell elements based on the pure deformational method', *Advanced Steel Construction*, 14: 90-114.

Teh, Lip H, and Murray J Clarke. 1998. 'Co-rotational and Lagrangian formulations for elastic three-dimensional beam finite elements', *Journal of Constructional Steel Research*, 48: 123-44.

Thai, Huu-Tai, and Seung-Eock Kim. 2011. 'Nonlinear inelastic analysis of space frames', *Journal of Constructional Steel Research*, 67: 585-92.

Thyssenkrupp, 2016. Product information for pickled hot-rolled steel with very tight thickness tolerances. https://www.thyssenkrupp-steel.com

Timoshenko, Stephen P, and James M Gere. 1961. 'Theory of elastic stability. 1961', *McGrawHill-Kogakusha Ltd, Tokyo*: 9-16.

Vlasov, Vasiliĭ Zakharovich. 1962. *Thin-walled elastic beams* (National Technical Information Service).

Vogel, U. 1985. 'Calibrating Frames', *Stahlbau,* 54: 295-301.

Wang, Wei-yong, Bing Liu, and Venkatesh Kodur. 2013. 'Effect of temperature on strength and elastic modulus of high-strength steel', *Journal of materials in civil engineering*, 25: 174-82.

Wang, YC, and DB Moore. 1995. 'Steel frames in fire: analysis', *Engineering Structures*, 17: 462-72.

White, Donald W, and Jerome F Hajjar. 1991. 'Application of second-order elastic analysis in LRFD: research to practice', *Engineering Journal,* 28: 133-48.

Xia, Bing, Yuching Wu, and Zhanfei Huang. 2012. 'Implementation of total Lagrangian formulation for the elasto-plastic analysis of plane steel frames exposed to fire', *Frontiers of Structural and Civil Engineering*, 6: 257-66.

Yang, YB, Anquan Chen, Yuanyuan Yan, and Zhilu Wang. 2019. 'Using only elastic stiffness in nonlinear and postbuckling analysis of structures', *International Journal of Structural Stability and Dynamics*, 19: 1950112.

Yang, Yeong Bin. 1987. 'Stability of thin-walled beams—a general theory.' in, *Shell and Spatial Structures: Computational Aspects* (Springer).

Yang, Yeong Bin, and William McGuire. 1986. 'Stiffness matrix for geometric nonlinear analysis', *Journal of structural engineering*, 112: 853-77.

Yu, Cheng, and Benjamin W Schafer. 2007. 'Simulation of cold-formed steel beams in local and distortional buckling with applications to the direct strength method', *Journal of constructional steel research*, 63: 581-90.

Zhang, Xi, Kim JR Rasmussen, and Hao Zhang. 2015. 'Beam-element-based analysis of locally and/or distortionally buckled members: Application. ' Thin-Walled Structures 95 (2015): 127-137.

Zhang, Yijian, and Iris Tien. 2020. 'Methodology for regularization of force-based elements to model reinforced concrete columns with short lap Splices', *Journal of Engineering Mechanics*, 146: 04020073.

Ziemian, CW, and RD Ziemian. 2021. 'Efficient geometric nonlinear elastic analysis for design of steel structures: Benchmark studies', *Journal of constructional steel research*, 186: 106870.

Ziemian, Ronald D. 2010. *Guide to stability design criteria for metal structures* (John Wiley & Sons).

Ziemian, Ronald D, and William McGuire. 2002. 'Modified tangent modulus approach, a contribution to plastic hinge analysis', *Journal of Structural Engineering*, 128: 1301-07.

Ziemian, Ronald D, William McGuire, and Gregory G Deierlein. 1992. 'Inelastic limit states design. Part I: Planar frame studies', *Journal of Structural Engineering*, 118: 2532-49.

Zienkiewicz, Olek C, Robert Leroy Taylor, and Jian Z Zhu. 2005. *The finite element method: its basis and fundamentals* (Elsevier).